



HAL
open science

Nanoparticles syntheses and assemblies

Céline Burel

► **To cite this version:**

Céline Burel. Nanoparticles syntheses and assemblies. Chemical Physics [physics.chem-ph]. Université Pierre et Marie Curie - Paris VI, 2017. English. NNT : 2017PA066207 . tel-01680738v2

HAL Id: tel-01680738

<https://theses.hal.science/tel-01680738v2>

Submitted on 12 Jan 2018

HAL is a multi-disciplinary open access archive for the deposit and dissemination of scientific research documents, whether they are published or not. The documents may come from teaching and research institutions in France or abroad, or from public or private research centers.

L'archive ouverte pluridisciplinaire **HAL**, est destinée au dépôt et à la diffusion de documents scientifiques de niveau recherche, publiés ou non, émanant des établissements d'enseignement et de recherche français ou étrangers, des laboratoires publics ou privés.

Thèse présentée à
L'Université Pierre et Marie Curie
Ecole doctorale de Physique et Chimie des Matériaux

Synthèses et assemblages de nanoparticules

Nanoparticles syntheses and assemblies

par

Céline Burel

en vue de l'obtention du grade de

Docteur

Spécialité : Physique et Chimie des Matériaux

Le 25 septembre 2017

Devant le jury composé de :

Dr Véronique Schmitt	Directeur de recherche, CNRS, CRPP, Bordeaux	Rapporteur
Dr Benjamin Abécassis	Chargé de recherche, CNRS, ENS, Lyon	Rapporteur
Dr Jean-Baptiste Salmon	Chargé de recherche, CNRS, LOF, Bordeaux	Examineur
Dr Jean-François Joanny	Directeur de recherche, CNRS, UPMC, Paris	Examineur
Dr Rémi Dreyfus	Chargé de recherche, CNRS, COMPASS, Bristol, USA	Directeur
Dr Bertrand Donnio	Directeur de recherche, CNRS, IPCMS, Strasbourg	Co-directeur
Dr Ahmed Alsayed	Chercheur, Solvay, Bristol, USA	Invité

“The important thing in life is not the triumph but the struggle”.

Pierre de Coubertain

Acknowledgments

There are many people without whom this thesis could not have been carried out. I am greatly indebted to all of them. First and foremost, I would like to express my gratitude to both my advisors, Rémi Dreyfus and Bertrand Donnio, for accepting me as their student. During my time, they contributed to an enriching research experience by giving me broad intellectual freedom in my research and by supporting my attendance at various conferences. Rémi, you have always engaged me in new ideas, and demanded a high quality of work from me in all my endeavors. Thank you so much for always pushing me further and for teaching me how to highlight and promote my work. *Trugarez dit* Bertrand for your most valuable input to the many discussions that helped shape this project. I have always much-appreciated your constant support and optimism. Additionally, I would like to thank my reviewers Dr. Véronique Schmitt and Dr. Benjamin Abécassis for their assessment of my work as well as for their useful comments and suggestions. I also thank Dr. Jean-François Joanny for accepting to chair the examinations board.

Every result described in this thesis was accomplished with the help and support of fellow lab mates and collaborators at the Laboratory of the Future, Complex Assemblies of Soft Matter and University of Pennsylvania. My sincere thanks go to Larry Hough, Jean-Yves Delannoy and Denis Bendejacq who provided me an opportunity to join COMPASS. I am indebted to Dr. Jean-Baptiste Salmon who hosted me at the LOF for about a year while I was waiting for my visa and taught me the technique of microfluidic pervaporation. Jean-Baptiste you also deserve credit for initiating me to Matlab. I deeply want to thank Ahmed Alsayed who provided scientific insight and expertise that greatly assisted the research. I gained a lot from his vast chemistry knowledge and scientific curiosity, his knack for solving technical difficulties and his cheerful mental support. I also want to acknowledge the participation of Ludivine Malassis in the beginning of the project and without whom my work would have undoubtedly been more difficult. I also greatly benefited from her personal scientific experience throughout my time at COMPASS. I am grateful to Professor Chris Murray and Professor Arjun Yodh for hosting me at UPenn for two years and graciously allowing me to use their facilities.

During my Ph.D., I had the opportunity to mentor two students, Balkis and Sarah, who tirelessly and with much enthusiasm tackled difficult projects over the course of two summers. I was also fortunate to have the chance to work with Stan Najmr, who patiently taught me his method for synthesizing nanophosphors, in addition to TEM techniques. I would like to show my special appreciation to Jissy José for our fruitful discussions about elastic shells synthesis. I express my sincere gratitude to Rémi Giordanengo, Sylvain Caravieilhés and Courtney Shedden for their advice regarding analyses carried out during my Ph.D.. My truthful thanks also go to Jaime Hutchinson for her valuable help in the set-up of side work antibacterial tests. I would be remiss if I did not thank Lisa DeGeorge and Yolanda Judge, who provided much needed assistance with administrative tasks, reminding me of impending deadlines, helping organizing meetings and

keeping my work running smoothly. I am also grateful for the funding sources that allowed me to pursue my graduate school studies: the ANRT, the GIE-AIFOR, Solvay and the CNRS.

Finally, I would like to acknowledge friends and family who supported me during my time here. First, I truly thank Carl for sticking by my side when I didn't have faith in myself. I feel like we both learned a lot about each other through these past years and I have no doubt it strengthened our relationship for the long ride. I would like to thank the LOF's Ph.D. students and postdocs: Charles, Laura, fréro, Alexis, Sami and Shenghong who made my time in Bordeaux tremendously enjoyable. My ribs are still sore from laughing too hard with you guys, it almost feels like we were meant to meet each other. I would also like to thank my friends from both continents for supporting me throughout this adventure. Kevin, Ben, Thomas, Sabri, Marie, Axel, Cécile, Liz, Tommy, Stephen, Big Mac, Penfold, Marc, John, thank you for all the parties, the many Risk games, helping fixing my car, the numerous food cookout, the unconditional mental support and the English corrections. I will forever be thankful to John and Sherri for being awesome housemates and adoption family. They have been tremendous people to live with. Thank you both for helping whenever I was feeling down or sick. John, thank you for being the best personal bread baker in Philadelphia. Lastly, there are many people who helped me, named and unnamed, on this great adventure and I am grateful to all of them.

TABLE OF CONTENTS

Acknowledgements	3
Introduction and objectives	9

Chapter 1: State of the art

1. Introduction.....	11
2. Nanoparticles properties and applications	11
2.1. Nanoparticles across the ages	11
2.2. Nanoparticles surface plasmon resonance	12
2.2.1. Understanding the surface plasmon resonance.....	12
2.2.2. Factors affecting the plasmon resonance	15
3. Common approaches for synthesis of nanospheres	20
3.1. Gold nanospheres syntheses	20
3.2. Silver nanoparticles syntheses	23
3.3. Formation and growth of nanoparticles	25
4. Nanoparticles self-assemblies.....	28
4.1. Common self-assembly techniques	28
4.1.1. Spontaneous self-assembly.....	28
4.1.2. Directed self-assembly	30
4.2. The microfluidic pervaporation	36
4.3. Assembly on droplets	45
5. Colloidosomes and microcapsules syntheses	53
6. Conclusion	58

Chapter 2: Directed assembly of nanospheres using microfluidic pervaporation

1. Introduction.....	60
2. Fabrication of a microevaporator.	60
2.1. Design of the mask	61

2.2.	Manufacturing of the mold.....	62
2.3.	Fabrication of the PDMS microchip.....	62
3.	Calibration of a microevaporator.....	63
3.1.	Method.....	63
3.2.	Application of the methods to all the channels.....	64
4.	Concentration of colloidal dispersions.....	66
4.1.	Growth of dense states.....	66
4.2.	Particles aggregation during microfluidic pervaporation.....	66
4.3.	Latex particles.....	68
4.3.1.	Commercial latex.....	69
4.3.2.	Homemade polystyrene beads.....	76
4.4.	Gold nanoparticles.....	78
4.4.1.	Synthesis of gold nanospheres.....	78
4.4.2.	Functionalization of gold nanospheres.....	80
4.4.3.	Concentration of gold nanospheres by microfluidic pervaporation.....	81
5.	Conclusion.....	86

Chapter 3: Fabrication of hybrid microcapsules from Pickering emulsions

1.	Introduction.....	89
2.	Gold-silica microcapsules.....	89
2.1.	Pickering emulsion formation.....	90
2.1.1.	Adsorption at the interface.....	90
2.1.2.	Number of nanoparticles.....	91
2.1.3.	Decrease of an energy barrier.....	93
2.2.	Polycondensation of silica at the oil/water interface.....	94
2.3.	Synthesis of gold-silica microcapsules.....	95
2.3.1.	Effect of pH.....	95
2.3.2.	Effect of butanol.....	98
2.3.3.	Effect of PEOS concentration.....	98
2.3.4.	Effect of the oil phase.....	100

3. The silver-silica microcapsules	104
3.1. Pickering emulsion formation	104
3.2. Synthesis of Ag-Si microcapsules	105
4. The gold silver silica microcapsules	107
5. The gold acrylate microcapsules.....	109
5.1. Polymerization of acrylate at the oil/water interface.....	109
5.2. Synthesis of the gold-acrylate microcapsules.....	110
6. Conclusion	112

Chapter 4: Plasmonic microcapsules as optical strain and pH sensors

1. Introduction.....	114
2. Optical strain sensors	115
2.1. Current technologies.....	115
2.2. The gold-silica microcapsules	120
2.2.1. The gold silica microcapsules synthesis.....	120
2.2.2. Fabrication of polymer film doped with gold-silica microcapsules.....	121
2.2.3. Stretching test.....	122
2.2.4. Impact test	127
2.2.5. Perforation test	128
2.2.6. Au-Si microcapsules film aging.....	128
2.3. The gold-acrylate microcapsules	130
2.3.1. Gold-acrylate microcapsules synthesis	130
2.3.2. Fabrication of elastic films doped with elastic microcapsules.....	131
2.3.3. Stretching test.....	132
2.4. Plasmon-based mechanochromic microcapsules vs other strain sensors	133
3. Optical pH sensors	134
3.1. Current technologies.....	134
3.2. pH responsive gold-acrylate microcapsules	138
3.2.1. pH sensitivity of Poly(acrylic acid).....	138
3.2.2. Gold-acrylates microcapsules response to pH	140

3.2.3. Reversibility of the color change	145
3.2.4. Color as a function of pH	146
3.3. pH responsive microcapsules vs other pH sensors	149
4. Conclusion	150
Conclusion and perspectives	152
Bibliography	154
Annex 1: Characterizations	168
Annex 2: Publication	170

Introduction and objectives

In the last few decades, nanoparticles -very tiny dispersions on the nanoscale of materials- have emerged as one of the most interesting and promising building blocks in order to create new materials. They are interesting because they belong to and therefore connect many fields in science, from inorganic chemistry to quantum physics and from organic synthesis to optics. As such, they are remarkable objects to study and they have generated a wave of excitement in many scientific communities. They are also promising because the range of potential applications where these objects play a significant role is enormous and spans many fields such as diagnosis, water purification, surface treatment, bioremediation, electronics, photovoltaics and optics.

Many applications of these objects require fine-tuning and control of the way the nanoparticles are spatially organized. As such, there is a strong need to develop new processes to direct the assembly or self - assembly of nanoparticles. Many underlying general physical rules governing these processes remain to understand, and mastering of the physico-chemistry is a necessity.

In one sentence, my PhD work relates to the assembly of nanoparticles into bulky 3D materials and dispersed spherical materials.

The first chapter is devoted to a general state of the art summary in which this Ph.D. work lies. I will first present spherical gold nanoparticles, which are the ones I mainly studied throughout this work. I will describe their synthesis and I will emphasize on some of their optical properties, specifically their plasmonic properties. I will also describe the common methods used to assemble them.

The second chapter will be devoted to describing my efforts in mastering a specific technique of directed assembly of nanoparticles: the pervaporation technique. I will show how pervaporation can be used to assemble micron-size latex particles and gold nanospheres into nice 3D organized crystalline bulk materials. This work paves the way to further studies on assembling nanoparticles to create electromagnetic metamaterials.

In the third chapter, we will move beyond the assembly of nanoparticles into bulk materials, and show how nanoparticles can be assembled to form hollow hard and soft microcapsules. I have developed a novel way of synthesizing gold nanoparticle - based microcapsules which I will describe in detail in this chapter.

Finally, in the fourth and last chapter of this manuscript, I will present how these gold nanoparticles-based microcapsules can be used to develop new strain and pH sensors based on the optical plasmonic response of the nanoparticles. These sensors have many potential applications and this last part establishes the groundwork for myriad of future interdisciplinary research.

Chapter 1: State of the art

TABLE OF CONTENTS

1. Introduction.....	11
2. Nanoparticles properties and applications	11
2.1. Nanoparticles across the ages	11
2.2. Nanoparticles surface plasmon resonance	12
2.2.1. Understanding the surface plasmon resonance.....	12
2.2.2. Factors affecting the plasmon resonance	15
3. Common approaches for synthesis of nanospheres	20
3.1. Gold nanospheres syntheses	20
3.2. Silver nanoparticles syntheses	23
3.3. Formation and growth of nanoparticles.....	25
4. Nanoparticles self-assemblies.....	28
4.1. Common self-assembly techniques	28
4.1.1. Spontaneous self-assembly.....	28
4.1.2. Directed self-assembly	30
4.2. The microfluidic pervaporation	36
4.3. Assembly on droplets	45
5. Colloidosomes and microcapsules syntheses	53
6. Conclusion	58

1. Introduction

In this chapter, we present the main optical properties of gold and silver nanospheres. We show that their optical properties depend on their size, shape, environment and interparticles' spacing. Then, we detail the main synthetic methods to produce these nanoparticles. We evidence that some synthetic processes are less time consuming than other and allow us to post-functionalize the nanoparticles. We also briefly explain how the nanoparticles form and grow during synthesis. Finally, we present several of the most commonly used nanoparticle self-assembly techniques. Among them, we focus on the microevaporation and the assembly on emulsion droplets because we use these two techniques to design novel optical materials (Chapters 3 and 4).

2. Gold and silver nanoparticles properties and applications

2.1. Nanoparticles across the ages

Nanoparticles have always existed in nature and their history can be traced back in time. Inorganic nanoparticles are naturally produced by volcanic eruptions, forest fires or even microbial processes. The unique optical properties of nanoparticles provide a strong color to the media in which they are dispersed. Therefore, for a long time nanoparticles were used as pigments in the making of glasswares and lusterwares (see Figure 1). By the 4th century, the Romans had colored a glass cup with silver and gold nanoparticles. This cup is one of the most well-known examples of stained glass because it has the ability to change color depending on whether light passes through it or not. It appears red when illuminated from the inside and green when illuminated from the outside. In the 9th century in Mesopotamia, metallic ornaments based on copper and silver nanoparticles were handcrafted.

The most distinctive contribution in the nanoparticles history has been brought a long time after by Michael Faraday about 160 years ago. He synthesized for the first time gold particles the size of which could be controlled by changing the experimental conditions. His synthesis method was based on the reduction of a solution of gold chloride (HAuCl_4) by phosphor. He recognized that the red color of the particle dispersion was due to the small size of the gold particles. He also observed that the color of thin particle films was varying depending on the mechanical compression applied. His discoveries on the electronic and optical properties of nanoparticles led to the emergence of the modern colloidal chemistry¹.

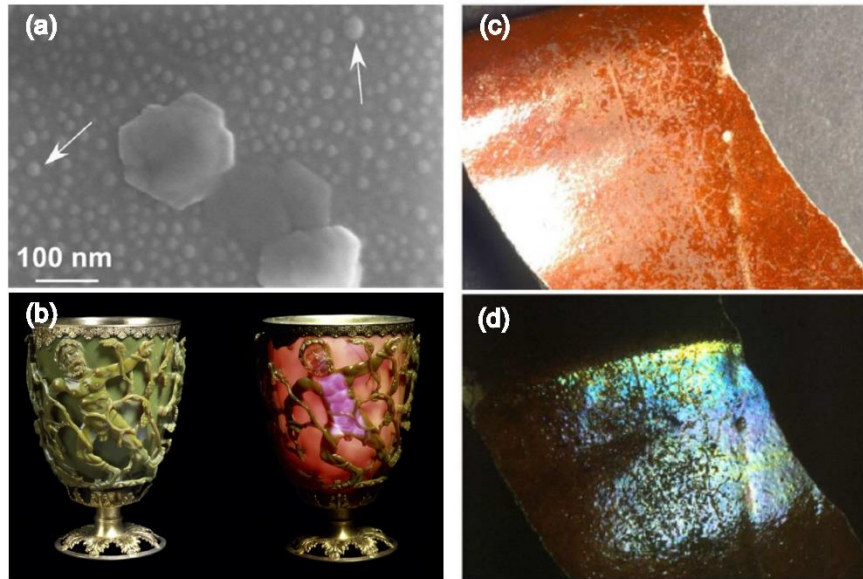


Figure 1 : (a) Gold nanoparticles in a quartz², (b) Roman Lycurgus up, 4th century kept at the British Museum, (c-d) 9th century lusterwares from Mesopotamia³.

2.2. Nanoparticles surface plasmon resonance

2.2.1. Understanding the surface plasmon resonance

Gold and silver are conductive metals. The free electrons (d electrons of the conduction band responsible for the electric conductivity of the metal) can move freely within the nanoparticles but are confined in the particles⁴. This confinement give rise to new optical properties not existing in the bulk solid metals. When a metal nanoparticle is exposed to light, the oscillating electromagnetic field of light induces a collective oscillation of the free electrons of the metal. Indeed, within an electromagnetic field, the free electrons of the nanoparticle move together entailing an accumulation of negative charges on one side of the nanoparticle and of positive charges on the other side as schematized in Figure 2. The electromagnetic wave being sinusoidal, the electrons displacement is regularly inverted. It results in an oscillation of the metal particles surface electrons. The amplitude of the oscillation reaches a maximum at a specific frequency: the surface plasmon resonance. The surface plasmon resonance induces a strong absorption of the incident light by the nanoparticles and thus can be measured using a UV–Vis spectrophotometer.

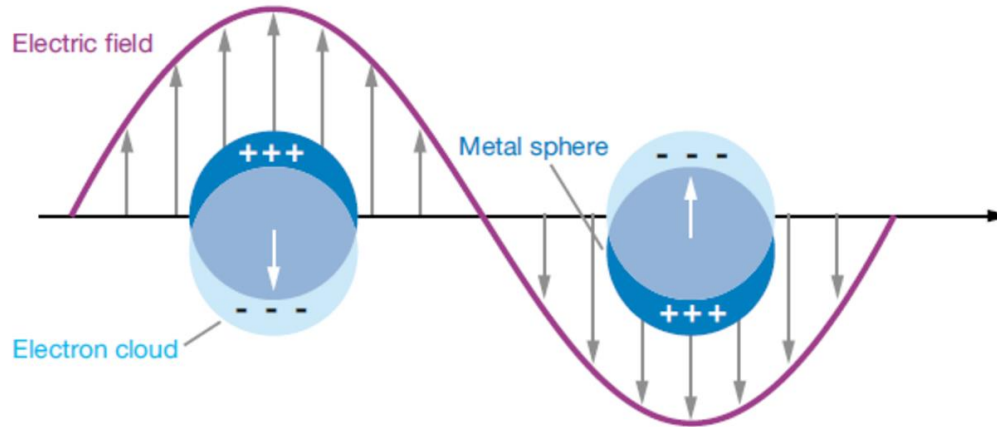


Figure 2: Illustration of the nanoparticles surface plasmon⁵.

In 1908, Gustave Mie⁶ solved Maxwell equations to model the interaction of light with spherical nanoparticles. His theory describes the extinction (absorption plus scattering) of spherical nanoparticles of different sizes. He demonstrated that for nanoparticles of diameter much smaller than the incident light wavelength ($2R \ll \lambda$, $2R < 20$ nm), the extinction cross-section of a metal sphere of radius R is given by:

$$\sigma(\omega) = \frac{9\omega\epsilon_m^{3/2}}{c} \frac{4\pi R^3}{3} \frac{\epsilon_2}{(\epsilon_1 + 2\epsilon_m)^2 + (\epsilon_2)^2}$$

Equation 1: Extinction cross-section of a metal sphere of radius R ⁷.

Where ω is the pulse of the exciting light, c is the speed of light and ϵ_m and $\epsilon_p = \epsilon_1 + i\epsilon_2$ are respectively the dielectric constants of the surrounding medium and the metal particle itself. ϵ_m is frequency-independent and ϵ_2 shows a weak dependence on the UV-Visible. One can observe that the maximum extinction occurs when the denominator of Equation 1 is minimal. This is the case when:

$$\epsilon_1(\omega) = -2\epsilon_m$$

Equation 2: Satisfied condition at the maximal extinction

When the condition in Equation 2 is attained, the surface plasmon resonance occurs and the light extinction (absorbance plus scattering) by the particle is maximal.

The extinction cross-section σ is related to the extinction coefficient ϵ ($\text{L. mol}^{-1}.\text{cm}^{-1}$) by Equation 3:

$$\epsilon = \frac{10^{-3}}{\ln(10)} N_A \sigma$$

Equation 3: Extinction coefficient. N_A is the Avogadro number.

And the absorbance measured by UV-spectrophotometry is directly related to the extinction cross-section by the Beer-Lambert law as shown in Equation 4.

$$A = \sigma N_A C l \frac{10^{-3}}{\ln(10)}$$

Equation 4: Beer-lambert for a dispersion of nanoparticles. N_A is the Avogadro number, C is the molar concentration of gold and l is the length of the cuvette used to perform the measurement.

The surface plasmon resonance is much more intense for noble metal, especially Au and Ag than other metals. The real part (ϵ_1) of the dielectric constant of the metal determines the surface plasmon resonance peak position and the imaginary part (ϵ_2) determines its bandwidth⁸. In the case of gold and silver nanoparticles, the absorption occurs in the visible range of the electromagnetic spectrum which explains the color of the dispersions of these nanoparticles as shown in Figure 3. The red color of a dispersion of gold nanoparticles explains why the Lycurgus cup turns red when illuminated with a transmitted light.

Gold and silver colloidal nanoparticles also give rise to light scattering phenomena that result in dichroic effects. Both types of nanoparticles show a different color when illuminated in transmission or in reflection. This dichroism is illustrated by the Lycurgus cup in which the gold component is mainly responsible for the reddish transmission and the silver for the greenish reflection.

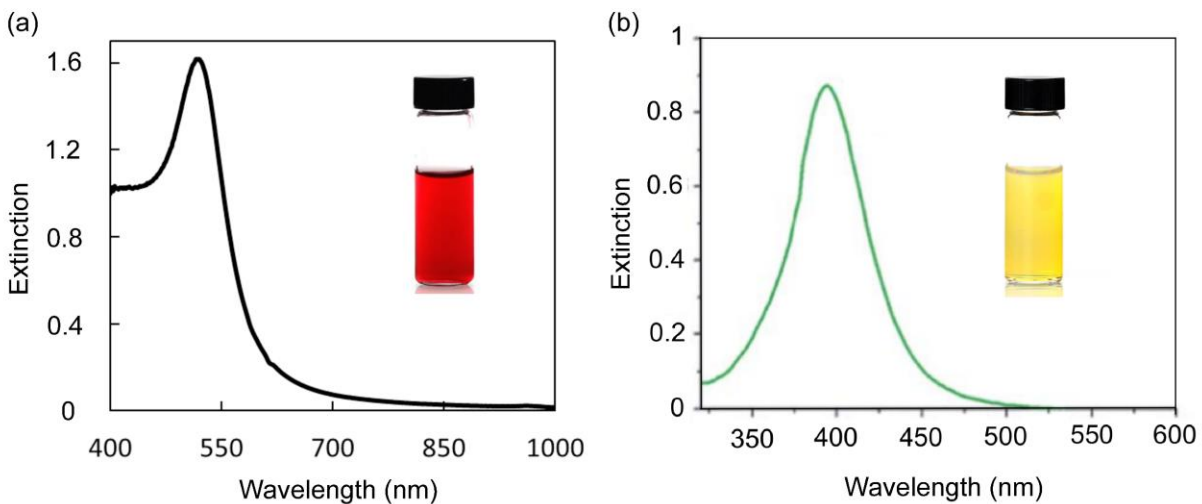


Figure 3: (a) Extinction spectrum of 13 nm gold nanoparticles and (b) of 10 nm silver nanoparticles in water⁹.

For larger nanoparticles (greater than about 20 nm in the case of gold), the expression of the extinction cross-section presented in Equation 1 becomes more complicated because one must take into account the dependency of the metal nanoparticle dielectric constant on the radius of the nanoparticles⁸. In the next section, we will show how the plasmon resonance wavelength and bandwidth is affected by the particle metal, size, shape, environment and interparticle distance.

2.2.2. Factors affecting the plasmon resonance

The plasmon resonance peak position and shape depend on the type, size and shape of nanoparticles as well as on the spacing between the nanoparticles and their surrounding media. In this part, we will discuss these effects focusing on spherical gold and silver nanoparticles.

- *Effect of the metal nature*

The Mie theory shows that there is a condition of resonance for very small metal nanoparticles compared to the incident light wavelength when $\epsilon_1(\omega) = -2\epsilon_m$. From this, it clearly appears that the resonance wavelength depends not only on the dielectric constant of the surrounding media but also on the nanoparticle dielectric constant. Silver and gold having different dielectric constants¹⁰, for similar nanoparticles size, the plasmon peak position will be different. Figure 4 shows the wavelength at which $\epsilon_1(\omega) = -2\epsilon_m$ and therefore gives a first approximation of the position of the maximum of the plasmon peak for gold and silver nanoparticles. We find that the plasmon peak position is respectively located at 520 nm for gold and 390 nm for silver. These values are of the order of the ones obtained experimentally: $\lambda_{Au} = 540$ nm and $\lambda_{Ag} = 396$ nm (Figure 3). The small difference in the position of the peak comes from the fact that the dielectric constants are obtained from measurements done on thin metal film whereas our experimental measurements are done on nanoparticles.

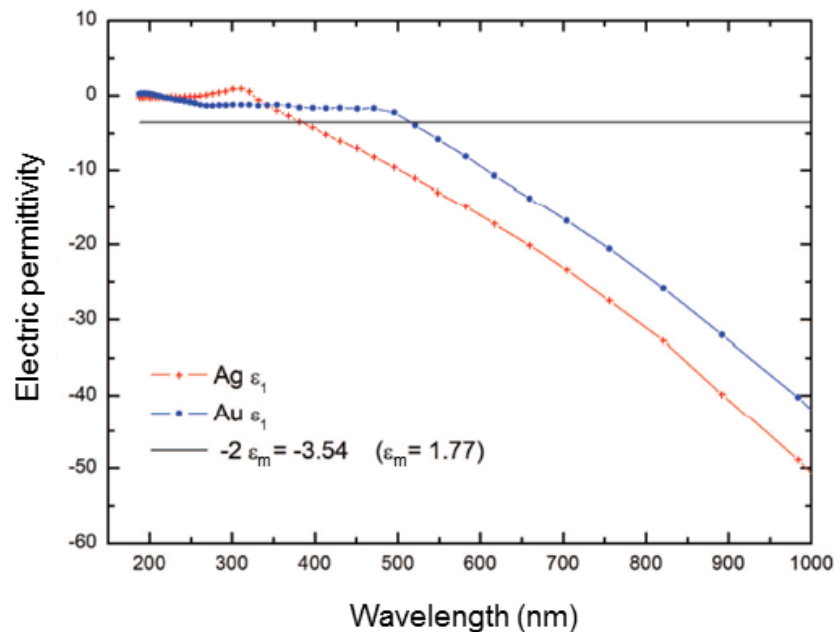


Figure 4: Real part (ϵ_1) of the dielectric constant of gold and silver as a function of the wavelength (Johnson and Christie) and the condition of resonance for nanoparticles in water ($\epsilon_m = 1.77$)¹¹.

- *Effect of the nanoparticles size*

Marzan *et al.*¹² have shown that the larger the gold nanospheres, the more red-shifted their plasmon peak is. In Figure 5 (a) we see that the position of the plasmon band is only slightly shifted for small gold spheres (from 9 to 22 nm) whereas it is strongly red-shifted for much bigger nanoparticles (from 22 to 99 nm). The size dependence of the plasmon bandwidth observed experimentally comes from the fact that the dielectric function of the metal nanoparticles itself is size dependent $\epsilon_p(\omega, R)$ thereby making the absorption cross-section size-dependent⁸.

Moreover, the width of the plasmon band decreases with the increase of the nanoparticle diameter. Indeed, it has been experimentally and theoretically demonstrated that the width of the plasmon peak is inversely proportional to the radius of small nanoparticles (for $R < 50$ nm)^{7,8}.

The normalization at 400 nm (wavelength at which only zero gold (Au^0) absorbs during inter-band transition) of the spectrum in Figure 5 (b) shows that the larger the spherical nanoparticle, the higher the intensity of the plasmon peak. In accordance with Mie's theory, the plasmon band intensity is directly proportional to the cubic radius of the nanoparticle (Equation 1).

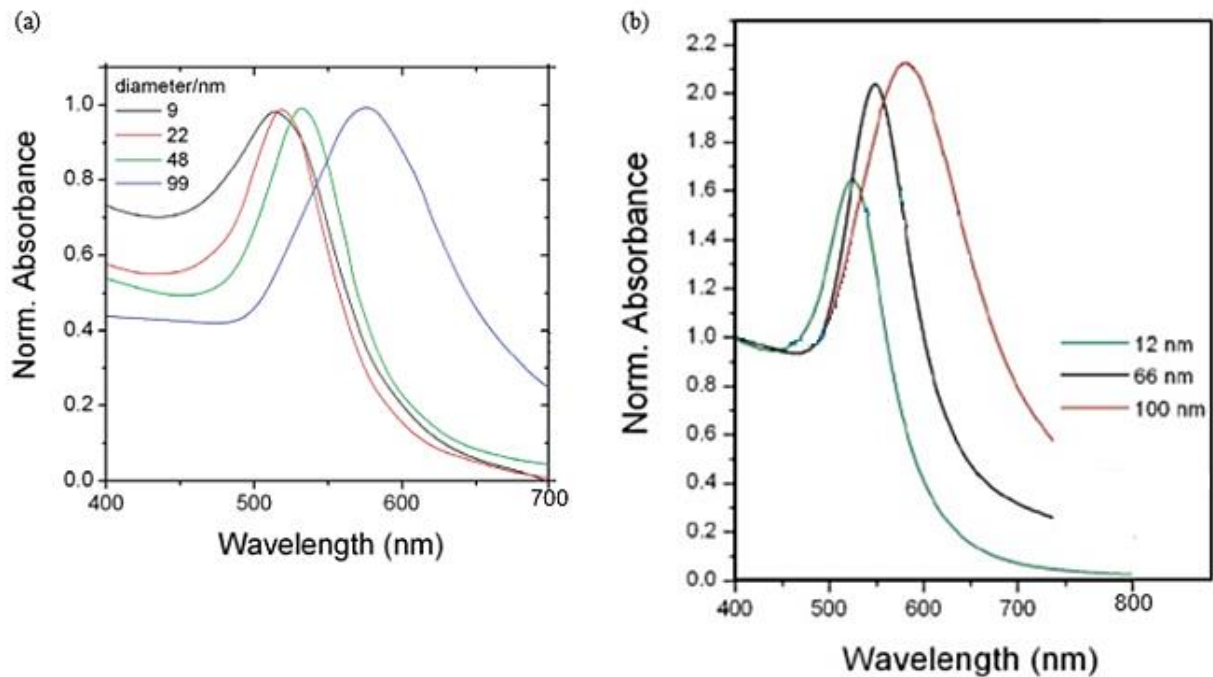


Figure 5: Extinction spectra of different gold nanospheres sizes (a) normalized at the plasmon peak¹² and (b) normalized at 400 nm¹³.

- *Effect of the nanoparticles shape*

The nanoparticles shape strongly affects the plasmon band position and shape^{14,15}. Chen *et al.*¹⁵ (Figure 6) have shown that for spherical or close-to-spherical gold nanoparticles, the extinction spectrum only shows one plasmon band whose position depends on the nanoparticle size. For gold nanorods, the extinction spectrum has two plasmon bands coming from two oscillation modes. The peak at the smaller wavelength is characteristic of the nanorod width and the peak at the larger wavelength is characteristic of its length. The transverse plasmon resonance does not depend on the nanorod aspect ratio and remains at the same wavelength than the one for gold nanospheres. As for the longitudinal plasmon, it increases with the aspect ratio.

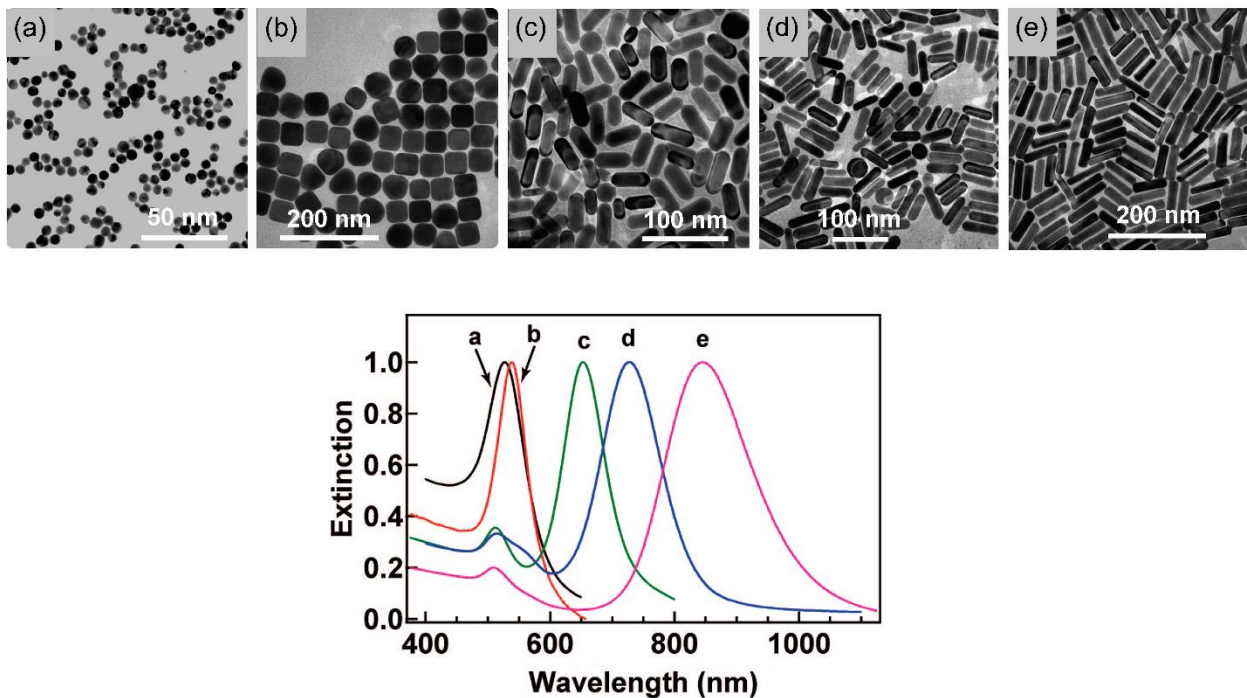


Figure 6: TEM (Transmission Electron Microscopy) images and corresponding extinction spectra. (a) 15 nm gold nanospheres; (b) 44 nm gold nanocubes; (c) 40 nm long and 17 nm large gold nanorods; (d) 55 nm long and 16 nm large gold nanorods; (e) 74 nm long and 17 nm large gold nanorods¹⁵.

- ***Effect of the nanoparticles surrounding environment***

Depending on the refractive index of the surrounding media, the plasmon peak is not positioned at the same wavelength. The Figure 7 presents the plasmon response of 50 nm gold nanospheres as a function of three different surrounding environments: air, water and silica. One can notice that as the refractive index, n , increases, the intensity of the extinction peak increases and the plasmon peak is shifted towards higher wavelengths.

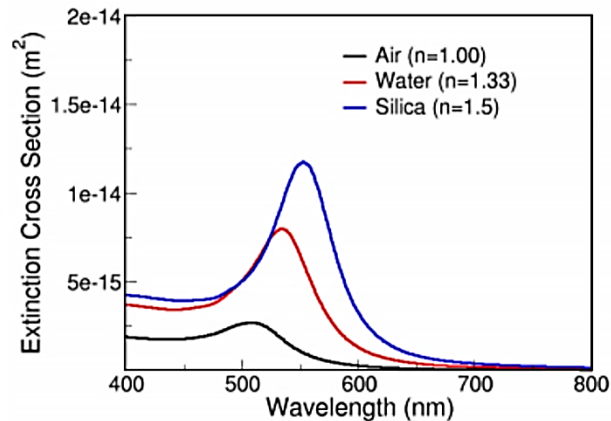


Figure 7: Effect of the surrounding environment refractive index on the plasmon response of 50 nm gold nanospheres¹⁶.

- ***Effect of the inter-nanoparticle distance: plasmon coupling***

One of the most interesting properties of metal plasmon nanoparticles is the dependence of their plasmon response with the distance s between the nanoparticles, (see Figure 8)^{17,18,19}. We will present here the different optical responses observed for gold nanospheres¹⁹.

First, when the nanoparticles are far from each other ((a), $s \approx \infty$), their extinction spectrum shows only one plasmon peak. The nanoparticles interact and their extinction spectrum looks like the one of a single nanoparticle. Then, when the nanoparticles are brought closer to each other, the plasmon band becomes wider ((b), $s \approx 7$ nm) and the plasmon peak is red-shifted. Dolinnyi¹⁹ showed that 40 nm gold nanospheres start interacting with other gold nanoparticles when the distance separating them is in the order of 40 nm. For intermediary inter-nanoparticle distances, the plasmon peak is divided in two modes ((c-f), $0.4 \leq s \leq 4$ nm). The peak of the first mode remains at the same position when nanoparticles get closer to each other but its intensity decreases. As for the peak of the second mode, its peak is shifted towards higher wavelengths and its intensity decreases as the inter-nanoparticle distance increases. When the nanospheres are very close to each other ((g), $s \leq 0.4$ nm), an additional mode develops at about 620 nm.

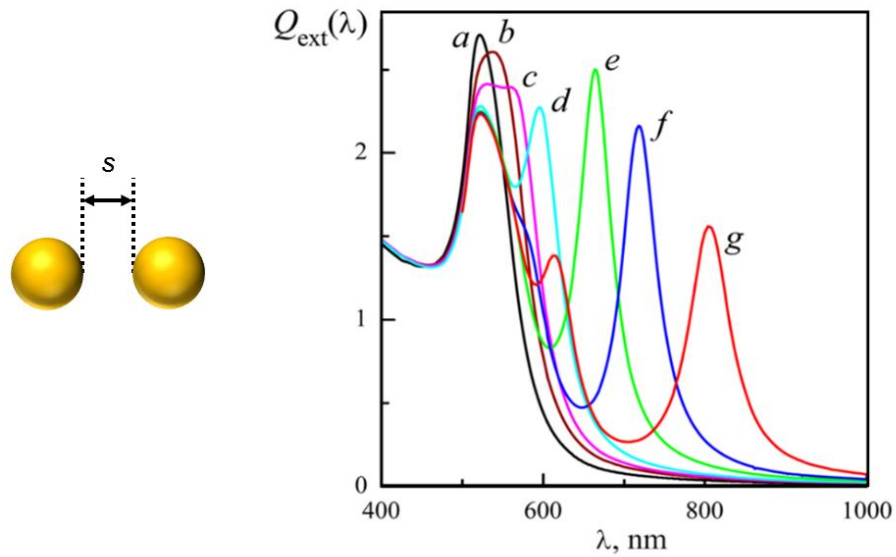


Figure 8: Simulated extinction (Mie theory) for pairs of 40 nm gold nanospheres under non-polarized light in water and for different inter-nanoparticle distances, s : ∞ (a), 7 (b), 4 (c), 2 (d), 0.7 (e), 0.4 (f), and 0.2 nm (g); Q_{ext} is the extinction¹⁹.

For a better understanding of the plasmon coupling phenomenon, the incident light can be polarized. Jain *et al.*²⁰ have evidenced two distinct plasmon behaviors when a pair of gold nanodiscs is illuminated under polarized light. The behavior depends on the distance between the nanodiscs. When the polarization is parallel to the interparticles axis, the electron coupling leads to a red shift of the plasmon peak and to an increase of the peak intensity (see Figure 9 (a)). When the polarization is orthogonal to the interparticles axis, the electron coupling leads to a small blue shift of the plasmon peak and a decrease of the peak intensity. In both cases, the closer the nanoparticles, the larger the shifts.

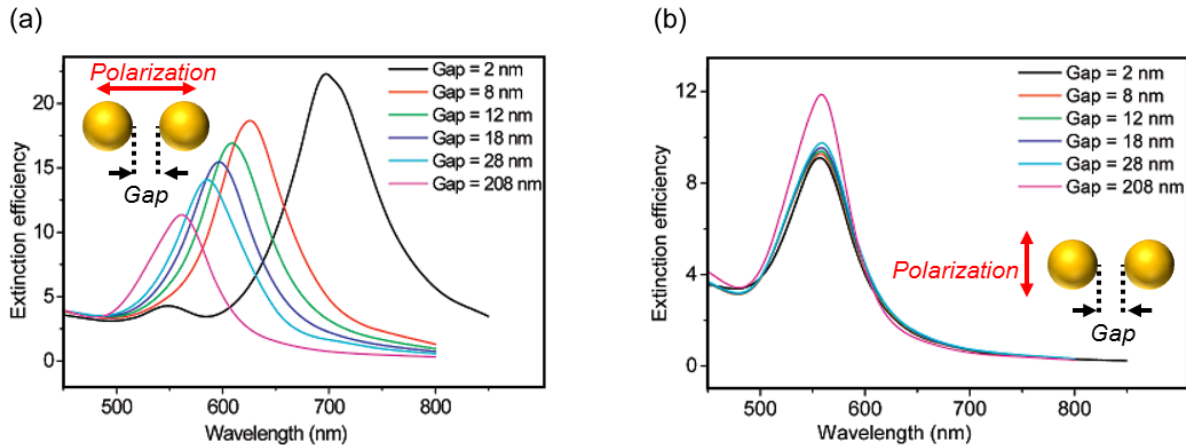


Figure 9: Simulated extinction spectra of pairs of gold nanodisc pairs (diameter = 86.5 nm and height = 25.5 nm) in air for varying interparticle separation gap (gap = edge to edge nanoparticles) for incident light polarization direction (a) parallel and (b) perpendicular to the interparticle axis²⁰.

The results presented in this part of the manuscript are valid for gold nanospheres. However, Sheikholeslami *et al.*²¹ as well as Zhao *et al.*²² showed similar results obtained in polarized light with silver nanospheres pairs. As for gold, an incident light polarization direction parallel to the interparticle axis entails a red shift of the plasmon band whereas a perpendicular polarization leads to a blue shift. Furthermore, the closer the nanoparticles, the more shifted the plasmon peak.

In this section, we have presented the concept of plasmon resonance of gold and silver spherical nanoparticles and its dependence with the nanoparticles metal, size, environment and interparticle distance. In the following sections, we will review the different plasmonic nanospheres syntheses methods and show the most efficient techniques to assemble them into large close packed arrays.

3. Common approaches for the synthesis of nanospheres

A gigantic library of gold and silver nanosphere syntheses exists. More than 30'000 articles are available online (Web of Science). In the context of this thesis we will focus on the most well-known and the most used protocols. Generally, metallic nanoparticles are synthesized via reduction of the corresponding metal salt. A protective agent such as a surfactant or a polymer is used to avoid the nanoparticles aggregation and precipitation during synthesis. The choice of the reduction technique, the reaction time, the solvent and the stabilizing agent determines the size and shape of the nanoparticles. Thusly, spheres^{13,23}, nanorods^{15,24}, cubes¹⁵, discs, nanowires, tubes, triangles²⁵ and polyhedrons²⁶ have already been obtained with gold, silver and other metals. One of the most striking issues encountered during the generation of nanoparticles is the reproducibility of the synthesis method and the quantity of nanoparticles made. Indeed, the volume and the Au⁰ concentration usually used during synthesis are small (typically [Au⁰] = 10⁻⁴ M and the final volume of the gold solution is 250 mL^{13,27}). The obtained nanoparticles are not exactly the same from one synthesis batch to the other. In this manuscript, we focus on the synthesis of gold and silver spherical nanoparticles obtained in water or in water-miscible solvent with a specific emphasis on the reduction methods using sodium citrate and ascorbic acid. In the following, the terms nanoparticles, and a fortiori nanospheres will refer to spherical nanoparticles.

3.1. Gold nanospheres syntheses

The synthesis of small spherical gold nanoparticles is generally performed by the Turkevich method (1951)²⁸. A solution of gold salt (HAuCl₄) is reduced by sodium citrate. The reaction temperature, gold/citrate ratio and the order of addition of the reagents controls the nanoparticle size dispersion. This method leads to monodisperse nanospheres with diameters of about 15 nm. In 1973, Frens²⁹, inspired by the work of Turkevich, edited the method to synthesize

gold nanospheres of controlled sizes in the range 16 to 147 nm. The ratio between the reducing agent (tri-sodium citrate) controls the nanoparticle final diameter. In these two methods, citrate acts as both reducing and stabilizing agent. Even if the quality of the obtained nanoparticles is not optimum (shape, size and size distribution), these methods are widely used because they are easy to implement.

A more efficient method to control the size and shape of gold nanospheres was proposed in 2000 by Natan *et al.*³⁰. In their work, large spherical gold nanoparticles are synthesized by a seed growth process as shown in Figure 10. Small seed nanoparticles are first synthesized and further grown via the reduction of the metal salt in the presence of surfactants to stabilize the nanoparticles. Seeds are generated using a first reducing agent (sodium borohydride or sodium citrate) whereas the growth is done with a second milder reducing agent (often ascorbic acid). The ascorbic acid reduces the metal salt in an intermediate state which becomes zero gold (Au^0) only after a catalyzed reduction occurs at the surface of the seeds. Even if the work of Natan *et al.* gave good spherical gold nanoparticles, gold nanorods were also obtained during the synthesis, affecting strongly the resulting batch monodispersity. In 2011, Bastús *et al.*³¹ successfully synthesized citrate-stabilized monodisperse gold nanospheres via seed growth. The factors influencing the size distributions of the nanoparticles obtained as shown in Figure 10 are the initial seeds concentration, the number of growth steps and of secondary nucleations.

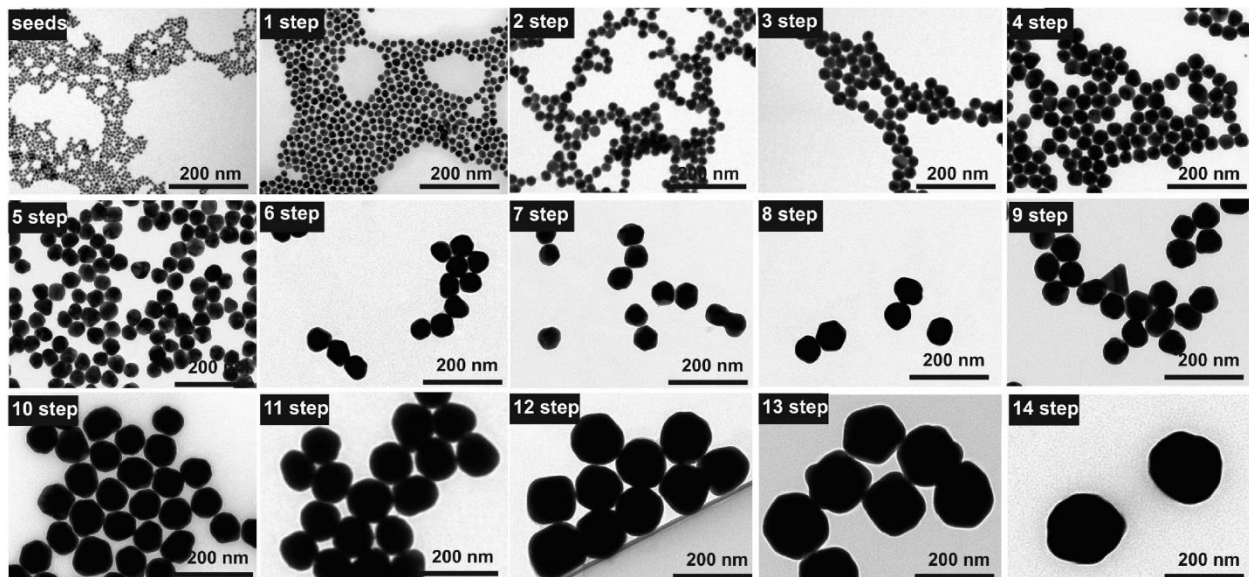


Figure 10: Monodisperse gold nanospheres synthesized by seed growth method with citrate. The nanoparticle diameter increases from 8.4 nm to 180.5 nm and its concentration decreases from 3×10^{12} to 5×10^9 NPs/mL³¹.

In 2006, following the work of Jana *et al.*³², Liz-Marzán's¹³ team came up with a new seed growth method to synthesize very monodisperse gold nanoparticles to a diameter up to 181 nm. The TEM images of the nanoparticles obtained via this method are presented in Figure 11. The CTAB (hexadecyl-trimethyl-ammonium bromide) used as surfactant during the seed growths enables a better control of the final morphology of the gold nanoparticles. This new process gave gold nanoparticles a more spherical appearance while forming less gold nanorods. However, this method leads to nanoparticles that are not easily functionalizable a posteriori, which can be disadvantageous. Indeed, the CTAB is strongly anchored onto the gold nanoparticles and ligand exchange with another molecule having an affinity for gold surface is not straightforward, requires multiple steps and specific synthesis conditions¹⁷.

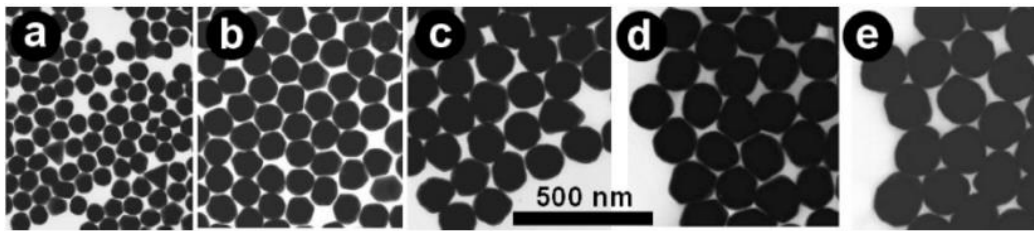


Figure 11: TEM images of gold nanospheres after seed growth. The mean diameters are (a) 66 nm (b) 100 nm, (c) 139 nm, (d) 157 nm et (e) 181 nm¹³.

In 2016, Malassis *et al.*³³ demonstrated that it is possible to obtain rather spherical monodisperse gold nanoparticles of different sizes by reduction of gold salt with ascorbic acid by tuning the pH of the mixture. The real advantage of this synthesis is its easy implementation. Indeed, the synthesis method only involves one step as compared to the multiple synthesis steps necessary in the seed growth process. Moreover, ascorbic acid is very easily exchanged by other stabilizing agents allowing multiple post-functionalization of the obtained gold nanoparticles.

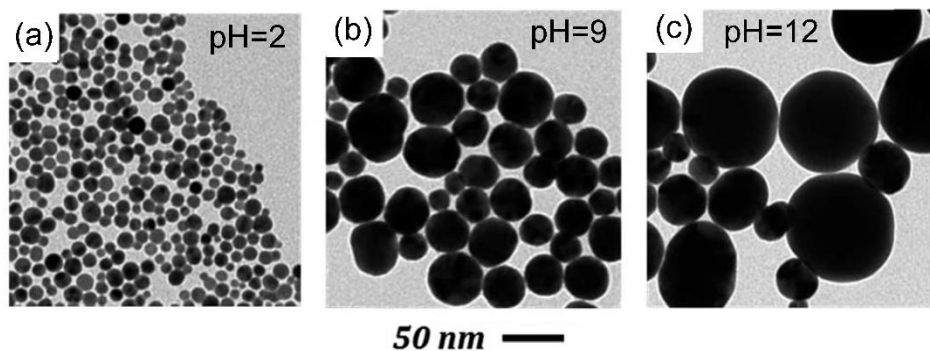


Figure 12: TEM images of gold nanospheres obtained by Malassis *et al.* as a function of the pH.³³

3.2. Silver nanoparticles syntheses

Commonly, silver nanoparticles are obtained by chemical synthesis via a reduction process of silver precursor (usually AgNO_3). The reducing agents used can be: sodium citrate³⁴, alcohols³⁵, sodium borohydride. Polymers such as PVP (polyvinylpyrrolidone)³⁶, PVA (polyvinyl alcohol) and surfactants are also added to the synthesis in order to stabilize the nanostructures formed. The obtained nanoparticles size and shape can be controlled via the reagents concentration, the temperature, the pH, the reducing agent type and the stabilizing agent type.

We will focus here on three synthesis methods often used in the literature to produce silver nanospheres. They are: the reduction by citrate, the polyol process and the reduction by ascorbic acid. We will use the observations made during the analysis of these three methods to design our own silver nanoparticle synthetic protocol presented in Chapter 3.

One of the most accessible methods to synthesize silver nanospheres is the synthesis of Lee and Meisel (1982)³⁴. This method is very close to the Turkevich method to form small spherical gold nanoparticles. Citrate ions are used as both stabilizing and reducing agents. However, unlike the Turkevich method, this method gives polydisperse nanoparticles of different shapes. Theoretical study revealed that the citrates preferentially anchor to the facet $\text{Ag}(111)$ rather than to the facet $\text{Ag}(100)$ ³⁷, which could be a reason for the nanoparticle anisotropy. Tuning the pH brings an additional control over the size and shape but it does not give very uniform nanospheres. Due to the simplicity of this synthesis, this process is still often used specially to obtain large quantities of nanoparticles.

The polyol process is a robust and versatile synthetic method which allows for a great control over the silver nanostructures size and shape. The polyol (ethylene glycol, 1,2-propylene glycol or 1,5-pentanediol) is used as a solvent but also as a reducing agent. The silver precursor and a second stabilizing agent are mixed with the pre-heated polyol solution. The reduction of silver ions leads to the formation of silver nanoparticles (Ag^0). At the beginning of the reduction, small nanoparticles are obtained. As the reaction goes on, these seeds grow and can differentiate into three types of particles: single crystalline, single twinned or multiple twinned. Then, these three types of particles evolve preferentially towards certain particle shapes as shown in Figure 13. A better control over the size and shape of the final particles is obtained using different reducing and stabilizing agents. Moreover, the careful selection of the stabilizing agent can favor the growth of anisotropic nanoparticles. Indeed, Xia *et al.*³⁶ have demonstrated the selective growth of silver nanorods and silver nanowires using PVP as a capping agent. PVP preferentially anchors at specific silver nanoparticle facets, inhibits the growth of the corresponding planes and enables the synthesis of anisotropic nanoparticles as illustrated in Figure 14. Therefore, with PVP, the synthesis preferentially leads to nanorods, bipyramids and cubes. The silver nanospheres synthesis does not require the use of PVP because their growth must be isotropic.

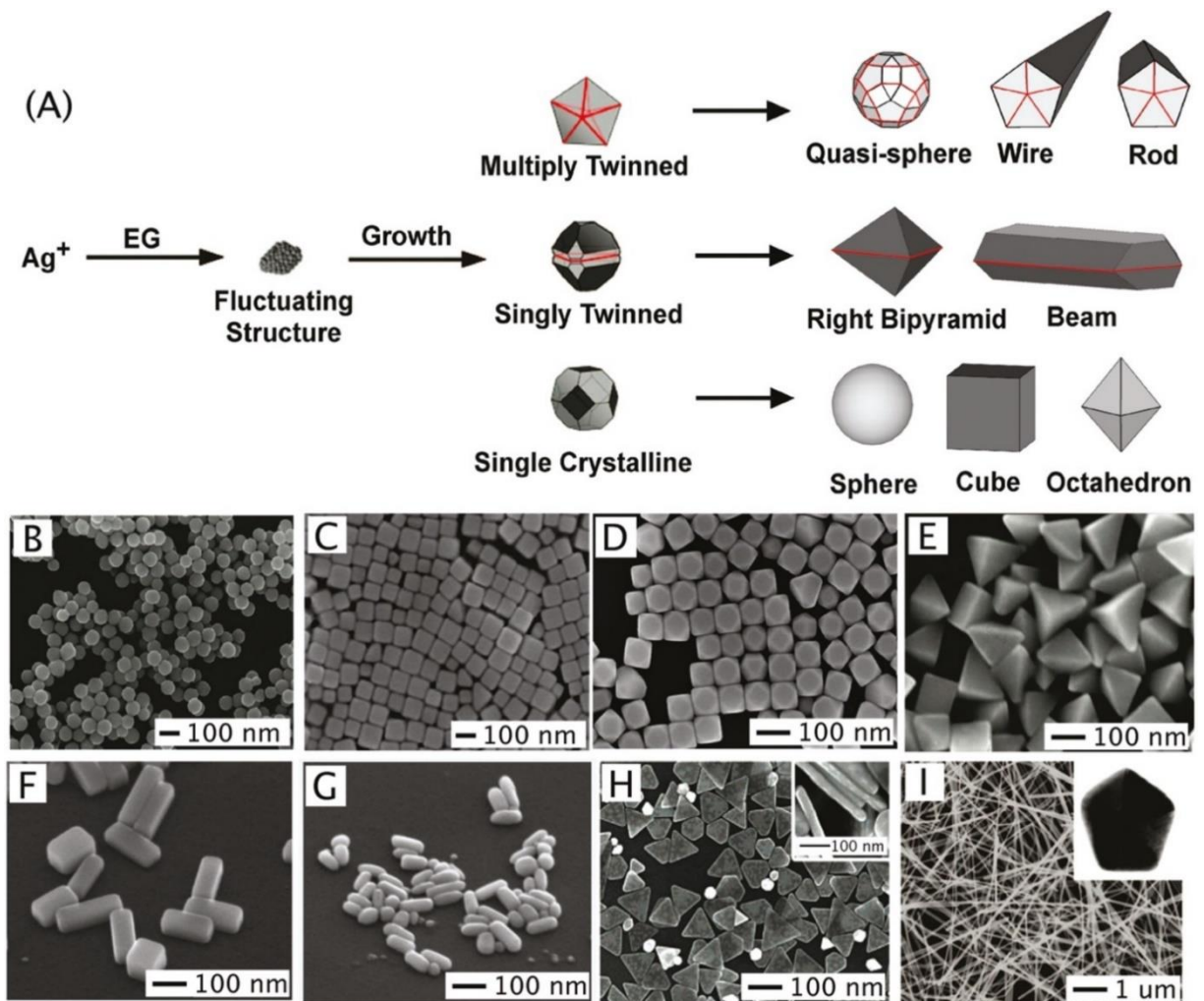


Figure 13: Syntheses of silver nanostructures by the polyol process. (A) Formation mechanisms of the different nanostructures : (B) spheres, (C) cubes, (D) truncated cubes, (E) bipyramids, (F) bars, (G) spheroids, (H) triangular plates and (I) nanowires³⁵.

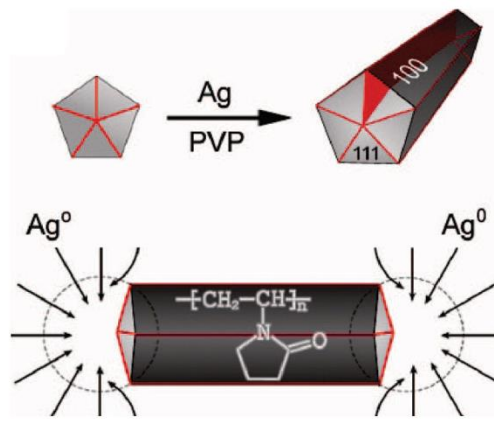


Figure 14: Twinned decahedral seeds lengthened into rods. PVP selectively adsorbed on the (100) side facets so that Ag⁰ atoms could only add to the (111) facets at the ends of each rod³⁶.

In 2010, Qin *et al.*³⁸ came up with an easy one-step synthesis of spherical silver nanospheres. They demonstrated that the size of spherical silver nanoparticles was tunable by using ascorbic acid as the reductant. Variation of the reactivity of ascorbic acid with pH was effective to tune the final size of the nanoparticles. The higher the pH, the smaller the nanoparticles. The shape of the nanoparticles could be more spherical-like by promoting the intraparticle ripening. Like gold nanoparticles, silver nanoparticles stabilized by ascorbic acid can be easily post-functionalized by other ligands.

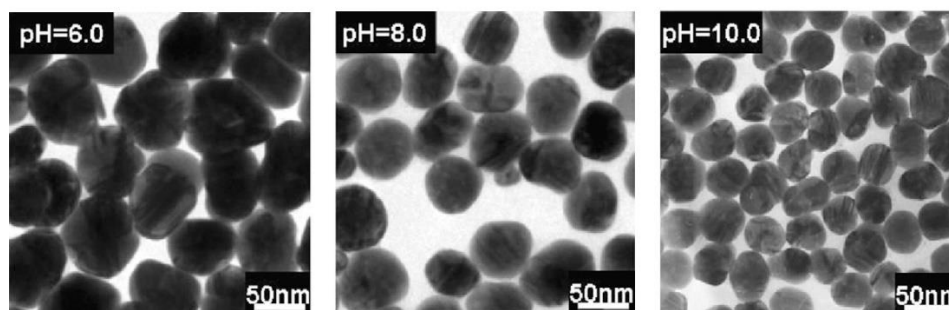


Figure 15: TEM images of aged silver nanospheres obtained with the method of Qin *et al.* as a function of the pH.³⁸

In this section, we have shown that many routes are available to synthesize gold and silver nanospheres. Depending on the final applicative role of these nanoparticles, the size, size distribution, sphericity and amount of nanoparticles requisites are different. The synthesis method must be selected according to all these specifications. As part of this thesis, in Chapter 2 we will see that the synthesis of very monodisperse gold nanospheres is crucial to obtain crystalline arrays of close-packed nanoparticles. In Chapter 3, we will show that the amount of silver and gold nanoparticles is an essential parameter in the fabrication of nanoparticle-stabilized emulsions.

3.3. Formation and growth of nanoparticles

Understanding the mechanisms of formation and growth of nanoparticles is essential for a better control of the nanoparticle size and shape during synthesis. Several approaches exist and we will present here two of them.

- ***LaMer model***

The LaMer model³⁹ is a commonly accepted model describing the general mechanism of the nanoparticle formation process. The mechanism described in Figure 16 (a) suggests a reaction scheme divided in three steps: the generation of Au⁰ atoms, the nucleation of Au⁰ clusters and their growth into nanoparticles. First, the Au³⁺ ions are reduced in Au⁰ species and the concentration in Au⁰ increases until it reaches a « critical limiting supersaturation (C_{max}) ». At that point, the Au⁰ aggregate into small clusters via a nucleation process. Once the clusters have reached a critical radius, r^* , the clusters grow into nuclei (see Figure 16 (b)) because it favors the decrease of the

free energy. These nuclei grow rapidly by consuming the metal atoms present in the bulk solution. Therefore, a decrease in the concentration of the Au^0 is observed during growth. If the Au^0 concentration falls rapidly below the supersaturation ($[\text{Au}^0] < C_{min}$), the nucleation ends, and only the nuclei already present in the reaction mixture grow to form nanoparticles with homogenous size distribution. In this model, the thermodynamic stability along with the reduction kinetics determine the size and the number of nanoparticles. In this mechanism the reduction reaction can be promoted by raising the temperature⁴⁰, thus favoring the formation of nuclei and resulting in a larger number of small nanoparticles.

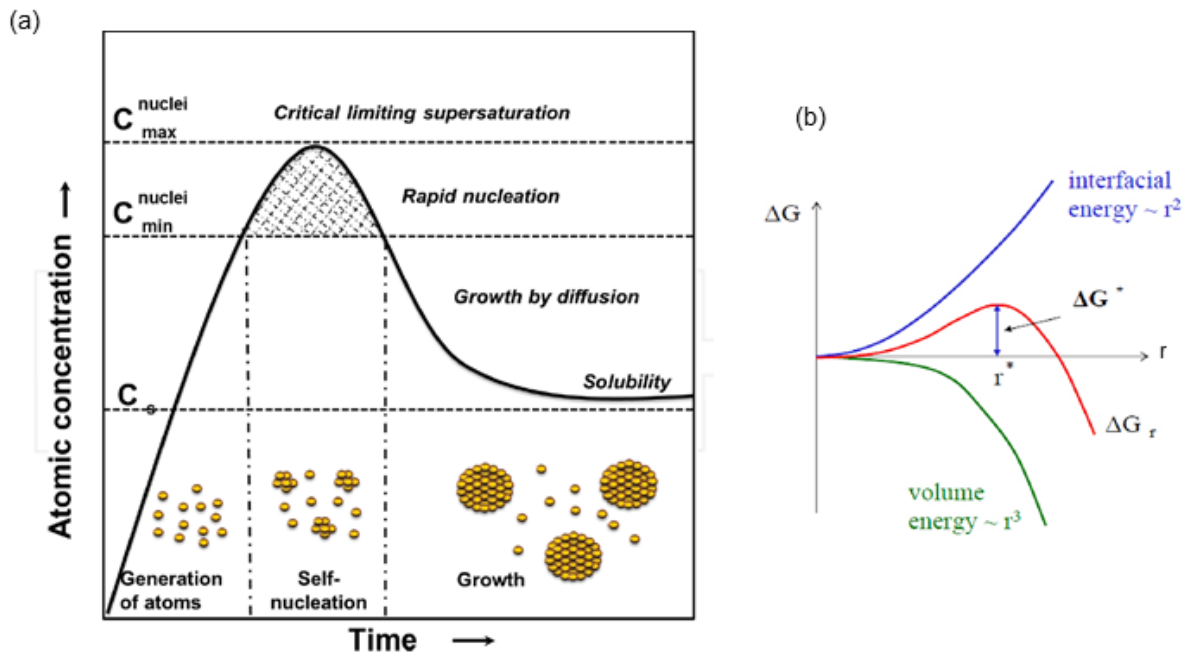


Figure 16: (a) Schematic illustration of La Mer's nucleation condition⁴⁰. (b) Variation of the free energy (G) associated with the nucleation of a nanosphere at $r = r^*$ ⁴¹.

- **Polte model**

J. Polte et al.^{42,43} studied the formation and growth of metal nanoparticles from a different perspective. They experimentally followed the formation of gold nanoparticles synthesized using the Turkevich process, which we explained before. They demonstrated that the formation of the gold nanoparticles is governed by the colloidal stability of the system rather than by the thermodynamic laws. Their studies suggest a model for the formation and growth of gold nanoparticles in 3 main stages as illustrated in Figure 17: the generation of Au^0 atoms (step 1), the coalescence of Au^0 clusters (step 2) and their growth into nanoparticles (step 3). In the first step, the Au^{3+} ions are reduced by the sodium citrate in Au^0 atoms. Then, these Au^0 atoms form small clusters which coalesce to form small nanoparticles. In this model, the growth is governed by

colloidal stability implying that clusters always grow to a size above which they cannot overcome the energy barrier of aggregation or coalescence. Since the aggregation barrier increases with increasing particle size, the coalescence/aggregation stops at a critical nanoparticle size. This critical size usually corresponds to the size at which the clusters are big enough to be effectively electrostatically stabilized by the citrate ions. Then, the residual gold ions (existing because the sodium citrate is a mild reducing agent and do not reduce very fast the gold ions) diffuse in the electric double layer (EDL) of these small nanoparticles, get reduced, and grow onto the existing nanoparticles (step 3). In this model, the minimal particle size is determined by the colloidal stability.

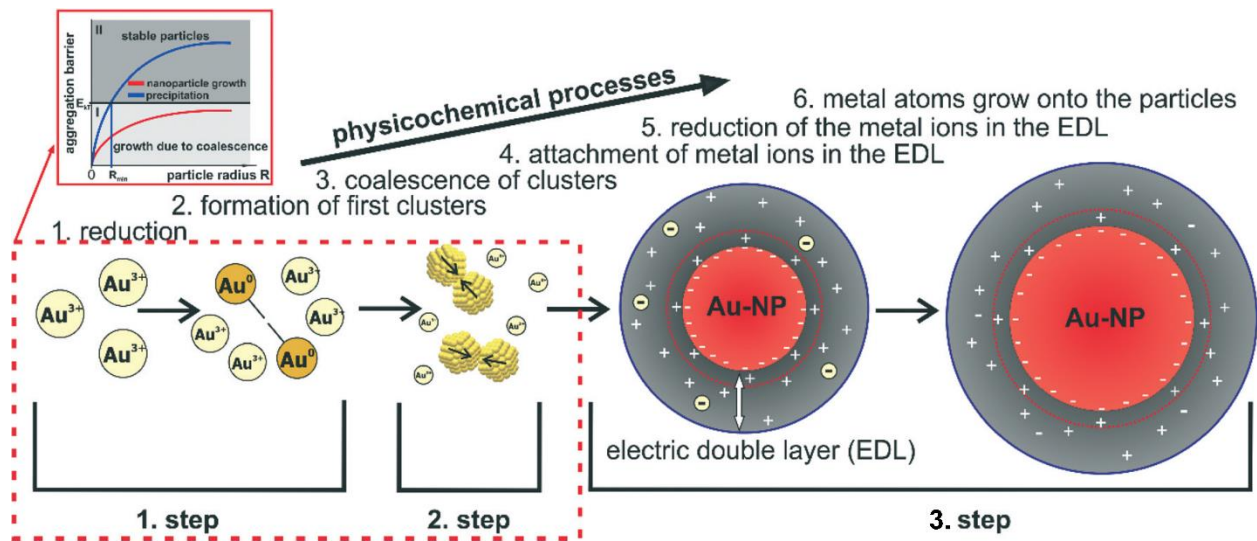


Figure 17: Schematic of the refined 3-step nanoparticle growth mechanism of the Turkevich method⁴².

These two models do not provide any universal explanatory mechanism for all the existing nanoparticle syntheses. Indeed, many factors can impact the growth of nanoparticles. For instance, the type of ligands capping the nanoparticles⁴⁴ or the chemical reactivity of the different precursors. Thus, more detailed models are required to aid for a better understanding of the important factors responsible for the nanoparticles formation.

In the section 3 of this chapter we have described the most common syntheses for the formation of spherical gold and silver nanoparticles. We also briefly explained their formation mechanisms. The next section is dedicated to the different techniques existing to assemble these nanoparticles into close pack arrays.

4. Nanoparticles self-assemblies

Self-assembly of colloids is a “bottom-up” approach for the fabrication of nanomaterials from stable colloidal dispersions. A very large number of self-assembly techniques exist and an exhaustive review would be impossible. We will sort them in two main categories: spontaneous and directed self-assemblies. The spontaneous assembly can be defined as the assembly mediated by colloidal interactions (electrostatics, steric, depletion, Van Der Waals) driven only by the thermodynamic. In this process, the colloids spontaneously organize into ordered structures of length scales on the order of 1 -100 μm . Due to the fabrication process, the collection for further use of these ordered structures is not straightforward. In contrast, the directed self-assembly uses external forces such as external fields, physical confinement, or evaporation of solvent to trigger the organization of colloids. The structures obtained with this method are organized on a larger length scale, on the order of several microns to the millimeter. The directed self-assembly techniques include nonexhaustively sedimentation, Langmuir-Blodgett, electrophoresis, spin-coating, dip-coating and drying. A template such as a simple glass slide or more exotically a specifically functionalized substrate, is often used to facilitate the organization of the nanoparticles. However, and this may be a drawback, in most cases this template becomes part of the final nanomaterial structures. The self-assembly of nanoparticles can occur at the liquid-liquid, liquid-air or liquid-solid interfaces. In this section, we will describe the most recurrent techniques in the literature such as: Langmuir-Blodgett, sedimentation, evaporation of solvent and adsorption of nanoparticles on droplets. We will focus on the technique of microevaporation microfluidic and on nanoparticles assembly on droplets because these two techniques give rise to the fabrication of 2 different types of materials: bulky 3D and dispersed materials.

4.1. Common self-assembly techniques

4.1.1. Spontaneous self-assembly

The dipolar, Van-der-Waals and electrostatic interactions play a major role in the type of structures obtained through the organization of nanoparticles^{45,46}. These forces can be tuned by changing the solvents polarity, the nanoparticles charges, the nanoparticles wetting or the size and shape of the colloidal nanoparticles. Here, we briefly present two examples which illustrate these phenomena. These two examples show the fabrication of dispersed materials via spontaneous self-assembly of nanoparticles.

Nie *et al.*⁴⁷ were able to organized polymer-CTAB-gold nanorods-polymer nanoparticles (see Figure 18) into different structures with varying geometries. These nanoparticles are nanorods which sides are coated with CTAB and which ends are coated with a polystyrene polymer. By changing the solvents quality, the authors were able to solvate either the sides or the ends of the nanorods. Both DMF and THF are good solvents for the polystyrene block however, water reduces

the solubility of the polystyrene. The CTAB is poorly soluble in THF but is well solvated in water. Nanochains are obtained when the nanoparticles aggregate by the ends (see Figure 18 (a)). Nanospheres form when the nanoparticles aggregate side by side and by the ends (see Figure 18 (b)). The self-assembly is reversible.

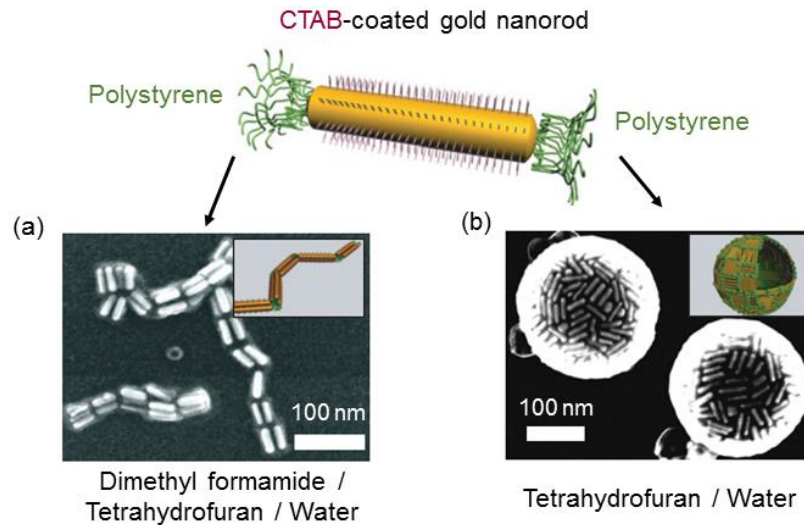


Figure 18: Self-assembly of CTAB-coated gold nanorods in selective solvents forming (a) nanochains and (b) nanospheres. The insets show the corresponding schematic diagrams of the nanorod assemblies⁴⁷.

Another interesting example was provided by Hickey *et al.*⁴⁸. They have fabricated polymersomes based on the co-assembly of hydrophobic inorganic iron oxide particles and amphiphilic polymers (poly(acrylic acid)-*b*-polystyrene) at an oil/water interface. They demonstrated that the size of the nanoparticles affects the size of the final polymersomes. Larger nanoparticles induce higher curvatures of the polymer membrane and smaller vesicles. We will describe how nanoparticles assemble at a liquid/liquid interface in the following section 4.3 of this chapter.

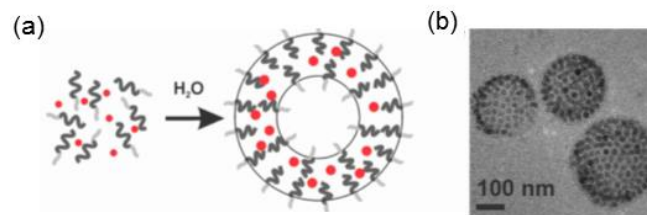


Figure 19: (a) Schematic representation of the self-assembly of magneto-polymersomes. (b) TEM images of magneto-polymersomes⁴⁸.

4.1.2. Directed self-assembly

- *Sedimentation*

Particles left to rest in a solvent of density lower than the particles' density, slowly sediment under gravity following the Stokes law. The particles generally form face-centered cubic (FCC) lattices because it is the most thermodynamically stable structure (theoretical calculations show a lower Gibbs free energy for FCC lattices) (Figure 20)⁴⁹. However, a precise control over the size, the density, the volume fraction of the colloids and the solvent in which the particles are dispersed are necessary to successfully assemble them in well-organized arrays. Sedimentation being a rather slow process, the fabrication of crystalline lattices can last up to several weeks with this method. Moreover, during sedimentation, several “nucleation” sites can appear in different places within the assembly which can lead to polycrystalline domains. For these reasons, it is unsuited for large scale production and other, more controllable and faster routes are more commonly used.

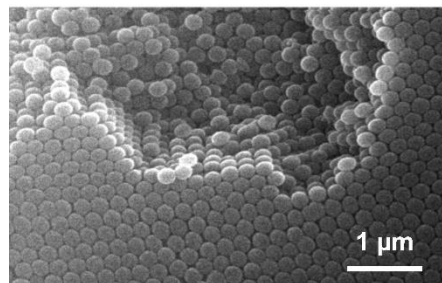


Figure 20: SEM (Scanning Electron Microscopy) image of spherical 225 nm core-shell Au@SiO₂ assembled by sedimentation. Nanoparticles are organized in a face-centered cubic lattices (FCC) ⁵⁰.

- *Drying*

Drying is the most used method in the self-assembly of nanoparticles. It includes: the horizontal deposition (Figure 21) where a droplet is left to dry on a substrate^{51,52,53}, the vertical deposition⁵⁴ where a substrate is pulled out of a colloidal solution vertically (Figure 22) or the drying in confined geometries^{55,56,57} (Figure 24). Nanoparticles are directly assembled on solid surfaces by local increase of the nanoparticles concentration as shown in Figure 21 (b-c). The assembly is conducted by solvent evaporation and assisted by capillary interactions guiding the nanoparticles. For a better control over the final assembly, several parameters have to be taken into account: the choice of the substrate, the substrate tilt angle, the type of substrate, the evaporation rate, the ambient temperature, the initial concentration in colloids and the ambient humidity.

Regarding the horizontal evaporation, the solvent evaporation rates on the edges of the liquid area are larger than at the center. This evaporation gradient creates a convective flux dragging the particles from the center towards the periphery of the liquid area as represented in Figure 21 (a). It has to be highlighted that the concentration of particles is possible only if the

particles diffusion rate is lower than the solvent evaporation rate. Because of the capillary forces, when the thickness of the liquid layer is of the same order than the particle diameter, the particles reaching the periphery are pinched onto the substrate and against the neighboring particles. Thus, a colloidal crystal is formed from the edges towards the inside of the liquid area. At the end of the evaporation process, the particles concentration in the liquid area is very low which lead to the appearance of a central ring containing no particles. Horizontally evaporating drops containing different nanoparticles, Ming *et al.*⁵³ have obtained different organizations as presented in Figure 21 (d-f). Lattices with hexagonal symmetry were achieved using polyhedra, lattices with tetragonal symmetry were obtained by evaporating nanocubes, and smectic superstructures were formed with nanorods.

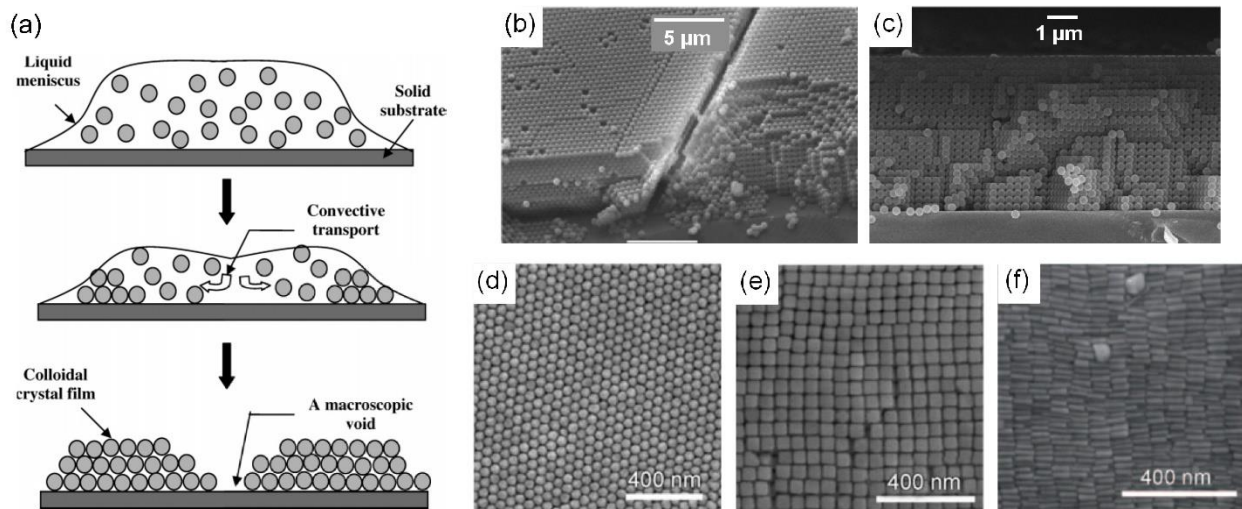


Figure 21: (a) Schematic representation of the inward self-assembly mechanism for colloids evaporated on a horizontal solid substrate. (b-f) SEM images: (b) of a side view of a colloidal crystal film grown on glass substrates from polystyrene sphere of 0.40 μm in diameter and 8.0 wt % in concentration, (c) of the cross sections of colloidal crystal films (polystyrene spheres of 0.26 μm in diameter) deposited on a silicon substrate⁵², (d) hexagonally packed Au polyhedra, (e) tetragonally packed Au nanocubes, (f) smectic Au nanorod superstructure⁵³.

In the case of the vertical evaporation, a meniscus is formed during the immersion of the substrate in the colloidal dispersion. The evaporation being more important at the meniscus, a convective flux is created bringing the nanoparticles from the bulk towards the meniscus as shown in Figure 22 (a). The particles crystallization is initiated by attractive capillary immersion forces, mediated in the solvent meniscus between particles at the drying front. For the particles to reach the meniscus, the sedimentation rate must be smaller than the solvent evaporation rate. Moreover, the balance between capillary forces and convective particle flux during the solvent evaporation is essential for the monotonic formation of 2D colloidal arrays⁵⁸. Large crystalline arrays and binary lattices can be obtained by vertical evaporation as seen in Figure 22 (b-c).

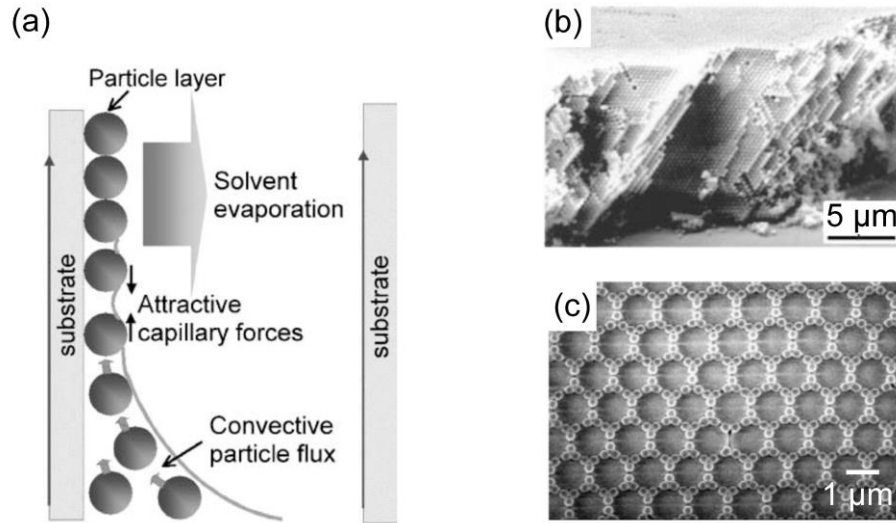


Figure 22: (a) Schematic illustration of the mechanism of colloidal self-assembly in the vertical deposition technique⁵⁸, (b) SEM cross-sectional images of close-packed arrays of 298.6 nm silica spheres (~50 layers)⁵⁴, (c) co-assembly of binary dispersions of microspheres: the large spheres are 1.28 μm polystyrene beads and small spheres are 290 nm silica beads⁵⁹.

By tuning the electrical charges on different types of sterically stabilized nanoparticles, Shevchenko *et al.*⁴⁵ obtained multiple binary superlattices of controlled stoichiometry as presented in Figure 23. In their experiment, a substrate was placed in a glass vial containing a colloidal solution of quantum dots and the vial was placed tilted by 60° - 70° inside a low-pressure chamber to evaporate the solvent and concentrate the nanoparticles.

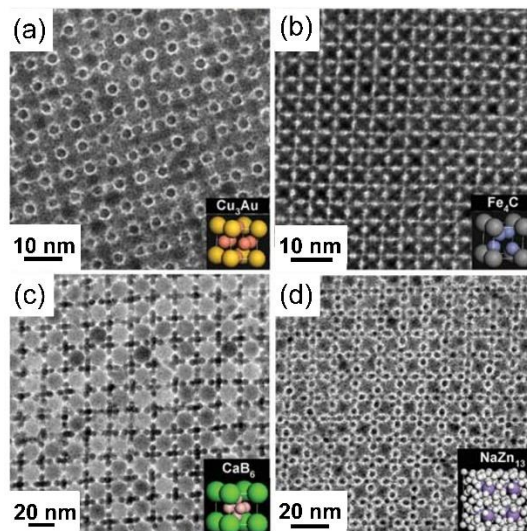


Figure 23: TEM images of binary superlattices obtained by self-assembly of two types of nanoparticles and modelled unit cells of the corresponding three-dimensional structures⁴⁵. The nanoparticles used are : (a) 7.2 nm PbSe and 4.2 nm Ag (b) 6.2 nm PbSe and 3.0 nm Pd (c) 5.8 nm PbSe and 3.0 nm Pd (d) 7.2 nm PbSe and 4.2 nm Ag.

In 1999, Park *et al.*⁵⁵ showed that when colloids are subjected to a physical confinement, the crystals obtained demonstrate much better ordering and orientation compared with crystals grown on a bare substrate. By injecting polystyrene beads into the confinement of a rectangular cell of controllable dimensions and evaporating the water (Figure 24 (a)), they were able to obtain large defect-free colloidal crystals (Figure 24 (b-c)) and to control the number of layers formed. In 2003, Kumacheva *et al.*⁵⁷ have generated two-dimensional colloidal lattices in microchannels by coupling the laminar flow of dispersions of spherical colloids and geometrical confinement. They have demonstrated that different types of lattices can be obtained (hexagonal and rhombic) depending on the ratio of the width of the channel to the diameter of the particle. Microfluidic pervaporation in PDMS (polydimethylsiloxane) microchannels is another method to concentrate very dilute colloidal dispersions into organized structures⁵⁶. This method will be precisely explained in section 4.2.

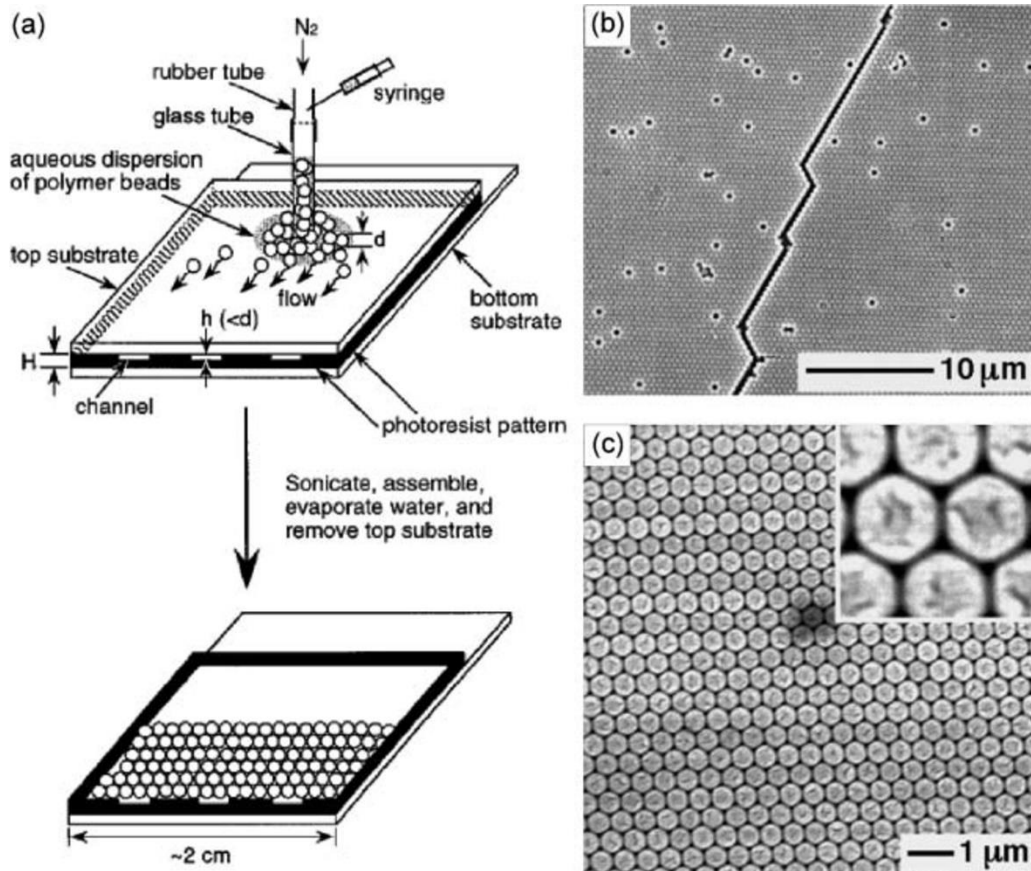


Figure 24: Crystallization of colloidal particles confined in between two parallel glass plates sealed with resin. (a) Scheme of the fabrication process, (b-c) SEM images of the obtained colloidal crystals⁵⁸.

- **Langmuir-Blodgett**

Initially, the Langmuir-Blodgett technique was developed to assemble amphiphilic molecules at the air/liquid interface and to transfer the assemblies on a solid substrate. Later, this method has been used to form hydrophobic nanoparticles monolayers at the liquid/water interface and to transfer these layers on a solid substrate. Water is generally used as the bottom phase because the very high water surface tension (73 mN/m at 20°C) enables the air/water interface to hold small dense particles⁶⁰.

The assembly of nanoparticles at the liquid/water interface via the Langmuir technique follows three steps which are schematized in Figure 25. In a first step, a solution of nanoparticles dispersed in a solvent immiscible with water is deposited at the air/water interface. Then, the solvent evaporates and leaves a light film of nanoparticles at the air/water interface. Finally, the nanoparticles are compressed thanks to movable barriers in order to form an organized layer of close-packed nanoparticles.

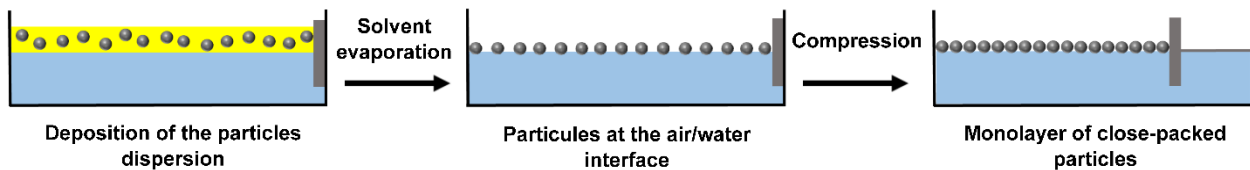


Figure 25: Schematic representation of the formation of a Langmuir layer.

Pieranski⁶¹ demonstrated that nanoparticles are trapped at the air/water interface because they reach a minimum of energy at the interface. The gain of energy, ΔE , obtained when placing a nanoparticle of radius r at the air/water interface can be expressed as follows:

$$\Delta E = -\pi r^2 \gamma_{a/w} (1 - |\cos(\theta)|)^2$$

$$\text{with } \cos(\theta) = \frac{\gamma_{a/s} - \gamma_{w/s}}{\gamma_{a/w}}$$

Equation 5: Gain of free energy (ΔE) by placing a nanoparticle of radius r at the air/water interface. θ is the three-phase contact angle; $\gamma_{a/s}$, $\gamma_{w/s}$ and $\gamma_{a/w}$ are respectively the interfacial tensions air/solid, water/solid and air/water.

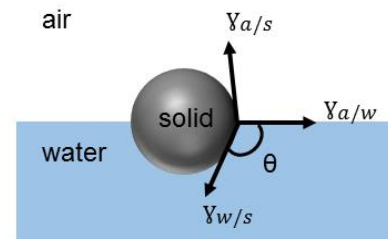


Figure 26: Schematic representation of the three-phase contact angle (θ) at the interface air/water/solid.

During compression, information about the nanoparticle's packing is obtained following the variations of the surface pressure. The surface pressure (π) is the difference between the surface tension air/water without nanoparticles (γ_0) and the surface tension air/water with nanoparticles (γ). It corresponds to the decrease of the film's surface tension in presence of nanoparticles. γ is measured by a Wilhelmy plate during compression of the nanoparticles and is used to calculate

the surface pressure. The plate is situated on the “left side” of the barrier where the particles are deposited and compressed. The surface tension on the “right side” of the barrier equals the surface tension of water.

$$\pi = \gamma_0 - \gamma$$

Equation 6: Surface pressure.

The curve following the variations of the surface pressure is called surface pressure isotherm. It provides access to the surface pressure as a function of the area allocated to each nanoparticle at fixed temperature. A typical surface pressure isotherm obtained with gold nanoparticles is presented in Figure 27 (a). Before the film is compressed, the nanoparticles are far from each other, the surface tension γ is unchanged and the surface pressure remains constant. During the compression of the nanoparticle layer, the surface tension γ decreases (more particles/surface area) entailing an increase of the surface pressure π . When the compression is important, a dense film of nanoparticles is formed at the air/water interface, γ strongly decreases and therefore the surface pressure increases dramatically.

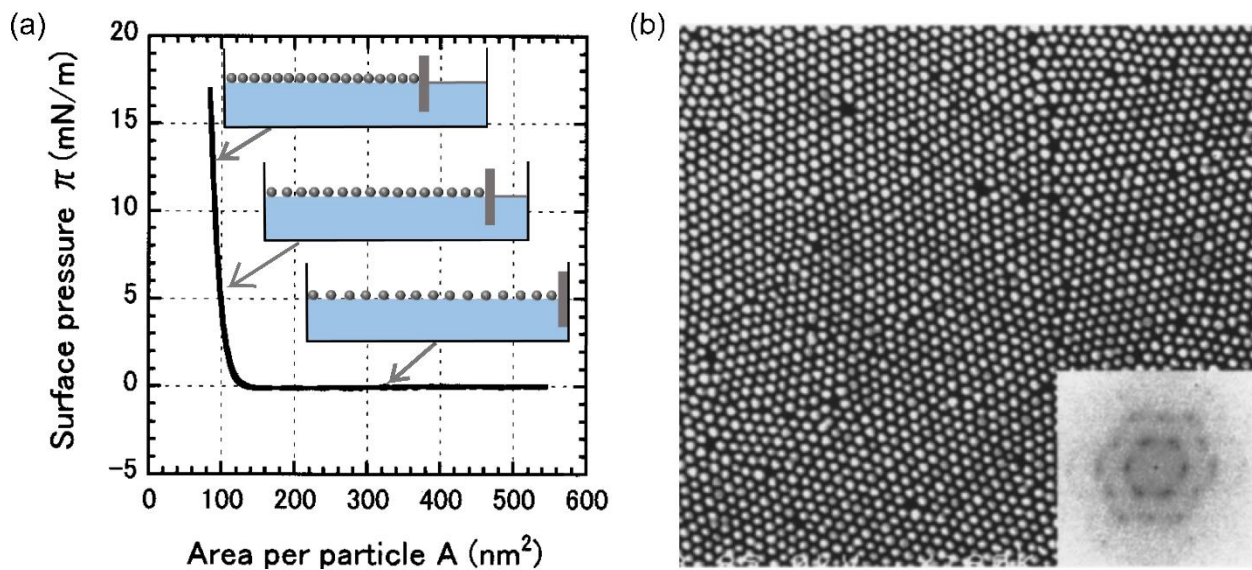


Figure 27: (a) Surface pressure–area per nanoparticle isotherm for 8.3 nm gold nanoparticles encapsulated by dodecanethiol and (b) SEM image of a monolayer made from these nanoparticles: obtained with the Langmuir-Blodgett technique⁶².

The transfer of the dense film of nanoparticles obtained by the Langmuir technique is done following the method developed by Blodgett. The transfer is performed by successive immersion and emergence of a solid hydrophobic substrate perpendicularly to the dense film as schematized in Figure 28. During the emergence, the nanoparticles deposit on the substrate thanks to hydrophobic-hydrophobic interactions. An example of dense film of gold nanoparticles is presented in Figure 27 (b).

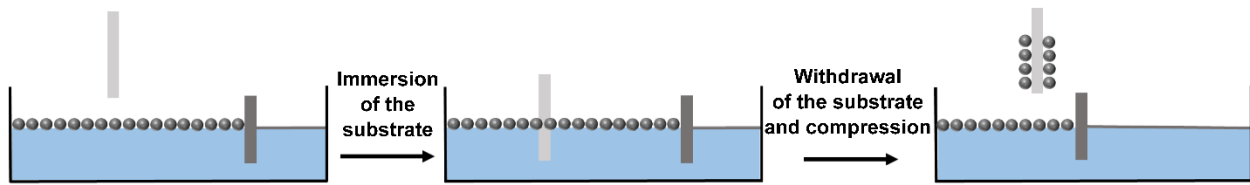


Figure 28: Illustration of the Langmuir layer transfer by immersion and emergence of the substrate.

Many parameters influence the quality of the obtained films. During her Ph.D. candidacy, Ludivine Malassis¹¹ studied them in detail. We are mentioning a few here: the nature of nanoparticles (charges, hydrophobicity...) ^{63,64}, the nature of the substrate, the transfer mode, the particles deposition speed on the substrate, the solvent volatility and the initial nanoparticles concentration ⁶². A lack of control over these parameters can cause disruptions that limit the structural order of the nanoparticles assembly.

4.2. The microfluidic pervaporation

Pervaporation is a classical process in which solvent is transported through a permeable matrix towards the atmosphere. It occurs following three steps as shown in Figure 29. First, the solvent is solubilized in the matrix (i); then, the solvent diffuses in the matrix (ii) and finally, it evaporates when entering in contact with air (iii). This phenomenon induces a net flow per unit of surface, J (m/s), of the solvent pervaporating through the permeable matrix. Based on the Fick law, and in the case where the air is dry, J depends on the solvent molar volume ρ_s , solvent diffusivity in the matrix D_s , and solvent solubility in the matrix c_s , as well as on the thickness of the membrane e (see Equation 7). For pervaporation of water ($c_s = 40 \text{ mol/m}^3$, $D_s \approx 8.5 \cdot 10^{-10} \text{ m}^2/\text{s}$, $\rho_s = 1.85 \cdot 10^{-5} \text{ m}^3/\text{mol}$) through a PDMS (Poly(dimethylsiloxane)) layer ($e \approx 10 \text{ }\mu\text{m}$), J is in the order of 100 nm/s.

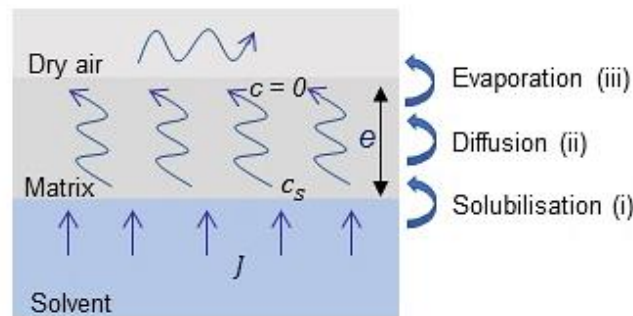


Figure 29: Transport of solvent through a permeable matrix, J.B. Salmon[©].

$$J = \frac{\rho_s c_s D_s}{e}$$

Equation 7: Solvent flow per unit of surface pervaporating through a permeable matrix.

In the 90s, Favre *et al.*⁶⁵ and Watson *et al.*⁶⁶ have quantified the pervaporation of several solvents such as water, chloroform, butanol and methanol through a PDMS layer. In 2004 and 2005, Verneuil *et al.*⁶⁷ and Randall *et al.*⁶⁸ have used this phenomenon to study the pervaporation-induced flow within microchannels molded in a PDMS block, the so-called “micro-evaporators” (see Figure 30). Because of the pervaporation of water through the permeable PDMS, there is a net flux per unit of length, q_e , of water leaving the microchannel, diffusing into the PDMS, up to the air where it evaporates. The pervaporation of the water through the PDMS thus induces a flow of water from the reservoir towards the end of the channel.

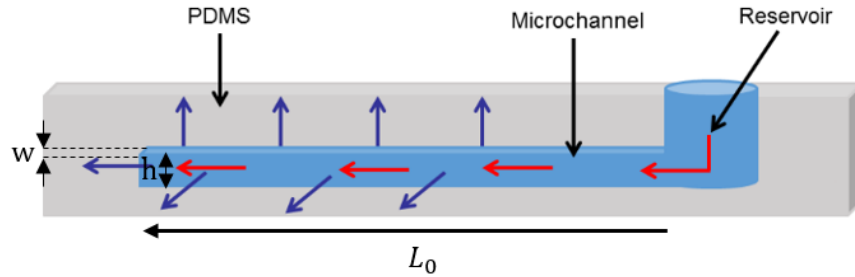


Figure 30: Microchannel filled with water in a PDMS matrix. The blue arrows indicate the pervaporation of water through the PDMS and the red arrows correspond to the induced flow from the reservoir.

Randall *et al.*⁶⁸ modeled the mass transfer of water pervaporating from one microchannel into a thick layer of PDMS surrounding the channel. Their model links the net flux per unit of length q_e of water pervaporating, to the geometry of the channel (Figure 31). They found out that for thick PDMS layer surrounding the microchannel (large R), q_e , weakly depends on R (see Equation 8).

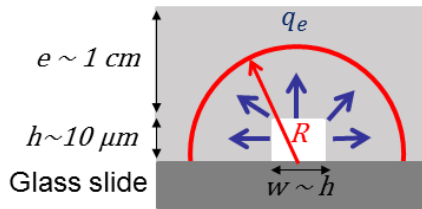


Figure 31: Model of Randall.⁶⁸

$$q_e(R) = -\frac{\pi c_s \rho_s D_s}{\ln\left(\frac{w}{4R}\right)}$$

Equation 8: Net flux of water per unit of length. w is the channel width and R is the PDMS thickness surrounding the microchannel.

Thus, for a microchannel molded in a thick PDMS block (~ 1 cm), the net flux of water per unit of length, q_e , can be approximated as in Equation 9. In that case, $q_e \sim 0.1 \mu\text{m}^2/\text{s}$ and the water flow rate being pervaporated per volume of channel $Q_e = q_e L_0$ is about 1 nL/h. Therefore, when the microchannel is molded within a thick PDMS layer, the pervaporation of water through the PDMS is very low.

$$q_e \sim \rho_s c_s D_s$$

Equation 9: Evaporation rate per unit of length.

To speed up the pervaporation process and allow a better control of spatial and temporal pervaporation, Leng *et al.*⁶⁹ have improved the microevaporator design by adding a thin PDMS membrane (in the order of tenths of microns) through which water pervaporates very fast (Figure 32). With their design, the pervaporation of the water is focused in a specific portion of the channel. A microfluidic channel with a width w , a height h and a length L is molded into a PDMS matrix. The channel is closed by a thin PDMS membrane of thickness e . A portion of the microchip is placed on a glass slide. The portion of the microchannel that does not face the glass slide corresponds to the “Evaporation zone”. We call the “evaporation length”, L_0 , the part of the microchannel going from the end of the channel to the glass slide. Typical dimensions of microevaporators are $h \sim 10 - 100 \mu\text{m}$, $w \sim 10 - 500 \mu\text{m}$, $L_0 \sim 0.5 - 1 \text{ cm}$ and $e \sim 10 - 50 \mu\text{m}$.

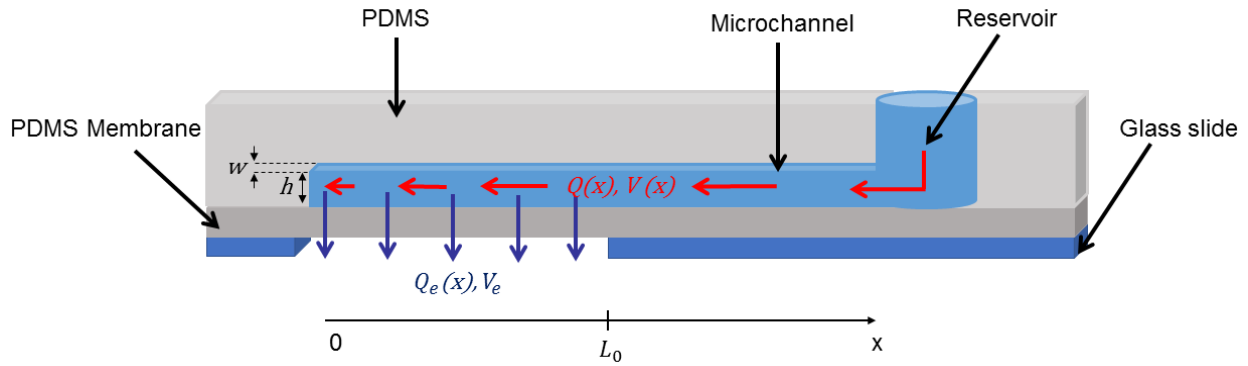


Figure 32: Sketch of a microfluidic evaporator as developed by Leng *et al.*⁶⁹.

From the flow rate of water which pervaporates through the membrane, Q_e (m^3/s), one can define the “evaporation velocity” V_e (m/s) using:

$$Q_e = wL_0V_e$$

The latter quantity corresponds to the flow velocity (m/s) of water through the membrane in case pervaporation only occurs through the membrane (i.e. in the case of a negligible pervaporation through the “upper” PDMS block, see Figure 32).

With the aforementioned microevaporator typical dimensions, q_e is of the order of $1 - 10 \mu\text{m}^2/\text{s}$ and Q_e is of the order of $10 - 100 \text{ nL/h}$. We notice that the thin membrane of PDMS allows to increase the flow rate of pervaporation by a factor 10 to 100.

The pervaporation of water through the membrane induces a compensating flow from the reservoir to the tip of the channel. Thus, at the position x in the microchannel, the water flow rate $Q(x) = hwV(x)$ is equal to the evaporation rate of the water through the membrane from the tip of the channel till the position x , $Q_e(x) = xwV_e$.

Therefore, at the position $x \leq L_0$ in the channel, the velocity is given by:

$$V(x) = \frac{V_e x}{h}$$

Equation 10: Velocity profile of the water in the microchannel for $x \leq L_0$.

The flow velocity is linear along the microevaporator. This was also experimentally observed by Verneuil *et al*⁶⁷.

For $x \geq L_0$, the velocity of the water is constant and is given by:

$$V(x = L_0) = V_0 = \frac{V_e L_0}{h}$$

Equation 11: Velocity profile of the water in the microchannel for $x \geq L_0$.

From the Equation 10 and Equation 11 we can draw the typical velocity profile in a microchannel as shown in Figure 33.

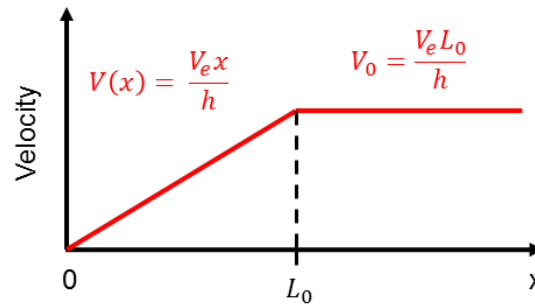


Figure 33: Typical velocity profile in a microchannel.

Pervaporation of a solvent across a thin membrane casts a typical timescale on the process: the “evaporation time”, T_e . It is the time needed to empty one volume of channel whL_0 . For the above mentioned typical dimensions of microevaporators, T_e is of the order of 100 - 1000 s.

$$T_e = \frac{hwL_0}{Q_e} = \frac{h}{v_e}$$

Equation 12: Evaporation time.

The technic of microfluidic pervaporation can be used to concentrate many different types of solutions such as: electrolytes⁶⁹, polymers^{70,71}, surfactants⁷², nanoparticles⁷³, or colloids⁵⁶. The concentration of such solutes is a consequence of the pervaporation of water through the PDMS. As the water is evaporated, more solutes are dragged from the reservoir to the end of the channel. Solutes that are too big and not volatile cannot permeate through the PDMS. Therefore, they concentrate at the tip of the microchannel. Verneuil *et al.* showed this phenomenon (Figure 34). They followed the concentration of fluorescent bead dispersions in a microchannel by looking at the variation of the fluorescence intensity. At the beginning of the experiment, the channel is black

and the fluorescence intensity is very low because the beads are not very concentrated. Over time, the fluorescence intensity increases at the tip of the channel meaning that more beads concentrate in this area.

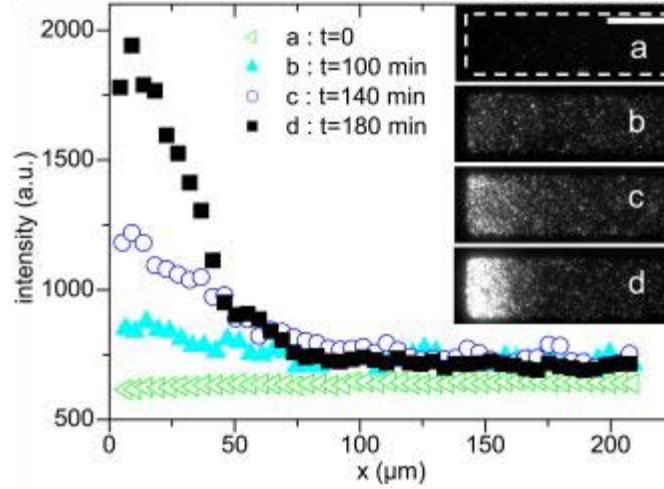


Figure 34: Fluorescence intensity measurements in a microchannel at different times t after injection of fluorescent beads. Insert: top view of fluorescence images taken at the close end of a channel at different time. The white bar represents $50 \mu\text{m}$ ⁶⁷.

During the microfluidic pervaporation, the solutes that cannot permeate through the PDMS are conveyed up to the end of the channel by a convective flux, j_c . Since the solutes are blocked at the tip of the channel, their concentration is not homogenous in the channel. A gradient of concentration builds up implying diffusion of the solutes from the highly concentrated areas towards the less concentrated part of the channel. This diffusion flux is noted j_d for dilute solution. The convective and diffusion fluxes are defined by:

$$j_c = \phi(x)V(x) \quad \text{and} \quad j_d = -D\partial_x\phi$$

Equation 13: Convective and diffusion fluxes expressions.

where D is the diffusion coefficient of the solute and ϕ is the volume fraction of solute along x . In the case of homogenous concentration across the dimensions h and w , the convection and diffusion fluxes can be schematically represented as in Figure 35. Both fluxes balance each other out at a certain position, $x = p$, in the microchannel when $j_c \approx j_d$:

$$\phi \frac{p}{T_e} \approx D \frac{\phi}{p}$$

A characteristic length scale, p , of a virtual accumulation box where the solutes accumulate appears. p is defined by the relation: $p = \sqrt{DT_e}$. For $x < p$, the diffusion prevails over the convection; whereas for $x > p$, the convection dominates (see Figure 35). In other words, to concentrate solutes in a microevaporator, the length of the channel must be longer than the length of the accumulation box p .

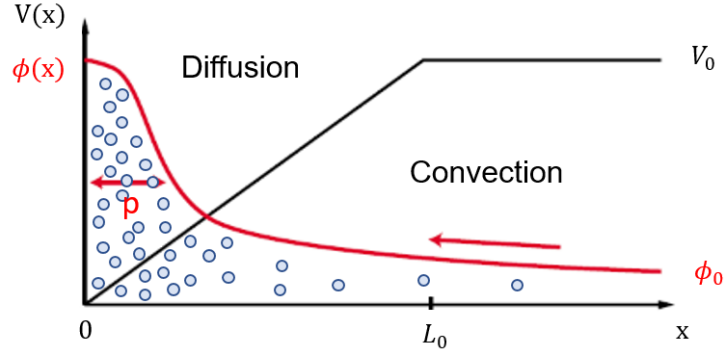


Figure 35: Typical velocity profile (in black) in a microevaporator inducing the concentration (in red) of solutes from the reservoir down to the accumulation box of size p close to the tip of the microchannel⁷⁴.

Leng *et al.*⁶⁹ have shown the dependence of the size of the accumulation box on the mobility of the solute (see Figure 36). Different sizes of solutes were concentrated in channels of same dimensions. Results show that the smaller the solutes, the bigger the size of the accumulation box. Therefore, the faster the solutes can diffuse, the bigger the accumulation area. The size of p depends as well on the geometry of the microevaporator, via the evaporation time.



Figure 36: Evaporation-induced concentration of different sizes of solutes⁶⁹.

The volume fraction variation of the solute, $\Delta\phi$, in the accumulation zone can be estimated from the mass conservation of the solutes inside a microchannels upon two assumptions. First, When the diffusion-dominated region is permanently fed with solutes that do not permeate through the PDMS and second assuming that the volume fraction of the solutes is homogenous in the box p . Under these conditions, the solutes entering the accumulation zone of volume pwh are delivered at a rate whj_0 (j_0 being the incoming flux of solutes) which induces a concentration increase expressed as following:

$$\frac{\Delta\phi}{\Delta t} \approx \frac{j_0wh}{pwh} \quad \text{where} \quad j_0 = \phi_0 V_0 = \phi_0 \frac{L_0}{T_e}$$

The variation of concentration in the accumulation zone is then defined by:

$$\frac{\Delta\phi}{\Delta t} \approx \frac{\phi_0 L_0}{T_e p}$$

This estimate shows that the concentration rate in the accumulation zone varies linearly in time. The concentration of dispersions of particles in the accumulation zone depends on the type of solutes (via its diffusion coefficient), the initial concentration of solutes in the reservoir (ϕ_0) and the geometry of the microevaporator (via L_0 and T_e).

For classical microfluidic devices, ($h \approx 15 \mu\text{m}$, $w \approx 50 \mu\text{m}$, $L_0 \approx 5 \text{ mm}$ and $e \approx 50 \mu\text{m}$) it takes approximately 12 days to concentrate a dilute dispersion ($\phi_0 \approx 10^{-5}$) up to a dense state ($\phi_d \approx 1$) at the channel tip. We want to minimize the duration of the microfluidic pervaporation experiments and bring it down to several hours only. We know that the concentration process is efficient only for $p \ll L_0$. For typical microevaporators, $p \approx 100 \mu\text{m}$, this value can be used to set the minimal size of the microchannels. As seen above, $\Delta t \sim (\Delta\phi T_e p) / (\phi_0 L_0)$; we can then minimize the duration of the experiment by increasing the length L_0 up to one centimeter, using thin channel ($h \approx 10 \mu\text{m}$) and/or decreasing T_e using thin membrane ($e = 15 \mu\text{m}$).

The pervaporation of solvents contained in PDMS microchannels can be further sped up for small channel width and well separated channels with a distance d , in-between the channel set to $d \geq 10h$ ⁷⁵. Indeed, channels evaporate independently if they are far from each other so that the permeation rate of water in the PDMS is the same for each channel. If channels are too close to each other, the PDMS in-between the channels saturates very fast with water and the evaporation rates of these channels are decreased.

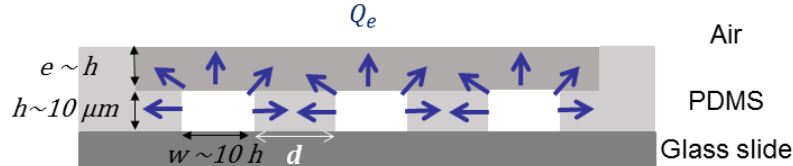


Figure 37: Optimal distance in-between microchannels.

Over time, the solutes concentrating inside the microchannels form dense states. The design of Leng *et al.* allows the collection of these dense states from the microchannels (see Figure 38). After removal of the glass slides, the membrane is peeled off and the micromaterial is deposited on a conducting tape for electron microscopy imaging.

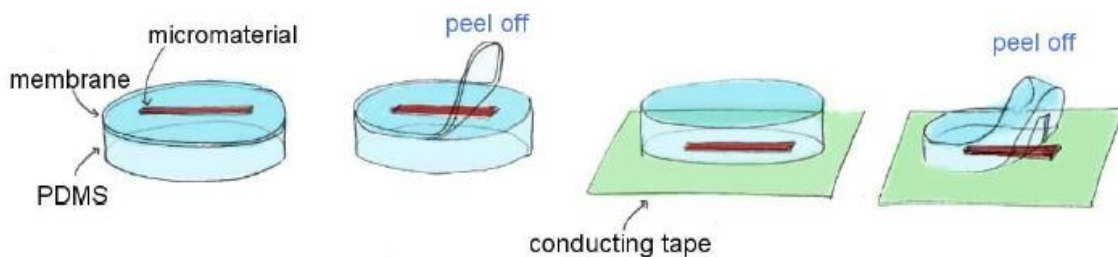


Figure 38: Transfer of the micromaterial on conducting tape for imaging, J. Leng and J.B. Salmon[©].

Aurore Merlin⁵⁶ used microevaporators to concentrate dispersions of colloids. She followed the growth of dense states of colloids in microchannels by optical microscopy (Figure 39 (a)). Initially, the microchannel is filled with a dilute dispersion of transparent colloids and therefore also appears transparent. The tip of the channel becomes more opaque upon accumulation of colloids. At a given time, referred to as the “nucleation” time, a front appears and grows toward the entrance of the channel. The dense material formed in the microchannel is more transparent than the rest of the channel filled with beads. This difference in transmission of light suggests a colloidal organized texture leading to specific photonic properties. Indeed, the dense front Bragg-diffracts the light when shone with a diffuse white light (Figure 39 (b)). Electronic microscopy analysis finally proved the crystallinity of the dense state (Figure 39 (c)).

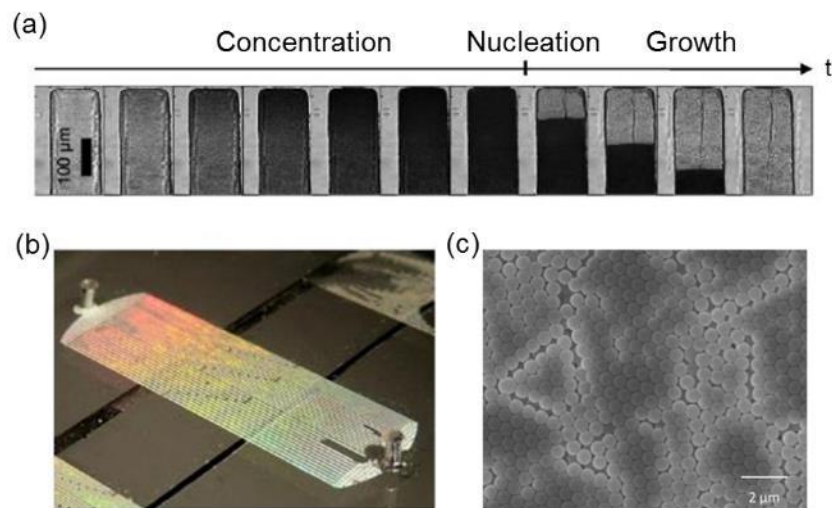


Figure 39: (a) Series of snapshots obtained close to the tip of one single channel (width = 50 μm) during the concentration of a colloidal suspension of polystyrene beads in water ($R = 250$ nm and $\phi_0 = 0.3\%$). The time elapsed in between two consecutive images is 15 minutes. (b) Picture showing 2x2 of 8 microsystems fabricated in one microchip. (c) SEM image of the obtained colloidal crystal⁵⁶.

Following the work of Aurore Merlin, Julie Angly concentrated spherical (Figure 40a) and anisotropic (Figure 40 (b)) metal nanoparticles in microevaporators. She obtained micromaterials made of densely packed nanoparticles showing no order. For comparison, she evaporated commercial silica beads which gave a material showing long-range crystallization (hexagonal packing). From her experiments, it appears that the polydispersity and the shape of the nanoparticles impact the formation of crystalline material. She also showed that heterostructures can be engineered by growing side-by-side materials made of different types of nanoparticles (Figure 40 (d)). These structures are obtained by sequential filling of the microchannels with different dispersions of nanoparticles.

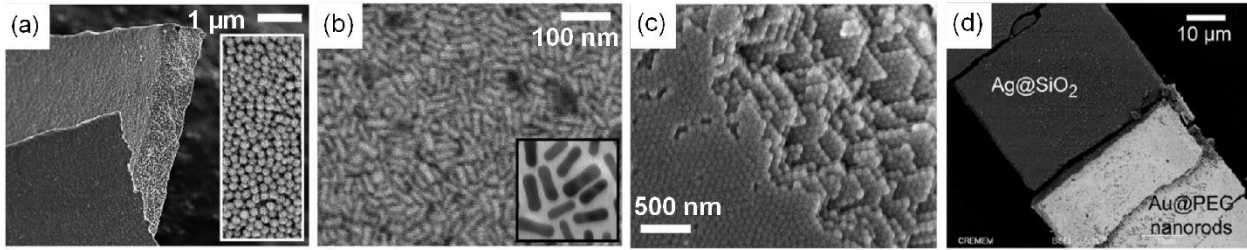


Figure 40: Dense structures generated using the technique of microfluidic pervaporation and observed with SEM. (a) Au@PEG 60 nm diameter (inset is a SEM image of the surface of the material), (b) Au@PEG nanorods (inset is a TEM image of nanorods), (c) 80 nm diameter silica NPs, (d) a double junction made of Ag@SiO₂ next to Au@PEG nanorods⁷⁶.

The technique of microfluidic pervaporation also allows the concentration of solutes inside complex-shaped microchannels as shown in Figure 41. The Figure 40 and Figure 41 reveal the potential of microfluidic pervaporation technique to create new functional microscale materials.

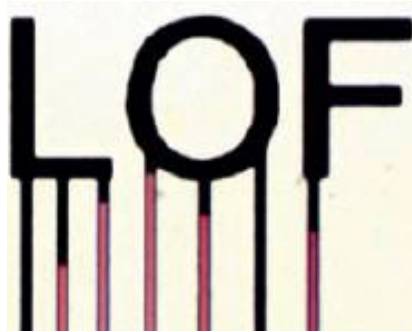


Figure 41: Nanoparticles concentrated in microchannels.

The growth of a dense state in a microevaporator can be recorded by optical imaging. A typical growth profile is represented in Figure 43. x_f corresponds to the position of the dense state front during the concentration of the dispersion of solid particles in pure water.

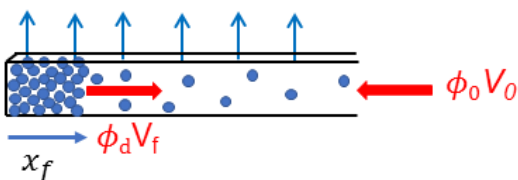


Figure 42: Solute mass conservation in one microchannel.

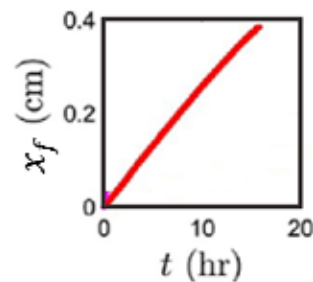


Figure 43: Growth profile of Ag@SiO₂ nanoparticles in one microchannel.

A simple mass conservation (Figure 42) balancing the volume growth rate of the dense state with the flux of incoming particles gives:

$$\phi_0 V_0 = \phi_d V_f$$

And

$$x_f = (t - T_n) \frac{\phi_0 V_0}{\phi_d}$$

Where

V_0 is the entrance velocity obtained from the calibration

ϕ_0 is the initial volume fraction of gold nanoparticles in water

ϕ_d is the volume fraction of gold nanoparticles in the dense state

V_f is the growth rate of the dense state

Making all the variables dimensionless we obtain:

$$\frac{x_f}{L_0} = \frac{\phi_0}{\phi_d} \left(\frac{t - T_n}{T_e} \right)$$

Equation 14: Extraction of the dense state packing fraction.

Knowing the dimensions of the microevaporator, the initial volume fraction of the solutes in the dispersion and assuming the final packing fraction (for instance 0.74 for FCC packing of monodisperse hard spheres), we can predict the growth rate of a dense state forming from the concentration of the solutes accumulating inside the microchannel.

In this section, we have seen that microfluidic pervaporation is a good technique to assemble colloids at a controlled pace. It works for a large set of solutes, from molecules to large colloids. It permits to grow and shape-up extended, three-dimensional long thick lattices of densely packed nanoparticles with a fine control as to the positioning and composition of the array. It also allows to predict and tune at which rate the colloidal dense state will grow. In Chapter 2, we use the technique of microfluidic pervaporation to assemble micro- and nano-size particles into bulky 3D materials.

4.3. Assembly on droplets

Emulsions are metastable colloids composed of two immiscible liquids such as oil and water, one being dispersed as droplets in the other. Such systems are usually stabilized by active surface agents. Ramsden⁷⁷ (1903) and Pickering⁷⁸ (1907) were the first to use solid particles to stabilize emulsions. Such particles adsorb at the liquid/liquid interface and provide a barrier to prevent droplets coalescence⁷⁹. After the preliminary description of this new type of emulsion, this discovery fell into oblivion. Only towards the end of the 90s, Pickering emulsions gained interest again. The first extensive use of Pickering emulsions as templates for particle assembly was reported by Velev *et al.*⁸⁰ They demonstrated the technological potential of oil-in-water emulsions stabilized by latex particles for microencapsulation. Since that time, particle stabilized emulsions have been largely used for many applications in cosmetics⁸¹, in food industry⁸², for oil recovery^{83,84}

and more recently in pharmaceuticals⁸⁵. A wide range of solid particles have been used as stabilizing agents: iron oxide particles, silica⁸⁶, latex⁸⁷, calcium carbonate^{88, 89}, carbon black⁹⁰, microgel particles⁹¹, gold particles⁹², etc (see Figure 44).

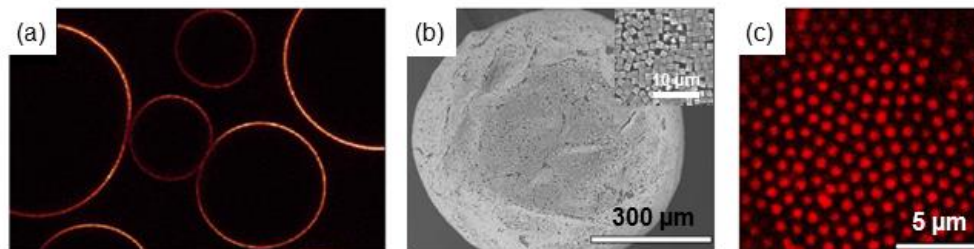


Figure 44: (a) Fluorescent confocal microscope image (excitation: 488 nm, emission: 610 nm) of a water-in-toluene emulsion (size 10 to 100 microns) stabilized by CdSe nanoparticles of diameter 4.6 nm⁹³. (b) SEM image of a dried emulsion stabilized by Neighborite cubes (shown in inset)⁹⁴. (c) Confocal microscope image of an emulsion stabilized by PNipam microgel particles⁹⁴.

We had to wait the work of Finkle *et al.*⁹⁵ to understand that the type of particles used determines the types of emulsions (oil-in-water or water-in-oil). Their ideas were then reinforced by the experiments of Schulman and Leja⁹⁶. Together, they demonstrated that particles preferentially wet by the water phase (for instance silica particles) stabilize oil-in-water emulsions; whereas particles preferentially wet by the oil phase (such as carbon black) stabilized water-in-oil emulsions. Water-in-oil emulsions are typically named inverse emulsions.

The contact angle, θ (by convention measured in the aqueous phase), quantifies the wettability of a spherical particle at the oil/water interface and can therefore be used to predict the type of emulsion formed from a certain type of particles. In the case of a water-in-oil emulsion 50%/50% by volume; when $\theta < 90^\circ$, particles stabilize an oil-in-water emulsion; but when $\theta > 90^\circ$, particles stabilize a water-in-oil emulsion as schematized in Figure 45. It should be noted that if the particles are too hydrophilic (θ very small) or too hydrophobic (θ very large), they tend to remain in their respective phase resulting in unstable emulsions. Finally, the type of emulsion can be reversed by changing the volume ratio of the two liquid phases. Increasing the dispersed phase volume leads to a « catastrophic phase inversion »⁹⁷, the dispersed phase becomes the continuous phase. Such emulsions are often unstable and coalesce⁹⁸. It is important to note that the contact angle as shown in Figure 45 applies to spherical particles individually adsorbing at the interface. The representation of the contact angle becomes more complicated in the case of irregularly shaped particles or aggregated particles.

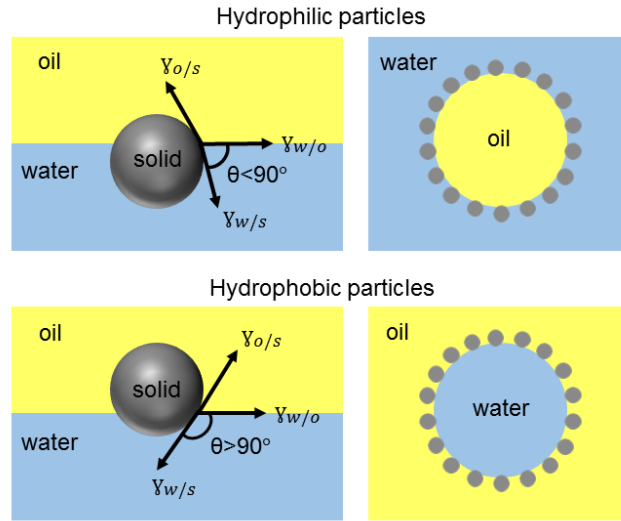


Figure 45: Contact angle and corresponding emulsion type.

The contact angle of a spherical small particle at a liquid/liquid interface is defined by the action of three interfacial tensions: oil/solid interfacial tension ($\gamma_{o/s}$); water/solid interfacial tension ($\gamma_{w/s}$) and water/oil interfacial tension ($\gamma_{w/o}$). Young's equation (Equation 15) defines the position of the particle at the interface from these three interfacial tensions.

$$\cos(\theta) = \frac{\gamma_{o/s} - \gamma_{w/s}}{\gamma_{w/o}}$$

Equation 15: Young's equation

($\gamma_{o/s}$ oil/solid interfacial tension; $\gamma_{w/s}$ water/solid interfacial tension and $\gamma_{w/o}$ water/oil interfacial tension).

When a particle is moved from the continuous phase towards the emulsion interface, a contact surface area oil/water is replaced by contact areas particle/oil and water/particle. This leads to a decrease of the total interfacial free energy of the system. A particle of radius r adsorbed at the interface leads to a decrease of energy quantified by:

$$\Delta E = -\pi r^2 \gamma_{o/w} (1 - |\cos(\theta)|)^2$$

Equation 16: Free energy gain by placing a particle of radius r at the oil/water interface. Where $\gamma_{o/w}$, $\gamma_{p/w}$ and $\gamma_{p/o}$ are the interfacial tensions oil/water, particle/water and particle/oil⁹⁹.

When the new minimum of free energy is very small compared to thermal energy ($k_B T$), particles are trapped at the liquid/liquid interface and the emulsion is stabilized by solid particles. The gain of energy is maximum for a 90° contact angle (see Equation 16). Thus, a micron size particle at a typical oil/water interface ($\gamma_{o/w} \sim 50$ mN/m) with $\theta = 90^\circ$ is trapped in an energy well of about $10^6 k_B T$ ⁷⁹. This observation has led researchers to prepare amphiphilic particles also known as

« Janus » particles¹⁰⁰. Half the surface of these particles is covered by hydrophobic groups whereas the other half is covered by hydrophilic groups.

The formation of particle-stabilized emulsions depends on many factors. We will emphasize the most important ones such as the particle diameter, the oil/water interfacial tension and the particles' hydrophilicity.

Let's start with the particle size and shape. Nanoparticles as small as 4.2 nm can stabilize an emulsion⁹³ as depicted in Figure 44 (a) showing an image of water in toluene droplets stabilized by CdSe nanoparticles. In the case of a mixture of polydisperse nanoparticles, the competition between the thermal fluctuations and the interfacial energy leads to a size selective assembly. Small particles are replaced in favor of larger particles of the same type simply because the reduction of the free energy is more important for larger particles. The emulsion stability also strongly depends on particle shape. For instance, the emulsion stability increases with the increase of the particle aspect ratio due to stronger capillary forces¹⁰¹.

Then, the oil polarity directly impacts the value of the contact angle and the subsequent type of emulsions (water/oil or oil/water). Binks and Lumsdon¹⁰² have showed that the contact angle that partially hydrophobic silica particles make with the oil/water interface depends on the nature of the oil. These particles are “more hydrophobic” at polar oil/water interfaces, preferring water-in-oil emulsions (they form a large contact angle with the water phase) (see Figure 46). On the contrary, they are “more hydrophilic” at non-polar oil/water interfaces, forming oil-in-water emulsions (small contact angle with the water phase). Moreover, for non-polar oils^{103,104}, the oil/water interface is negatively charged, which can prevent the adsorption of particles at the interface due to electrostatic repulsions. The electrostatic barrier can be lowered by adding electrolytes but this would also impact the particles wettability.

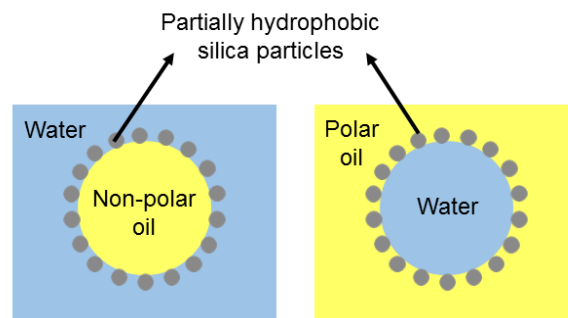


Figure 46: Effect of the oil polarity on the type of emulsion.

The wetting properties of the nanoparticles can be tuned by using different methods. One of the most popular methods is the surface modification of the particles before emulsification. For instance, charged hydrophilic particles can be rendered hydrophobic by adsorbing surfactants of opposite charges on the particles¹⁰⁵. In this system, the surfactant will be used in very low concentration so that it does not contribute to the stabilization of the emulsion on its own. Likewise,

hydrophilic silica particles can be rendered hydrophobic by grafting silane groups on the particles¹⁰⁶. Another method consists in modifying the surface charges of the particles by changing the pH or the ionic strength. Hydrophobic particles coated with ionizable groups dispersed in water can become hydrophilic by increasing pH. Indeed, the increase of the pH increases the particles charges which renders the particles hydrophilic^{107, 108}. This phenomenon was clearly demonstrated by Binks and Lumsdon¹⁰² for partially hydrophobic silica particles. At $\text{pH} < 9$, particles are preferentially dispersed in oil whereas at $\text{pH} > 12.5$, they are preferentially dispersed in water. At the surface of the silica particles, SiOH groups dissociate into SiO^- increasing the hydrophilicity of the particles. Thus, at low pH, water-in-oil emulsions are obtained whereas at high pH, oil-in-water emulsions are observed (see Figure 47).

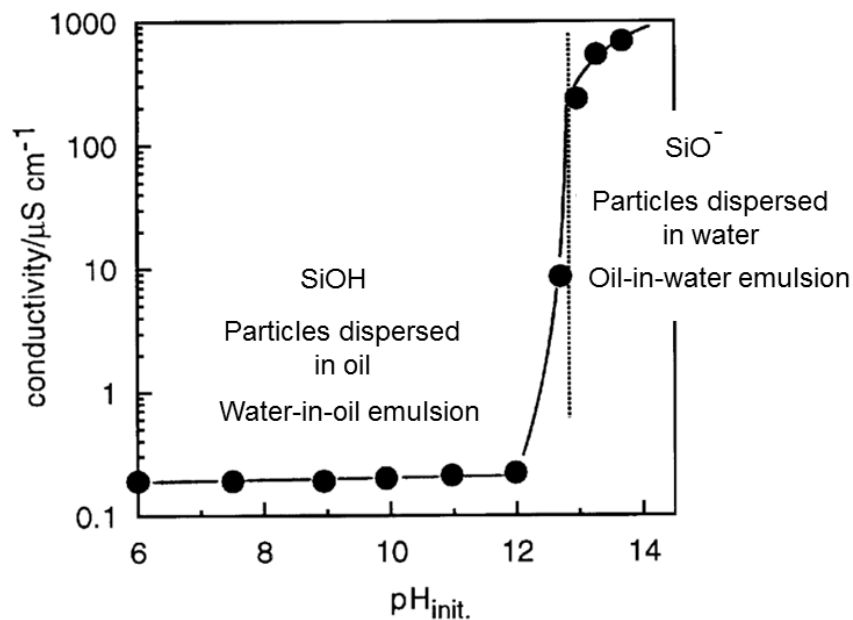


Figure 47: Conductivity and type of water/toluene (50/50) emulsions stabilized by 2 wt% partially hydrophobic silica particles in oil as a function of initial pH in water.

Golemanov *et al.*¹⁰⁹ have shown that electrolytes, by screening charges at an interface, lead to particles aggregation if the screening is too strong. This observation explains why slightly flocculated particles (with a low charge but still stable) are better to stabilize the emulsions (Figure 48). If the screening of the charges is too strong, the aggregation of the particles in solution is irreversible and the emulsions are unstable. The same authors demonstrated that the Schulze-Hardy rule can apply to emulsions. This rule states that the critical concentration of particles coagulation by adding salts scales as $1/z^6$, where z is the counter-ion valence. The quantity of the electrolyte which is required to coagulate a definite amount of a colloidal solution depends on the valency of the ion (z) having a charge opposite to that of the colloidal particles. The greater is the, the faster is the coagulation. Indeed, the greater the charge of the ions, the greater is the attractive electrostatic forces between ions, the faster is the coagulation. Hence, for the coagulation of

negatively charged particles, trivalent cations are far more effective than divalent cations which in turn are more effective than monovalent cations.

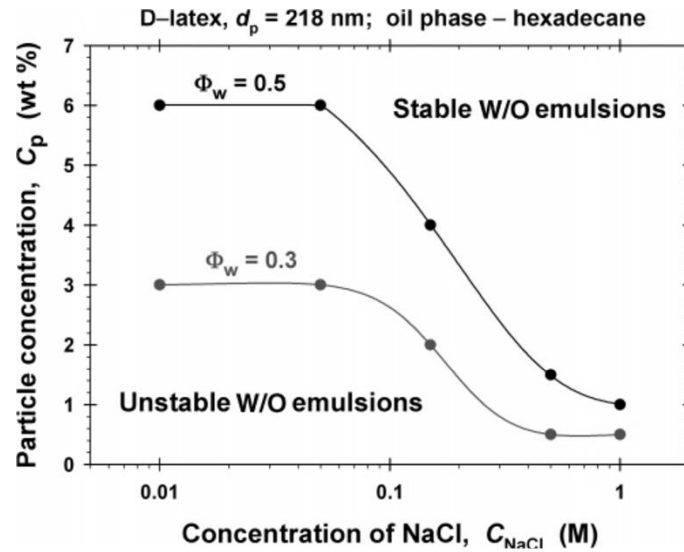


Figure 48: Stability-instability diagram for water-in-oil emulsions stabilized by polystyrene latex particles at various salt concentrations. Φ_w is the water mass fraction¹⁰⁹.

Controlling the particles surface charges is a good way to tune the surface coverage of nanoparticles stabilized emulsions. Gautier *et al.*¹¹⁰ showed that the mean surface coverage of latex stabilized emulsions can vary as a function of pH. In this example, pH is modified to screen the particles' surface charges. At very low pH (pH = 1), a close-packed homogenous monolayer of particles covers the droplets (Figure 49 (a)). At higher pH (pH = 4.8), the droplets are also not homogeneously covered, as shown in Figure 49 (b).

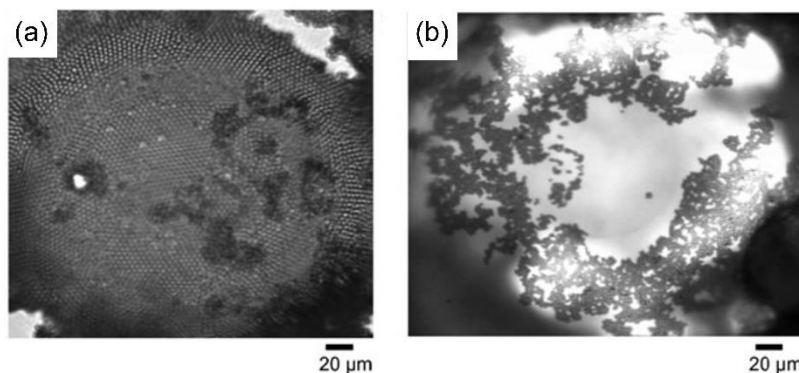


Figure 49: Microscope image of a drop covered by latex particles at: (a) pH=1 et (b) pH=4.8¹¹⁰.

Pickering emulsions being only stabilized by particles, the number of available particles impacts the final emulsion stability and the droplets size. Indeed, poorly covered droplets can coalesce. The coalescence process stops as soon as the oil/water interface is sufficiently covered.

Assuming that all the particles are irreversibly adsorbed at the oil/water interface, the mean diameter of the fully covered droplets, D , is given by:

$$\frac{1}{D} = \frac{m_p}{4C\rho_p d_p V_d}$$

Equation 17: Estimation of the final drop diameter (D) as a function of the particles weight (m_p), the particles density (ρ_p), the particles diameter (d_p), the volume of the dispersed phase (V_d), and the fraction of the droplet interfacial area covered by the particles (C)¹¹¹.

The C parameter corresponds to the packing density of the particles at the liquid/liquid interface. For hexagonally-close-packed monodisperse particles C is equal to 0.9¹¹⁰. In that case, when C reaches 0.9, the process of coalescence stops. From Equation 17, the emulsion droplets size is inversely proportional to the particles weight, all the other parameters being constant. Numerous studies^{110,111} underscore this linear dependence as presented in Figure 50. The packing parameter C is deduced from the slope of the curve $1/D = f(m_p)$.

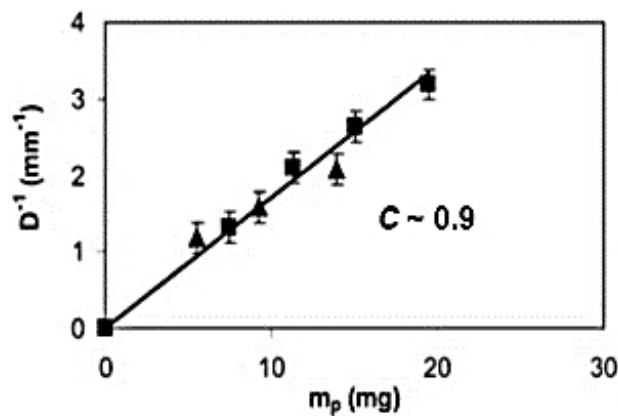


Figure 50: Influence of the mass of particles on the drop size for emulsions stabilized by latex particles.

Once the particles are adsorbed at the interface, their mobility in the normal direction is greatly confined due to their high adsorption energy. They are more likely to move laterally, and the final particles packing also depends on the particles interactions equilibrium.

Electrostatic and dipole-dipole repulsions, Van Der Waals attractive forces as well as capillary attraction are the most important particle-particle interactions at an emulsion interface. These forces partly govern the particles behavior at the interface of two immiscible liquids.

When the particles are at an oil/water interface, their surface charges are dissociated due to the inhomogenous environment surrounding the particles¹¹². In the water phase, groups of opposite charges come close to the charged particle and lead to the electrostatic repulsion of neighboring particles at the interface. Repulsions may also occur through the oil due to water trapped on the surface of the particle¹¹² (Figure 51).

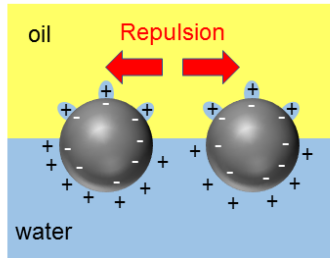


Figure 51: Electrostatic repulsion through the oil and the water.

Pieranski⁶¹ identified long-range repulsive interactions between two particles placed at a water/air interface. His results were then applied to oil/water interfaces^{112,113}. The particle's surface charges become inhomogeneous when they are partially immersed in a water phase and an oil phase. This leads to the formation of a dipole orthogonal to the interface. One of the poles corresponding to the solvated charge groups and the other corresponding to the counterions. (Figure 52). Neighboring dipoles repulse each other and this leads to a dipolar repulsion between particles at the interface.

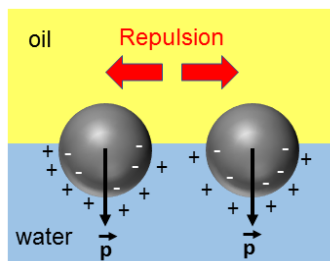


Figure 52: Dipole repulsion.

Binks and Horozov established that Van Der Waals forces between two particles close to each other at the liquid/liquid interface depend on the interparticle distance and on the contact angle (θ). Van Der Waals forces are significantly attractive when the spacing between the particles is of the order of nanometers¹¹³.

Chan *et al.*¹¹⁴ modelled the capillary forces between two spherical particles at a liquid/liquid interface and showed that they strongly depend on the particle size and density. Capillary forces can either be repulsive or attractive. For big or heavy particles, the particles deform the oil/water interface¹¹² and lead to non-negligible capillary forces. In the case of particles of diameter smaller than 1 μm , capillary interactions are negligible¹¹⁵. In the next chapters, the particles used are small therefore capillary forces are not considered.

In this section, we have seen that Pickering emulsions, compared to the other self-assembly techniques, permit the formation of large interfacial areas homogeneously covered by nanoparticles. We explained that the adsorption of particles at the water/oil interface results from a decrease in the total free energy. Pickering emulsions are usually very stable because it takes lots of energy to

desorb the particles from the interface. Many parameters such as particle size, particle wettability or particle charges can be tuned to ease the interfacial adsorption of particles. In the next section, we will present how these solid-stabilized emulsions have been used to design new functional dispersed materials such as microcapsules.

5. Colloidosomes and microcapsules syntheses

Recently, Pickering emulsions have been used as template to create supracolloidal structures such as colloidosomes or microcapsules. Particles are used as building blocks in the design of these structures. In many applications, to fully benefit from their properties, colloidosomes and microcapsules have to keep their spherical shape upon drying, when adding surfactants or during their transfer in a different media than the synthesis media. For this reason, different methods were implemented to improve their mechanical performances. Throughout several examples, we will show how such supracolloidal structures are formed and which tricks are used to improve their overall performances.

The first spherical hollow microcapsules were synthesized by Velev *et al.*⁸⁰ by self-assembly of latex particles at the interface of octanol-in-water emulsions droplets. The particles were placed at the interface of the emulsion due to their surface functionalization with lysine hydrochloride. Lysine adsorbs on the negative charges of the latex particles and renders the particles partially hydrophobic. The latex particles are then bridged together at the emulsion interface by adding HCl and CaCl₂, which are known to be efficient flocculating agents for latex spheres. Velev *et al.* have shown that the obtained microcapsules keep a spherical shape upon disruption of the oil/water interface by adding an alcohol.

Permeable capsules obtained by self-assembly of close-packed colloidal particles were later named « colloidosomes » by Dinsmore *et al.*¹¹⁶. They explored other ways to lock the particles together, by sintering the colloidal particles (heating above the glass transition temperature of the particles) (Figure 53); and adding a binder (the poly-L-lysine). The main breakthrough was the successful transfer of the obtained capsules in a liquid identical to the liquid contained inside the capsules. Their work led to the synthesis of polystyrene microcapsules of controlled size, porosity and mechanical properties therefore demonstrating the high potential of these microcapsules for encapsulation and controlled release of drugs. Later one, Hsu *et al.*¹¹⁷ showed that the particles need to be sintered, otherwise the colloidosomes buckle during the evaporation of the internal phase.

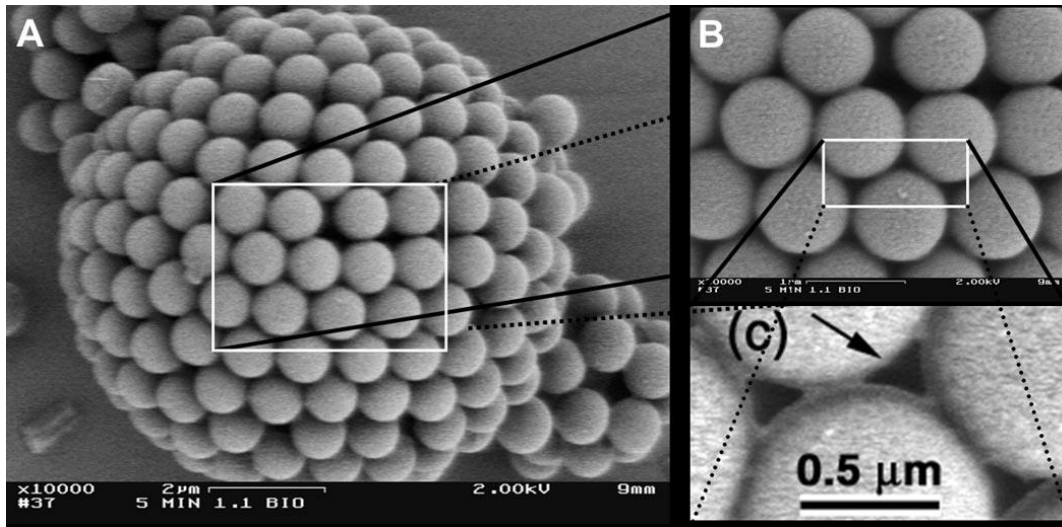


Figure 53: (a) SEM image of a dry colloidosome made from polystyrene particles of diameter $0.9 \mu\text{m}$. (b) and (c) Zoom onto the colloidosomes surface, the latex particles were locked together by sintering¹¹⁶.

Apart from sintering and addition of binders, more advanced techniques enable to lock together the particles forming the colloidosomes. For instance, Thompson *et al.*¹¹⁸ and Fielding *et al.*¹¹⁹ have cross-linked silica or latex particles comprising alcohols groups on their surface with a polymer comprising isocyanate groups therefore forming urethane bonds. Likewise, Bon *et al.*¹²⁰ have crosslinked poly(methyl methacrylate) particles forming colloidosomes with divinylbenzene. They went further and also copolymerized divinylbenzene-styrene at the interface of the emulsion finally embedding the microgel particles in a polymer shell. The as obtained shell elasticity can be tuned by adding a third monomer, the n-butyl methacrylate, the glass transition temperature of which is close to the ambient temperature. Other types of polymerizations will also be detailed in the following examples. In the remainder of the manuscript, we will call “microcapsules”, colloidosomes having nanoparticles embedded in a shell.

In order to demonstrate the encapsulation potential of colloidosomes and microcapsules we will refer to several papers including the ones of Patra¹²¹ and Möller^{122,123}. Patra has shown that large polymer chains (such as Dextran $M_w = 500\text{k}$) encapsulated inside Fe_3O_4 colloidosomes cannot permeate through the barrier formed by the particles (diameter = 11 nm) whereas smaller polymers (such as Dextran $M_w = 40\text{k}$) can (Figure 54 (a)). Martin Möller’s team, has studied the evaporation profiles of oil and water encapsulated in microcapsules made of silica particles and silica shell (Figure 54 (b)). The silica shell is obtained by polycondensation of a small silica oligomer, the polyethoxysiloxane (PEOS), at the oil/water interface. Due to the thin porous silica shell, the release is of the order of the hour.

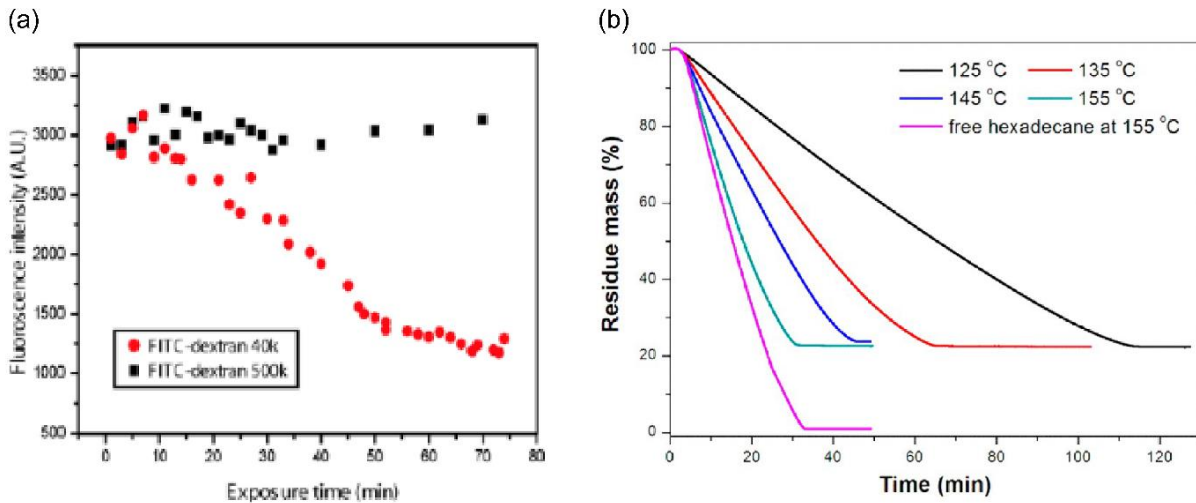


Figure 54: (a) Release of Dextran molecules of different sizes encapsulated in Fe_3O_4 particles stabilized colloidosomes (the particle diameter is 11 nm) (b) Evaporation of hexadecane encapsulated in silica microcapsules at different temperatures.¹²³

Recent work show how specific types of colloidosomes can be used to design new innovative microstructures responsive to external stimuli such as pH¹²⁴, temperature¹²⁵, etc. Lawrence *et al.*¹²⁵ have synthesized temperature sensitive colloidosomes using microgel particles (poly(N-isopropylacrylamide)-co-acrylic acid) as stabilizing agent. These colloidosomes can shrink or expand depending on the temperature. Their size change is reversible if it does not exceed 13%. Later on, Shah *et al.*¹²⁶ have improved the thermal response of these colloidosomes by crosslinking the PNIPam (poly(N-isopropylacrylamide)) particles at the interface via an amine-aldehyde condensation reaction. They obtained a size decrease in the order of 80% while increasing the temperature with a full reversibility (Figure 55). This type of colloidosomes could be very useful in the formulation of cosmetics or pharmaceutical products which require a controlled release of active ingredients.

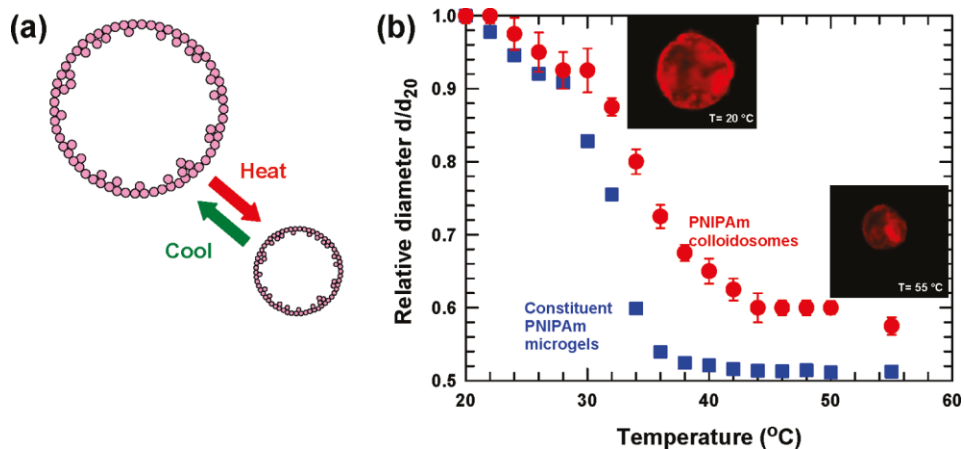


Figure 55: (a) Schematic illustration of thermo-responsive PNIPam colloidosomes. (b) Relative diameter of PNIPam colloidosomes and of PNIPam particles as a function of the temperature¹²⁶.

During her Ph.D. candidacy, Debabrata Patra¹²¹ demonstrated the catalytic potential of microcapsules made of gold nanoparticles and β -galactosidase enzyme (Figure 56 (a) and (b)). The β -galactosidase is used to hydrolyze chlorophenol red- β -D-galactopyranoside substrate. The β -galactosidase in the enzyme-NPs microcapsules retains 76% enzymatic activity as compared to free β -galactosidase. Zhang *et al.*¹²⁷ reported the encapsulation of a Laccase solution in silica colloidosomes of different shell structures and the study of catalytic performance of the encapsulated enzyme in toluene. A water/oil interfacial silanization (using PEOS) was performed to link the silica particles. Thanks to the silica shell porosity, the catalytic substrates can pass through the shell and react with the laccase (Figure 56 (c) and (d)). The rate of the enzymatic reaction is controlled by the diffusion of the substrate and product molecules across the colloidosome shell. By varying the shell structure (monolayer or bilayer of particles), the catalytic activity of the enzyme can be controlled.

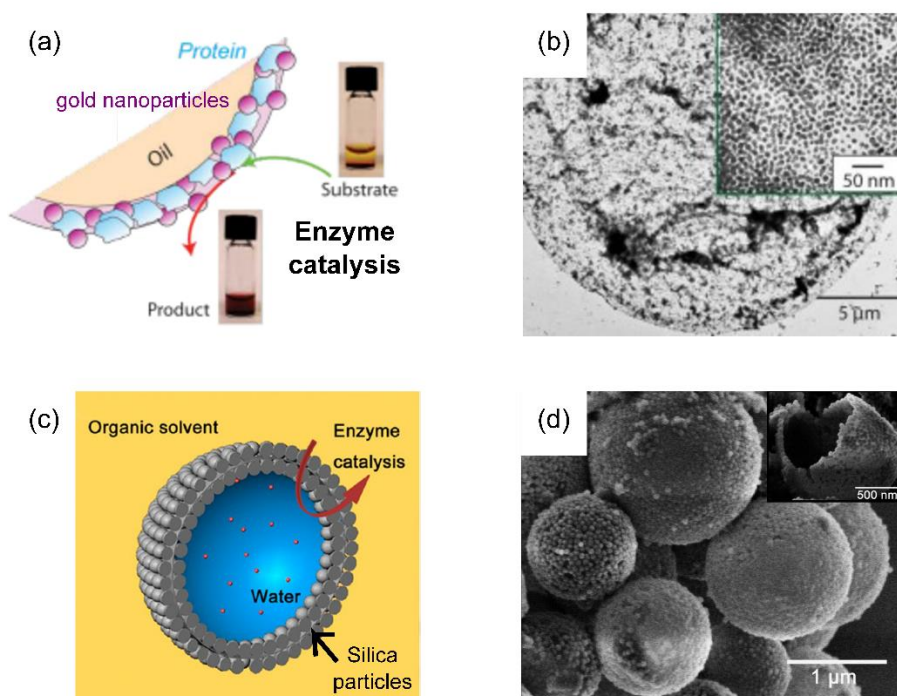


Figure 56: (a) Schematic representation of enzymatic microcapsules through electrostatic assembly of negatively charge enzymes with positively charge gold nanoparticles followed by the assembly of the resulting enzyme-nanoparticle conjugates at the oil/water interface of an emulsion¹²¹. (b) TEM image of the emulsions stabilized by the gold nanoparticle - enzyme complex (inset: zoom on the surface). (c) Laccase catalysis through a porous silica layer formed with silica particles in a silica shell. (d) SEM image of the silica colloidosomes used in (c) for the catalysis of laccase (inset: SEM image showing the capsular structure)¹²⁷.

In order to provide mechanical strength to colloidosomes, Noble *et al.*¹²⁸ have thought of solidifying their internal phase. They have fabricated « hairy colloidosomes » made of rodlike particles 1 μm width and of length between 10 and 70 μm . The internal phase of these

colloidosomes was gelled and the obtained capsules were easily transferred in water. A similar approach was undertaken by Cauvin *et al.*¹²⁹. They synthesized laponite armored polystyrene latex via Pickering emulsion polymerization. The styrene-in-water droplets were stabilized by the laponite particles and the internal phase of the droplets was subsequently polymerized. This technique leads to more resistant colloidal structures. However, the final microspheres are not hollow, and in some cases, this can be a drawback.

Microfluidic is a powerful tool to make droplets of controlled size. Lee and Weitz¹³⁰ used this technique to make water-in-oil-in-water double emulsions stabilized by silica nanoparticles dispersed in the oil phase. The oil phase evaporation leads to the formation of colloidosomes with particles bilayer¹³⁰ (Figure 57 (a) and (b)). In the case where multiple water droplets are dispersed in the oil phase, nonspherical colloidosomes with multiple independent compartments are obtained¹³¹ (Figure 57 (c) and (d)). These discoveries could allow the encapsulation of different components at the same time and to only mix them together upon breakage of the capsule. A direct application could be in the pharmaceuticals, where the capsule would contain several drugs that must not be mixed before reached the targeted organ.

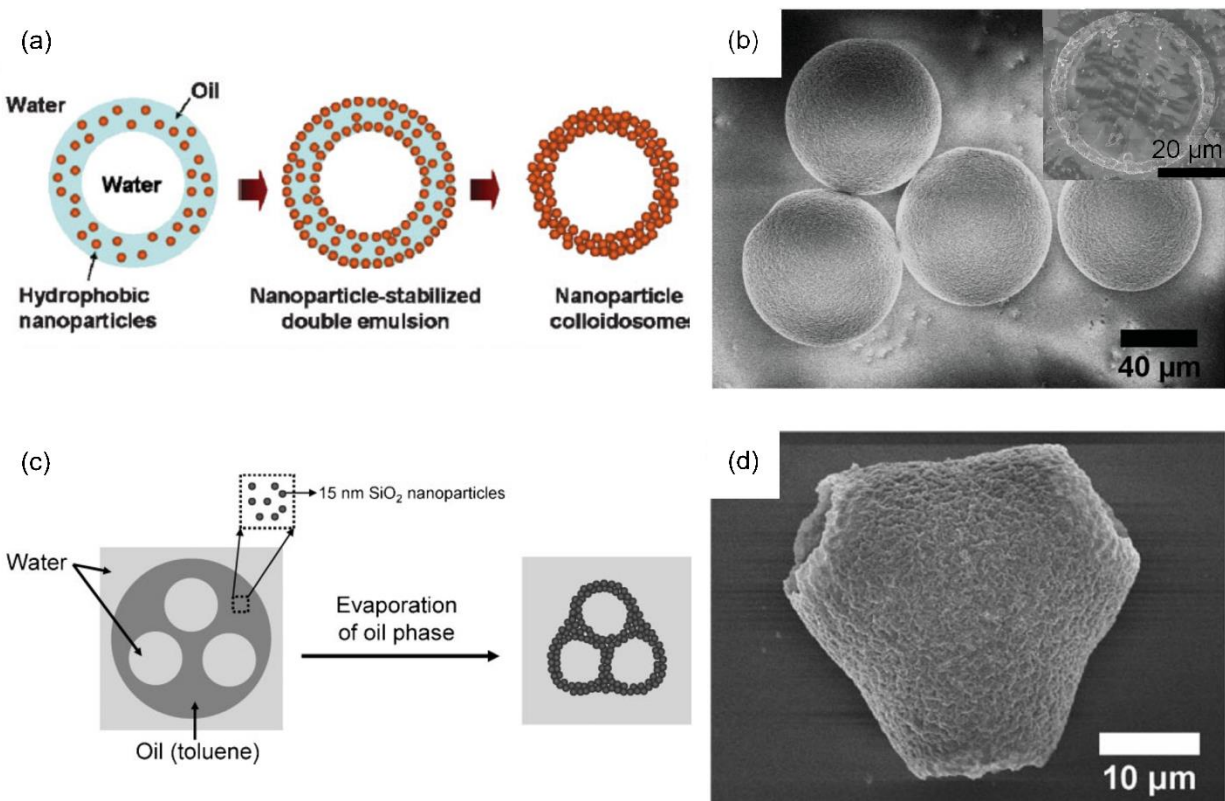


Figure 57: (a) Schematic for the formation of nanoparticle colloidosomes from nanoparticle-stabilized water-in-oil-in-water double emulsions¹³⁰, (b) colloidosomes obtained from (a). (c) Schematic illustration of the formation of multi-compartmentalized colloidosomes from double emulsion, (d) multi-compartmentalized nonspherical colloidosomes obtained following the method exposed in (c). In the two cases, silica nanoparticles are used.

Subramaniam *et al.*¹³² have produced Janus colloidosomes using a microfluidic chip allowing the control of the particle assembly on the droplets (Figure 58 (a)). The obtained colloidosomes have a jammed colloidal shell and are very monodisperse (Figure 58 (b)).

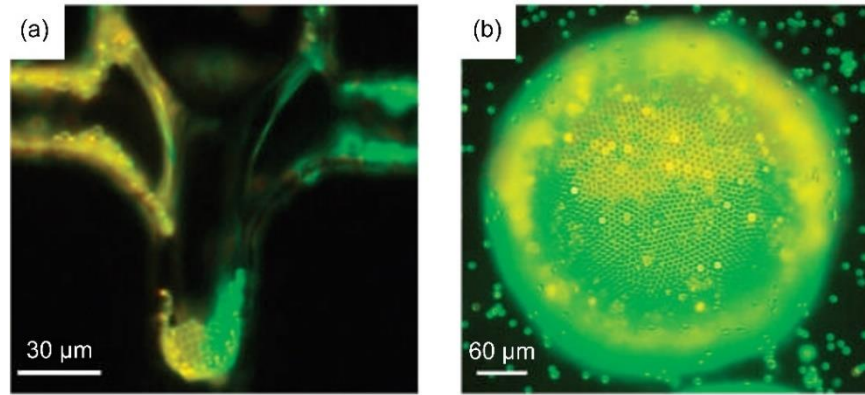


Figure 58: (a) Assembly of particles on an air/water interface to produce Janus crystals. The yellow particles are 4.9 μm diameter polystyrene particles dyed with rhodamine, and the green particles are 4.0 μm particles dyed with fluorescein. (b) An example of the Janus shell, with two hemispheres of different size particles and fluorescence¹³².

From the above-mentioned research materials, we can note that the intended primary end uses of the colloidosomes are the encapsulation and the controlled release of active ingredients. The release depends on the porosity of the capsules which is set by the particle size and packing. In many cases, particle jammed state does not confer enough armor intrinsic stability, thus external locking steps are required. The colloidosomes mechanical resistance may be improved by self-adhesion, particles cross-linking, macromolecules physico/chemsorption, internal phase gelation or polymerization. The final microcapsules properties depend on the size and type of particles and shell.

6. Conclusion

In this chapter, we have presented and explained the plasmonic properties of gold and silver nanospheres. We have seen that these properties depend on the size, shape, environment and spacing between the nanoparticles. Then, we have presented the different syntheses approaches to make gold and silver nanospheres. In Chapter 2 and 3, the nanospheres syntheses are inspired from these methods. Finally, we have detailed different techniques to self-assemble nanoparticles. Among them we have selected the microfluidic pervaporation and the assembly on emulsion droplets in order to design new functional optomaterials. In Chapter 2, we use the technique of microfluidic pervaporation to concentrate particles into bulky 3D materials. In Chapter 3, we assemble gold and silver nanoparticles on emulsions and we lock the nanoparticles by polymerizing the interface. We obtain microcapsules which interesting optical properties are tested in Chapter 4.

Chapter 2: Directed assembly of nanospheres using microfluidic pervaporation

TABLE OF CONTENTS

1. Introduction.....	60
2. Fabrication of a microevaporator.	60
2.1. Design of the mask	61
2.2. Manufacturing of the mold.....	62
2.3. Fabrication of the PDMS microchip.....	62
3. Calibration of a microevaporator.....	63
3.1. Method.....	63
3.2. Application of the methods to all the channels.....	64
4. Concentration of colloidal dispersions.....	66
4.1. Growth of dense states.....	66
4.2. Particles aggregation during microfluidic pervaporation	66
4.3. Latex particles.....	68
4.3.1. Commercial latex	69
4.3.2. Homemade polystyrene beads	76
4.4. Gold nanoparticles.....	78
4.4.1. Synthesis of gold nanospheres	78
4.4.2. Functionalization of gold nanospheres.....	80
4.4.3. Concentration of gold nanospheres by microfluidic pervaporation	81
5. Conclusion	86

1. Introduction

In the first chapter, we have presented several bottom-up techniques to assemble nanoparticles into close-packed assemblies. The microfluidic pervaporation stands out from the other assembly methods because it permits the concentration of dispersions of nanoparticles into dense states at a controlled pace, compounded with the ability for fine tuning of the composition of the array. In the first part of this chapter, we present the method of fabrication of the microevaporators. Then, we explain how, after calibration of our system, we can follow the growth of gold and polystyrene nanospheres dense states and extract the packing fraction of the particles within the obtained materials. We explain the discrepancies observed between the calculated packing fraction and the one estimated from electron microscopy images analyses. In this chapter, we show that many parameters such as the concentration of pollutants in the particles dispersion and the shrinkage of the channel's cross section during evaporation can impact the assembly of nanospheres. Using the technique of microfluidic pervaporation, we are able to form crystalline assemblies of nanoparticles with diameters ranging between 40 nm to 1 μm . Our results pave the way to the fabrication of photonic crystals or metamaterials by the technique of microfluidic pervaporation.

2. Fabrication of a microevaporator.

Our microevaporators are made of a PDMS microchip stuck onto a glass slide as shown in Figure 59. Each microchip consists in 8 units. Each unit is made of 8 microchannels of same height and width but with different lengths connected to one reservoir. This design allows us to carry multiple experiments on one single microchip.

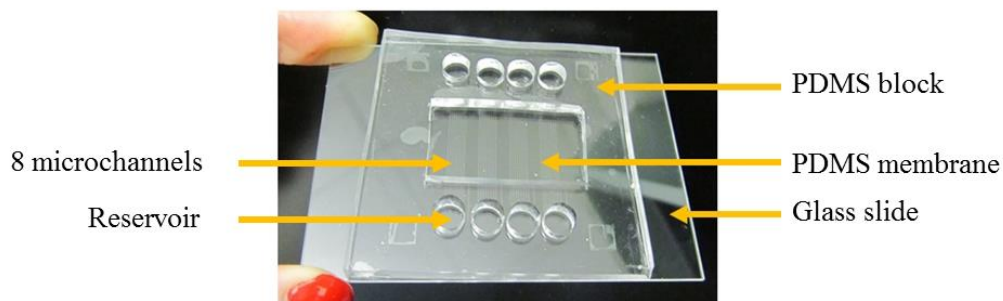


Figure 59: Image of our microevaporator. The reservoir holes are 4 mm in diameter.

Following the results established in Chapter 1, we designed our microevaporator in such a way that we can concentrate very dilute dispersions into dense arrays in a few hours only. To do so we choose carefully the dimensions of our microchannels. To speed up the pervaporation process, we used a small height, a thin membrane, long channels and a distance between neighboring channel large enough to avoid interactions between channels.

- e (membrane's thickness above channels) $\approx 14\text{-}19\ \mu\text{m}$
- h (channel's height) $\approx 10\ \mu\text{m}$
- w (channel's width) $\approx 100\ \mu\text{m}$
- L_0 (channel's length) $\approx 0,4\text{-}1,1\ \text{cm}$
- length between two channels, edge to edge $\approx 400\ \mu\text{m}$
- reservoir volume $\approx 50\ \mu\text{L}$

A schematic representation of one of the 8 microchannels is shown in Figure 60. One must note that the microchannel design is different than the one presented in Chapter 1. This new design permit an easier collection of the materials formed inside the microchannels.

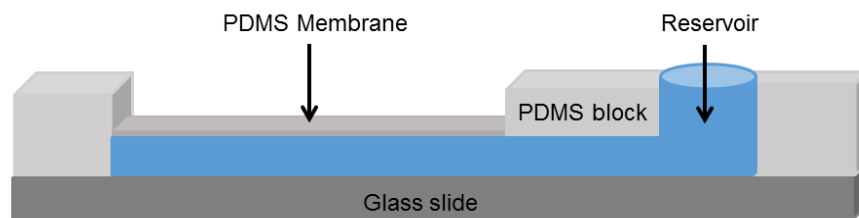


Figure 60: Side-view of one microchannel¹³³.

The protocol used to make microevaporators is called “soft-lithography” and was developed by Whitesides *et al.*¹³⁴. It consists of three main steps. The first one is the design of the mask. The second step is to make a mold with a fingerprint of the mask, using lithography. The third one is to mold the network of channels with PDMS.

2.1.Design of the mask

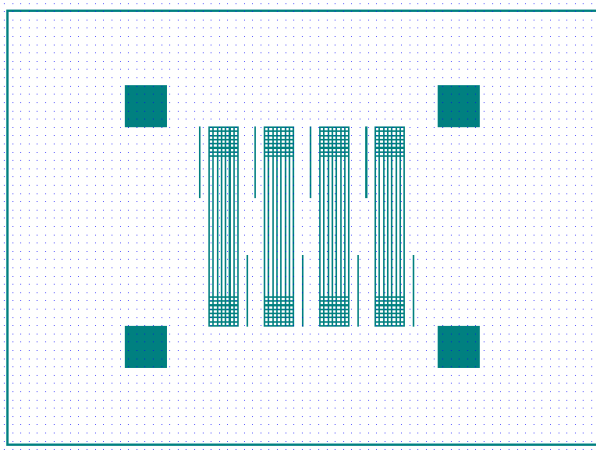
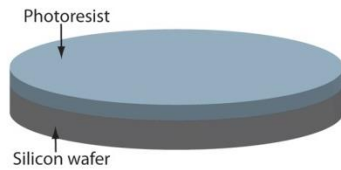


Figure 61: Mask design done with CleWin.

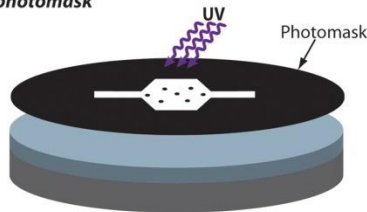
The pattern of the mask is drawn with the software CleWin as shown in Figure 61. Then, the design is printed with a high resolution on a transparent mask.

2.2. Manufacturing of the mold

1. Spin-coat photoresist on a silicon wafer



2. Expose photoresist to UV light through a photomask



3. Develop exposed wafer with photoresist

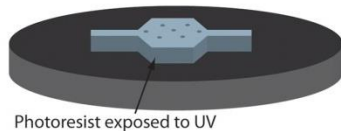


Figure 62: Fabrication of the mold.

The main steps to prepare the mold are summarized in Figure 62. To fabricate the mold, we use a UV curable resist (SU-8 MicroChem). The photoresist is spin-coated on a silicon wafer. The viscosity of the resist, the speed and the duration of the rotation control the thickness of the coating. The final height of the microchannel depends on the thickness of the photoresist. The resist is then heated to 95°C to evaporate the solvent, this is the “soft bake”. Then, the resist is exposed to UV radiation through the mask. The resist is then heated again at 95°C to evaporate the solvent, this step is called the “post exposure bake”. Finally, the resist is developed using (PGMEA: 1,2-propanediol monomethyl ether acetate). This last step is necessary to remove the excess of resist which did not reticulate. After the development, the mold is cleaned with isopropanol and functionalized with silanes to facilitate the subsequent release of the PDMS. The height of the channels is checked with a mechanical profilometer (Veeco Dektak 6M). This mold can be reused many times to make PDMS microchips.

2.3. Fabrication of the PDMS microchip

A mixture of PDMS (Dow Corning Sylgard 184) and its curing agent is prepared at a weight ratio 10/1. The mixture is degassed to remove the air bubbles. Some of it is poured inside a petri dish (to form a block) and the rest is spin-coated onto the mold to form the membrane (see Figure 59). The rotation speed and time define the membrane thickness. In our case, the desired membrane thickness is about 10 μm . Both PDMS parts (membrane and block) are cured at 65°C for 1hr. The middle part of the PDMS block is cut and removed in order to set the evaporation zone. The block is then stuck onto the membrane by plasma and they are placed in the oven at 65°C for one hour to firmly bind the two PDMS parts. Then, the block + membrane are carefully peeled of the mold and holes are punched to make the reservoirs. The block + membrane are then deposited on a clean glass slide and we obtain the microchip on glass (Figure 59).

3. Calibration of a microevaporator

3.1. Method

Before each experiment, the calibration of the microevaporator is performed to extract the evaporation rate V_e , the evaporation time T_e and the initial speed V_0 which corresponds to the velocity of the flow at the beginning of the channel (Figure 63).

The calibration method consists in filling the microchannels with water and removing the excess water in the reservoir. Due to the pervaporation of the water through the membrane, an air/water meniscus is formed in the channel and progresses towards the tip of the channel. Its displacement is recorded by optical microscopy (Figure 63). The microevaporator characteristics are obtained either following the meniscus in the block or in the membrane areas.

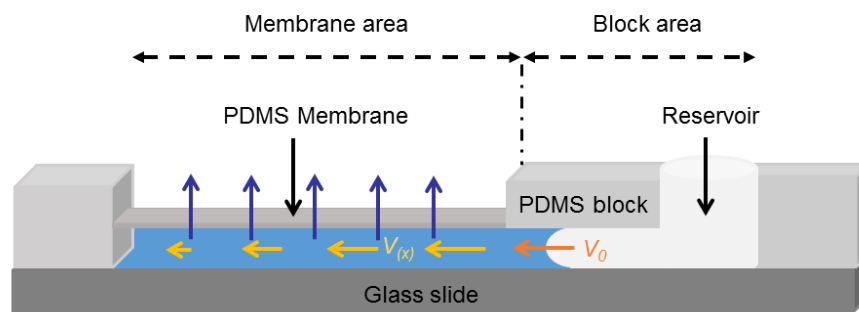


Figure 63: Calibration of a microevaporator. Due to the pervaporation of water, an air/water meniscus is formed in the channel. In the PDMS block part, the meniscus migrates at a constant rate V_0 . In the membrane area, the rate of the meniscus decreases until it reaches 0 at the very end of the channel.

Images sequences are monitored by a stereo microscope linked to a CCD camera (Hamamatsu). The time interval between two images is 1 second. The meniscus position is obtained by image analysis with Matlab. Briefly, two successive images are subtracted. The resulting image is black except at the position of the meniscus which corresponds to the maximum of the intensity in the channel. This maximum of intensity is plotted as a function of time. The Figure 64 shows the position of the meniscus in the channel as a function of the time. V_0 is the slope of the linear curve. For one channel of length equal to 1 cm, we obtain: $V_0 = 1.6 \cdot 10^{-5}$ m/s. From this value, we deduce the evaporation rate and time: $V_e = V_0 h / L_0 = 2 \cdot 10^{-8}$ m/s and $T_e = h / V_e \sim 490$ s. This characteristic time means that it takes 8 min to empty one channel.

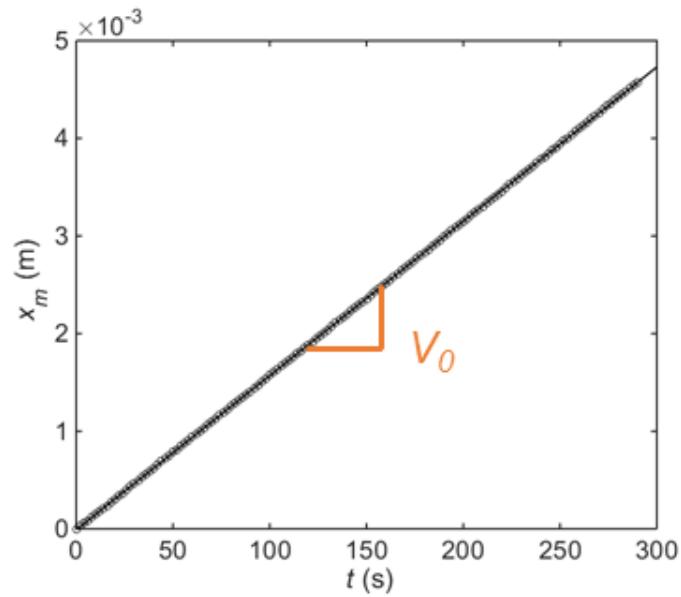


Figure 64: Position of the meniscus in the channel as a function of the time. The slope of the fit gives V_0 .

3.2. Application of the methods to all the channels

In this part, we calibrate the eight microchannels of different lengths but same height and width connected to one reservoir. We calculate the V_0 for each one of the 8 channels. Figure 65 show V_0 as a function of the channels' length. We observe that V_0 obeys a linear law as a function of L_0 .

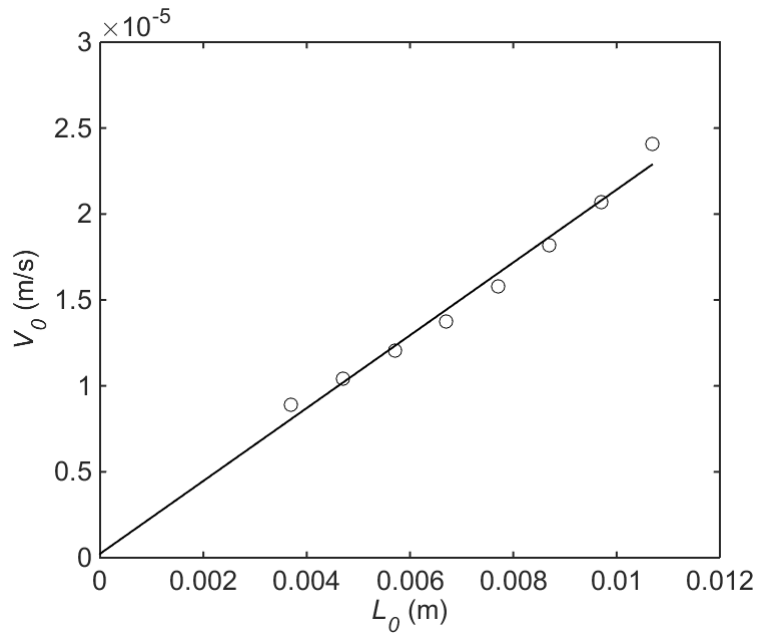


Figure 65: Entrance velocity in the 8 microchannels of different lengths. Calibration done three times (subscript numbers correspond to the calibration numbers).

From the entrance velocity V_0 in the eight channels of different lengths we can calculate the evaporation time for each channel. The Figure 66 shows the obtained T_e . In a perfect system, the evaporation times obtained for each one of the channels should be the same because T_e does not depend on the length of the channels. However, one can see that all the evaporation times we obtained are not exactly equal. The evaporation time of the first (shortest) and the last (longest) channels are smaller than the evaporation time of the intermediate channels. This occurs because these channels have neighbors only on one of their side (Figure 66). Therefore, in these channels, water pervaporates at a faster rate than in the channels that have neighbors on both sides, as previously explained in Chapter 1, Figure 37. The separation between two microchannels ($40h$) is not large enough to fully avoid the “communication” between the channels. We continued our experiments with such a geometry, keeping in mind that the first and last channels evaporate a little faster than the other.

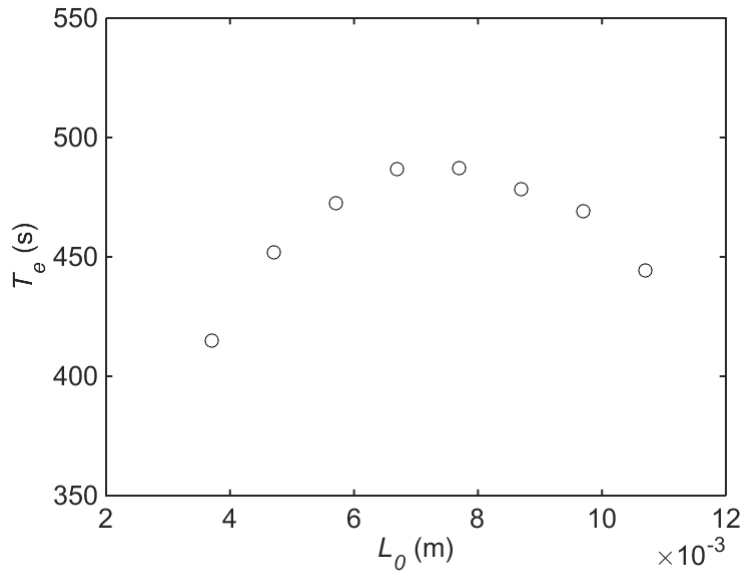


Figure 66: Evaporation time for each one of the 8 channels.

4. Concentration of colloidal dispersions

This part is dedicated to the study of the concentration of nanoparticles dispersions inside microchannels. Several dispersions of nanoparticles are tested. First, we explain how to follow the growth of dense state by video-microscopy and how to extract the particles' packing fraction of the resulting assembly. Then, we present the obtained results for three types of dispersions: 500 nm latex particles, 1 μm latex particles and 40 nm gold nanoparticles.

4.1. Growth of dense states

We use the microfluidic evaporators made of 8 microchannels of different lengths connected to a reservoir of about 50 μL . For such devices, evaporation times vary between 400 and 480 s (Figure 66). We fill the microchannels with dilute dispersions of nanoparticles (of volume fraction ϕ_0) at time t_0 . For each one of the experiments presented in the following, we measure accurately the length of each microchannel, the external room humidity and we perform the calibration of the microevaporators to extract precisely the parameters T_e and V_0 .

The growth of dense states in the 8 microchannels are simultaneously followed using a stereo microscope. Images are taken every minute in order to follow the kinetics of formation of the dense states. The image analysis is done with Matlab. It consists of determining the position of the dense front, x_d , as a function of time. First, a channel is manually selected. Then, the image at time $t + dt$ is subtracted from the image taken at time t . The front of the dense state appears brighter than the rest of the resulting image. The maximum of the intensity of the image corresponds to the position of the dense front, x_d . The analysis is reproduced for the other channels.

In the following sections, we study the rate at which the dense states growth in the 8 microchannels having different lengths. We also study the effect of the initial volume fraction of the dispersion (ϕ_0), and the effect of the concentration of salts on the growth. Two types of nanoparticles were concentrated in microevaporators: polystyrene and gold particles.

4.2. Particles aggregation during microfluidic pervaporation

During microfluidic pervaporation of particles dispersions, any type of solutes is concentrated in the microchannels. Therefore, during time, the concentration of salts, surfactants or polymers increases at the tip of the channel. Depending on their amount, these solutes can impact the growth of the dense states. During her Ph.D. candidacy, Julie Angly showed that charged stabilized gold nanoparticles are bad candidates for the formation of dense states via microfluidic pervaporation¹³⁵. According to her investigations, there is a critical salt concentration above which the nanoparticles aggregate in the microevaporators. Charge-stabilized nanoparticles

are easily destabilized by ionic species such as salts due to the screening of the nanoparticles surface charges by the salt ions. As previously seen in chapter 1, the addition of salts decreases the electrostatic repulsion and when the latter is too small compared to the Van Der Waals forces, the nanoparticles aggregate. Figure 67 summarizes the different scenarios that can be encountered while concentrating dispersions of charge-stabilized nanoparticles in presence of ionic species such as salts. In case (a), the dense state grows before the concentration of the ionic species reach the critical concentration. In that case, the particles can assemble without being destabilized by the ionic species. In case (b), the ionic species concentration increases faster than case (a). A dense state starts to grow when the concentration of the ionic species is below the critical concentration, but the growth stops when the critical concentration is reached. The ionic species concentration decreases the Debye length and the nanoparticles aggregate. In case (c), the ionic species concentrate much faster than the particles. The limit concentration is reached very quickly, no dense state is formed and the particles aggregate in the channel.

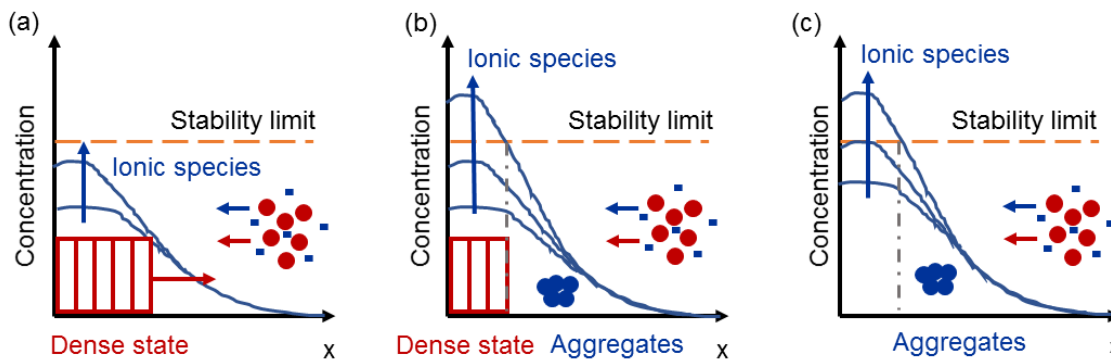


Figure 67: Schematic representation of the growth of a dense state and/or the aggregation of particles due to the concentration of ionic species in a microevaporator. (a) Formation and growth of a dense state, (b) formation of a dense state followed by aggregation of particles, (c) precipitation of the particles without formation of a dense state.

These three possible outcomes during concentration process depend on the ratio of the initial salt concentration (c_0) to the initial volume fraction of the particles (ϕ_0). The stability chart in Figure 68 delineates these three cases⁷⁶. Cases (a), (b) and (c) correspond to the three regimes called growth, kinetic, and precipitation respectively. We notice that charge-stabilized nanoparticles aggregate at very low volume fraction in particles. Indeed, for very dilute dispersions of particles ($\phi_0 \approx 10^{-5}$), a low concentration in salts is sufficient to destabilize the particles ($c_0 \approx 10^{-3}$ mM). Increasing ϕ_0 by a factor 10 or 100, by centrifugation for instance, is a good way to escape the instability zone.

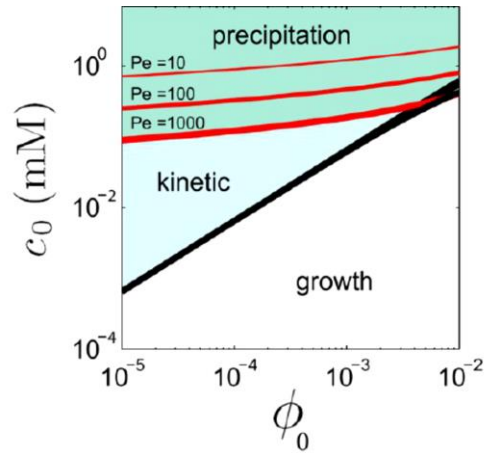


Figure 68: Stability chart giving the outcome of the concentration of salts with charge-stabilized particles. P_e stands for the Péclet number of the salt ($P_e = L_0 V_0 / D$, when $P_e > 1$, the salt concentrate in the accumulation box p , the one of the nanoparticles being considered infinite⁷⁶).

As a conclusion, before concentrating dispersion of electrostatically stabilized nanoparticles, we have to make sure that the concentration of salts or any other charge-destabilizing species in the sample is sufficiently low compared to the volume fraction of the particles in the reservoir. Indeed, in the following section, we will see that if it is not the case the particles aggregate.

4.3. Latex particles

In this section, polystyrene particles are assemble to form artificial colloidal crystals¹³⁶. Colloidal crystals have been widely studied in the last decades for their potential applications in photonics. Indeed, as a consequence of the different refractive index contrast within the crystal ($n_{air} = 1$ and $n_{polystyrene} = 1.6$), light is scattered and/or diffracted from the different crystalline faces and can produce a band of forbidden frequencies for which no light can propagate in the medium¹³⁷. Such range of forbidden frequencies is usually called “photonic bandgap”. The greater the refractive index contrast, the wider the photonic band gap. Light can then be directed through a specific path within the photonic crystal by introducing defects in the crystal. The light will propagate following these defects because it cannot propagate anywhere else within the crystal. This can be beneficial for the manipulation of light around bends for instance.

Colloidal self-assembly of polymer or silica spheres is one of the most favored and low-cost methods for the formation of photonic crystals as artificial opals. The methods currently used for colloidal self-assembly are the vertical deposition, the Langmuir-Blodgett, the dip coating, and the spin coating techniques (all described in Chapter 1, part 4). In this section, we show the potential of the microfluidic pervaporation for the growth of large tri-dimensional colloidal crystals. Two sizes of latex particles were assembled into crystalline arrays by microfluidic pervaporation: 0.5 μm commercial latex and 1 μm latex synthesized in the laboratory.

4.3.1. Commercial latex

Carboxylate-modified latex microspheres of mean diameter $0.49 \pm 0.015 \mu\text{m}$ at 2% and 1% volume fraction were concentrated in microevaporators. The initial charge-stabilized latex dispersion at 2% contains 2 mM azide salt. For this experiment, the membrane thickness was 18 μm , all the others parameters set in the part 3 of this chapter were unchanged. For such devices, evaporation times are of the order of 500 s (Figure 66). We studied the growth profile of compact material made of these latex beads. As pervaporation occurs, we observe that, depending on the salts concentration, complex phenomena arise.

We analyze the kinetics of the growth of the dense phase in 8 channels of different lengths (Figure 69). Two volume fractions of latex beads are studied, each one of them before and after dialysis of the dispersions of latex particles. We dialyzed the latex dispersions to decrease the salt concentration in the sample. The dialysis process is explained below.

Results show that the “nucleation” of dense states and their subsequent growths occur faster with a higher initial volume fraction in particles. The “nucleation” times are represented by black circles for the four dispersions. The “nucleation” times for the different dispersions appear in the following order: 1% dialyzed, 2% dialyzed, 1% non-dialyzed, 2% non-dialyzed. The growth profiles are linear in all cases except for the dispersion of 2% latex non-dialyzed. We will give an explanation for this observation later in this section. The growth kinetics of the dense states depends on the length of the microchannels. The longer channels evaporate faster. Thus, dense states grow faster in the longer channels.

Dialysis process: 1 mL of latex solution at 2% is incorporated in a dialysis tubing (Spectra/Por, Molecular weight cut-off: 25 kD) previously rinsed twice with deionized water. The dialysis tubing was then immersed in 1L deionized water and the dialysis is performed under stirring for 2 days. After that period of time, we assume that the salt concentration has reached equilibrium. The azide salt concentration in the dialyzed 2% latex solution is about 2 μM . The same method is applied to dialyze the 1% latex dispersion. After dialysis, the salt concentration in the 1% latex dispersion is about 1 μM .

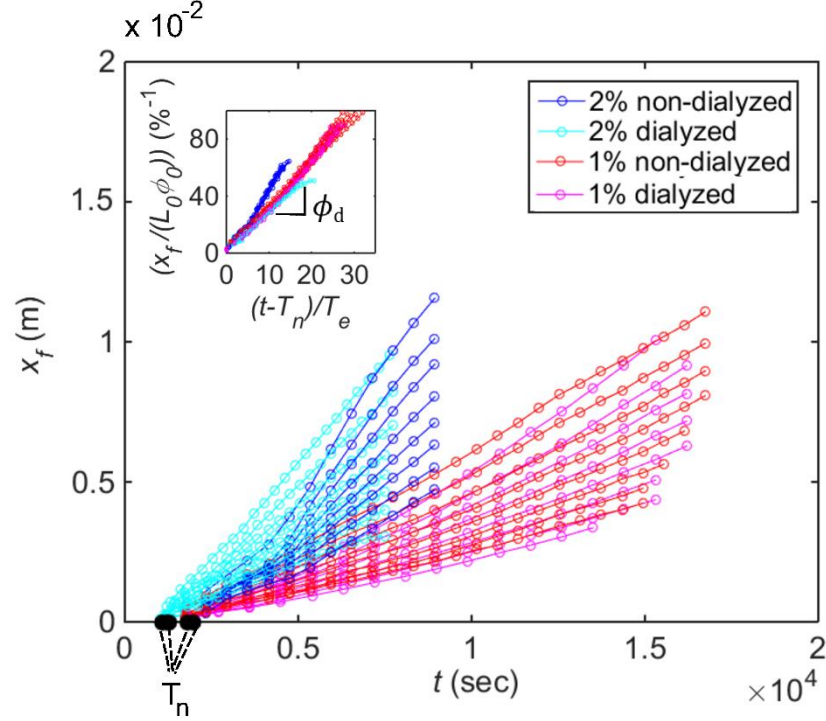


Figure 69: (a) Temporal analysis of the growth kinetics of latex dense states in 8 channels of different lengths. Inset: Normalization of the fronts with the respective lengths L_0 of the channels and the volume fraction ϕ_0 , as well as the time from “nucleation” with the evaporation time T_e .

The growth trajectories collapse when the fronts, x_f , are scaled by the channels’ length L_0 and by the volume fraction of the particles ϕ_0 , as well as the time by the evaporation time T_e (inset of Figure 69). The dispersion at 2% non-dialyzed does not collapse well onto the other growth curves due to an acceleration of the growth after 79 min of evaporation.

In Chapter 1 (Equation 14), we have shown that a simple mass conservation balancing the volume growth rate of the dense state with the flux of incoming particles gives access to the packing fraction, ϕ_d , of the nanoparticles in the dense state.

$$\frac{x_f}{L_0} = \frac{\phi_0}{\phi_d} \left(\frac{t - T_n}{T_e} \right)$$

Equation 14: Extraction of the dense state packing fraction.

The final volume fraction of the particles, ϕ_d , in the dense states is given by the slope of the trajectories in Figure 69, inset. For the linear growths, we obtain $\phi_d \approx 32\%$. This value is low compared to the theoretical maximal packing fractions 64% and 74% obtained for hard monodisperse spheres organized in a random close packing or in a face-centered cubic crystal.

To understand why all the trajectories do not perfectly rescale in Figure 69, and why the packing fraction estimated from these curves is pretty low, we closely looked at the “nucleation” and growth of the dense states for the 4 types of dispersions. For each type of dispersion, we focus on the tip of one of the eight channels (the second channel of length ~ 1 cm, see Figure 70) and discuss the different phenomena occurring as beads concentrate. Since the phenomena observed are similar for every all the dispersions, we show it in detail for the 1% dialyzed dispersion of latex (see Figure 70) and then we compare all the dispersions in Table 1.

Based on the stability chart in Figure 68, we can forecast if the nanoparticles will aggregate or not during their concentration in microfluidic microchannel. At the salt and latex concentrations studied; the stability chart predicts an aggregation of the 2% non-dialyzed latex beads ($[\text{salt}] = 2$ mM) and of the 1% non-dialyzed latex beads ($[\text{salt}] = 1$ mM). Our experimental results corroborate with these predictions. Indeed, these two dispersions precipitate during the concentration of particles as shown in Table 1. The aggregation is more intense for the highest concentration in salt (2% non-dialyzed latex beads, $[\text{salt}] = 2$ mM). The particles are continuously aggregating until the dense front reaches about one fourth of the channel length (at $t \approx 79$ min). At that time, there is no more obvious precipitation of the particles before their incorporation into the dense state. This time corresponds to the change of slope noticed during temporal analysis of the growth kinetics.

According to the same stability chart, the 2% dialyzed latex beads ($[\text{salt}] = 2$ M) and the 1% dialyzed latex beads ($[\text{salt}] = 1$ M) should not aggregate during their concentration in microfluidic microchannel. However, experimentally we observe that the particles aggregate (Table 1 and Figure 70 (b)).

In all cases, once the dense front has grown a little bit in the channel, a white front appears at the tip of the channel and migrates toward the reservoir (Figure 70 (b)). We will call this white front the “drying front”. It is closely followed by the invasion of air in the channel. The microchannel slightly shrinks during that stage which probably further compacts the particles in the dense state. For the 1% dialyzed latex beads ($[\text{salt}] = 1$ M), a strong delamination of the material from the microchip is observed while air enters the channel and the material cracks to release the stress due to the compaction of the microspheres during drying (Figure 70 (b)).

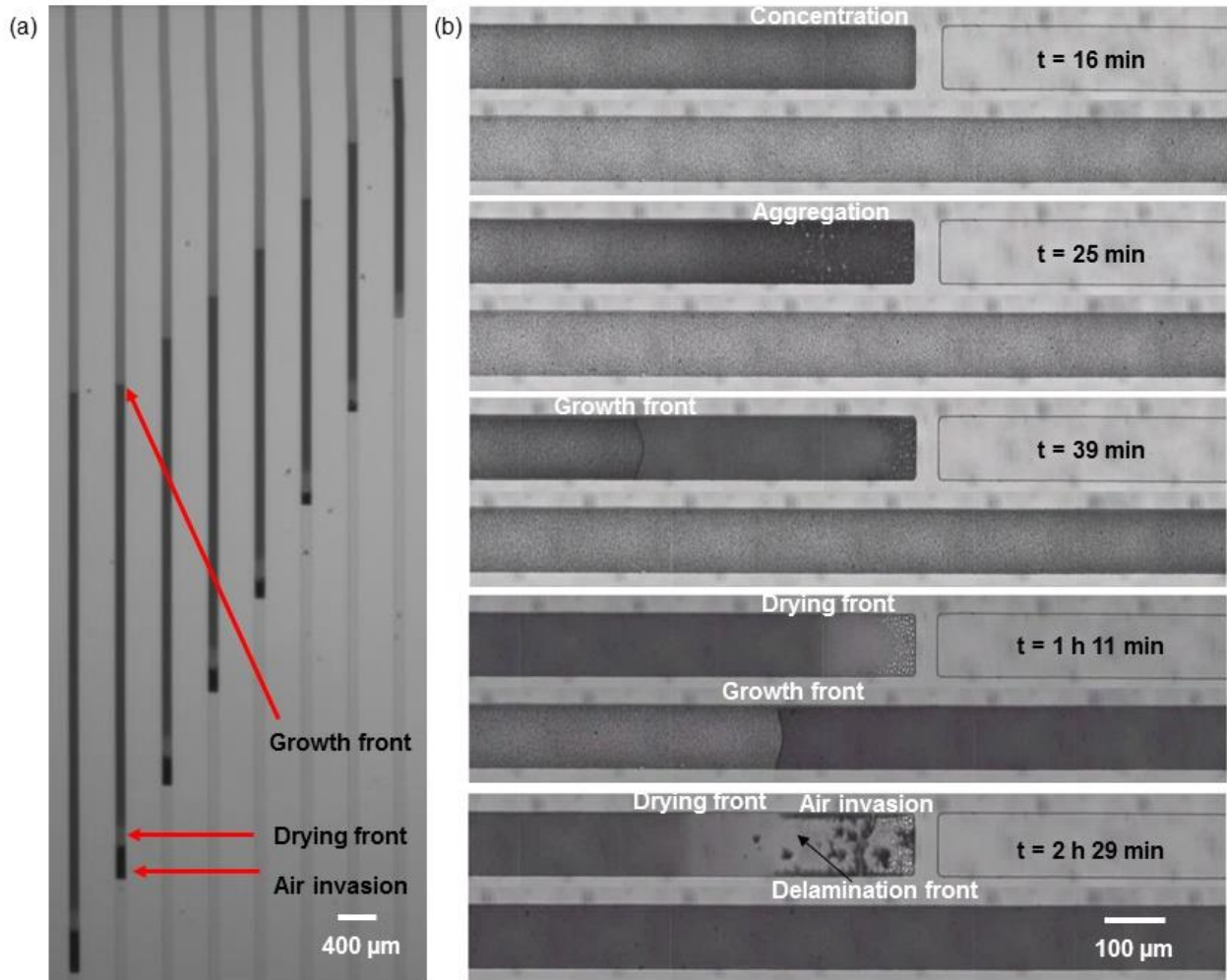


Figure 70: Dense state “nucleation”, growth and drying for 1% latex dialyzed. (a) Far view of the 8 microchannels during concentration. (b) Optical images of the tip of the second longest microchannel taken at different times during concentration. The particles concentrate homogeneously in the microchannel ((b) top image). A small aggregation of the particles is observed before “nucleation” of the dense front ((b) second image). Once the particles reach their maximum packing fraction, a dense state “nucleates” and grows ((b) third image). Once the dense state has reached a critical length (in this case, 50% of L_0), a white front appears at the tip of the channel (“drying front”, (b) fourth image). This step is closely followed by air invading the channel ((b) bottom image).

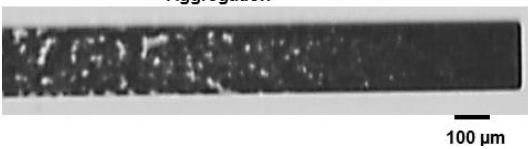


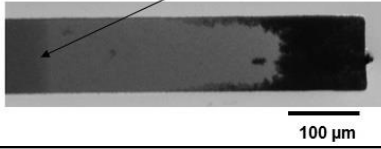

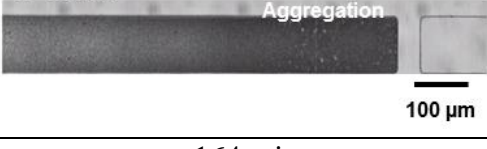
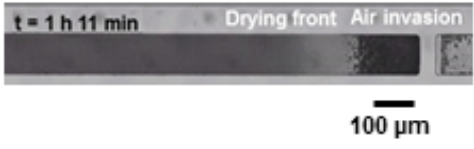

0.5 μm latex particles	2% non-dialyzed, 2 mM salt	2% dialyzed, 2 μM salt
Time at which the particles start to aggregate (tip of the channel)	9 min 	19 min 
Time at which the air invasion starts	49 min 	90 min 
0.5 μm latex particles	1% non-dialyzed, 1 mM salt	1% dialyzed, 1 μM salt
Time at which the particles start to aggregate (tip of the channel)	30 min 	~ 26 min 
Time at which the air invasion starts	149 min 	164 min 

Table 1: Comparison of the growth of dense states for the 4 dispersions of latex.

To further investigate the concentration of the latex particles in microevaporators, we performed optical profilometry measurements while concentrating 1% dialyzed latex beads in microchannels. The aim of this experiment was to find out if the channels height has shrunk during the microfluidic pervaporation experiment. Since the height of the microchannel is set by the position of the membrane, we will follow the deformation of membrane's top layer during microfluidic pervaporation (see Figure 71). The results were split in two graphs, the first one in Figure 72 (a) presents the membrane's deformation during concentration of the bead dispersions before air invades the channel. The second graph in Figure 72 (b) shows the membrane's deformation while concentrating latex during air invasion. We are calling x_l the position along the microchannel at which the optical profilometry measurements are recorded. x_l is constant during the concentration of the latex dispersions. x_d and x_a are respectively the positions of the dense front and the air front in the microchannel.

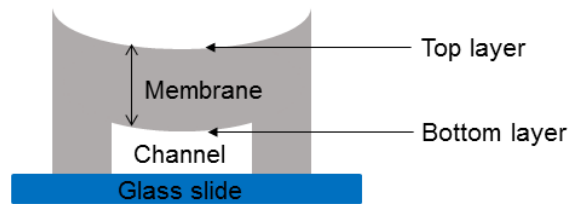


Figure 71: Schematic representation of the cross section of one microchannel with the membrane slightly caving inside the channel.

The Figure 72 (a) gives the profile of the membrane before injection of the latex dispersion (blank curve). Initially the membrane is slightly caving in towards the microchannel ($y = -0.6 \mu\text{m}$ compared to the zero axis). Right after injection of the solution, the profile remains the same ($x_d = 0 \text{ mm}$; $t = 0 \text{ min}$) meaning that our manual method of injection does not deform the membrane. During the growth of the dense front, the membrane is not further deformed ($x_d > x_l$; $t = 1 \text{ h}$). However, when the dense front has reached 50% of the channel's length, the channel starts to dry and the membrane is more deflected ($x_d > x_l > x_a$; $y = -1.6 \mu\text{m}$, $t = 2 \text{ h}$ and $t = 2 \text{ h } 35 \text{ min}$). This caving in of the membrane upon drying of the channels corroborates with a compaction of the dense states. When air invades the channel (see Figure 72 (b)), the material delaminates from the membrane. The membrane deflected at the beginning of the air invasion ($x_d > x_l > x_a$; $y = -1.6 \mu\text{m}$, $t = 5 \text{ h } 30 \text{ min}$) relaxes to its initial position ($x_d > x_a > x_l$; $y = -0.6 \mu\text{m}$, $t = 6 \text{ h } 15 \text{ min}$) when the air front has passed x_l .

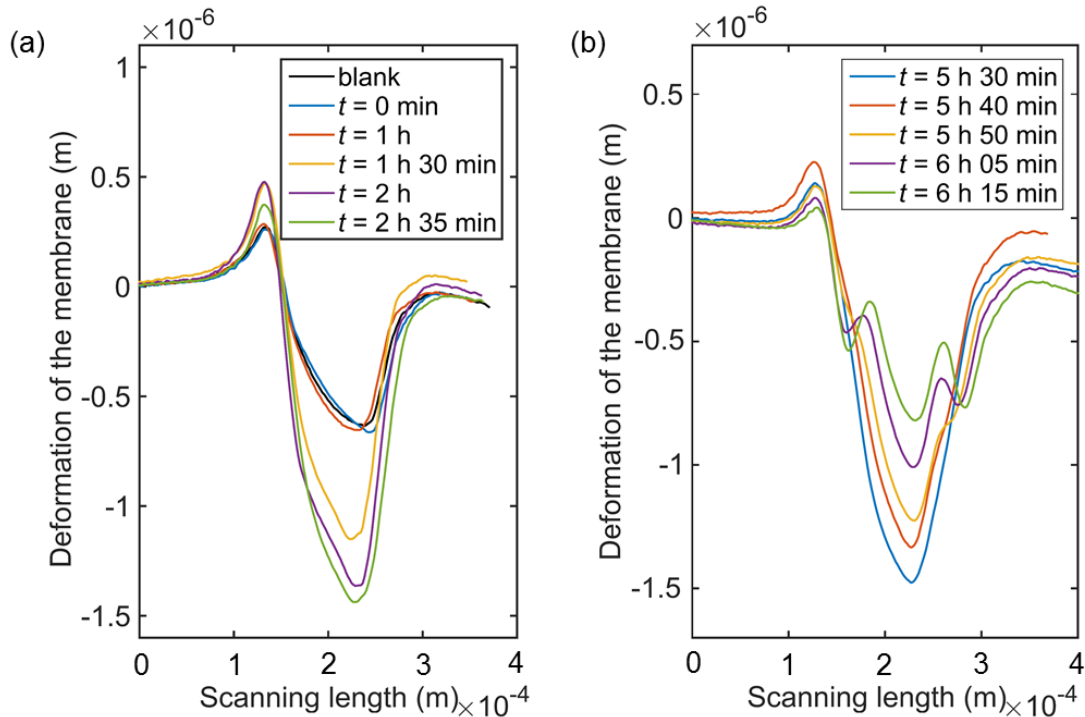


Figure 72: Sequence of optical profilometry measurements of the membrane's deformation while concentrating 1% dialyzed latex beads (a) before air invading the channel and (b) during air invasion.

From these profilometry measurements, assuming that the bottom layer of the membrane follows the deformation of the top layer, we can conclude that the height of the microchannels do not shrink during microfluidic pervaporation of 1% dialyzed dispersions of latex beads. The most significant deformations (caving in of the membrane by $1.6 \mu\text{m}$) occurring after the growth of the material in the microchannel, they do not impact the growth kinetics of the latex beads.

We monitored under SEM the final materials obtained concentrating 2% and 1% dialyzed dispersions of latex beads. In both cases, latex particles mixed with impurities are visible at the tip of the channels. These pollutants were most likely contained in the initial dispersion of nanospheres and concentrated at the tip of the channel during microfluidic pervaporation. Further from the tip, the latex beads on the top layer of the material are well-organized into hexagonal packing as seen in Figure 73 (b). It is difficult to conclude on the organization of the particles inside the material. The Figure 73 (c) and (d) show successful close-packing of about 20 layers of latex beads. The Figure 73 (d) specially highlights the three-dimensional character of the bulk assemblies obtained using the microfluidic pervaporation technique; the very flat surfaces and the sharp edges of the micromaterial directly resulting from the microevaporator's geometry. Measurement of the material cross-section gives a $100 \mu\text{m}$ wide and $8 \mu\text{m}$ thick material. The measurement of the material thickness is in close agreement with the height of the channel obtained with optical profilometry. Taking into account the small shrinkage of the channel height during

the concentration of the latex beads in the microchannels we obtain a packing fraction of the beads in the dense material, $\phi_d = 40\%$ using mass conservation arguments. We do not have any clear explanation of this discrepancy with the clearly higher packing fraction observed in SEM images. Maybe the dispersion solid content provided by the supplier was not accurately estimated. This could entail an error on the initial volume fraction of the latex beads and therefore on the estimation of the packing fraction in the dense state.

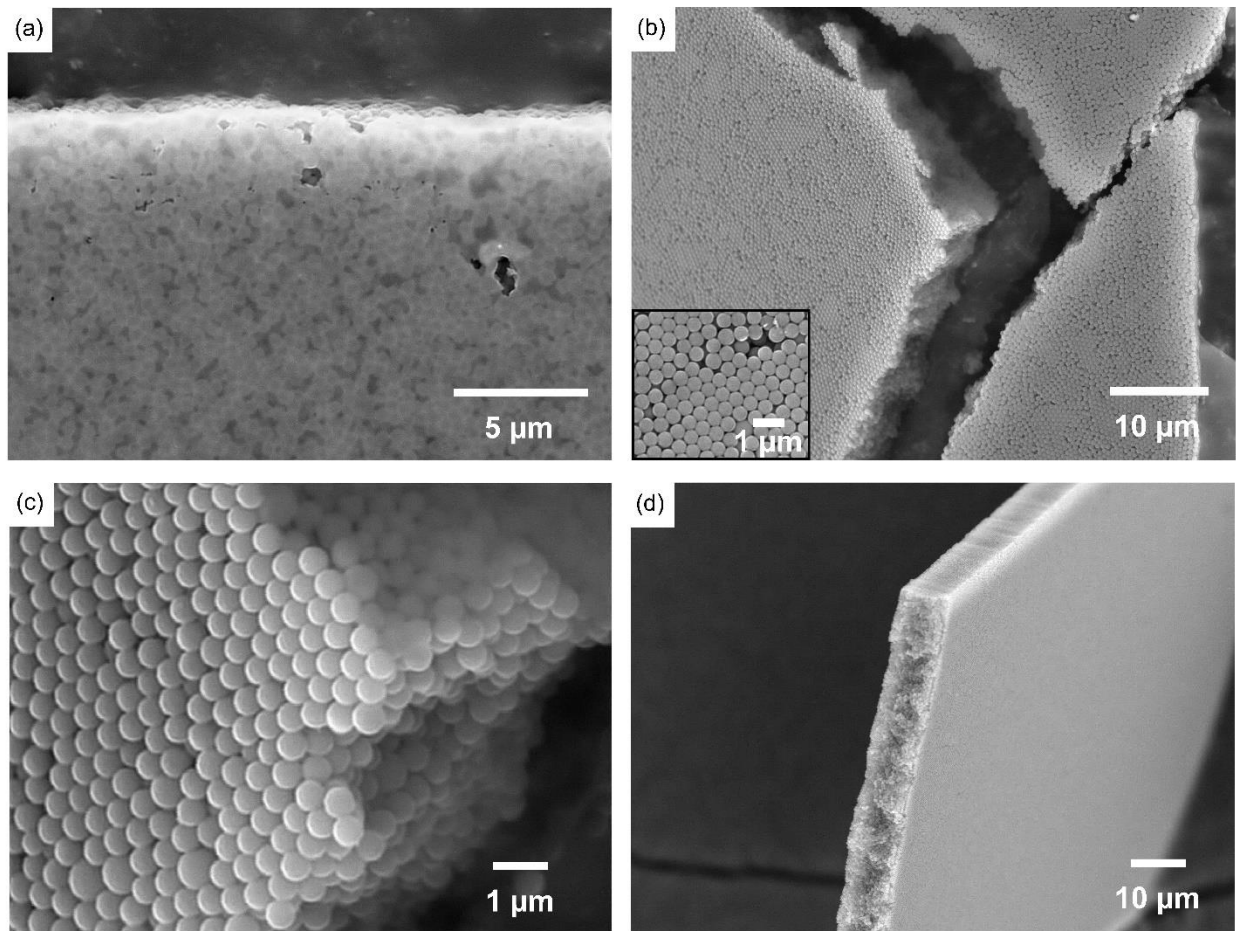


Figure 73: SEM images of microevaporated 1 % dialyzed latex beads (a-c) and 2 wt% (d). (a) Image taken at the tip of the channel, (b-d) images taken far from the tip. Inset of (b) shows typical lattice of the latex beads.

4.3.2. Homemade polystyrene beads

In a collaborative project with Wei-Han, student in the laboratory of Daeyon Lee at the University of Pennsylvania, we concentrated linear polystyrene particle (LPS, $d = 1\ \mu\text{m}$) by the technique of microfluidic pervaporation. The aim of the collaboration was to test the LPS for making 3D.

The LPS are made by dispersion polymerization. The polymerization is initiated by ammonium persulfate upon heating the solution. The obtained beads have a negative charge coming from the persulfate groups. The particles were washed 10 times and sonicated for 10 minutes before concentration in the microevaporators. The washing steps are necessary in order to remove any pollutants coming from the synthesis process and the sonication is performed to brake any small particles aggregates potentially formed during washing. The volume fraction of the particles as pervaporated was 0.5%.

The growth was not followed by optical imaging for this type of particles. SEM imaging show two different regions within the microchannels. At the tip of the channel, the polystyrene particles are loosely assembled and no order is shown as seen in Figure 74a. Far from the tip, the polystyrene beads are very well organized into crystals planes showing hexagonal order as seen in Figure 74 (b-d). The Figure 74 (d) shows successful close-packing of 10 layers of LPS. The organization is crystalline over 1 cm length. This observed phenomenon can be explained by an increase of the salt concentration destabilizing the particles at the tip of the channels.

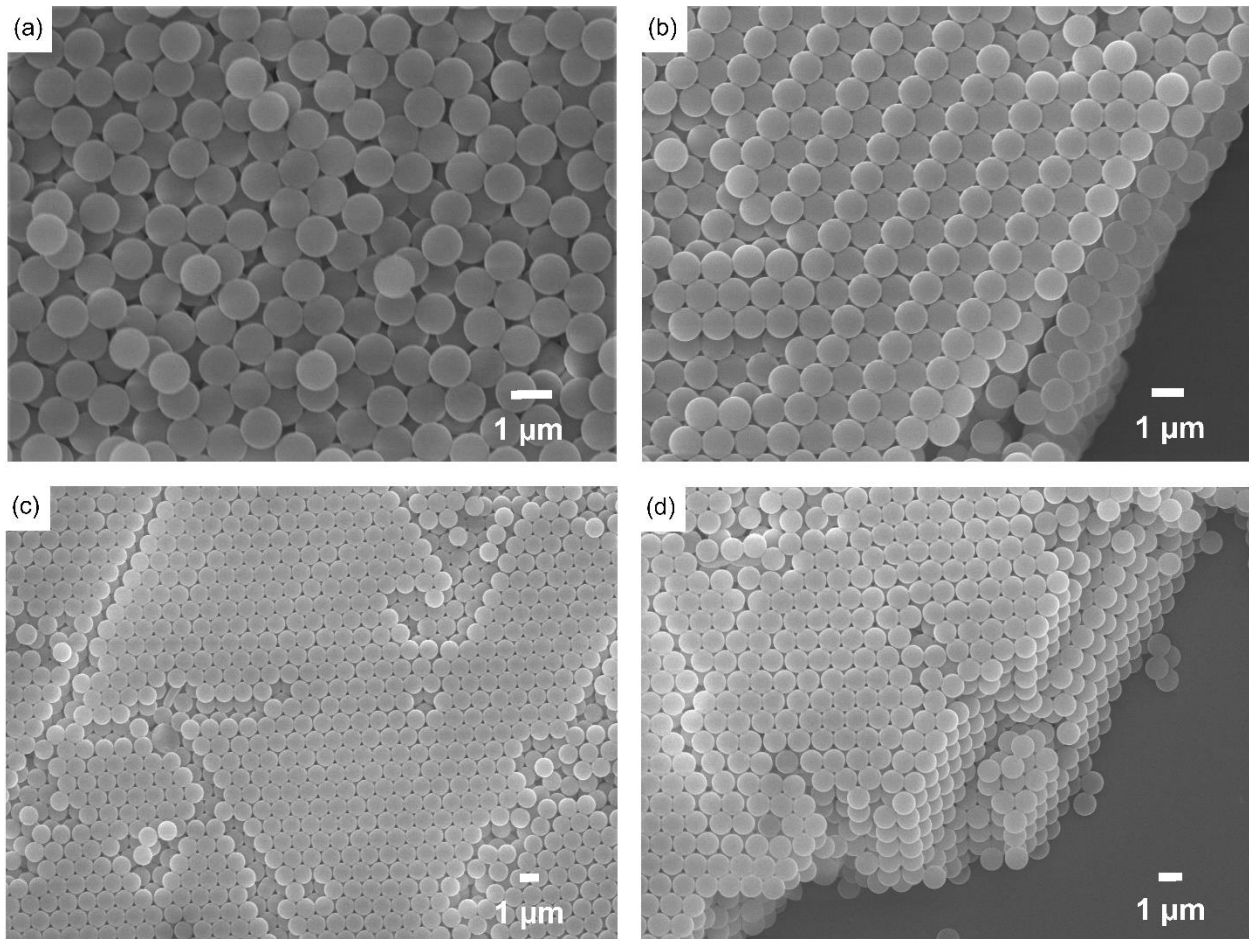


Figure 74: SEM images of microevaporated polystyrene beads at 0.5 wt%. (a) Image taken at the tip of the channel, no order appears. (b-d) Images taken far from the tip, the assembly is crystalline.

In this section, we have proven that the technique of microfluidic pervaporation is very efficient to tailor large silica beads crystals. However, the concentration of these particles into well-organized close-packed lattice depends on the salts concentration within the particle dispersion.

4.4. Gold nanoparticles

The aim of this section is to show the potential of our microfluidic tool to design new homogenous metamaterials with a high degree of bulkiness. As explained in Chapter 1, gold nanoparticles strongly absorb and scatter light in the visible spectrum. The tunable optical properties of gold nanoparticles make them very good candidates for the design of locally resonant materials or plasmonic enhanced materials. In this part of the manuscript we present a method of synthesis of spherical nanoparticles and their directed-assembly through microfluidic pervaporation.

4.4.1. Synthesis of gold nanospheres

As we showed in Chapter 1, there are many possible routes to synthesize nanoparticles. We have selected one of the most common one to synthesize 40 nm gold nanoparticles. The synthesis is inspired from the method of Liz-Marzán and colleagues. Briefly, gold nanoseeds are synthesized following the Turkevich process²⁸. Then, these seeds are diluted and subsequently grown via a growth step. Finally, the spherical nanoparticles can be separated from the other non-spherical particles by a purification step.

Let's detail each one of the three steps:

i. Seeds synthesis

Small particles of diameter 13nm are prepared by reducing gold salt with sodium citrate.

500 mL of a gold salt solution $\text{HAuCl}_4 \cdot 3\text{H}_2\text{O}$ at 0.5 mM in MilliQ water is prepared. Protected from light, this solution is brought to boil and then 25 mL of a 0.1 M sodium citrate solution is quickly added under strong stirring. Protected from light, the solution is stirred for 30 min and left to cool down to room temperature. After the synthesis, the solution is allowed to sit in the fridge for 2 or 3 days before the growth step.

The obtained seeds are very monodisperse as evidenced by the TEM image and the histogram shown in Figure 75. The mean diameter of the seeds is $d = 12.8 \pm 1.5$ nm. The optical response of the seeds is presented in Figure 77. A sharp plasmon peak is observed at 517 nm.

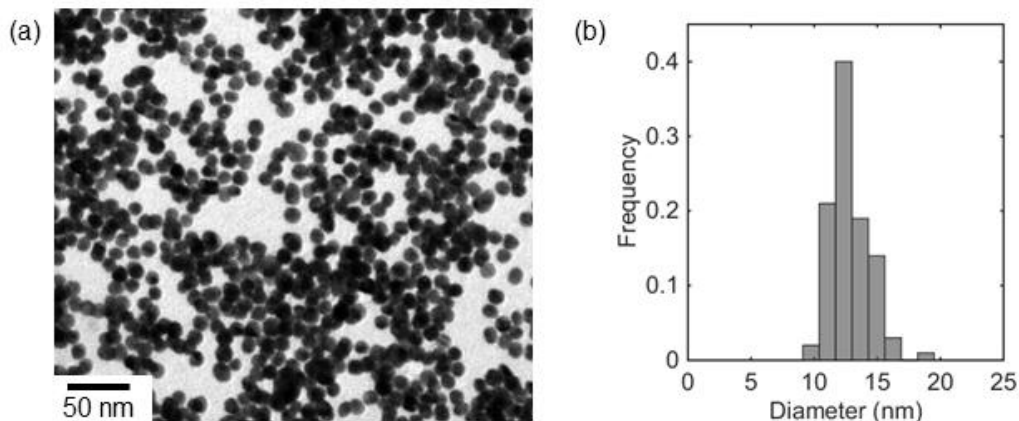


Figure 75: (a) TEM image of the gold seeds and (b) histogram of their size distribution.

ii. Seeds growth¹¹

The seeds are grown up to 40 nm by reducing more gold salt in a mixture of ascorbic acid and CTAB (cetyltrimethylammonium bromide). Ascorbic acid is the reducing agent and CTAB serves as capping agent to stabilize the gold nanoparticles and avoid their aggregation.

In a 750 mL round bottom flask, 500 mL of a 6.9 mM CTAB solution (MilliQ water) and a volume of gold salt, V_{HAuCl_4} , at 1.18 M are mixed. The mixture must be heated up to 35°C in order to be above the crystallization temperature of the CTAB. 20 mL of a 0.25 M solution of ascorbic acid is added under strong stirring: after a few seconds, the orange solution becomes colorless. Then, $V_{Au_{seed}}$ previously calculated using the following equation is added under strong stirring. In 30 seconds, the solution becomes red. The reaction is carried on at 35°C for 1 hour.

$$V_{HAuCl_4} = \frac{[HAuCl_4]_r}{[HAuCl_4]_i} \cdot V_t$$

$$[Au_{seed}] = \frac{(r_{seed})^3 \cdot [HAuCl_4]_r}{(r_{particle})^3 - (r_{seed})^3}$$

$$V_{Au_{seed}} = \frac{[Au_{seed}]}{[Au_{seed}]_i} \cdot V_t$$

Where r_{seed} is the radius of the seeds

$r_{particle}$ is the radius of the particles after growth (parameter set according the desired size)

$[HAuCl_4]_i$ is the concentration of the initial mother solution of gold salt

$[HAuCl_4]_r$ is the gold salt concentration in the mixture (set value, 5 mM in our case)

$[Au_{seed}]$ is the gold zero concentration of the seeds to add to the mixture

V_t is the volume of the mixture

$[Au_{seed}]_i$ is the gold zero concentration in the seeds' solution

The final gold nanospheres have a mean diameter $d = 38.2 \pm 6.1$ nm. TEM image and histogram of the size distribution can be found in Figure 76. The gold nanospheres are particularly monodisperse. This shows the efficiency of the synthesis process. The optical response of the gold nanospheres after growth shows a sharp plasmon peak at 532 nm.

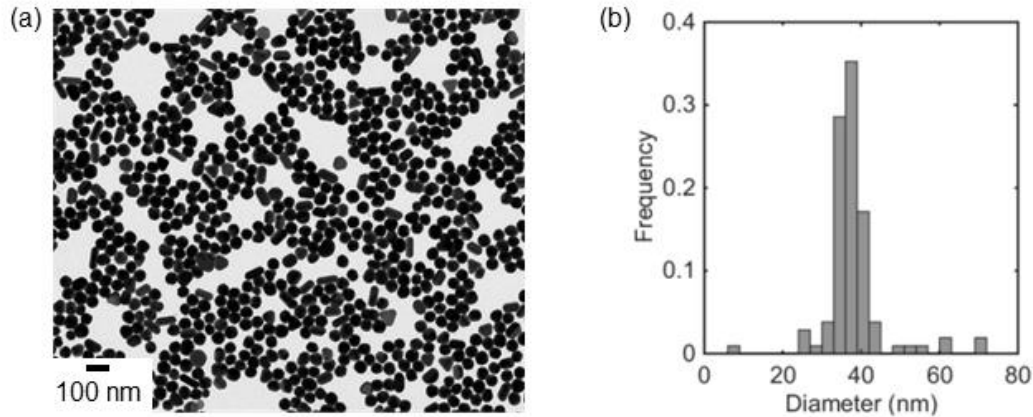


Figure 76: (a) TEM image of the gold nanospheres after growth and (b) histogram of their size distribution.

iii. Purification of the spherical nanoparticles

If needed, the gold nanospheres can be isolated from the other non-spherical nanoparticles such as the nanorods by selective precipitation with excess of CTAB following the process of Jana *et al*¹³⁸. We did not do it for the gold nanospheres we obtained because the nanorods were sparse and very small.

4.4.2. Functionalization of gold nanospheres

To free ourselves from any potential screening-induced destabilization, we exchanged the stabilizing CTAB with a non-charged polymer, PegSH 5000 (O-[2-(3-Mercaptopropionylamino)-ethyl]-O'-methylpolyethylene glycol). The 500 mL dispersion of gold nanospheres is centrifugated to remove the excess of CTAB and concentrated to a volume of 10 mL. Then, 1 mL of a 0.4 M solution of PegSH is added drop by drop under strong stirring. The dispersion is left under mild stirring overnight. The excess of PegSH is then removed by washing the particles with water (2 washes were performed). The optical response of the Au@PegSH before and after washing is presented in Figure 77. The plasmon peak remains at the same position (532 nm) but some aggregates might have formed upon ligand removal during washing because the shoulder at about 700 nm has a higher extinction.

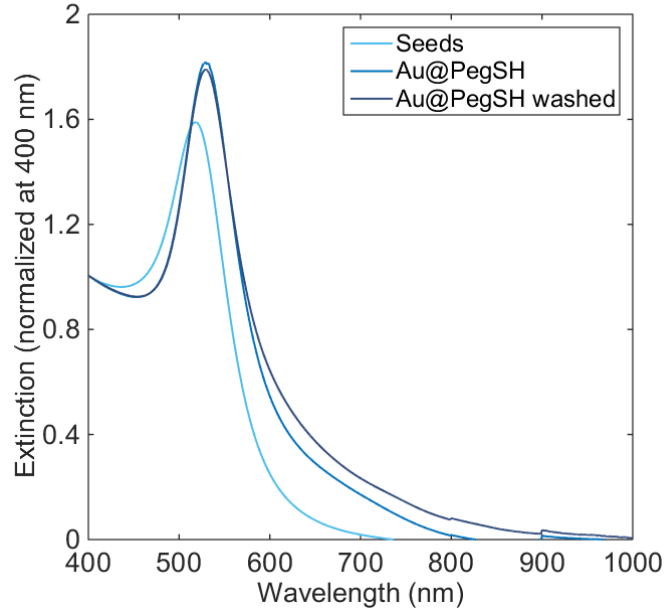


Figure 77: Extinction spectra of the 13 nm seeds, the 40 nm Au@PegSH and the 40 nm Au@PegSH washed.

To summarize, we have synthesized monodisperse spherical gold nanoparticles. These Au NPs are post-functionalized with a small polymer to prevent aggregation during their concentration inside microevaporators.

4.4.3. Concentration of gold nanospheres by microfluidic pervaporation

The Au@PegSH are then concentrated by the technique of microfluidic pervaporation. For this experiment, the membrane thickness is 14 μm , all the others parameters are unchanged (Figure 78). For such devices, evaporation times are of the order of 500 s (Figure 66). For gold nanoparticles, the volume fraction is:

$$\phi_0 = \frac{[Au^0]M_{Au}}{\rho_{Au}}$$

With M_{Au} the molar mass of gold, ρ_{Au} the volumetric mass density of gold and $[Au^0]$ the concentration of gold zero. The initial concentration $[Au^0]$ in our dispersion of gold nanoparticles is 0.049 M, thus the initial volume fraction of our gold nanoparticles in water is $\phi_0 = 5.10^{-2} \%$.

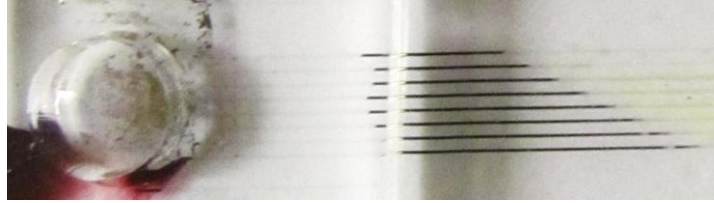


Figure 78: Microfluidic pervaporation of dispersions of Au@PegSH in the 8 microchannels.

After injection of the Au@PegSH dispersion in the microchannels, we observed later a “red front” migrating from the reservoir toward the tip of the channels Figure 79 (a). Moreover, the red color intensifies while getting closer to the tip of the channels as seen in Figure 79 (b). The color red corresponds to the color of a concentrated dispersion of gold nanoparticles but the existence and the progression of this front remains unexplained. During her Ph.D. candidacy, Julie Angly observed a similar red front with smaller gold nanoparticles¹³⁵.

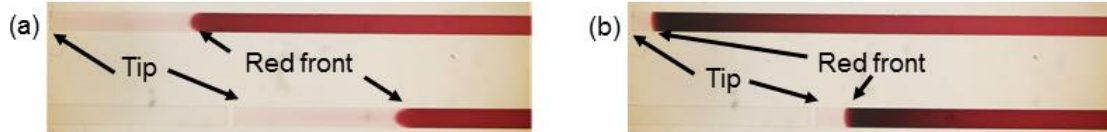


Figure 79: “Red front” migrating from the reservoir towards the tip of the channels at the beginning of the microfluidic pervaporation of dispersions of Au@PegSH.

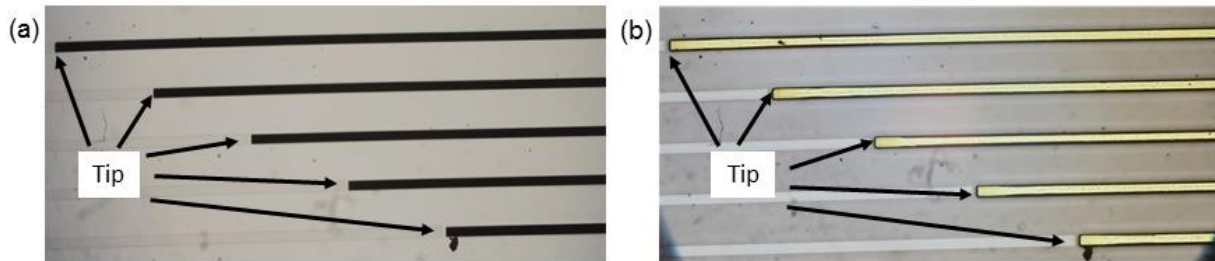


Figure 80: Optical microscope images of Au@PegSH dense states in microchannels: (a) in transmission, (b) in reflection.

After the “red front” has reached the tip of the channel, a dense state “nucleates” at the tip of the channel and grows towards the reservoir. We refer to “nucleation” as the first visible appearance of a dense material forming inside the microchannel. A dense state grows simply because the particles cannot be concentrated anymore. Figure 80 shows optical images of the dense states in five of the eight microchannels. The picture taken in transmission mode highlights the opacity of the material formed. The picture taken in reflection mode shows the shiny “gold bar-like” color of the material. The growth of the dense states is recorded by optical microscopy and is characterized using the image-processed position x_f of the front (Figure 81). The time at which the dense states “nucleates” is the “nucleation” time, T_n . After the “nucleation” time $T_n = 1200$ s, the growth is linear meaning that the dense states grow at a constant rate during time. In such case,

there is always pervaporation through the packed bed of particles. The profile is similar for all the different lengths. The growth rate of the dense material depends on the evaporation length L_0 .

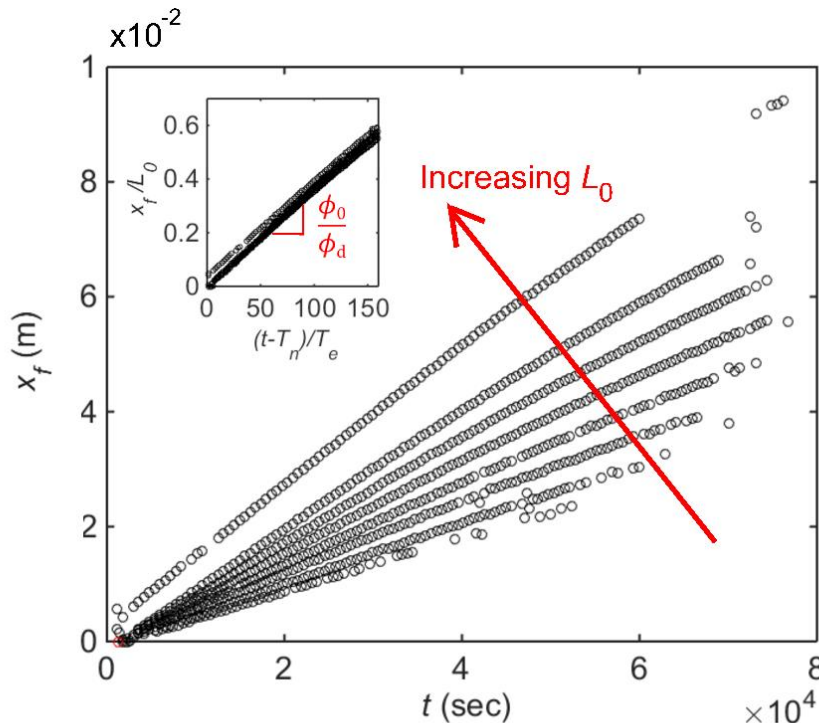


Figure 81: Temporal analysis of the growth kinetics of Au@PegSH dense states in 8 channels of different lengths. Inset: normalization of the fronts with the respective lengths L_0 of the channels and the time from “nucleation” with the evaporation time T_e .

By scaling the front position x_f by the respective lengths L_0 of the channels, and the time from “nucleation” by the evaporation time T_e , all the curves collapse on a single master curve (inset of Figure 81). The slope of the growth curves gives the packing fraction of the nanoparticles in the dense states. As first approximated, we find for gold nanoparticles that $\phi_d = 13.9\%$, is too low to give a really dense material. However, SEM images of the material (Figure 83) demonstrate that the packing fraction of the gold nanoparticles is much higher than 13.9%.

Other factors can impact the final packing fraction obtained using this method. The first one is the possible shrinkage of the microchannels during microfluidic pervaporation of the colloidal solutions. The schematic representation of one microchannel in Figure 82 (b) shows how the shrinkage of the channel’s section impacts the dense state. The SEM image of the cross section of one microchannel in Figure 83 (b) highlights the shrinkage of the microchannels in width and in height. Our initial channel’s dimensions were $w = 100\ \mu\text{m}$ and $h = 10\ \mu\text{m}$. The new dimensions obtained from the SEM images are $w = 95\ \mu\text{m}$ and $h = 4.5\ \mu\text{m}$ (measured in the middle of the channel). The packing fraction of the dense material re-evaluated including channel shrinkage is:

$$\frac{x_f}{L_0} = \frac{\phi_0 S_0}{\phi_d S_d} \left(\frac{t - T_n}{T_e} \right)$$

Scaling with the new channel's dimensions, we obtain $\phi_d = 32.5\%$. This value is still very far from the theoretical 64% or 74% corresponding to the maximal packing of hard monodisperse spheres organized in a random close-packed state or in a face-centered cubic crystal.

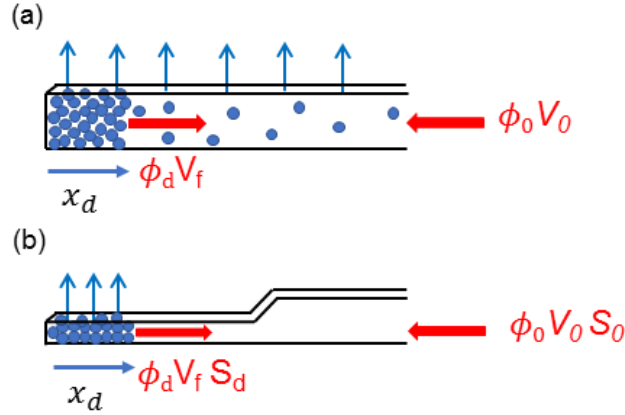


Figure 82: (a) Theoretical mass conservation and (b) mass conservation with channel shrinkage during microfluidic pervaporation experiment.

Another approximation explains the remaining discrepancy. Indeed, we approximated that the dispersion of nanogold is perfectly monodisperse and that the radius of the particles is the radius of the gold particles alone. In fact, as evidenced earlier by TEM imaging, our gold nanoparticles dispersion contains few nanorods and is therefore not perfectly monodisperse. The presence of nanorods in the dense state will inherently decrease its packing fraction by adding defects. In addition, the radius of the nanoparticles concentrated by the technique of microfluidic pervaporation is not exactly the radius of the gold particles alone but the radius of the gold particles with its capping ligand (the PegSH). The radius of the gold nanoparticles, R_{Au} , is about 19 nm. The thickness of the capping layer, R_{PegSH} , can be estimated from the spacing in between two particles from the SEM images in Figure 83 (c) and (d). We found $R_{PegSH} \approx 5.6$ nm, which is close to 4 nm gyration radius of the PegSH. The new initial volume fraction including the capping layer, ϕ'_0 , is:

$$\phi'_0 = \phi_0 \left(\frac{R_{Au} + R_{PegSH}}{R_{Au}} \right)^3$$

We find $\phi'_0 = 0.1\%$. Using this higher initial volume fraction and taking into account the shrinkage of the channel, we obtain $\phi'_d = 71.7\%$. This final packing fraction value is very close to the theoretical packing fraction for face-centered cubic lattices and is in good agreement with the observed structures in Figure 83.

One last parameter also has to be considered in the evaluation of the packing fraction of the dense states. After the microfluidic pervaporation experiment is complete and before SEM imaging, the water remaining in the dense states is fully evaporated. The material observed under SEM can appear denser than during the microfluidic pervaporation experiments due to the capillary forces bringing the particles closer during evaporation of the residual water. Therefore, the packing fraction measured graphically can be lower than the packing fraction estimated from the SEM pictures.

Complementary electron and optical microscopy analyses give more information about the structure of the material. After peeling off the membrane of the microfluidic chip and stamping the material onto a conductive tape adhered on an SEM metallic pic, we analyze the structure of the micromaterial under high-resolution scanning electron microscope. This method of transfer is not optimized and sometimes the materials break at places (Figure 83 (a)). We took advantages of these cracks to take images of the cross section of the materials (Figure 83 (b)). Focusing in on such areas reveals a brick-like edifice with neat facets and edges. The surface of the material for its part, is very flat. This highlight how microfluidic can be used to shape up materials. It looks like a polymer layer is formed on the edges of the microchannels. No nanoparticles are observed in this polymer layer and it seems that the nanoparticle's dense state is starting further towards the inside of the channels. A higher magnification (Figure 83 (c) and (d)) show that the material is made of tightly packed nanoparticles with apparent hexagonal packing (face-centered cubic and hexagonal close-packed) in specific areas. To our knowledge, it is the first time that crystalline arrays of gold nanospheres are obtained in microevaporators. More than 120 layers of gold nanoparticles were stacked on top of each other.

The technique of microfluidic pervaporation opens new ways in the design of the next-generation optical devices based on the unique plasmonic properties of gold nanoparticles. For instance, these assembled nanomaterials could be used as collective resonators. They could also lead to high refractive index materials as demonstrated by Iazzolino *et al*¹³⁹ or to new photonic crystals in which the plasmon resonance of the gold nanoparticles could be enhanced¹⁴⁰.

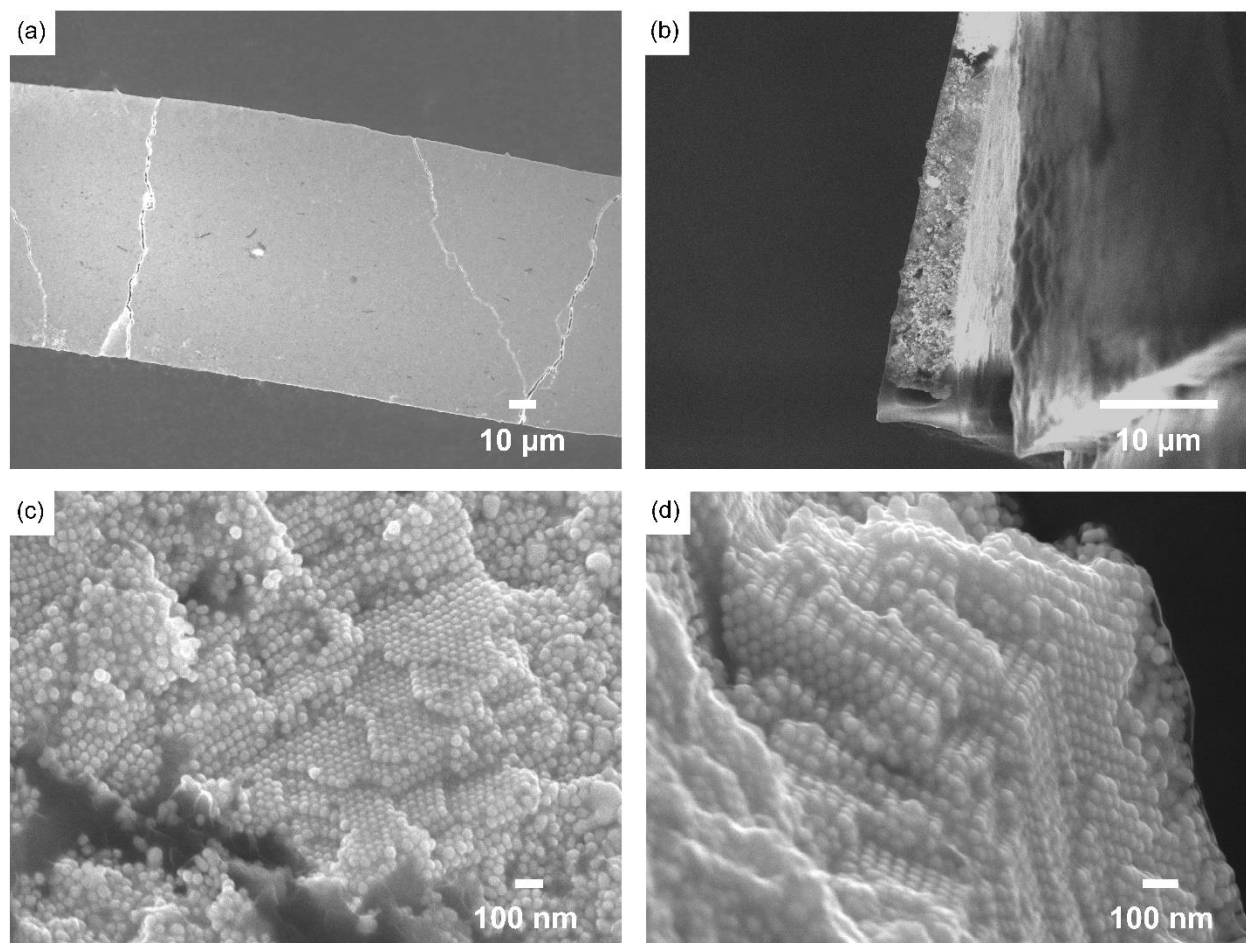


Figure 83: SEM images of microevaporated Au NPs@PegSH at 0.9 wt% (a) top view of a microchannel, (b) cross section of one microchannel, (c-d) typical crystallites formed inside microchannels.

5. Conclusion

The principal objective of this chapter was to assemble nanoparticles into tridimensional bulky materials. To do so we used the technique of microfluidic pervaporation. Two types of nanospheres were concentrated in microchannels: gold nanoparticles and polystyrene particles.

First, two different sizes of polystyrene particles were assembled into dense materials. Regarding the 0.5 μm latex, the salts contained in the dispersion led to a strong aggregation of the particles during their concentration. The precipitation of the particles was decreased by decreasing the salt concentration through dialysis of the dispersion. The growth kinetics of the dense states led to a packing fraction of the particles in the material, $\phi_d \approx 40\%$. 20 layers of packed latex particles were obtained. For the 1 μm polystyrene particles, the growth kinetics of the material were not followed. SEM analysis evidenced large crystals of latex particles organized in hexagonal lattices. Since the particles were bigger for the same microchannel height, only 10 layers of

nanospheres were stacked on top of each other. These results open new perspectives as for the fabrication of photonic crystals via microfluidic pervaporation.

Then, we have synthesized 38 nm gold nanoparticles stabilized by a small polymer and assembled them into crystalline dense states. The growth kinetics of these dense states were studied and the packing fraction of the gold nanoparticles in the dense states, ϕ_d , was obtained from a mass conservation based model. We measured $\phi_d \approx 10\%$. Analyses of SEM images showed a strong shrinkage of the channels occurring either during microfluidic pervaporation experiment of the dispersions or because of the material drying after the experiment. Rescaling our data with the new channels dimensions, we obtained $\phi_d \approx 32\%$. SEM imaging also evidenced the presence of lots of polymer separating the nanoparticles. Assuming that the real diameter of the microevaporated nanoparticles is actually the diameter of the gold particles plus the layer of its capped agent, we reached a packing fraction of about 72% in good agreement with the hexagonal lattices observed within the dense states. More than 120 layers of close-packed gold nanospheres were successfully organized using our microfluidic set up. The directed-assembly of these plasmonic nanospheres using the microfluidic pervaporation technique offers solid ground as for the design of new plasmonic materials with properties arising from the collective interactions between the nanoparticles.

Microfluidic pervaporation is therefore a powerful tool to form large tri-dimensional self-standing films assemblies of well-organized particles. The control over the evaporation rate and the tunable materials' shape are definitely the biggest advantages of the microfluidic pervaporation compared to other commonly used technics such as the vertical deposition or the Langmuir-Blodgett method. Moreover, it does not rely on a specific type of colloids, as long as they feature sufficient colloidal stability and actually works for a large set of nanoparticles. We have shown it for gold nanoparticles and polystyrene beads but many other types of nanoparticles or mixture of nanoparticles can be assembled through this technique. The versatility of the method leads to numerous applications in the design of new functional microscale optomaterials.

Chapter 3: Fabrication of hybrid microcapsules from Pickering emulsions

TABLE OF CONTENTS

1. Introduction.....	89
2. Gold-silica microcapsules.....	89
2.1. Pickering emulsion formation	90
2.1.1. Adsorption at the interface	90
2.1.2. Number of nanoparticles	91
2.1.3. Decrease of an energy barrier.....	93
2.2. Polycondensation of silica at the oil/water interface	94
2.3. Synthesis of gold-silica microcapsules.....	95
2.3.1. Effect of pH.....	95
2.3.2. Effect of butanol.....	98
2.3.3. Effect of PEOS concentration	98
2.3.4. Effect of the oil phase.....	100
3. The silver-silica microcapsules	104
3.1. Pickering emulsion formation	104
3.2. Synthesis of Ag-Si microcapsules	105
4. The gold silver silica microcapsules	107
5. The gold acrylate microcapsules.....	109
5.1. Polymerization of acrylate at the oil/water interface.....	109
5.2. Synthesis of the gold-acrylate microcapsules.....	110
6. Conclusion	112

1. Introduction

In this chapter, we move beyond the assembly of nanoparticles into bulk materials, and show how nanoparticles can be assembled to form hollow hard and soft microcapsules. We present a method to synthesize two kinds of plasmonic nanoparticles: silver nanoparticles (Ag NPs) and gold nanoparticles (Au NPs). The nanoparticles are synthesized by reduction of a metallic salt with ascorbic acid in presence of a polymer capping agent. Then, by tuning the surface charges, the nanoparticles are assembled at the interface of an emulsion. The obtained Pickering emulsion is then used as template to form hard or soft microcapsules by polymerizing the interface. To the best of our knowledge, it is the first time that microcapsules with highly packed Au and Ag NPs at the surface are obtained by self-assembly on emulsion droplets. Our hybrid microcapsules, cumulate properties directly resulting from the intrinsic particles and shell properties. Indeed, depending on the type of nanoparticles and shell, the microcapsules exhibit different optical and mechanical properties. The results presented in this chapter were patented (RD_2017_004_US_PSP_2017).

2. Gold-silica microcapsules

This part is dedicated to the fabrication of gold-silica microcapsules (Au-Si microcapsules). First, we explain the synthesis of gold nanoparticles and the formation of the Pickering emulsions. Then, we describe the formation of a silica shell at the interface of the emulsion. Finally, we make the Au-Si microcapsules. By adjusting the microcapsules synthesis parameters, we are able to tune the thickness of the silica shell.

The preparation of Au-Si microcapsules is illustrated in Figure 84. The first step consists in mixing an aqueous phase containing the Au NPs with an oily toluene phase in which polyethoxyorthosilicate (PEOS) is dissolved. The two phases are then strongly agitated by sonication (15 min), forming an oil-in-water emulsion. We found that within the right conditions, that we will describe and explain, the Au NPs adsorb onto the oil droplets to form the so-called Pickering emulsions. To obtain a stable Pickering emulsion, three conditions have to be fulfilled: (i) Au NPs in the vicinity of droplets must adsorb at the interface by reaching a minimum of energy, (ii) the solution should contain enough Au NPs to cover the emulsion droplets and (iii) The energy barrier hindering adsorption of Au NPs must be lowered. These three conditions detailed in section 2.1 guided our Au NPs synthesis protocol. The second step consists in polymerizing the PEOS at the interface of the emulsion and is explained in section 2.2.



Figure 84: Schematic representation of the formation of gold-silica microcapsules.

2.1. Pickering emulsion formation

2.1.1. Adsorption at the interface

The adsorption of Au NPs at the water/oil interface results from a decrease in the system free energy^{93,122,141}. Equation 18 shows the free energy of adsorption of a nanoparticle at the interface, where γ_{ow} is the oil/water interfacial tension (in our case, $\gamma_{ow} = 37.1 \text{ mN/m}$)¹⁴², θ_{ow} is the three-phase contact angle between the solid and the oil/water interface; R is the radius of the nanoparticles.

$$\Delta G = -\pi R^2 \gamma_{ow} (1 - |\cos(\theta_{ow})|)^2$$

Equation 18: Gain of free energy by adsorption of a nanoparticle at the oil/water interface.

It is clear from Equation 18 that particles are best adsorbed at the interface for $\theta_{ow} = 90^\circ$, when particles have equal affinity for oil and water. To tune this property, the Au NPs were partially functionalized with poly(diallyldimethylammoniumnitrate-co-1-vinylpyrrolidone) (PVP-DADMAN, see Figure 85). PVP is a neutral amphiphilic polymer known to adsorb onto gold nanoparticles^{143,144}. The long backbone of the PVP results in increased hydrophobicity of the functionalized Au NPs, therefore facilitating the adsorption of the particles at the toluene/water interface by bringing the contact angle closer to 90° .

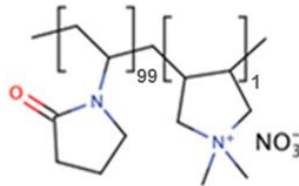


Figure 85: Chemical structure of PVP-DADMAN (99:1). PVP-DADMAN contains 1 unit of diallyldimethylammonium-nitrate (DADMAN) for 99 units of Polyvinylpyrrolidone (PVP) ($M_w = 60 \text{ kg/mol}$, $pK_a = 5$).

2.1.2. Number of nanoparticles

The number of nanoparticles necessary to form a stable Pickering emulsion can be approximately estimated from Equation 19 where N_p is the number of Au NPs needed to cover droplets of radius R with particles of radius r , f is the packing density of the particles and V is the total volume of the oil dispersed phase.

$$N_p = \frac{3fV}{\pi Rr^2}$$

Equation 19: Number of Au NPs needed to cover one droplet.

The above equation is obtained by assuming that the nanoparticles are equally wet by the water and oil phases. An estimation shows that for 1 mL of dispersed phase, a surface packing fraction $f = 0.74$, nanoparticles of 40 nm in diameter and colloidosomes of 10 μm in diameter; approximately 10^{14} Au NPs are needed.

As previously discussed in Chapter 1, the most common methods used to synthesize monodisperse 40 nm Au NPs use metal-ion assisted reduction, require low concentration of gold salt or multiple syntheses steps^{13,32,145}. Therefore we chose to follow an easier synthesis approach at larger scale, adapted from the method explored by Malassis *et al.*³³ and described below. This straightforward one-step synthetic method uses PVP-DADMAN as an Au NPs capping agent. It leads to polydisperse gold nanoparticles, which are analyzed by transmission electron microscopy (TEM) (see Figure 86 (a)). The mean diameter d was $d = 40 \text{ nm} \pm 25 \text{ nm}$ as shown by the histogram in Figure 87 (a).

Gold nanoparticles synthesis: The Au NPs used in this procedure are synthesized by reduction of HAuCl_4 with ascorbic acid in presence of PVP-DADMAN. A solution of $5.7 \cdot 10^{-6} \text{ M}$ PVP-DADMAN and $2.5 \cdot 10^{-3} \text{ M}$ HAuCl_4 is brought to boil. Then, 12.5 mL of ascorbic acid (0.1 M) is added. The solution protected from light by aluminum foil is stirred for 1 h at 97°C. After synthesis, the Au NPs are left to rest for one day to remove the biggest nanoparticles. The rest of the dispersion is centrifuged and concentrated into a 5 milliliters solution.

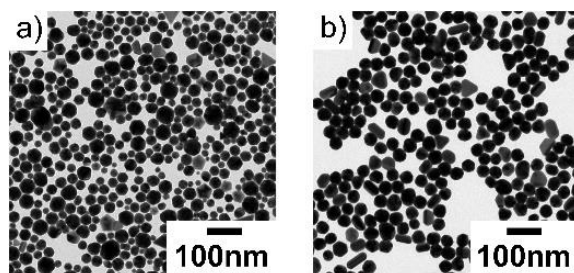


Figure 86: a) TEM image of gold nanoparticles used in the synthesis of microcapsules. b) TEM image of Au NPs synthesized via seed growth method.

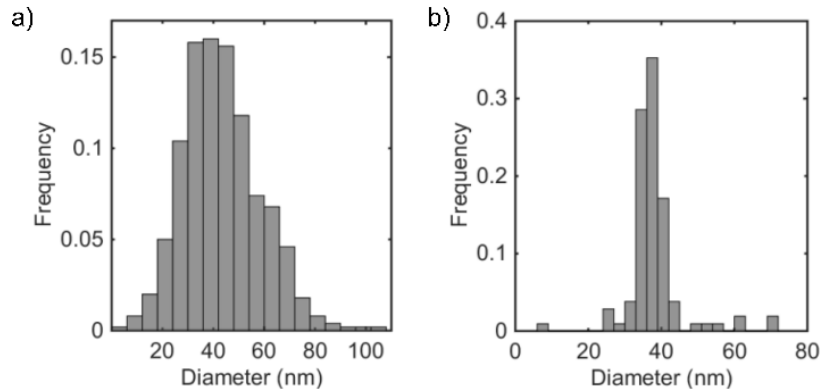


Figure 87: Histograms showing the size of a) Au NPs used in the synthesis of microcapsules; b) Au NPs synthesized by seed growth.

We compare in Figure 88 the extinction curves of the polydisperse 40 nm dispersion of Au NPs@PVP-DADMAN and a monodisperse 40 nm dispersion of Au NPs synthesized using traditional seed growth method¹³ (described in Chapter 2). TEM images and histograms of the gold nanoparticles size distributions for monodisperse 40 nm particles are provided in Figure 86 (b) and in Figure 87 (b). Interestingly, at this size range, the polydispersity does not alter the optical response of the particles. Indeed, the plasmonic peak maximum of the Au NPs@PVP-DADMAN dispersion is at the same position as that of a monodisperse 40 nm dispersion of gold nanoparticles as shown in Figure 88. This is consistent with the theoretical results of Myroshnychenko *et al.*¹⁴⁶ which show that in this range of Au NP diameters and surrounding refractive index, the position of the extinction peak shifts in a small range of 20 nm. For these reasons, the polydispersity of Au NPs@PVP-DADMAN does not affect the position of the plasmonic peak but results in a small broadening of the peak.

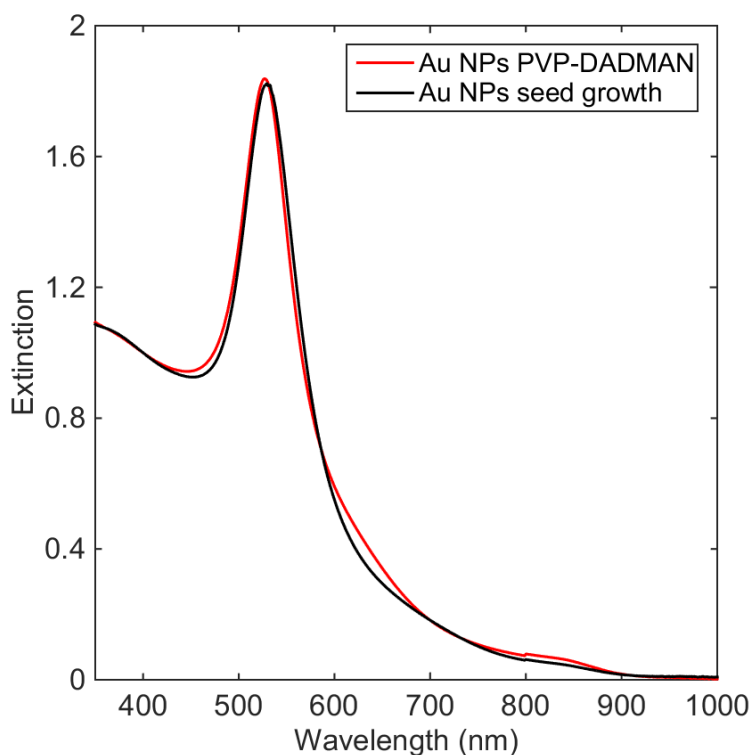


Figure 88: Comparison between the extinction curves normalized at 400 nm of the Au NPs synthesized using the one-step method (red) and the Au NPs synthesized via a seed growth method (black).

2.1.3. Decrease of an energy barrier

Malassis et al. have shown that bare Au NPs are stable due to the presence of residual negative charges from ascorbic acid at their surface³³. Above pH = 4, Au NPs appear to be weakly negatively charged (ζ potential ~ -5 mV) and well dispersed in water showing a sharp plasmon peak ($\lambda \sim 527$ nm) and a red color as shown in the left picture of Figure 89. Below pH = 4, Au NPs seem to have no charge (ζ potential ~ 0 mV) and therefore flocculate forming a blue solution as seen in the right picture of Figure 89 which has a large red-shifted plasmon peak ($\lambda \sim 720$ nm). By decreasing the pH below 4, the charges at the droplets surface are decreased thus cancelling any electrostatic repulsion and enabling the adsorption of Au NPs at the oil/water interface.

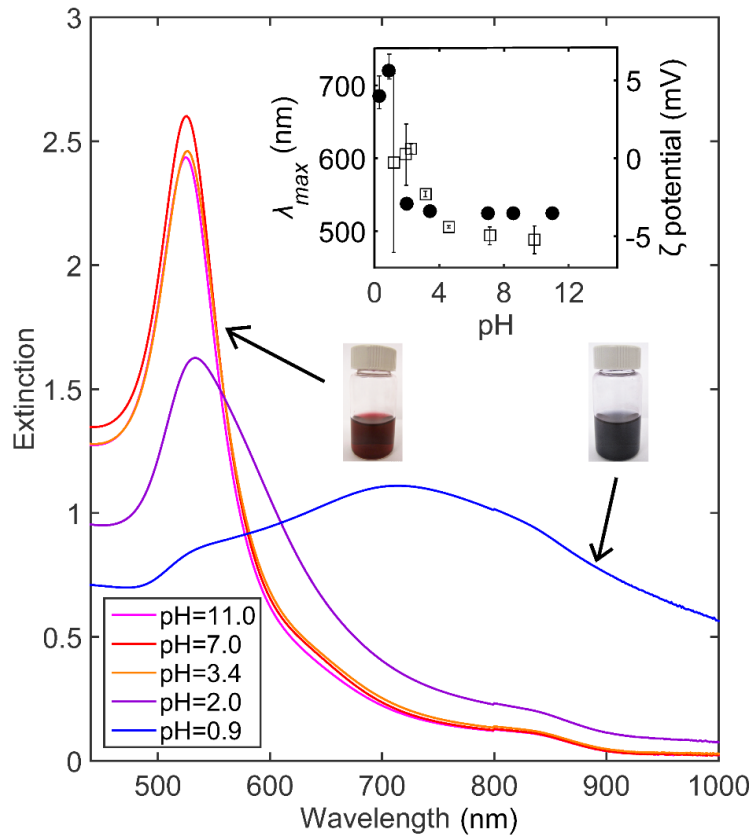


Figure 89 : Plasmonic response of Au NPs solutions $[Au] = 0.57$ mM as a function of pH. The two pictures respectively show a well dispersed solution of Au NPs (red) and a solution of flocculated Au NPs (blue) of the same concentration. Inset: plasmonic peak maximum as a function of the pH (filled circular points) and Zeta potential of the Au NPs at $[Au] = 0.57$ mM, $[NaCl] = 10^{-2}$ M as a function of the pH (square unfilled points).

2.2. Polycondensation of silica at the oil/water interface

The second step in the formation of the gold-silica microcapsules as presented in Figure 84 is the formation of a silica shell at the interface of the emulsion droplets. PEOS, a very hydrophobic hyperbranched silica polymer soluble in oil only is used as a silica precursor. The polymerization of PEOS at the oil/water interface follows two steps as schematically represented in Figure 90. i) PEOS is hydrolyzed at the interface of the emulsion by the acidic water¹²³. During this step, the alkoxy groups of the PEOS are converted in silanol groups forming a hydrolyzed layer of PEOS between water and oil. ii) The hydrolyzed PEOS reacts with other hydrolyzed (alcohol condensation) or non-hydrolyzed (water condensation) PEOS molecules to form a silica crust.

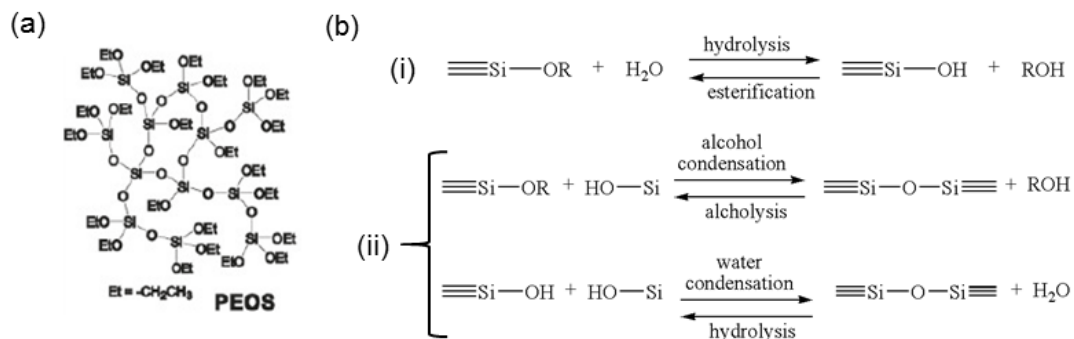


Figure 90: (a) PEOS formula¹²³. (b) Polycondensation reaction.

The PEOS used in the silica microcapsules syntheses is a commercial product. It was characterized by chromatography and NMR analyses. The results presented in Annex 1 show that PEOS has a number-average molecular weight M_n of 766 g/mol. Traces of ethanol were found in the PEOS commercial solution. PEOS was used as is for the synthesis of gold-silica microcapsules.

2.3.Synthesis of gold-silica microcapsules

2.3.1. Effect of pH

In section 2.1.3, we have demonstrated that the Au NPs surface charges depend on pH. In the following paragraphs, we show that these surface charges control the adsorption of Au NPs at the oil/water interface.

- **Synthesis at pH > 4**

PEOS (0.2 g/mL) was diluted in 1 mL of toluene. The water phase (5 mL) of the emulsion contains a solution of dispersed Au NPs ($[\text{Au}^0] = 0.02 \text{ M}$), butanol (0.22 M) and ammonia (10^{-4} M) to adjust pH above 4. The oil and water phases were emulsified together with a Brandson 3210 ultrasonic bath at 30°C for 15 minutes. Shortly after the sonication, the emulsion droplets are transparent suggesting that the Au NPs did not adsorb on the surface of the droplets, as seen in Figure 91 (a). After 3 days, the silica shell was fully formed. The microcapsules were recovered, cleaned and concentrated by simple sedimentation. Optical microscopy and SEM images show colorless microcapsules without Au NPs embedded in their silica shell (Figure 91 (b-d)).

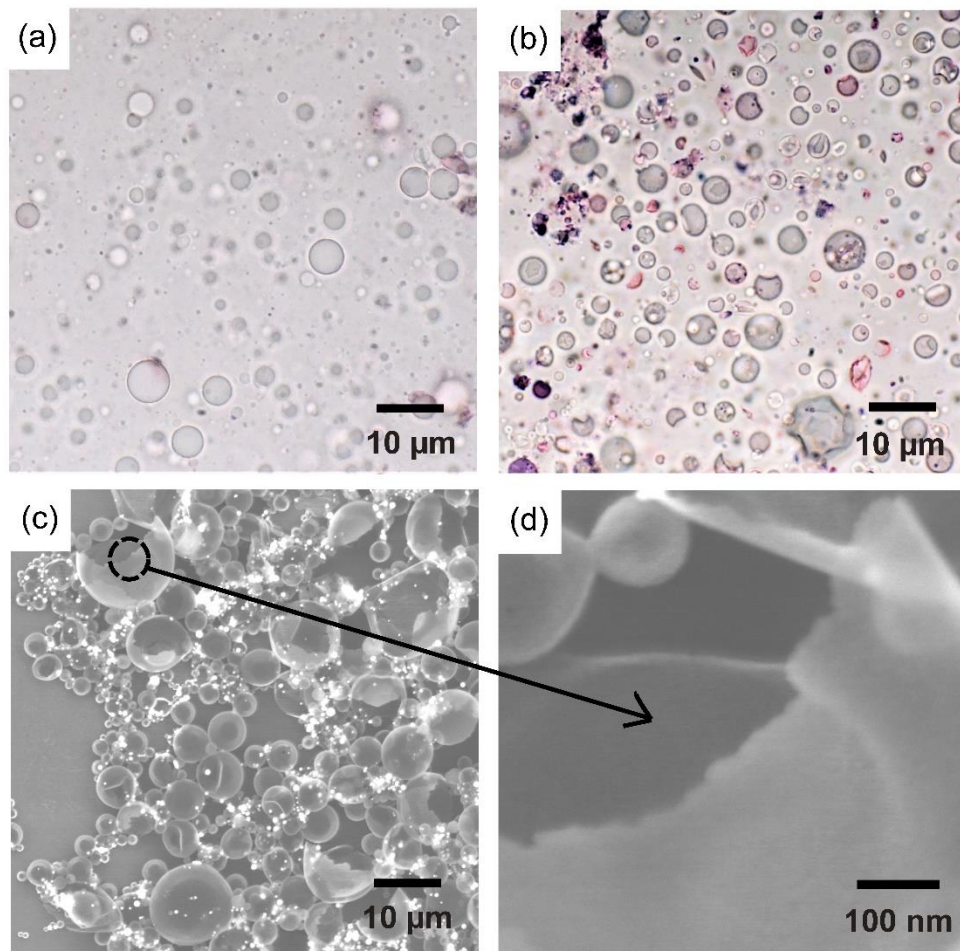


Figure 91: Optical microscope images of (a) emulsion obtained at 0.02 M of gold and pH ~ 10 , (b) microcapsules after polymerization at 0.02 M of gold and pH ~ 10 . (c-d) SEM images of (c) microcapsules and (d) surface of microcapsules obtained at 0.02 M of gold and pH ~ 10 .

- **Synthesis at pH < 4**

PEOS (0.2 g/mL) was diluted in 1 mL of toluene. The water phase (5 mL) of the emulsion contains a solution of diapered Au NPs ($[\text{Au}^0] = 0.02 \text{ M}$), butanol (0.22 M) and HCl (0.1 M) to adjust pH below 4. The oil and water phases are emulsified together with a Brandson 3210 ultrasonic bath at 30°C for 15 minutes. Shortly after the sonication, the emulsion exhibits a strong pink color due to the adsorption of the AuNPs as seen in Figure 92 (a). Indeed, by decreasing pH below 4, the oil droplets and the Au NPs surface charges are decreased, thus cancelling any electrostatic repulsion and enabling the adsorption of Au NPs at the oil/water interface. The emulsion becomes blue after one day. This change of color proves that nanoparticles adsorb and get more and more densely packed at the interface as time goes on. The emulsion is then gently shaken mechanically for a few days to allow the formation of the silica shell by polymerization of the PEOS at the interface.

PEOS hydrolyzes at the emulsion interface and condensates to form a silica shell, which embeds the nanoparticles¹²³. After a day, the silica shell is visible by optical microscopy. It takes about 3 days to fully convert the PEOS to a thin silica film because of the slow interfacial sol-gel reaction under acidic conditions¹²³. The Au-Si microcapsules can be recovered, cleaned and concentrated by simple sedimentation. Images of the dried microcapsules formed after 3 days are shown on Figure 92 (c-d). The color, shape and size of the microcapsules were analyzed by optical microscopy and SEM. The resulting microcapsules are spherical with dimensions ranging from several hundredths of nanometers to several tenths of micrometers (2 - 20 μm). As seen in Figure 92 (b), the microcapsules present a deep blue color which comes from a monolayer of densely packed gold nanoparticles on their surface (see inset of Figure 92 (c)). Under the high vacuum of the SEM, the gold silica capsules tend to buckle due to the thin silica shell ((see inset of Figure 92 (d)). The silica shell thickness as measured from SEM images ranged between 45 and 55 nm (this is described later in Figure 95 (c)).

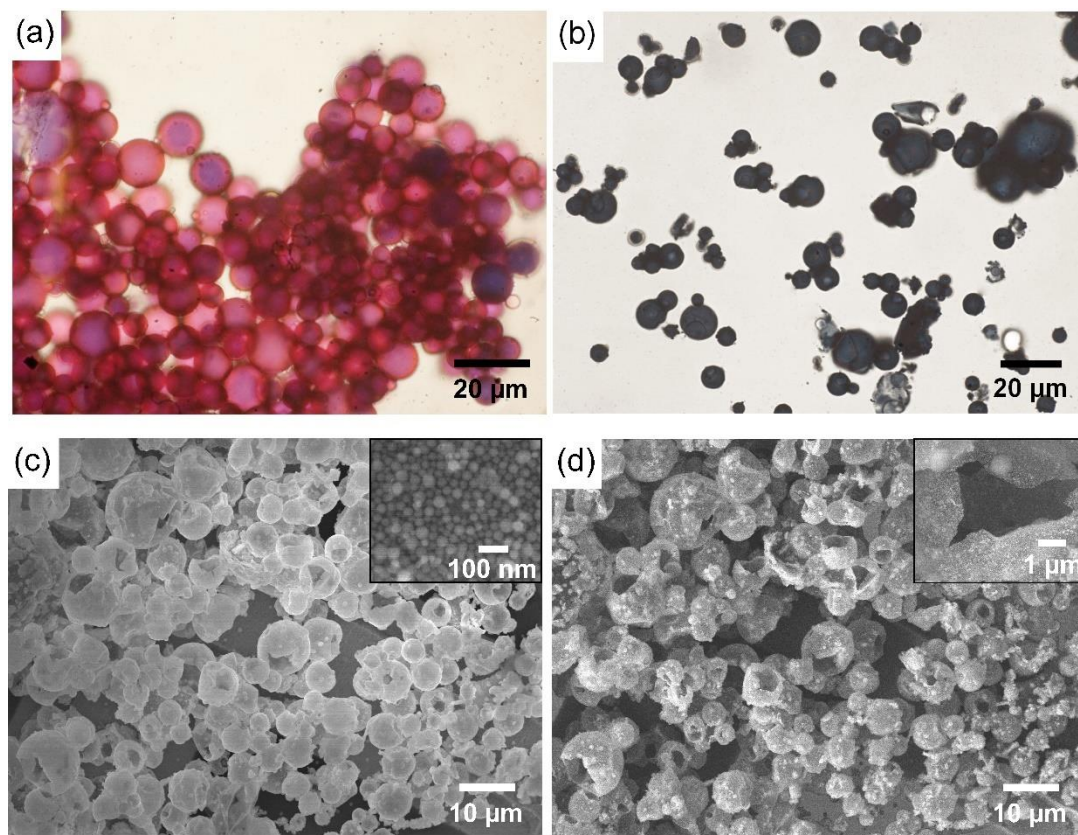


Figure 92: (a-b) Optical images of (a) Au NPs stabilized and (b) gold-silica microcapsules. (c-d) SEM images of typical gold-silica microcapsules obtained with optimal recipe (pH \sim 1); (c) shows the thick silica shell (inset: surface of one microcapsule) and (d) evidences the Au NPs embedded in said shell (inset: zoom onto an open microcapsule). The oil phase is toluene.

2.3.2. Effect of butanol

The synthesis of gold-silica microcapsules as presented in section 2.3 requires the addition of a small co-surfactant, the butanol, to maintain the stability of the emulsion droplets against coalescence. With butanol, spherical microcapsules are obtained as shown in Figure 93 (a). Without butanol, very few microcapsules are obtained and most of the Au NPs aggregate in solution as shown in Figure 93 (b).

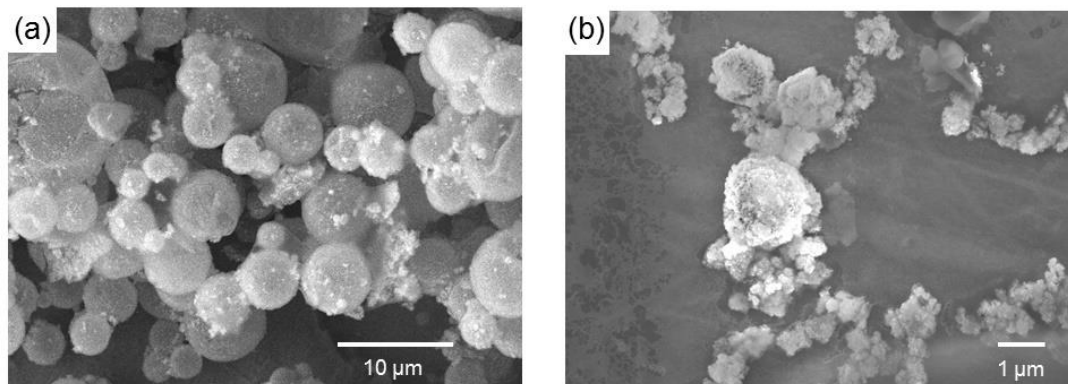


Figure 93: SEM images of Au-Si microcapsules (a) with and (b) without butanol.

2.3.3. Effect of PEOS concentration

The mechanical properties of the silica shell depend on its thickness and therefore on the initial concentration of PEOS, [Peos] (g/mL). Figure 94, Figure 95 and Figure 96 summarize the results. When [Peos] is low (0.05 g/mL) the shell formed is very thin (Figure 95 (a)) and the microcapsules fully collapse upon drying as shown in Figure 94 (a). When [Peos] = 0.1 g/mL, the thickness of the shell increases up to about 25-35 nm and the dried microcapsules buckle into “hemispheres”. The “top half” of the shell fell inside the “bottom half” of the shell (see Figure 94 (b)). Upon increase of the concentration of Peos (0.2 g/mL), the shell formed is thicker (45 to 55 nm) as judged by the depth of the Au NPs in the silica shell (Figure 95 (c)). At that concentration, the microcapsules keep their spherical shape upon drying as shown in Figure 94 (c). For [Peos] \geq 0.3 g/mL, the obtained microcapsules remain spherical upon drying (see Figure 94 (d)) and the silica shell is even thicker (Figure 95 (d)). The thickness of the shell as a function of the PEOS concentration is plotted in Figure 96. Based on the SEM images analysis, three distinct areas were squared in the graph. These areas correspond to the formation of spherical capsules, “hemispheres” and totally buckled capsules. Each area is defined by a certain quantity of PEOS and a subsequent shell thickness. This graph shows that the required concentration of PEOS to form Au-Si microcapsules which do not collapse upon drying is 0.2 g/mL.

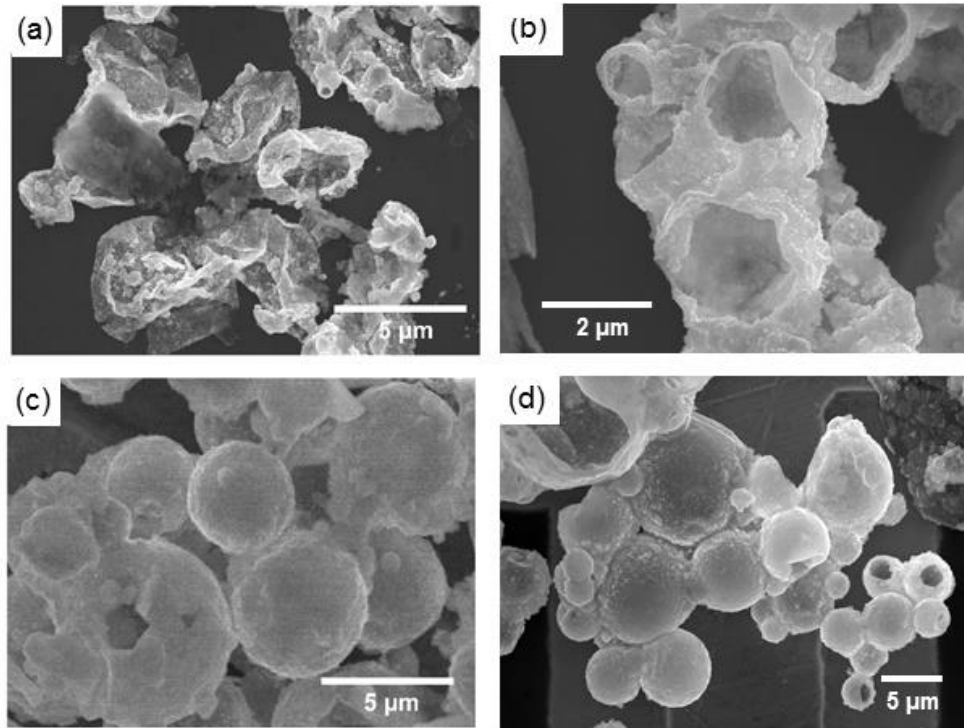


Figure 94: Influence of the quantity of PEOS on the formation of the gold microcapsules. SEM images of Au-Si microcapsules synthesized with (a) 0.05, (b) 0.1, (c) 0.2 and (d) ≥ 0.3 g/mL PEOS. The oil phase is toluene.

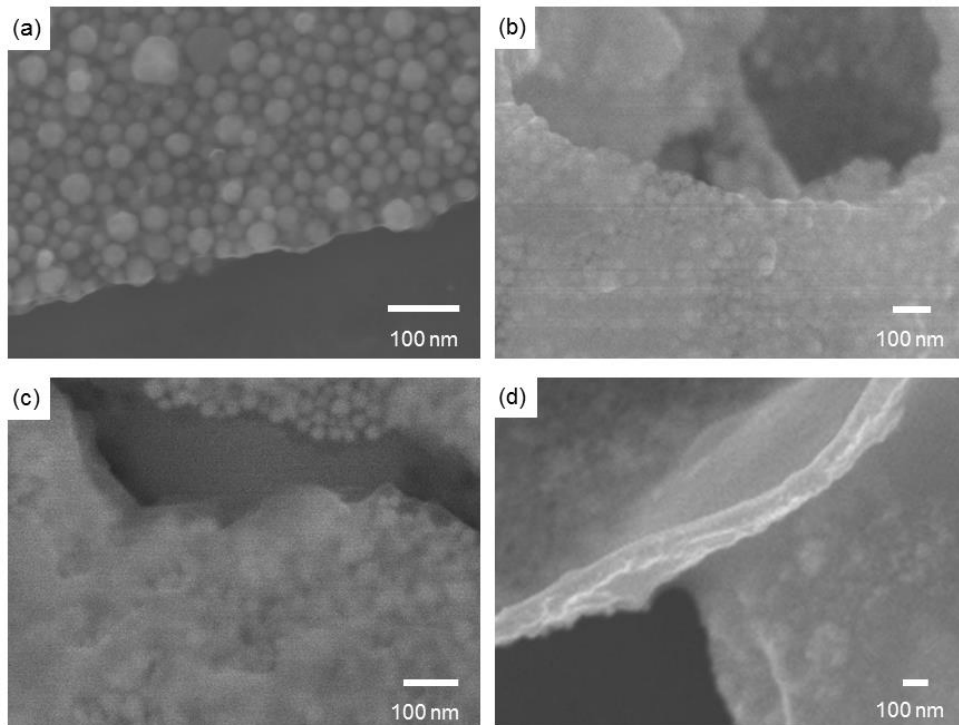


Figure 95: SEM images of the shell of the gold-silica microcapsules obtained with PEOS at (a) 0.05, (b) 0.1, (c) 0.2 and (d) 0.4 g/mL. The oil phase is toluene.

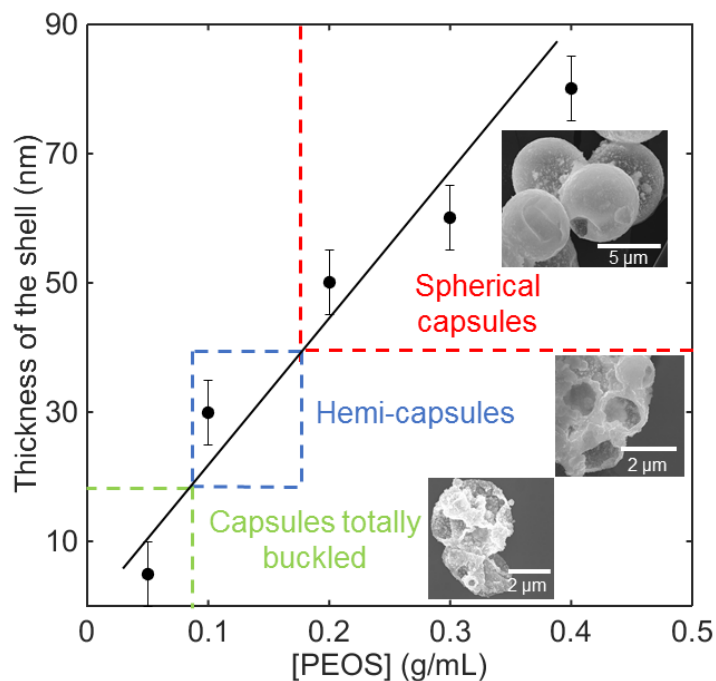


Figure 96: Au-Si microcapsules shell thickness and buckling as a function of the concentration of PEOS (g/mL).

2.3.4. Effect of the oil phase

So far, we have demonstrated the possibility to fabricate gold-silica microcapsules from toluene-in-water emulsion templates. Based on Equation 18, the stability of the Pickering emulsion increases as the of the oil/water interfacial tension increases. We tested this theoretical result by exchanging the toluene with two other oils. We kept the exact same formulation ($[Au^0] = 0.02$ M, $[butanol] = 0.22$ M, $[PEOS] = 0.2$ g/mL, $[HCl] = 0.1$ M). First, toluene was replaced by hexadecane. Au-Si microcapsules were obtained as shown in Figure 97 (a) and (c). The microcapsules are blue due to the close packed Au NPs embedded in their shells (see inset of Figure 97 (a)). The microcapsules are polydisperse. Most of them are less than $5 \mu\text{m}$. The silica shell obtained with hexadecane is thinner (< 10 nm) than the silica shell obtained with toluene (Figure 96). We explain this fact by the partial solubility of PEOS in hexadecane. It might limit the formation of the silica shell at the interface oil/water. Indeed, when PEOS is mixed in hexadecane, the obtained mixture is slightly blurry (due to the formation of a tiny emulsion or precipitation of PEOS in the solvent). Second, toluene is exchanged by a mixture of hexadecane/hexyl acetate 50/50 by volume. Hexyl acetate often used as a flavoring agent because of its fruity odor. It has a higher polarity than hexadecane. Upon addition of hexyl acetate in a mixture of hexadecane and PEOS, the blurriness of the mixture disappeared. PEOS is fully soluble in a mixture of hexyl acetate/haxadecane. After polymerization, the obtained Au-Si microcapsules

are blue due to the highly packed Au NPs embedded in the silica shell. However, the silica shell formed with hexyl acetate/hexadecane is about 10 nm and is not as thick as the one observed with toluene for the same concentration of PEOS (Figure 96). Upon addition of hexyl acetate with hexadecane, both PEOS and hydrolyzed PEOS solubilities increase in the oil phase due to the increase of the oil polarity. Thus, the hydrolyzed PEOS formed at the interface of the emulsion migrates inside the droplets instead of forming a layer at the interface¹²³. Therefore, after 3 days the Au-Si microcapsules also have a very thin silica shell.

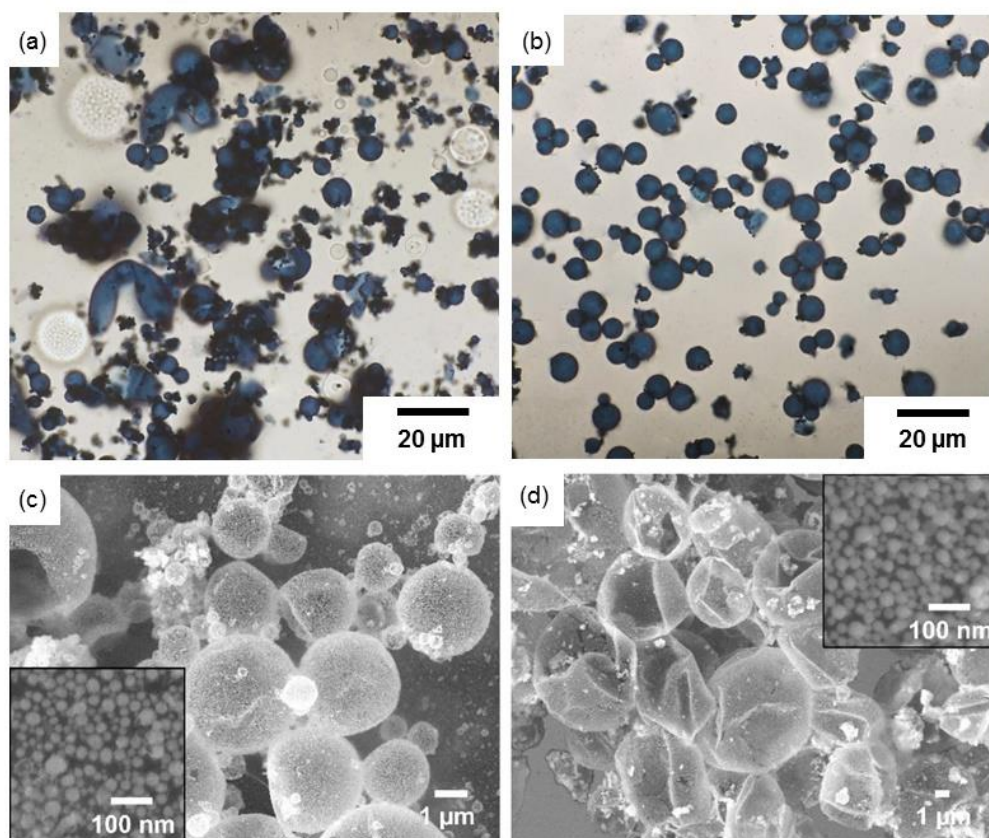


Figure 97: SEM images of gold silica microcapsules obtained with (a) hexadecane and (b) hexadecane/hexyl acetate 50/50 V/V. Insets show the surface of a typical microcapsules for (a) hexadecane and (b) hexadecane/hexyl acetate 50/50 V/V.

The diagram in Figure 98 summarizes the results obtained for $[\text{PEOS}] = 0.2 \text{ g/mL}$, using the three solvents used in the synthesis of Au-Si microcapsules: toluene, hexadecane and hexadecane/hexyl acetate (50/50 by volume). In this diagram, the thickness of the silica shell is plotted as a function of the solubility of PEOS and hydrolyzed PEOS in the different oils. The thickest silica shell is obtained with toluene. Indeed, it is the only oil in which PEOS is highly soluble and hydrolyzed PEOS is not.

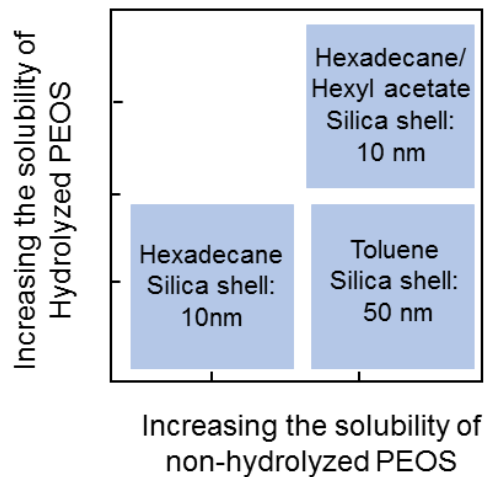


Figure 98: Thickness of the silica shell as a function of the solubility of the PEOS and hydrolyzed PEOS in toluene, hexadecane and mixture of hexadecane/hexyl acetate 50/50 by volume.

The influence of the PEOS concentration on the formation of the silica shell was studied with the mixture hexyl acetate/hexadecane. Gold-silica microcapsules from hexyl acetate/hexadecane-in-water emulsions were carried out at 4 different PEOS concentrations: 0.012, 0.05, 0.2 and 0.4 g/mL PEOS. The ESEM images in Figure 99 show that at low PEOS concentration (0.012 g/mL, Figure 99 (d)), the microcapsules collapse upon drying because the amount of PEOS was too low to form a mechanically resistant shell. At 0.05 g/mL of PEOS, and spherical capsules are observed showing that the shell formed is slightly thicker (Figure 99 (c)). At higher concentration of PEOS (0.2 g/mL, Figure 99 (b)), the silica layer became even thicker, as judged by very large microcapsules retaining their spherical shape. Higher concentration of PEOS did not give a noticeable thicker silica shell (0.4 g/mL, Figure 99 (a)). Even if a trend is observed, the more PEOS the thicker the shell, even at the highest PEOS concentration the shell remains ultra-thin (< 10 nm). This is attributed to the high solubility of the hydrolyzed PEOS in the hexyl acetate preventing the formation of a hydrolyzed layer of PEOS at the oil/water interface. This validate our previous observations.

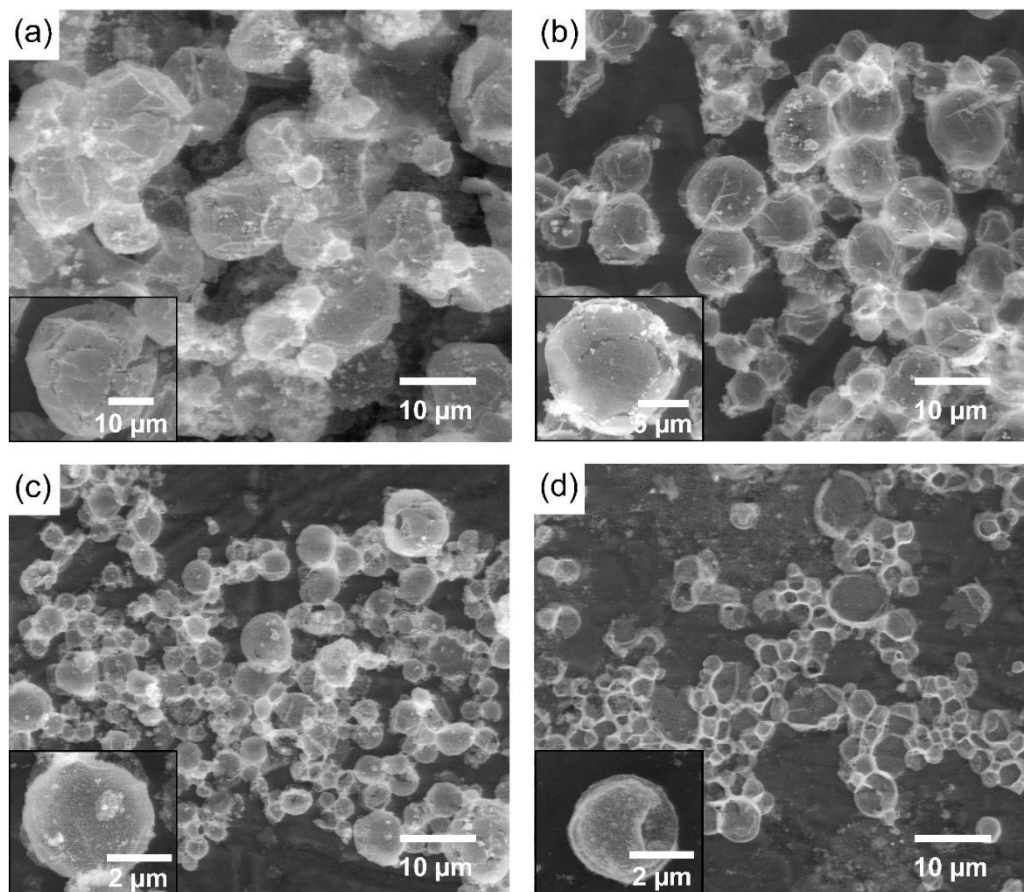


Figure 99: ESEM images of gold silica microcapsules obtained with hexyl acetate/hexadecane 50/50 by volume at (a) 0.4, (b) 0.2, (c) 0.05 and (d) 0.012 g/mL PEOS.

In this section, we have demonstrated the successful synthesis of gold-silica microcapsules. Our approach is based on the control of dense packings of Au NPs at the surface of emulsion droplets. By solidifying the interface of the emulsion with PEOS, we obtained solid capsules made of Au NPs embedded in a silica crust. As the Au NPs are densely packed at the surface of the capsules, they appear blue. Several oils were used to synthesize Au-Si microcapsules: toluene, hexadecane and hexadecane/hexyl acetate. Microcapsules with a thick silica shell are obtained from a toluene-in-water emulsion template at $[\text{PEOS}] \geq 0.2 \text{ g/mL}$. These microcapsules are resistant to drying. By tuning the concentration of PEOS and the polarity of the oil, we can control the thickness of the silica shell.

In the following part, we demonstrate the versatility of the silica microcapsules synthetic process using silver nanoparticles instead of gold nanoparticles.

3. The silver-silica microcapsules

3.1. Pickering emulsion formation

Based on the results presented in section 2 we know that three conditions have to be fulfilled in order to form Pickering emulsions highly covered by NPs. First, a high concentration of NPs is required. Second, the NPs should be partially wet by the oil and the water phase. Third, the NPs must have a low surface charge. Au NPs partly capped with PVP-DADMAN were successfully adsorbed on oil droplets by controlling their charges.

We challenged our understanding of the Pickering emulsions formation acquired working with Au NPs by trying to repeat the process with another type of nanoparticles. We chose silver nanoparticles for their very interesting optical, antibacterial and catalytic properties.

The synthetic process of silver nanoparticles (Ag NPs) explained below is similar to the fabrication process of Au NPs. It is a large-scale one-step synthesis leading to highly concentrated dispersions of silver nanoparticles. As presented in Chapter 1, section 3.2, PVP is known to be a good capping agent for silver nanoparticles³⁶. Instead of PVP, PVP-DADMAN was used in the synthesis of Ag NPs.

Silver nanoparticles synthesis: The Ag NPs used in this procedure are synthesized by reduction of AgNO₃ with ascorbic acid. A solution of $5.7 \cdot 10^{-6}$ M PVP-DADMAN and $5 \cdot 10^{-3}$ M of ascorbic acid mixed with 0.17 mL of sodium hydroxide (0.02 M) is brought to boil. Then, 0.53 mL of AgNO₃ (1.2 M) is added. The solution is protected from light by aluminum foil and stirred for 1 h at 95°C. After synthesis, the Ag NPs are left to rest for one day to remove the biggest nanoparticles. The remainder of the dispersion is centrifuged and concentrated into a 5 mL solution.

The obtained Ag NPs are polydisperse as shown by the TEM image in Figure 100 (a). The larger NPs on the image are nanoparticles that fused during electron microscopy analysis. The mean size of the Ag NPs, d , is estimated from the position of the maximum and the bandwidth of the plasmon peak of the dispersion of Ag NPs¹⁴⁷. We find $d = 58$ nm. Ag NPs appear to be uncharged (ζ potential ~ 0 mV) and well dispersed in water at all pH showing a sharp plasmon peak ($\lambda_{max} \sim 425$ nm) and a yellow color as shown in the two pictures of Figure 100 (b). This prove that the Ag NPs are sterically stabilized by the PVP-DADMAN and not electrostatically stabilized by the ascorbic acid, chemicals both present during the synthesis of the nanoparticles. This result is consistent with the literature referencing to Ag NPs capped by PVP³⁶ but contrast with what is observed with Au NPs. In the case of Au NPs, the nanoparticles are charged and therefore electrostatically stabilized.

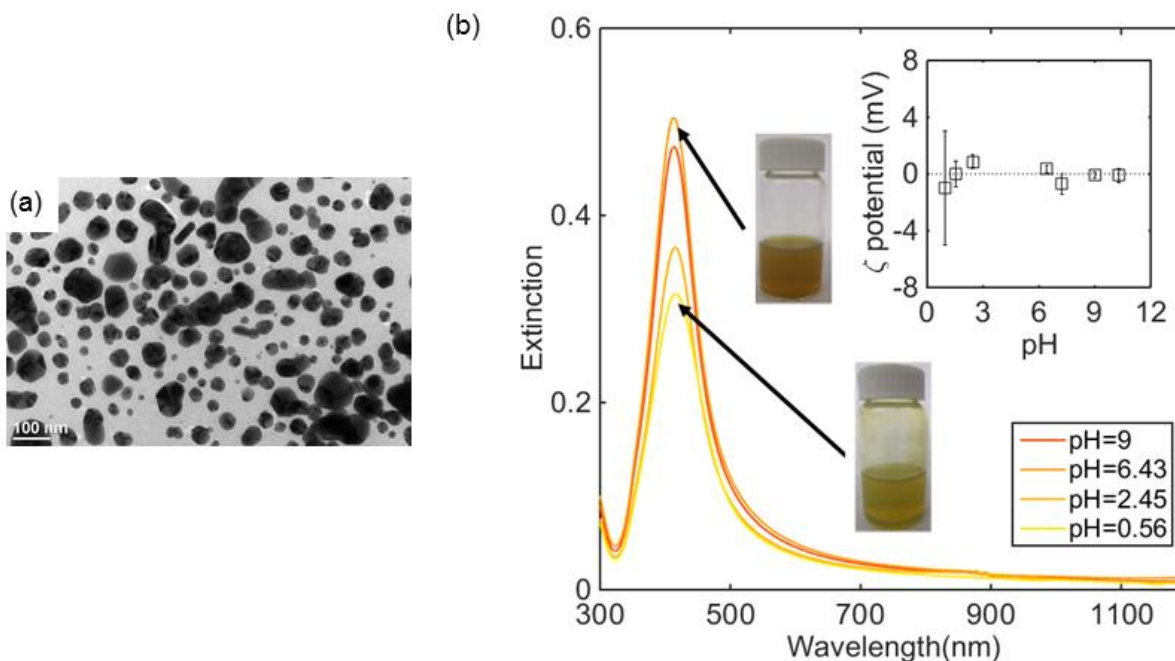


Figure 100: (a) TEM image of typical Ag NPs. (b) Plasmonic response of Ag NPs solutions as a function of pH. The two pictures respectively show dispersed solution of Ag NPs of the same concentration at pH = 9 and pH = 0.56. Inset: Zeta potential of the Ag NPs as a function of the pH.

3.2.Synthesis of Ag-Si microcapsules

Silver silica microcapsules are synthesized from Ag NPs stabilized oil-in-water emulsion. In this study, only the toluene is used as the oil phase because it led to the thickest shell among the solvents we have tested to form gold-silica microcapsules. We have previously demonstrated that Ag NPs have a very low surface charge, which does not depend on pH. The Ag NPs can therefore adsorb at the interface oil/water at any pH. To get comparable results, we synthesized silver-silica microcapsules at the same pH as the one set for the synthesis of gold-silica microcapsules (pH ~ 1). The obtained Pickering emulsion imaged in Figure 101 (a) has a yellow color. In contrast to the gold silica microcapsules, after a few hours we do not observe a color change of the emulsion. After silanization of the PEOS at the interface, silver-silica yellow microcapsules are obtained (Figure 101 (b)). Electron microscopy images in Figure 101 (c) and (d) respectively show the typical aspect of the silver silica microcapsules and the Ag NPs embedded in the silica shell. We notice that the Ag NPs are not as closely packed at the surface of the microcapsules as the Au NPs are. This observation explains the absence of plasmonic coupling between the Ag NPs and the yellow color of the silver-silica microcapsules. Silver nanoparticles very close to each other absorb light around 500 nm and therefore look red^{21,22}. In section 3.1 we have seen that the silver particles are capped by PVP-DADMAN. This polymer prevents the Ag NPs from getting too close to each other. Following our method of nanoparticle synthesis, we have intended to synthesize Ag NPs

with a smaller PVP ($M_w = 10\text{k g/mol}$) to see if we could reduce the interparticle distance on the microcapsule and decrease the spacing between the Ag NPs. The Ag NPs obtained with a shorter PVP were strongly aggregated in solution and no Ag NPs stabilized emulsions could be obtained using these nanoparticles. It seems that our longer PVP-DADMAN plays also an important role in stabilizing Ag NPs during their synthesis.

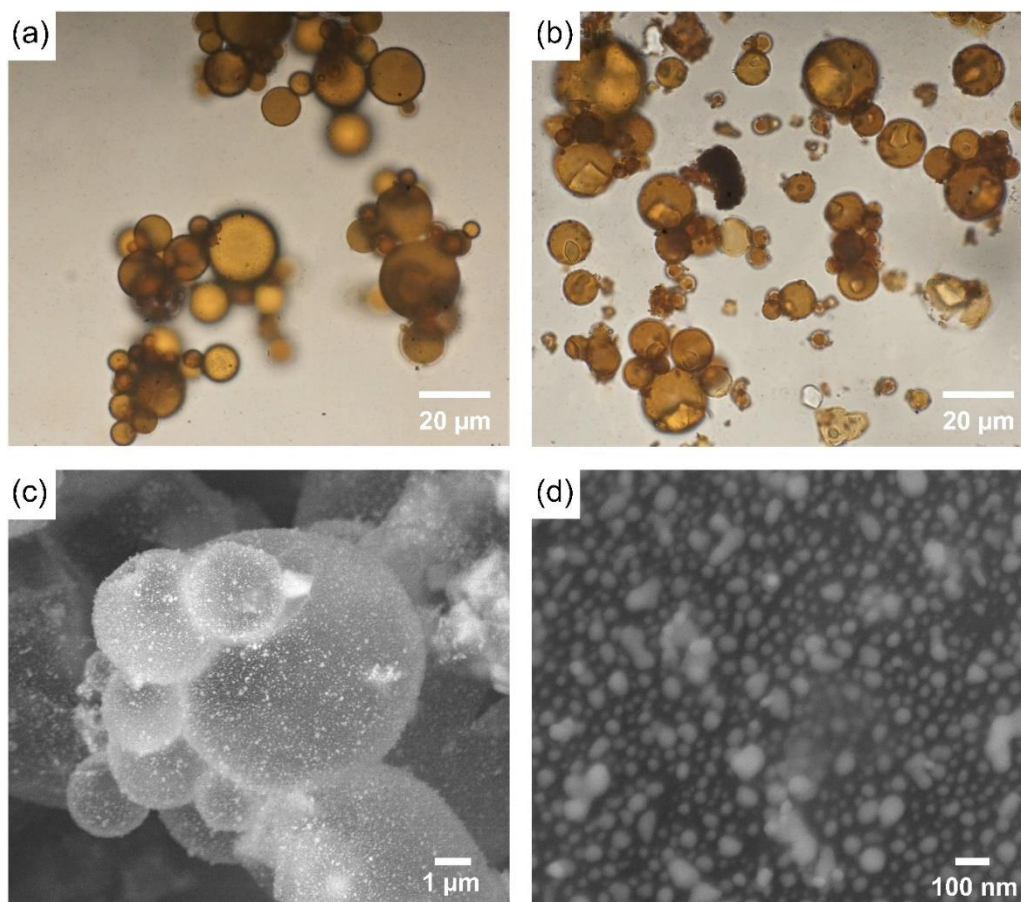


Figure 101: Optical images of (a) the Ag NPs stabilized oil-in-water emulsion, (b) the silver-silica microcapsules, (c-d) SEM images of (c) silver-silica microcapsules and (d) Ag NPs embedded in silica shell. Toluene is the oil phase.

The dispersion of Ag NPs was “washed” with water to remove some of the PVP-DADMAN capping the Ag NPs. The optical spectra and the ζ potential of the “washed” Ag NPs as a function of the pH is shown in Figure 102 (a). The maximum of the plasmon peak remains at the same position for all pH ($\lambda_{max} \sim 425\text{ nm}$). The ζ potential as a function of the pH show that the Ag NPs are uncharged at all pH (ζ potential $\sim 0\text{ mV}$). These results indicate that the polymer layer was not removed from the Ag NPs. The synthesis of Ag-Si microcapsules using the “washed” Ag NPs give yellow microcapsules indicating that the Ag NPs are indeed kept apart due to their capping layer.

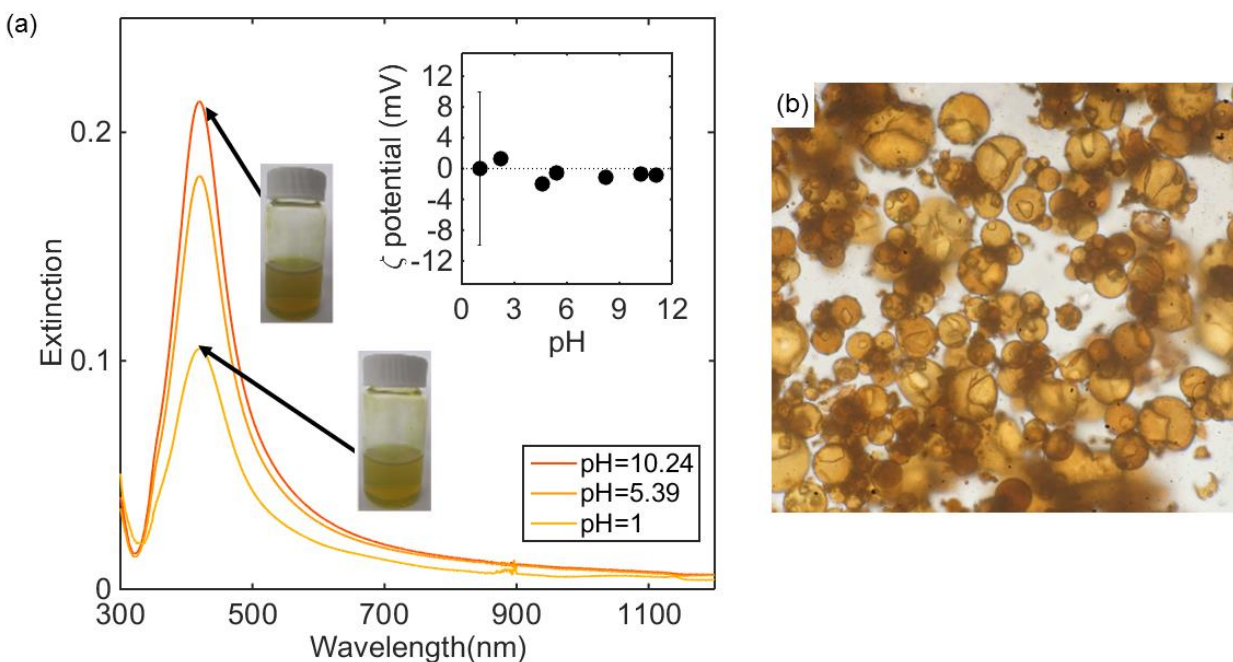


Figure 102: (a) Plasmonic response of “washed” Ag NPs solutions as a function of pH. The two pictures respectively show dispersed solution of Ag NPs of the same concentration at pH = 10.2 and pH = 1. Inset: Zeta potential of the Ag NPs as a function of the pH. (b) Ag-Si microcapsules synthesized with “washed” Ag NPs.

So far, based on our results, we have demonstrated that our method can be used to make silica microcapsules with either Au or Ag NPs embedded in the silica shell. Depending on the type of nanoparticles chosen and on the packing of the nanoparticles, microcapsules with different color can be obtained: pink or blue with Au NPs and yellow with Ag NPs. In the next section, we demonstrate that silica microcapsules bearing gold and silver nanoparticles can be synthesized.

4. The gold silver silica microcapsules

To show, as a proof of concept, that microcapsules can potentially cumulate several functionalities, we fabricated microcapsules bearing two different types of nanoparticles.

Mixtures of Au and Ag NPs at different ratios were prepared. Two different nanoparticles Au NPs/Ag NPs ratios were tested: 50/50 and 75/25 by weight %. The microcapsules are then synthesized using a water phase containing both types of NPs at these ratios. The optical microscope and SEM images corresponding to these experiments are presented in Figure 103. Depending on the ratio of Au NPs to Ag NPs, microcapsules of different colors are obtained as seen in Figure 103 (a) and (b). At the 50/50 ratio, the microcapsules are pink as seen in Figure

103 (a). At the 75/25 ratio, the microcapsules are purple as shown in Figure 103 (b). In both cases, spherical hollow silica microcapsules with closely packed nanoparticles embedded in a silica shell were obtained as depicted in Figure 103 (c) and (d). This experiment demonstrate that the optical response of the silica microcapsules can be finely tuned by changing the ratio between the Au and Ag NPs. It also shows that multifunctional microcapsules can be synthesized.

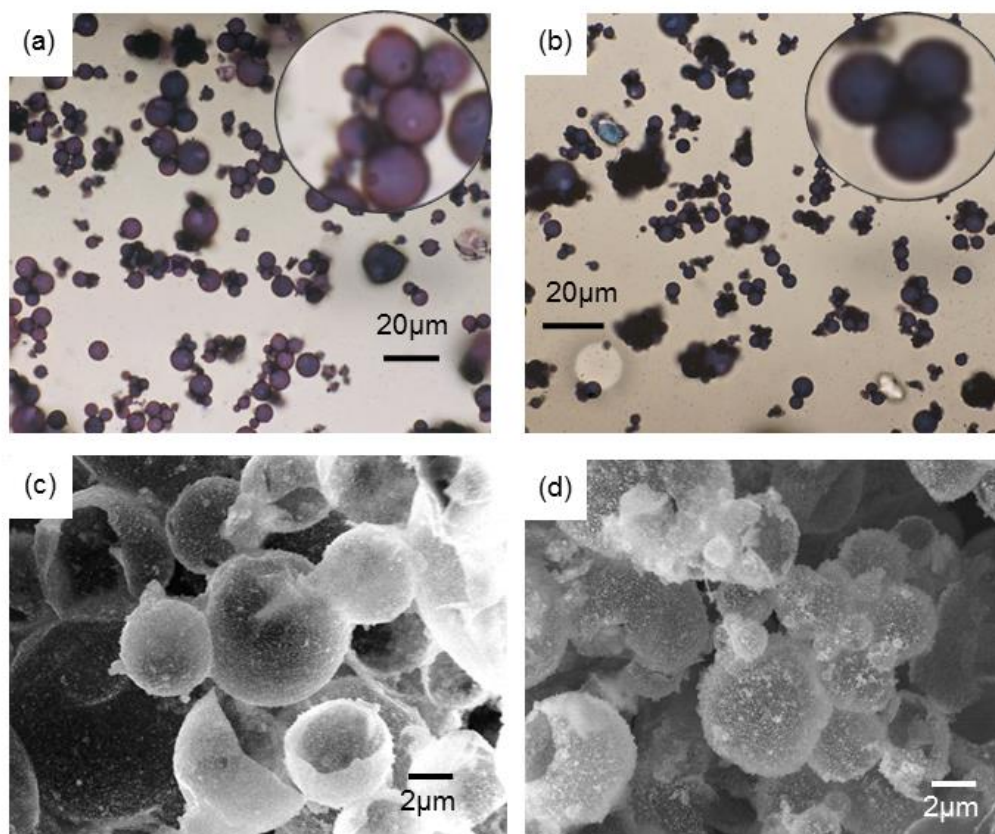


Figure 103: (a-b) Optical microscope images of gold silver silica microcapsules with (a) Au NPs/Ag NPs 50/50 wt/wt, (b) Au NPs/Ag NPs 75/25 wt/wt. (c-d) SEM images of gold silver silica microcapsules with (c) Au NPs/Ag NPs 50/50 wt/wt, (d) Au NPs/Ag NPs 75/25 wt/wt.

At this point of this chapter, we have shown that we can tune the type and the respective number of NPs in a capsule. We have demonstrated that gold-silica microcapsules, silver-silica microcapsules and gold-silver silica microcapsules can be engineered. Plasmon coupling between closely packed Au NPs is observed giving a blue color to the Au-Si microcapsules. Plasmon coupling is not observed in the case of the Ag-Si microcapsules due to the NPs capping layer preventing them from getting close together. The optical properties and color of the microcapsules can be finely adjusted by the ratio gold/silver NPs used during the microcapsules preparation. In addition to the optical response of the microcapsules, another feature that could be valuable to tune is the mechanical properties of the shell. So far, we have synthesized hard, fragile silica crust. It would be however very interesting to tune this property by making elastic soft shells. In the following section, we report the fabrication of polymer microcapsules.

5. The gold acrylate microcapsules

5.1. Polymerization of acrylate at the oil/water interface

The technique of formation of a polymer shell at the oil/water droplet interface is called suspension polymerization. In this technique, the polymeric chains are formed by free radical polymerization¹⁴⁸. The mechanism of free radical polymerization of methyl methacrylate, MMA, is presented in Figure 104. The polymerization occurs following three main steps. First, the monomers require an initiator such as Azobisisobutyronitrile (AIBN) to start the polymerization reaction. When heated, AIBN produces a free radical that, added to a monomer, starts the formation of one polymer chain (initiation step). Then, monomers are consecutively covalently linked of at the reactive end of a growing chain (propagation step). The last step consists in the formation of “dead chains” (chains that cannot react anymore) (termination step).

For thermal initiators such as AIBN, the decomposition rates are normally expressed in terms of their “half-life”. The half-life time is the time necessary to decompose one-half of the initiator originally present. The half-life time depends on the temperature. Therefore, temperature is an important parameter to control during polymerization so that free radicals are continuously formed during polymerization. AIBN presents a 10-hour half-life temperature of 65 °C¹⁴⁸, meaning that at 65°C, 50 % of the AIBN is consumed in 10 hours.

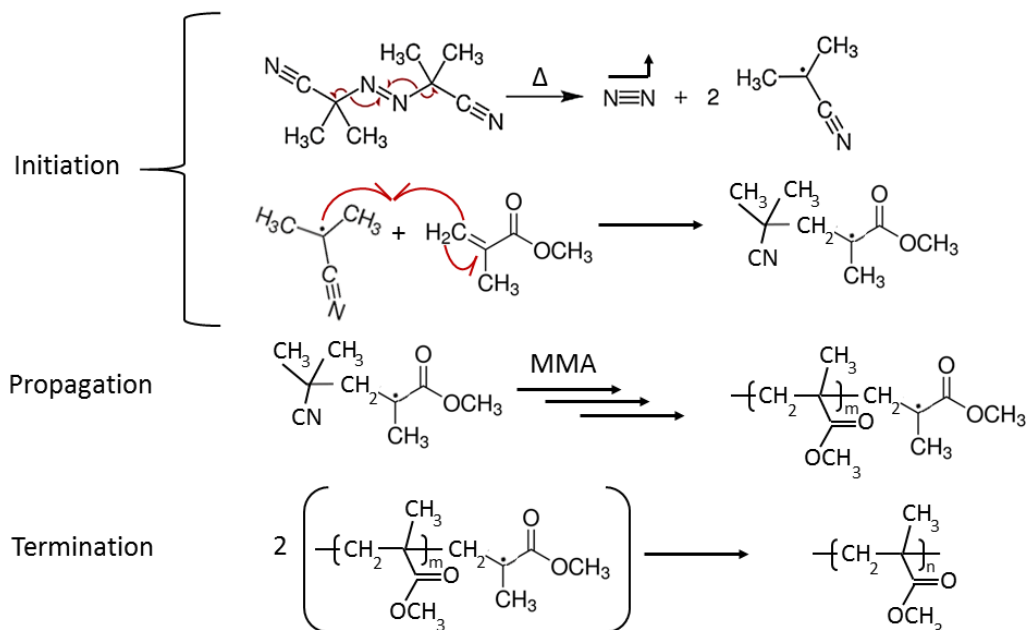


Figure 104: Free radical polymerization mechanism of PMMA.

In suspension polymerization, the shell formation starts at the water-oil droplet interface¹⁴⁸. As the polymerization reaction proceeds, the monomers are consumed and transferred from the oil phase to the interface, increasing the shell thickness. In the literature, we found different explanations to this phenomenon. In some cases, the formation of a polymer shell at the oil/water interface is justified by polarity arguments¹⁴⁸. When the polarities of the polymer and of the oil droplets are different, the polymer migrates from the inside of the droplets towards the interface. In other cases, the formation of a core/shell morphology is explained in terms of surface tensions. During suspension polymerization, an oil/water interface is replaced by a water/polymer interface and by an oil/polymer interface. The formation of a hollow capsules is favored when the sum of the interfacial tensions of these two new interfaces (interfacial tensions of the water/polymer interface and of the oil/polymer interface) is lower than the interfacial tension of the oil/water interface^{149,150}.

5.2. Synthesis of the gold-acrylate microcapsules

Au-acrylate microcapsules are obtained from toluene-in-water emulsions. We used three different monomers in the fabrication of Au-Si microcapsules: methyl methacrylate (MMA), methacrylate (MA) and butyl acrylate (BA). We show here the microcapsules obtained with: MMA/BA (Figure 105 (a-c)) and MA/BA (Figure 105 (d-f)) at 50/50 by weight. The observations made during the syntheses of both types of microcapsules are very similar and will be jointly explain. First, the acrylate monomers ($[MMA] = 2.2 \text{ M}$, $[MA] = 2.6 \text{ M}$, $[BA] = 1.72 \text{ M}$) and the polymerization initiator, AIBN (0.12 M) are mixed in toluene (0.5 mL). Then, the oil phase is emulsified in the water phase containing the nanoparticles ($[Au^0] = 0.02 \text{ M}$, 4 mL). An oil-in-water emulsion stabilized by the gold nanoparticles is obtained. We have previously shown that at $\text{pH} < 4$, the electrostatic repulsions between the Au NPs are suppressed and the particles adsorb at the oil/water interface. The synthesis of Au-acrylate microcapsules was carried out at $\text{pH} \sim 1$ ($[\text{HCl}] = 0.1 \text{ M}$) to trigger the adsorption of the Au NPs on the droplets. Immediately after sonication, the Au NPs stabilized emulsions are pink as imaged in Figure 105 (a) and (d). The polymerization of the acrylate monomers is initiated by increasing the temperature to 60°C . As the shell thickens, more Au NPs adsorb at the interface. After polymerization, the obtained microcapsules are blue as seen in Figure 105 (b) and (e). The microcapsules are spherical with dimensions ranging from 10 to $40 \mu\text{m}$ as illustrated in Figure 105 (c) and (f). SEM images in the insets of Figure 105 (c) and (f) show that the Au NPs are embedded in the polymer shell and form a monolayer of densely packed particles. The acrylate shell thickness was measured from SEM images and ranged between 80 and 100 nm. Under high vacuum, the acrylate capsules keep their spherical shape (Figure 105 (f)).

Due to the very harsh acidic conditions (HCl, pH ~1) during the synthesis of the acrylate shell. The ester groups of the poly(acrylate) can be hydrolyzed and form carboxylic acid groups^{151,152}. We have not yet quantified how many acids groups are being formed during the fabrication of Au-acrylate microcapsules but this analysis will be carried out in the future.

We have shown that we can synthesize soft polymeric acrylate microcapsules using methyl methacrylate, methacrylate and butyl acrylate monomers mixed at different ratios. We have shown two types of monomers mixtures but other acrylate monomers can be used. The glass transition temperature (T_g) of acrylate polymers and therefore of acrylate microcapsules depends on the types and ratio of acrylate monomers used as building block¹⁵³. Thus, the mechanical and chemical properties of the microcapsules can be finely tuned by choosing the right type of monomers or mixtures of monomers.

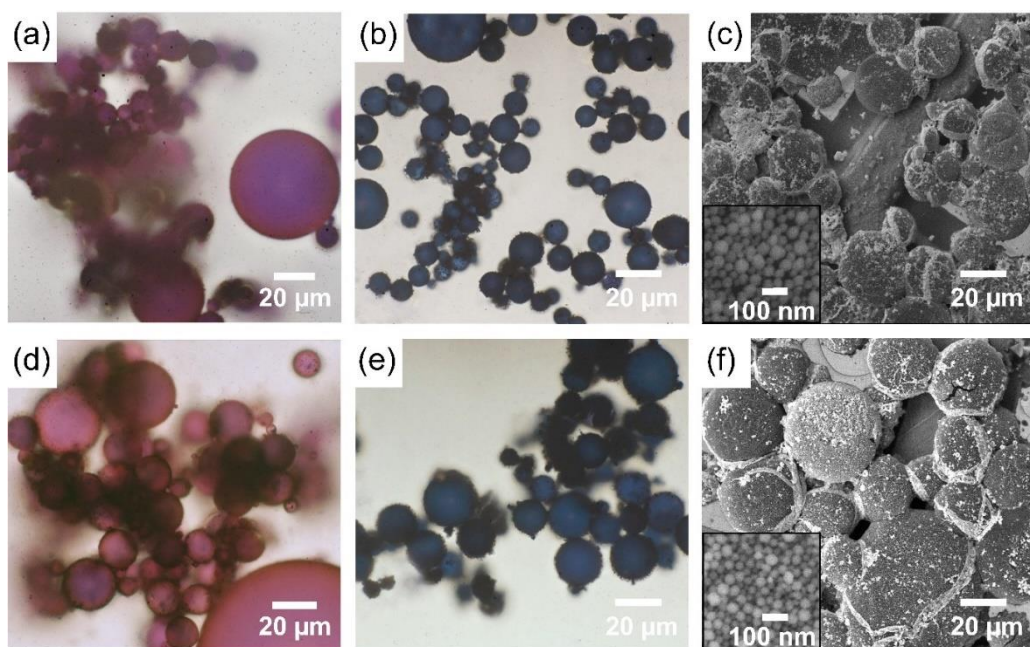


Figure 105: (a-c) Formation of gold methyl methacrylate-co-butyl acrylate microcapsules: optical images of (a) Au NPs stabilized oil-in-water emulsion, (b) gold methyl methacrylate-co-butyl acrylate microcapsules, (c) SEM image of gold methyl methacrylate-co-butyl acrylate microcapsules, inset shows the nanoparticles embedded in the polymer shell. (d-e) Formation of gold methacrylate-co-butyl acrylate microcapsules: optical images of (a) Au NPs stabilized oil-in-water emulsion, (b) gold methacrylate-co-butyl acrylate microcapsules; (c) SEM image of gold methacrylate-co-butyl acrylate microcapsules, inset shows the nanoparticles embedded in the polymer shell.

6. Conclusion

In conclusion, we have demonstrated the successful synthesis of hybrid NPs-polymer microcapsules. Our approach is based on controlled packing of NPs at the surface of emulsion droplets by tuning the charge and wettability of the metal nanoparticles. By solidifying the interface with PEOS or acrylate monomers, we obtained capsules made of NPs embedded in a hard silica crust or in a soft polyacrylate shell. We showed that Au NPs can be highly packed at the surface of the emulsion droplets. The close packed structure of the microcapsules adsorbs light at high wavelength due to the plasmon coupling between the Au NPs. If the polymer capping is too strong as it is the case of Ag NPs, the nanoparticles are not close enough on the microcapsules to observe a change of color due to plasmon coupling. The color of the silica microcapsules can be tuned from yellow to blue by mixing Au and Ag NPs in different ratios.

We believe that this full tunability of the hybrid microcapsules shell and solid particles widens the horizons in the design of new multi-functional microcapsules with properties arising from the individual or the combination of the properties of each one of its building blocks. In the Chapter 4, we show two applications based on the optical and mechanical properties of the Au-Si and Au-acrylate microcapsules.

Chapter 4: Plasmonic microcapsules as optical pH and strain sensors

TABLE OF CONTENTS

1. Introduction.....	114
2. Optical strain sensors	115
2.1. Current technologies.....	115
2.2. The gold-silica microcapsules	120
2.2.1. The gold silica microcapsules synthesis.....	120
2.2.2. Fabrication of polymer film doped with gold-silica microcapsules.....	121
2.2.3. Stretching test.....	122
2.2.4. Impact test	127
2.2.5. Perforation test	128
2.2.6. Au-Si microcapsules film aging.....	128
2.3. The gold-acrylate microcapsules	130
2.3.1. Gold-acrylate microcapsules synthesis	130
2.3.2. Fabrication of elastic films doped with elastic microcapsules.....	131
2.3.3. Stretching test.....	132
2.4. Plasmon-based mechanochromic microcapsules vs other strain sensors	133
3. Optical pH sensors	134
3.1. Current technologies.....	134
3.2. pH responsive gold-acrylate microcapsules	138
3.2.1. pH sensitivity of Poly(acrylic acid).....	138
3.2.2. Gold-acrylates microcapsules response to pH	140
3.2.3. Reversibility of the color change	145
3.2.4. Color as a function of pH	146
3.3. pH responsive microcapsules vs other pH sensors.....	149
4. Conclusion	150

1. Introduction

Recently, several studies have reported that gold nanoparticles can be used as optical sensors. Indeed, these nanoparticles absorb light in the visible range of the electromagnetic spectrum and color the media in which they are dispersed. Moreover, as we saw in chapter 1, they absorb light at a wavelength which depends on their interparticle distance. Pregnancy tests are one of the most well-known examples of such technology. This test is based on a color change due to the aggregation of Au NPs. A positive test is red when the nanoparticles are stabilized by human chorionic gonadotropin (hCG), a hormone produced by the embryo after implantation. A negative test turns blue upon the nanoparticles aggregation in the absence of hCG¹⁵⁴. Similarly, Ali *et al.*¹⁵⁵ have developed an analytical method based on gold nanoparticles enabling the detection of pork adulteration into chicken and beef halal preparations. The initial red gold nanoparticles dispersion turns blue upon aggregation of the particles by the presence of pork DNA. Several other examples of sensors based on the aggregation of gold nanoparticles exist. The aggregation of gold nanoparticles is triggered by external stimuli such as strain, a change in pH¹⁵⁶, temperature^{157,158}, hydrogen bond¹⁵⁹, or due to charges screening (see Figure 106).

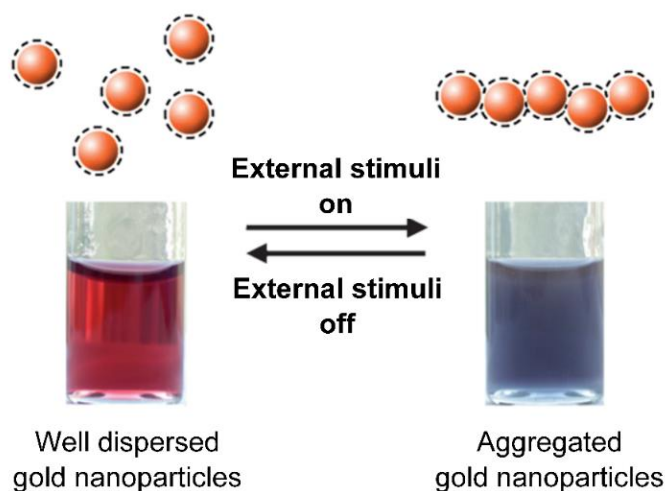


Figure 106: Aggregation and redispersion of gold nanoparticles by external stimuli.

In this chapter, we focus on two types of optical sensing techniques. The first type allows the detection of mechanical deformation, the second type allows the detection of pH change. We start by presenting the most common optical mechano-sensing and pH-sensing technologies. For each application, we explain why an alternative solution using plasmonic nanoparticles is useful. Finally, based on the results established in chapter 3, we synthesize Au-Si and Au-acrylate microcapsules and we demonstrate that they can be used as optical sensors to detect mechanical deformations in polymeric materials and local changes in pH.

2. Optical strain sensors

2.1. Current technologies

Polymeric materials are commonly used in daily life. They include plastics, composites and coatings. Depending on their applications, these materials may be subjected to high stresses which can lead to deformations, strains or cracks^{160,161,162}. In a wide variety of applications, finding an efficient method to detect and measure internal strains within polymeric materials is very important. For instance, in metals coated by polymers, detecting cracks responsible for the starting point of corrosion of the substrate would help providing a better protection to the substrate. Also, cracks entail the diminution of the mechanical performances of materials therefore their detection is important to be able to insure consistent performances over time. Moreover, the detection of damages in materials at a very early stage raises the possibility to repair the material before an irreversible breakage occurs. Knowing how, where and to which extent polymeric materials are damaged can help increasing the life span of plastics and composites.

Finding methods that give direct information on local stress is a significant industrial and technological challenge. Most of the methods already used to detect internal strain within polymeric materials are usually invasive or destructive and do not allow a real-time in-situ analysis^{163,164}. A direct and efficient method consists in incorporating in a material molecules (dyes), which change colors as stresses are applied on the material. This type of system has been developed since 1986 and already encompasses many examples. For instance, small mechanically active dyes crosslinked on a polymer backbone have shown color changes under mechanical deformation^{165,166,167}. The dissociation of dyes' inclusions under mechanical stress leading to modifications of the photoluminescent properties of the dyes has permitted to detect deformations^{168,169,170}. Other example includes fluorescent dyes that have been entrapped within hollow fibers¹⁷¹ or encapsulated^{172,173,174} in polymer shells to improve the detection of damaged areas in plastics. In the following paragraphs, we will present more in detail some of the most commonly reported examples of mechanochromic materials as well as their mechanisms of action.

One of the existing technologies permitting the visual detection of material damages is the incorporation of microencapsulated dyes within polymeric materials as illustrated in Figure 107. Vidinejevs *et al.*^{175,176}, Li *et al.*¹⁷² and Odom *et al.*¹⁷³ have worked on a similar approach. Here we present the method developed by Li *et al.* Microcapsules entrapping a yellow dye, the 2',7'-dichlorofluorescein (DCF), are dispersed in an epoxy-amine resin (Figure 107 (a) and (b)). Under a stress such as a compression or a wearing, the microcapsules brake and release their content. When the DCF enters in contact with the amine groups of the resin, its pH changes and its originally acid form (yellow) turns basic (orange) and precipitate. The release of the DCF allows the detection of the deformation by outputting a sharp color change (Figure 107 (c)). This method enables the detection of cracks as small as 10 microns (size of the small capsules) but requires that the inside of the capsules reacts with the polymer matrix in which they are embedded.

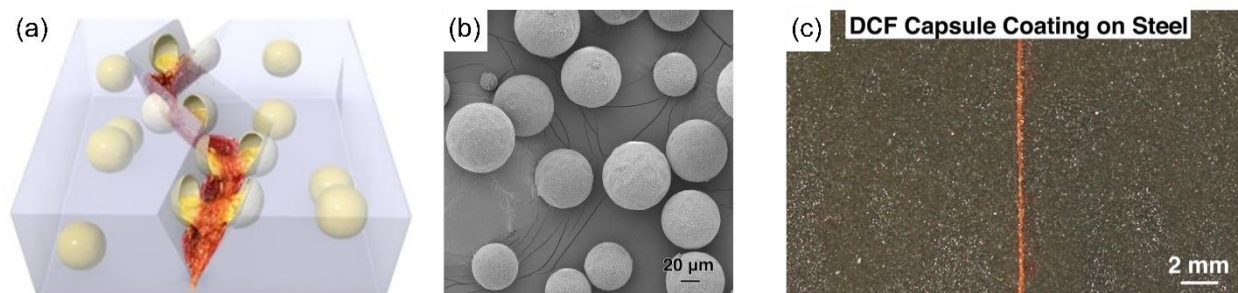


Figure 107: (a) Schematic representation of DCF- microcapsules embedded in a coating. (b) SEM image of the DCF-microcapsules. (c) Optical image of epoxy-amine resin doped with DCF-microcapsules coated on an iron substrate.¹⁷²

Spiropyran is one of the most well-known mechanochromic molecules^{165,166}. Upon mechanical stress, this molecule isomerizes through the opening of one of its backbone rings. This change of conformation entails a change of color of the molecules and therefore a change of color of the polymeric material to which spiropyran is covalently linked. It is important to notice that the opening of the C-O bond occurs only if the spiropyran is attached to the polymer via the 5 and 8 positions (spiropyran 5,8) as shown in Figure 108 (a). Davis *et al.*¹⁶⁵ have demonstrated that the increase of the distance between the junction points spiropyran-polymer (SP-polymer) enables the cleavage of the C-O bond. Indeed, if the spiropyran is only attached to the polymer at the junction point 8, no cleavage is observed. Figure 108 (b) and (c) shows two examples of mechanochromic polymers doped with spiropyran 5,8. The first system is an elastomer film made of polymethylacrylate (PMA). The second system shows beads of polymethylmethacrylate (PMMA). In the two cases, when the polymers undergo mechanical stress, stretching in the first example and compression in the second case, a change of color is observed. The intensity of the color change increases with the mechanical deformation. A contrario, if the spiropyran is only substituted in the 8 position, no color change is observed during deformation of the film or of the beads. This observation validates the work of Davis *et al.* In addition, the coloration of the polymer appears way before the final breakage of the material when the applied stress becomes too important. This observation highlights the potential of the spiropyran molecules for the detection and mapping of mechanical strains.

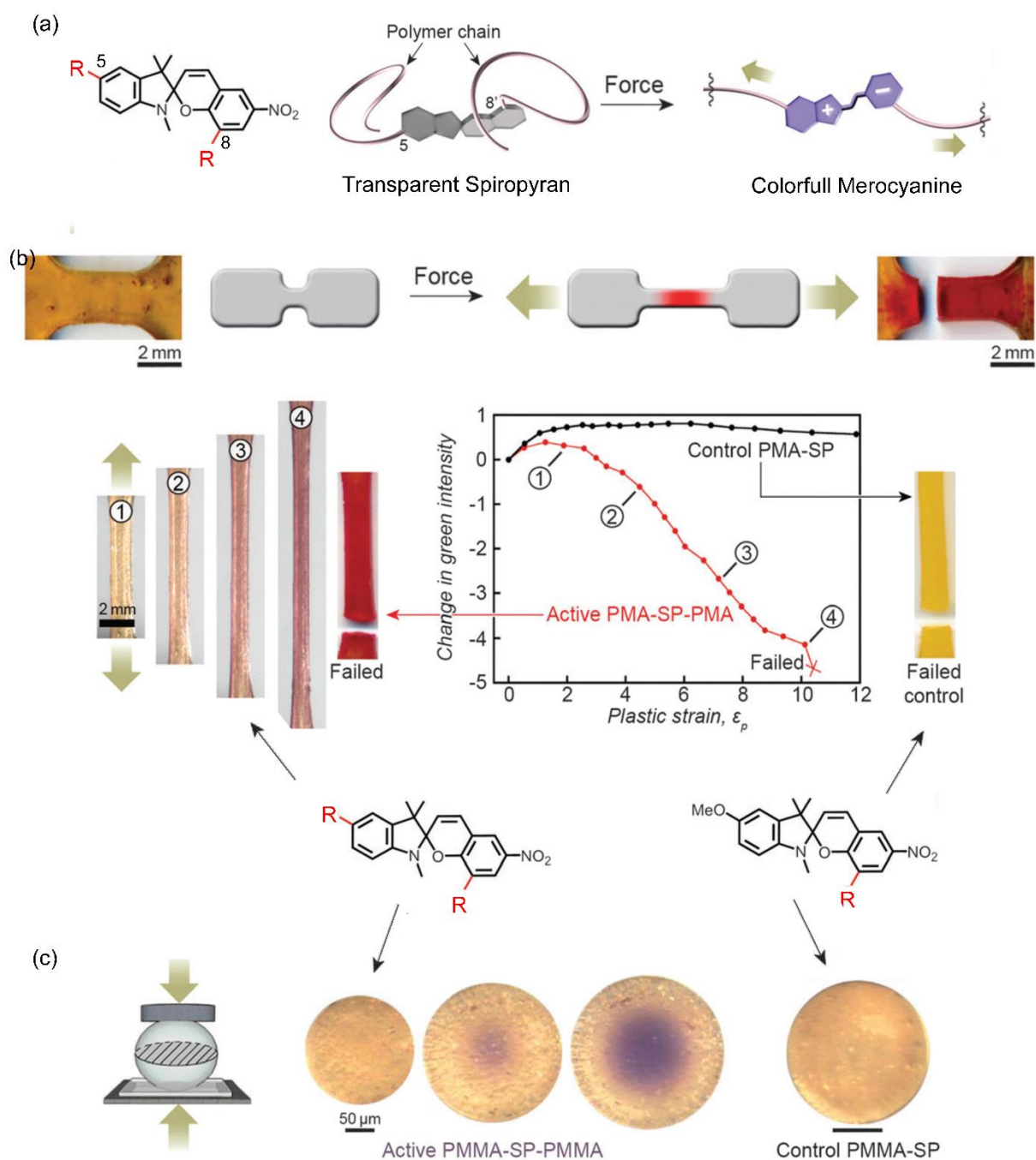


Figure 108: Mechanochromic spiropyran. (a) Isomerization of the acrylate-spiropyran-acrylate co-polymer under tensile stress. (b) Color change of a PMA-Spiropyran 5,8-PMA co-polymer film under stretching. The negative control is a PMA-Spiropyran 8 co-polymer film (c) Colorimetric response of PMMA-Spiropyran 5,8-PMMA co-polymer beads under compression. Negative control is a PMMA-Spiropyran 8 co-polymer bead^{165,166}.

Fluorescent emission spectroscopy is one of the most promising techniques for tracking mechanical deformations within a polymeric material. This non-invasive and non-destructive technique allows in-situ measurements of deformations by recording the optical response of fluorescent molecules that are sensitive to their environment. The most impressive results were obtained by the group of Weder^{177,178,169,167}.

Fluorescent molecules (fluorophores) simply dispersed in a polymer matrix can form complexes called excimers^{179,180}. The excimers are obtained when a fluorophore in an excited state complexes with a fluorophore in a ground state. The excimers in an excited state dissociate into monomers of ground state energy while emitting fluorescent radiation. This excimer fluorescence has a higher wavelength than the wavelength at which it gets excited, and has a different fluorescence wavelength than the emission wavelength of its individual excited monomers. When a polymer film containing excimers is deformed, the excimers complexes are dissociated and the fluorescence of the film is only due to the monomers. Therefore, the ratio of the excited excimer emission intensity to the excited monomer emission intensity can be related to the deformation of the material. The more a polymer film is deformed, the less excimers exist in the deformed areas and the more intense the emission due to monomers is. Figure 109 shows stretched polyethylene films containing fluorophores. The excimers fluorescence is mostly observed in the non-stretched areas whereas the monomers fluorescence is noticed within the stretched area. To be able to form excimers, the fluorophores have to aggregate in the material. Moreover, in order to see a strong excimers emission, a high concentration of excimers and therefore an important doping of the film with fluorophores is required. Crenshaw and Weder¹⁷⁸ have shown that low concentration in cyano-oligo(p-phenylene vinylene) in polyethylene film generally gives a monomer-induced fluorescence (at about 500 nm) whereas a higher concentration generally gives an excimer-induced fluorescence (at about 600 nm).

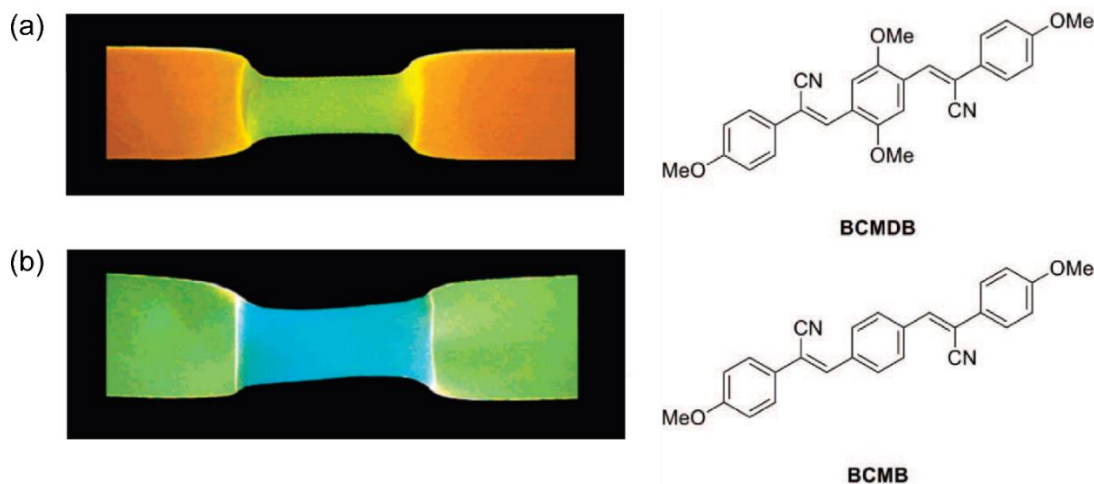


Figure 109: Images of polyethylene film under UV light (excitation wavelength = 365 nm) mixed with (a) 0.18 wt% of BCMDB, the green color corresponds to the monomer emission and the red color to the excimer emission and (b) 0.20 wt% of BCMB, the blue color corresponds to the monomer emission and the green color to the excimer emission¹⁷⁸.

Polymeric materials doped with dyes have demonstrated their strong potential for the detection of mechanical deformations. However, even if dyes are compatible with a large variety of polymers (plastics, elastics, rubbery, glassy...) their use has many downsides. Among the most commonly encountered drawbacks we can mention: the large-scale phase separation between the dye molecule and the polymer host¹⁷⁹, the temperature dependent fluorophore emission^{179,180} and, in some cases, the necessary crosslinking of the dyes with the host polymer matrix¹⁸¹.

In this chapter, we suggest an alternative to dyes permitting the detection of deformations in polymeric materials due to mechanical stresses (tensions, compressions, elongation, etc). We propose to use plasmonic particles instead of molecules.

Until now, very few studies reported the fabrication of plasmonic-based systems enabling the visual detection of mechanical deformations. Notwithstanding, we can cite the work of Han *et al.*¹⁸² who have designed in 2014, a colorimetric stress memory sensor based on disassembly of gold nanoparticle chains. Charged gold nanoparticles are assembled into chains by addition of salts and are embedded in polymer films. The more compressed the polymer film doped with gold nanoparticles, the larger the distance between the gold nanoparticles, and the redder the film (see Figure 110). In this example, the aggregated nanoparticles are metastable and external factors such as ionic strength or the temperature can break the aggregates and re-disperse the nanoparticles or lead to a much more severe aggregation (loss of the linear structure...) before their transfer into a polymer film.

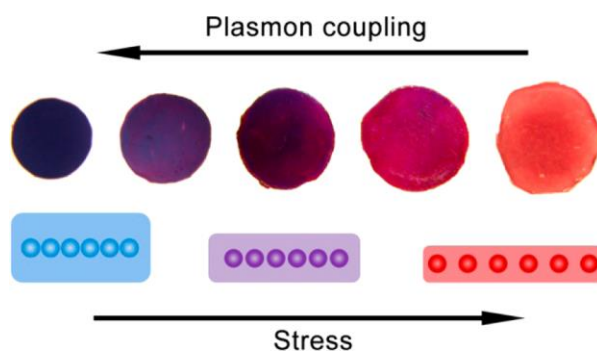


Figure 110: Polyvinylpyrrolidone-poly(ethylene glycol) film doped with gold nanoparticles chains as a function of the film compression¹⁸².

Along this manuscript, we have presented processes to assemble and lock the nanoparticles at the interface oil/water of an emulsion (formation of a shell, gelling of the internal emulsion phase...). Especially, in Chapter 3, we have shown the fabrication of several hybrid nanoparticle polymer microcapsules from Pickering emulsion templates. These microcapsules can be easily collected and further engineered. In sections 2.2 and 2.3 of this chapter, we show that these microcapsules can be utilized as optical sensors to detect mechanical deformations in polymeric materials. The results presented in this chapter were patented (RD_2017_004_US_PSP_2017).

2.2. The gold-silica microcapsules

In this section, we show that our gold-silica microcapsules can be used as optical sensor to detect different types of mechanical strains by outputting a color change. The Au-Si microcapsules are embedded in a polymer matrix further mechanically deformed. The results presented in this section were accepted for publication in the journal *Small* (Annex 2).

2.2.1. The gold silica microcapsules synthesis

The Au-Si microcapsules used in this section are synthesized by following the protocol described in Chapter 3. The synthesis parameters were adjusted to obtain Au-Si microcapsules with a close packed layer of Au NPs and with a silica shell thick enough to ensure a spherical shape upon drying. The first step consists in mixing an aqueous phase containing the Au NPs ($[Au^0] = 0.02 \text{ M}$), butanol (0.1 mL) and HCl (0.2 mL, pH ~ 1) with an oily toluene phase (1.2 mL) in which polyethoxyorthosilicate (PEOS, 0.2g) is dissolved. The two phases are then strongly agitated by sonication with a Brandson 3210 ultrasonic bath at 30°C for 15 minutes, forming an oil-in-water emulsion. By decreasing the electrostatic charges of the nanoparticles, they adsorb onto the oil droplets (see Chapter 3). Shortly after the sonication, the emulsion exhibits a strong pink color due to the adsorption of the AuNPs as seen in Figure 111 (a). The emulsion becomes blue after one day as shown in Figure 111 (b). This change of color proves that nanoparticles adsorb and get more and more densely packed at the interface as time goes on. The emulsion is then gently shaken mechanically for a few days to allow the formation of the silica shell by polymerization of the PEOS at the interface of the emulsion. The microcapsules were recovered, cleaned and concentrated by simple sedimentation.

Images of the microcapsules formed after 3 days are shown in Figure 111 (c-e). The color, shape and size of the microcapsules were analyzed by optical microscopy and SEM. The resulting microcapsules are spherical with dimensions ranging from several hundredths of nanometers to several tenths of micrometers (4 - 30 μm). As seen in Figure 111 (c), the microcapsules present a deep blue color which comes from a monolayer of densely packed gold nanoparticles on their surface as shown in Figure 111 (f). Under the high vacuum of the SEM, the gold silica capsules tend to buckle due to the thin silica shell. The silica shell thickness as measured from SEM images ranged between 30 and 60 nm.

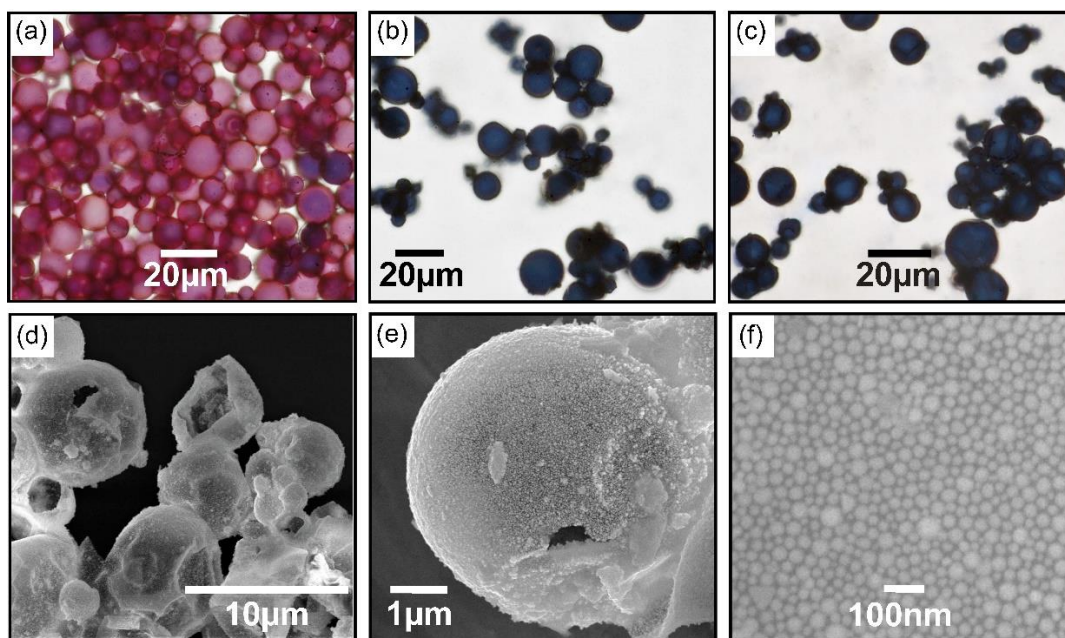


Figure 111: (a-b) Optical microscope images of typical emulsions at 0.02 M of gold at pH ~ 1 right after sonication and after one day respectively. (c) Optical microscope images of typical microcapsules after polymerization at 0.02 M of gold and pH ~ 1. (d-e) SEM images of dried microcapsules obtained at 0.02 M of gold and pH ~ 1. (f) SEM image of a typical microcapsule surface covered by Au NPs at 0.02 M of gold and pH ~ 1.

2.2.2. Fabrication of polymer film doped with gold-silica microcapsules

To test the chromatic properties of our gold-silica microcapsules under strain we embedded these capsules inside a polymer matrix made of PVA (polyvinyl alcohol) to which we applied different mechanical deformations.

The PVA films preparation follows this protocol: 20 g of a 10 wt% solution of PVA in water was prepared and degassed. Then the as previously synthesized microcapsules were concentrated in 1 g of water and dispersed in the PVA solution under gentle stirring to avoid the formation of air bubbles, which could make the final film inhomogenous and more fragile. The final polymer-microcapsules solution was left to dry at room temperature for several days.

During the drying step, the silica crust provides the blue microcapsules with enough rigidity to retain their spherical shape as seen in Figure 3b. Their intrinsic color conferred to the film a slight blue color as shown in Figure 112.

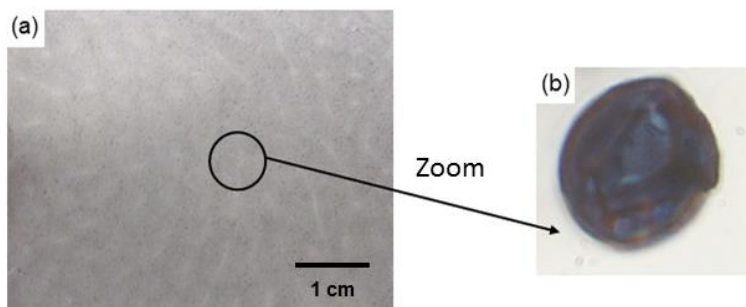


Figure 112: (a) Film doped with gold-silica microcapsules. (b) Zoom on one 20 μm microcapsules embedded in the polymer film.

2.2.3. Stretching test

After drying, a uni-axial stretching of the polymer film was then performed using a vise while heating the film above the glass transition as shown in Figure 113.

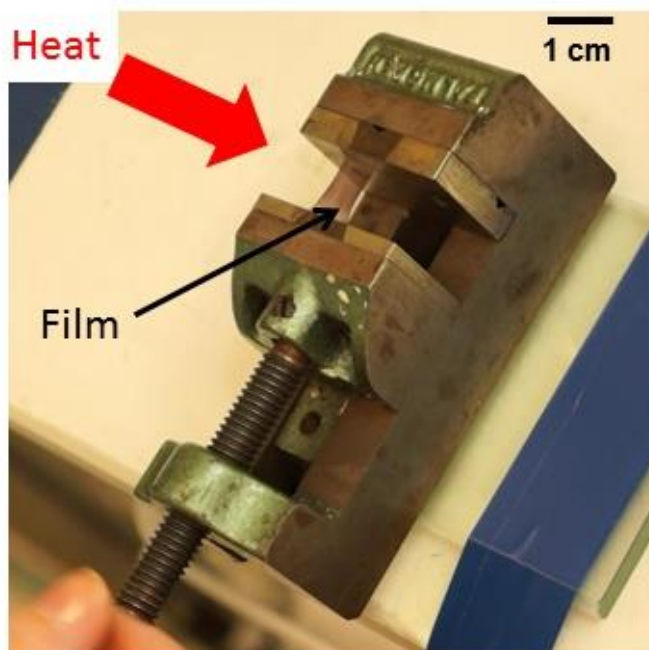


Figure 113: Film stretching.

A magnified view of the elongated polymer film shows pink stretched microcapsules as seen in Figure 114 (c). This change of color is noticeable by the naked eye and is attributed to the deformation of the spherical microcapsules into an ellipsoid-like shape. The mechanical deformation induces an increase of the interparticle distance, as schematically depicted in Figure 114 (d). During the anisotropic deformation, the distance between the Au NPs increases, thus entailing a color change.

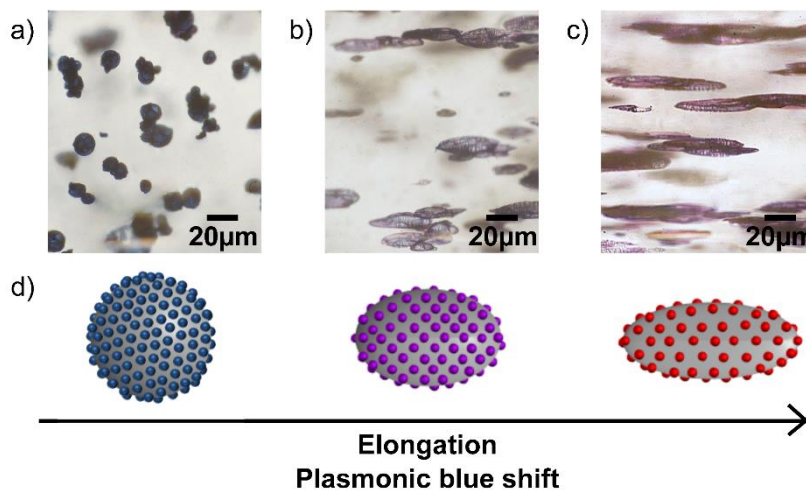


Figure 114: (a-c) Microcapsules dispersed in dried PVA film: (a) before strain, (b) during strain, (c) after strain. (d) Schematic representation of the microcapsules shape deformation and visible colors under one-dimensional mechanical stretching.

To support this observation, the film extinction curve was recorded by spectrophotometry for different film elongations. The experimental set-up is presented in Figure 115. The film pinched in the vise is placed in-between two optical fibers. A “background” extinction curve is measured and recorded on a PVA film which does not contain any Au-Si microcapsules.

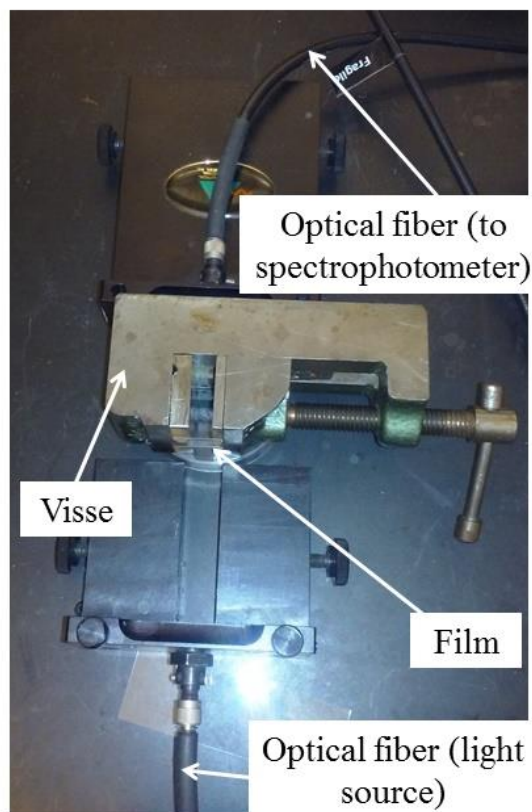


Figure 115: Extinction measurements set-up.

A typical extinction curve at small deformations of microcapsules results from two overlapping peaks. There is a first small plasmonic peak around 540 nm, indicated by a red arrow in the inset of Figure 116, which corresponds to single Au NPs and a second broad plasmonic peak at a higher wavelength. The second peak at a higher wavelength is broad because of the very large number of dipolar couplings between the randomly-placed Au NPs. As the microcapsules are stretched, the second peak's width decreases, its position shifts towards smaller wavelengths, and its amplitude decreases. The maximum of each extinction curve, λ_{max} , was measured by performing a crude first assessment of the position of the peak, followed by a more accurate measurement of the position of the maximum using a second-order polynomial fit around the maximum. Because the width of the second peak decreases as the particles are elongated, this procedure is fairly accurate at large deformations and less accurate at low deformations. λ_{max} was plotted as a function of the strain $\gamma = (L_f - L_0)/L_0$, where L_f is the length of the film after each stretching step and L_0 is the initial length of the film before mechanical deformation as seen in Figure 116. The error bars in Figure 116 reflect the difference in accuracy regarding the measurement of the position of λ_{max} . The λ_{max} - strain curve shows that for small strains ($\gamma < 0.3$), the film absorbs light in the red/infrared region ($\lambda_{max} \sim 850 - 900$ nm) of the visible spectrum, thus appearing blue. As the amplitude of the strains increases, the optical properties of the microcapsules embedded in the film

change and the maximum of the extinction curve is shifted towards the blue/green visible region of the spectrum ($\lambda_{max} \sim 540$ nm), thus the film appears pink. At very large deformations of the microcapsules, the second peak of the extinction curve becomes weak in amplitude compared to the first peak of single particles, and hard to measure as both peaks overlap. At that point, we consider λ_{max} to be the λ_{max} of single particles. This is the reason why there is a jump in the λ_{max} - strain curve in Figure 3e. This jump does not physically exist. λ_{max} reaches a plateau when the absorption of the stretched microcapsules ($\lambda_{max} \sim 540$ nm) is close to the absorption of the free Au NPs in solution ($\lambda_{max} = 527$ nm, as represented by the dashed line in Figure 116). The small difference in the absorption wavelength (~ 13 nm) is due to the silica shell surrounding the particles knowing to displace the absorbance maximum of gold towards slightly larger wavelengths¹⁸³. So far, we have demonstrated that the plasmon response of our films doped with Au-Si microcapsules can be shifted from high wavelength number to low wavelength number by an increase of the average Au NPs interparticle distance through uniaxial strain of the microcapsules.

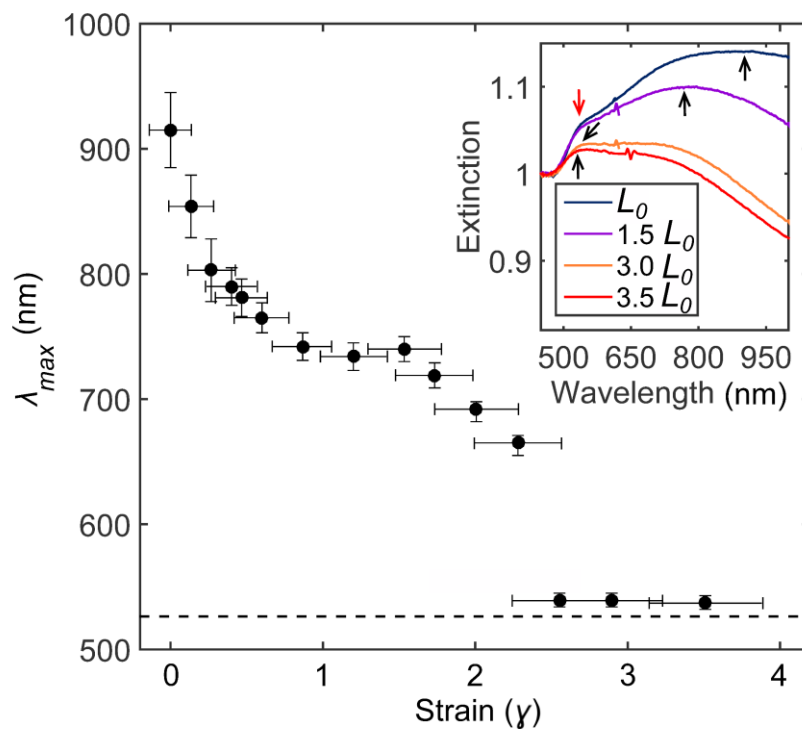


Figure 116: Position of the plasmonic peak maximum as the polymer is elongated. Dashed line corresponds to the wavelength of maximum extinction of the Au NPs in water. Inset: UV response as a function of film strain, black arrows show where the maxima are detected, the red arrow corresponds to the position of the maximum of extinction of single Au NPs (the extinction is normalized at 450 nm).

The incident light can be decomposed into two components using a polarizer. Depending on the polarization of the light, the optical response of two gold nanoparticles close or far from each other on a 2D plane shows different plasmon shifts (see Chapter 1). When the polarization is parallel to the interparticle axis, coupling leads to a strong red shift of the plasmon peak as well as to an increase of its intensity. When polarization is orthogonal to the interparticle axis, coupling leads to a light blue shift of the plasmon peak as well as a decrease of its intensity.

The optical response of doped PVA film with Au-Si microcapsules was studied under polarized light. The extinction of the film was recorded during uni-axial elongation without polarizer, with polarizer at a 0° angle and with a polarizer at a 90° angle. For these three cases, the maximum of the plasmon response as a function of the uni-axial strain (γ) is plotted in Figure 117. For clarity issues, the error bars are only shown for three points. In parallel polarization, the jump between $2 < \gamma < 2.5$ occurs at lower strain than in perpendicular polarization. At these strain values, the maxima of the plasmon peak corresponding to single Au NPs ($\lambda \sim 540$ nm) and of the second peak corresponding to close NPs ($\lambda \sim 680$ nm) have very close. Therefore, we do not believe the difference observed in the two polarizations can be attributed to optical effects. Thus, no real changed in the maximum of the plasmon extinction is observed under polarized light compared to no polarized light. These observations could be coming from the fact that under uni-axial elongation, not all the Au NPs are isotropically spaced. It is still unclear but possible that in some areas the distance between the Au NPs decreases while it increases in other regions of the capsules. More experiments would need to be performed in order to fully understand the complex coupling between the mechanical deformation of the Au-Si microcapsules and their optical response.

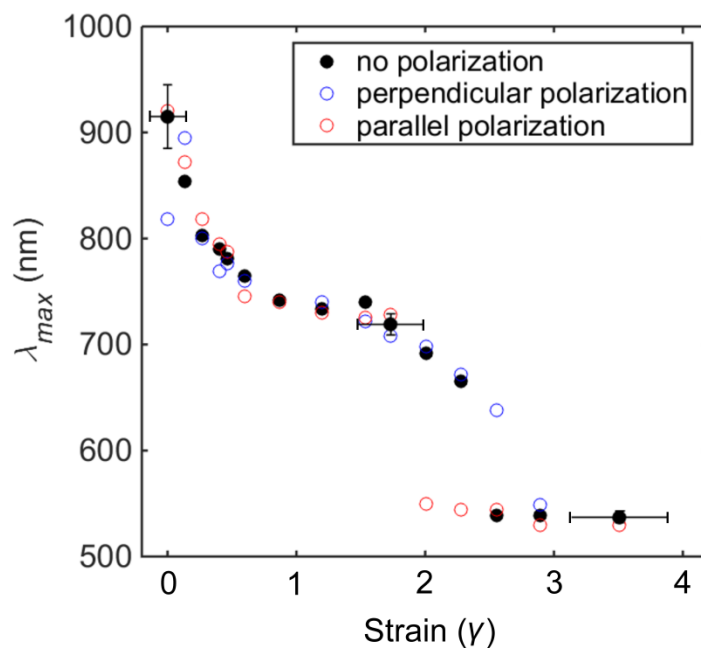


Figure 117: Film extinction measurements under polarized light during stretching.

2.2.4. Impact test

We tested the optical response of PVA films doped with microcapsules under impact. In this test, a 0.91 kg weight was dropped from several different heights on top of the film. The extinction was recorded for each impact height and the maximum of the extinction peak was plotted versus the kinetic energy of the weight at impact in Figure 118. The graphs show that as the kinetic energy of the weight at impact increases, the maximum of the extinction of the plasmonic peak shifts from the red/infrared region ($\lambda_{max} \sim 970$ nm) to the green/blue visible region of the spectrum ($\lambda_{max} \sim 540$ nm). Interestingly, at low impact energy, the analysis using the spectrophotometer exhibits a very small shift of the maximum of the plasmonic peak that cannot be detected by the human eye (circled in black on film on top picture, Figure 118). At higher kinetic energy of impact, the human eye is capable of seeing the area of impact by noticing a red spot at the impact zone as displayed in Figure 118 by the two bottom pictures.

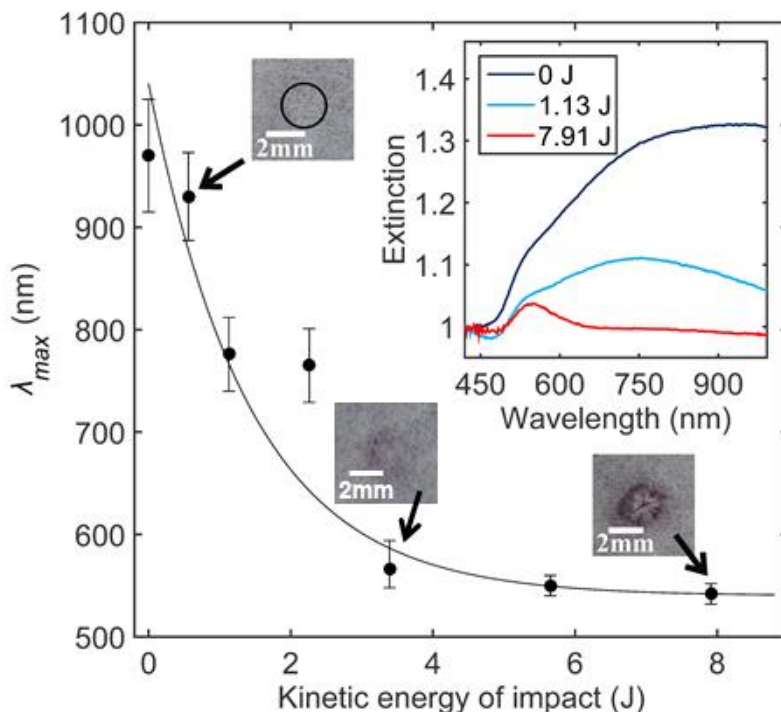


Figure 118: Position of the plasmonic peak maximum as a function of kinetic energy of impact. Inset: UV response as the polymer is impacted (the extinction is normalized at 420 nm).

2.2.5. Perforation test

The last test involves the perforation of the film using a paper puncher. As a hole is poked in the film, the polymer film undergoes very large strains in the vicinity of the hole (white dashed circle in Figure 119 (a)). Observations under an optical microscope show that the microcapsules lying far from the hole remain undisturbed and spherical and thus display a blue color as seen in Figure 119 (b), whereas these located close to the edge of the perforation are likely deformed into an ellipsoidal shape as indicated by their purple (Figure 119 (c)) and pink color (Figure 119 (d)). Nearby the hole, a color gradient from blue spherical microcapsules to pink elongated microcapsules is observed as imaged in Figure 119 (e).

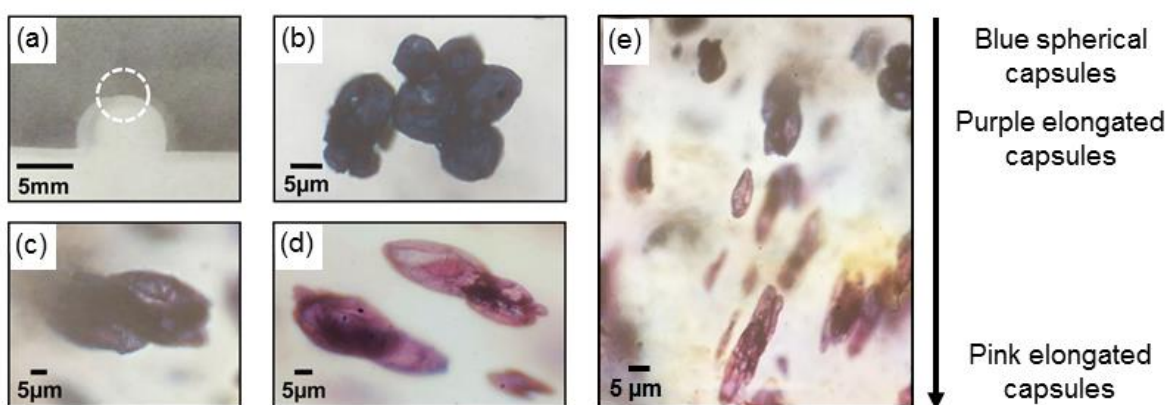


Figure 119: (a) Picture of the pinched polymer film with embedded microcapsules. (b-d) Optical microscope pictures of the microcapsules after pinching: (b) far from the hole, (c) closer to the hole, (d) nearby the hole, (e) gradient of color observed nearby the hole.

2.2.6. Au-Si microcapsules film aging

Polymer materials age with time^{184,185,186}. Usually, a combination of external factors such as temperature, exposure to ultraviolet light, visible light, humidity or liquids entails structural changes within polymers. Generally, the softer a polymer is, the more flexible its polymer chains are, and the more prone it is to aging. Silica and PVA are not free from these effects and it is interesting to know whether or not the Au-Si microcapsules in PVA exhibit identical response to the same mechanical stresses in time.

In this part of the manuscript, we check the aging behavior of Au-Si microcapsules embedded in a PVA polymer matrix. The film is left at room temperature for several months and the film optical response was measured as a function of strains at two different aging times (2 weeks and 5 months). The film extinction curve was recorded by spectrophotometry for different strain values. Then, the maximum of each extinction curve, λ_{max} , was plotted as a function of strain

γ as shown in Figure 120. At both aging times, for very small strains ($\gamma < 0.2$) the film absorb light at similar high wavelengths ($800 < \lambda_{max} < 900$ nm). Since the color of the microcapsule is related to the gold interparticle distance, at small strains, the Au NPs are still very close to each other at both aged times. For larger strains, $0.2 < \gamma < 2$, after long time aging, the film absorb light at higher wavelengths than at short time aging. Thus, it seems that, for identical elongation, the gold nanoparticles of the microcapsules embedded in the film for two weeks are brought further apart than the gold nanoparticles of the microcapsules embedded in the film for 5 months. It is possible that during aging the silica shell become glassier and breaks more easily into small pieces during elongation requiring larger strains to fully separate the AuNPs embedded in these pieces. At very large strains, $\gamma > 2$, both optical profiles collapse onto each other and the film absorb light at low wavelengths $\lambda_{max} \sim 540$ nm meaning that the gold nanoparticles are well separated. This experiment shows that aging process impacts the optical response of the Au-Si microcapsules during mechanical deformation.

The observed absorbance shift is here attributed to the AuSi microcapsule aging but one must not forget that the PVA film can also age and impact the overall mechanical response of the system to external strains. To surely demonstrate that the observed optical shift mostly comes from a change in the microcapsules structure the aging of the PVA film itself should be studied.

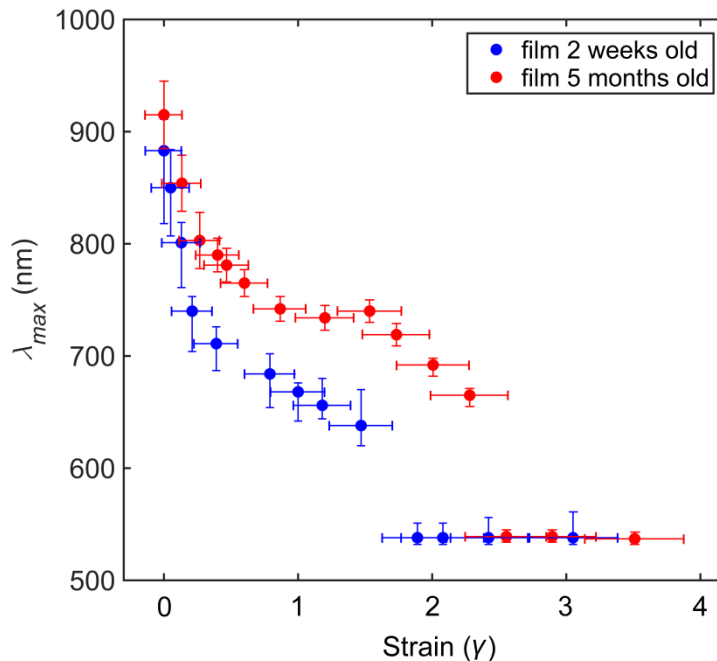


Figure 120: Optical response of the doped film at different aging time.

To conclude this section, we have evidenced the synthesis of plasmonic-based microcapsules, which can be used as strain sensors. Our approach is based on the dense packing of Au NPs at the surface of emulsion droplets. By solidifying the interface with PEOS, we obtained solid capsules made of Au NPs embedded in a silica crust. As the Au NPs are densely packed at the surface of the capsules, the microcapsule plasmon resonance is shifted towards the red region of the visible spectrum ($\lambda_{max} \sim 900 - 950$ nm). Moreover, when embedded in a polymer film any applied mechanical strain is found to deform the capsules, bringing the Au NPs further apart, therefore changing their extinction properties and underlying color. This is demonstrated by three experiments: a uniaxial strain, an impact test and a perforation test. It has to be highlighted here that despite the broad distribution of the particles size and microcapsules dimensions, our prototypical sensory device is sensitive enough to enable the detection of a color change by spectrophotometry arising from very tiny deformations not detectable by the eye.

2.3. The gold-acrylate microcapsules

2.3.1. Gold-acrylate microcapsules synthesis

The preparation of Au-acrylate microcapsules used in this section is based on the synthesis effort presented in Chapter 3. An aqueous phase containing the Au NPs ($[Au^0] = 0.02$ M) and HCl (50 μ L) is mixed with a toluene phase (0.5 mL) in which acrylate monomers (MMA 0.11 g and BA 0.11 g) and AIBN (0.12 M) are dissolved. The two phases are strongly agitated by sonication with a Brandson 3210 ultrasonic bath at 30°C for 15 minutes, forming an oil-in-water emulsion. By tuning pH to decrease the charges of the nanoparticles, a Pickering emulsion is formed. Shortly after the sonication, the emulsion exhibits a strong pink color due to the adsorption of the AuNPs as seen in Figure 121 (a). The polymerization is carried out at 60°C. The emulsion becomes blue after one hour as shown in Figure 121 (b) proving that Au NPs adsorb and get more and more densely packed at the interface during time. The polymerization is pursued for another hour to allow the formation of a polymer shell at the interface of the emulsion.

Images of the microcapsules are shown in Figure 121 (c) and (d). The color, shape and size of the microcapsules were analyzed by optical microscopy and SEM. The resulting microcapsules are spherical with dimensions ranging from 10 to 60 μ m. As seen in Figure 121 (c), the microcapsules have a deep blue color which comes from a monolayer of densely packed gold nanoparticles on their surface as shown Figure 121 (e). Under the high vacuum of the SEM, the gold acrylate capsules remain spherical (see Figure 121 (d)). The polymer shell thickness as measured from SEM images is in the order of 100 nm.

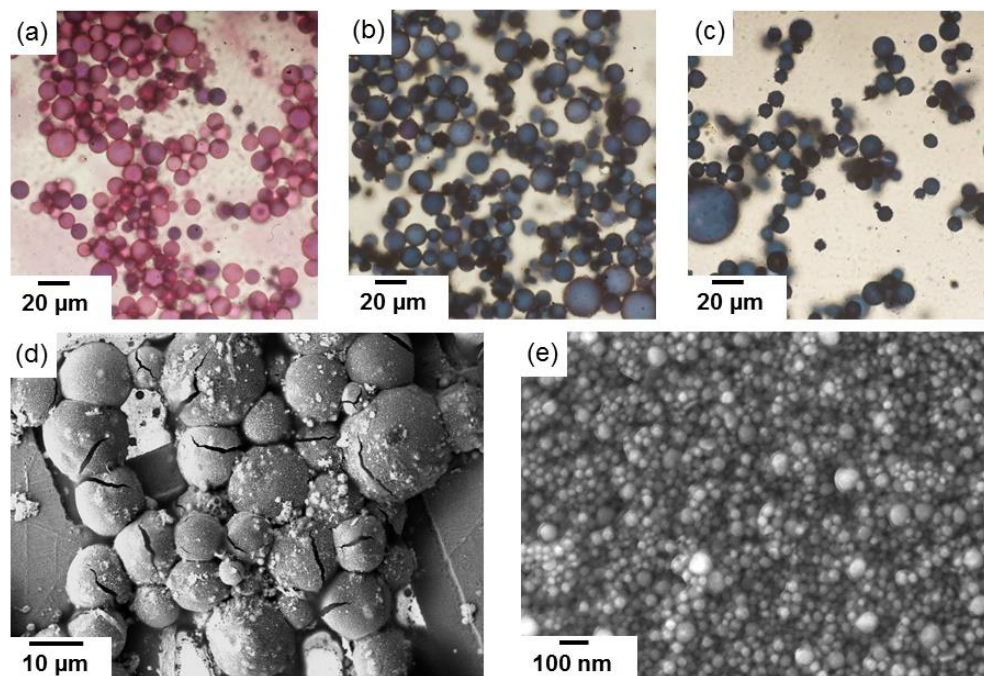


Figure 121: (a-b) Optical microscope images of typical emulsions at 0.02 M of gold at pH ~ 1 right after sonication, after one hour of polymerization and after polymerization respectively. (c) Optical gold-acrylate microscope images of typical microcapsules at 0.02 M of gold and pH ~ 1. (d) SEM images of microcapsules obtained at 0.02 M of gold and pH ~ 1. (e) SEM image of a typical gold-acrylate microcapsule surface covered by Au NPs at 0.02 M of gold and pH ~ 1.

2.3.2. Fabrication of elastic films doped with elastic microcapsules

To test the chromatic properties of our gold-acrylate microcapsules under strain we embedded these capsules inside an elastic polymer matrix made of latex beads coalescing upon drying at room temperature to which we applied different mechanical deformations.

The elastic films preparation is the following: 1.5 mL of a mixture of polyacrylate/polyvinyl acrylate beads at the ratio 10/90 by weight (50% solids) in water was prepared. The polyvinyl acrylate beads by themselves gave a very tacky film. The combination of both latexes provided elasticity and smoothness to the film. Then 0.25 mL of the as-previously synthesized gold-acrylate-microcapsules were dispersed in the latex solution under gentle stirring to avoid the formation of air bubbles. The final polymer-microcapsules solution was bar coated on a plastic substrate and was left to dry at room temperature overnight. The final thickness of the film is in the range of 500 microns to 1 millimeter depending on the bar used.

During the drying step, the gold-acrylate microcapsules retain their overall spherical shape as seen in Figure 122 (a). At such concentration of microcapsules in the film, the film is colorless and transparent but the concentration of microcapsules can be increased by a factor 100 and at that

concentration the film exhibits a very strong blue color due to the microcapsules color as shown in Figure 122 (b) and (c).

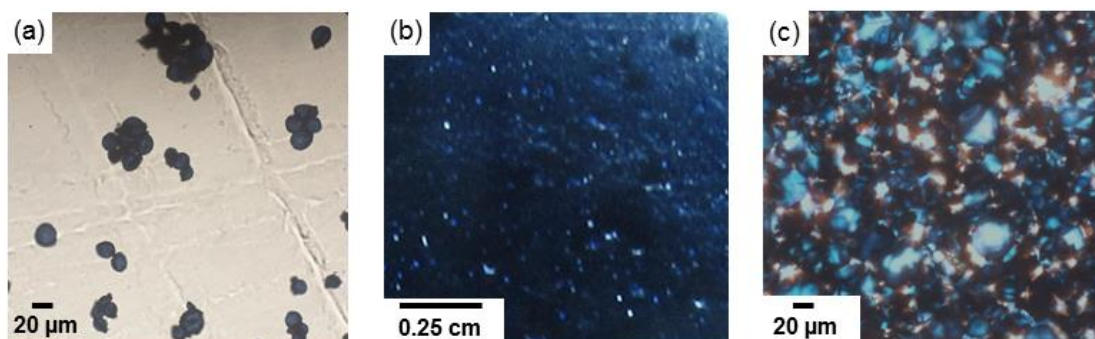


Figure 122: (a) Zoom on a latex film at low concentration in gold-acrylate microcapsules. (b) Color of the latex film at high concentration in capsules and (c) magnified view of the microcapsules embedded in this film.

2.3.3. Stretching test

The optical response of the gold-acrylate microcapsules was tested under uni-axial and bi-axial elongation. The films were elongated manually. The first results presented in Figure 123 show that the blue spherical gold acrylate microcapsules are elastic and can be stretched up to 400%. Upon uni-axial strain (400%), the microcapsules are elongated and turn purple as presented in Figure 123 (b). Upon bi-axial strain (400% in the horizontal direction and 200% in the vertical direction), the microcapsules turn pinker. When the stretch is 400% in both directions, the microcapsules turn fully pink. In all cases Figure 123 (b), (c), (d), when the stress is released, the deformed microcapsules recover their spherical shape and the return to their initial blue color as illustrated in Figure 123 (a). More accurate experiments will be conducted with a bi-axial vise recently ordered. The optical response of the gold-acrylate microcapsules will be recorded during stress and release of the stress applied on the microcapsules.

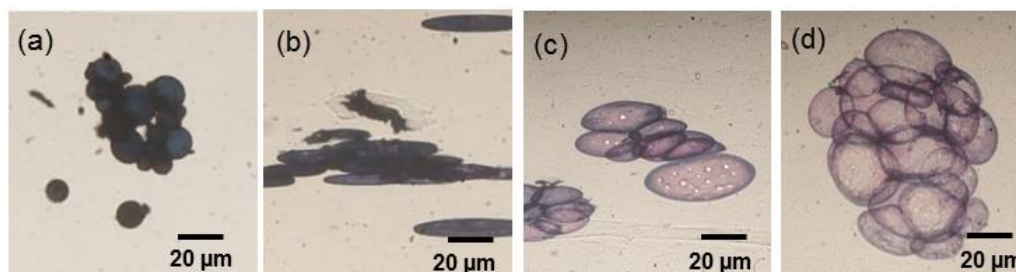


Figure 123: Polyacrylate microcapsules (a) before deformation, (b) after uni-axial elongation, (c-d) after bi-axial deformation.

In this section, we have shown that gold-acrylate microcapsules can be used as optical sensors to detect mechanical deformations in polymeric materials. Due to their elastic polymer shell, they can deform and relax upon application and release of strains. We have demonstrated it with a bi-axial stretching experiment.

2.4. Plasmon-based mechanochromic microcapsules vs other strain sensors

To establish the great potential of the Au-Si and Au-acrylate microcapsules as strain sensors, we are presenting in Table 2 their advantages and drawbacks and we compare them with the existing technologies presented earlier in the section 2.1.

Techniques	Advantages	Drawbacks
Dye encapsulated ¹⁷²	<ul style="list-style-type: none"> - Easy synthesis - Allows the detection of small cracks (~10 μm) 	<ul style="list-style-type: none"> - On/Off sensor, no correlation between strain and color - Needs to react with the polymer matrix to show a color change - Dye synthesis is not straightforward - Aging
Spiropyran ^{165,166}	<ul style="list-style-type: none"> - Straightforward relation between strain and optical response - Compatible with numerous polymers 	<ul style="list-style-type: none"> - Must be covalently attached to the support - Spiropyran synthesis is not straightforward - Aging
Excimers ^{179,180}	<ul style="list-style-type: none"> - Technology applicable to numerous polymers - Straightforward relation between strain and emission - Allow the detection of small and large strains 	<ul style="list-style-type: none"> - Fluorophore synthesis is not straightforward - Temperature dependent emission - Fluorophores can react with polymer matrix - Work at high concentration - Quenching - Aging
Au NPs chains in polymer ¹⁸²	<ul style="list-style-type: none"> - Facile chain assembly - Straightforward relation between strain and optical response 	<ul style="list-style-type: none"> - Gold chains can easily disassemble, not compatible with many polymers - Gold is expensive - Aging
Plasmon-based mechanochromic microcapsules	<ul style="list-style-type: none"> - Very easy synthetic process - Microcapsules are easily collected and incorporated in many types of polymer - Very sensitive optical response - Allow the detection of small and large strains - One microcapsule = one mechanosensor 	<ul style="list-style-type: none"> - Complex optomechanic coupling - Microcapsules' aging - Gold is expensive

Table 2: Plasmon-based mechanochromic microcapsules vs other technologies.

This quick comparison shows that the plasmon-based silica and acrylate microcapsules cumulate many advantages that other technologies only partially offer. However, more work must be done to improve the understanding of their complex optomechanic coupling.

3. Optical pH sensors

3.1. Current technologies

pH is a very important parameter in many applications such as cosmetics, pharmaceuticals, food-processing industry, etc. Optical pH sensors allowing the fast in-situ visual measurement of pH by outputting a color is of particular interest. Even if pH sensors are commonly used, the development of pH sensors which are sensitive, accurate, work on a large pH range, biocompatible or stable over a long time is of technological importance.

Optical pH sensors use pH indicator dyes which have distinct absorption (color) or fluorescence depending on their acidic (protonated) or basic (deprotonated) forms. A change of concentration of the hydronium ions H_3O^+ (pH) modifies the optical response of the dyes. It is important to understand the difference between electrochemical and optical determination of pH. The electrodes allow to determine the concentration of hydronium ions in aqueous solutions whereas the optical techniques allow to measure the concentration of the acid and basic forms of the pH indicator used.

Optical pH measurements of solutions containing an indicator use the Henderson-Hasselbalch equation (see Equation 20). This equation can be used in the case of dilute solutions where the ions concentration is below 0.1 M. At higher ionic concentrations, the activity must be used instead of the concentration in Equation 20.

$$pH = pK_a + \log\left(\frac{[A^-]}{[AH]}\right)$$

Equation 20: Henderson-Hasselbalch equation. $[A^-]$ and $[AH]$ are the concentrations of the basic and acid form of the pH indicator, respectively. pK_a is the negative logarithm of the acid dissociation constant K_a .

Most optical pH sensors consist of dyes immobilized in a hydronium ion-permeable solid matrix which can interact reversibly with the hydronium ions. The indicator molecules can be adsorbed, entrapped, covalently bonded¹⁸⁷ or encapsulated¹⁸⁸ in the support matrix. Depending on the type of matrix and indicator, each pH sensor has a different measurable pH range. The pK_a of the indicator is located at the center of this range. In the following pages, we present two examples of dyes that can be used as optical pH sensor.

Polyaniline polymer can be used to optically detect changes in pH¹⁸⁷. The imine nitrogen groups of the polyaniline are protonated in acidic conditions or deprotonated in basic conditions. (see Figure 124 (a)). The position of the maximum of absorption of the polyaniline polymer shifts from 750 nm in acidic solution to 575 nm in basic solution (see Figure 124 (b)). During protonation and deprotonation, a reversible color change from green to purple is observed. This color change is reversible. The absorbance was recorded at 575 and 750 nm over the pH range from 2 to 12. The apparent pK_a of the polyaniline polymer was found to be around 6.7 (see Figure 124 (c)).

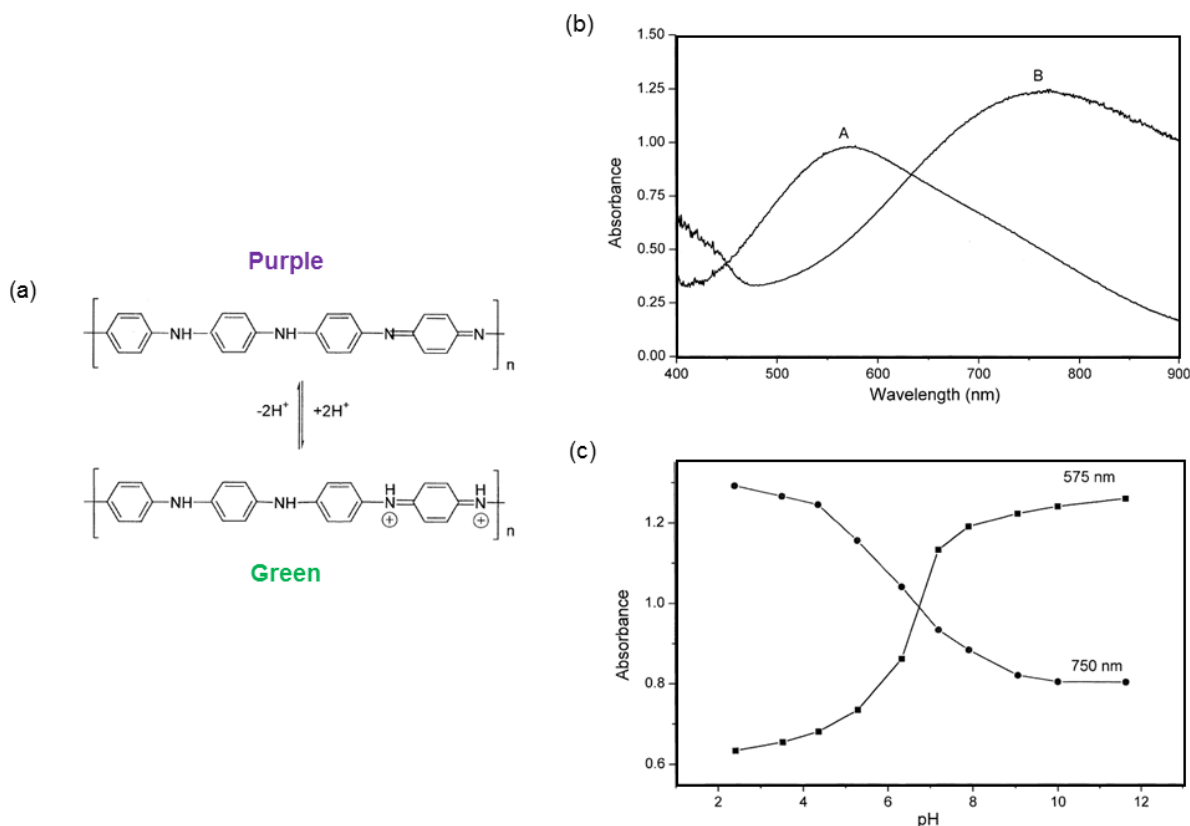


Figure 124: (a) Polyaniline base and protonated forms. (b) Absorption spectra of Polyaniline films in (A) 0.1 M sodium hydroxide and (B) 0.1 M HCl solutions. (c) Maximum of the absorption spectra of polyaniline film as a function of the pH¹⁸⁷.

pH-sensitive fluorescent dye (SNARF-1-dextran) loaded in polyelectrolytes microcapsules (see Figure 125 (a)¹⁸⁸) can serve as optical pH sensor. The emission wavelength of this fluorescent dye depends on pH. In its acidic form, the dye emits green and in its basic form the dye emits red (Figure 125 (b) and (c)). Magnetite NPs can be incorporated within the polyelectrolyte layer to recover the capsules by magnetic separation at any time. Moreover, the polyelectrolytes multi-layer can be functionalized with another dye bringing another asset to the system.

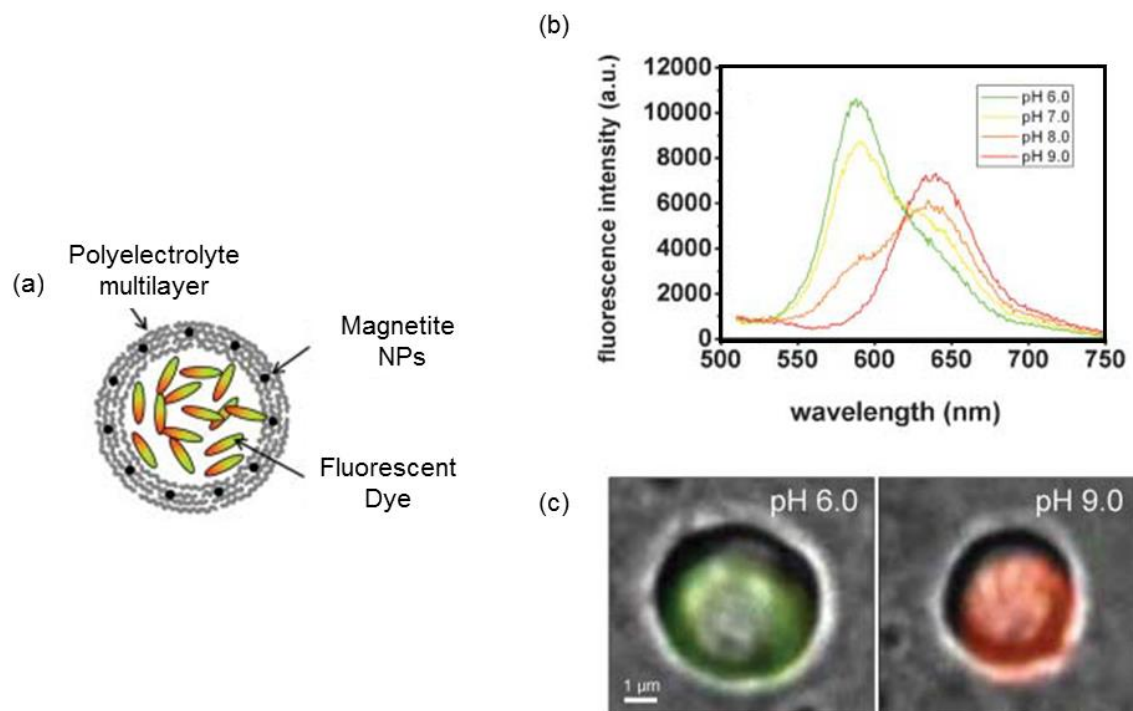


Figure 125: (a) Scheme of the capsules containing the dye (SNARF-1-dextran) (b) Fluorescence spectra of the fluorescent dye in water measured at different pH values. (c) Overlay of phase contrast and fluorescence microscopy images, capsules in acidic (green) and alkaline (red) pH¹⁸⁸.

The optical pH sensors based on the use of dyes are not always very efficient. Indeed, when dyes are entrapped within a polymer matrix, they can leach outside which limits sensor stability and make their long term use impractical¹⁸⁷. When dyes are covalently attached to the polymer matrix or encapsulated, their sensitivity (response to pH change) can be reduced^{187,188}. Therefore, other methods are still needed to measure pH optically. An alternative to dye molecules based on the use of Au NPs has been contemplated by several research groups. Among them Shen *et al.*¹⁸⁹ as well as Tokavera *et al.*¹⁵⁶ used the distance-dependent optical properties of Au NPs to design new generation of plasmon-based pH sensors.

Dual responsive gold nanoparticles coated with Nipam-terminated hyperbranched polyglycerols (HPG-Nipam) were synthesized by Shen *et al.*¹⁸⁹. The Figure 126 shows the stability of the Au NPs as a function of pH and temperature. Due to the thermo- and pH-responsive HPG-Nipam polymer, Au NPs are sensitive to pH and temperature. When $\text{pH} > \text{pK}_a$ of the Nipam amine (see Figure 126 (a)), the amine group is deprotonated whereas when $\text{pH} < \text{pK}_a$ of the amine, the amine group is protonated in a quaternary ammonium ion. As for PNipam, the solubility of HPG-Nipam polymer in water depends on temperature (T). When $T < \text{LCST}$, HPG-Nipam polymer is

soluble in water whereas when $T > \text{LCST}$, there is a phase separation between the solvent and the HPG-Nipam polymer. When temperature and pH are increased, initially well dispersed Au NPs aggregate. Aggregation is due to the increase of the polymer hydrophobicity coming from the desorption of the water molecules solubilizing the polymer chains (temperature effect) and the concomitant reduction of the charges (deprotonation of the ammonium ions) (pH effect). This aggregation is characterized by a large red shift of the Au NPs surface plasmon peak induced by a strong interparticle coupling when the nanoparticles are close to each other (see previously in chapter 1).

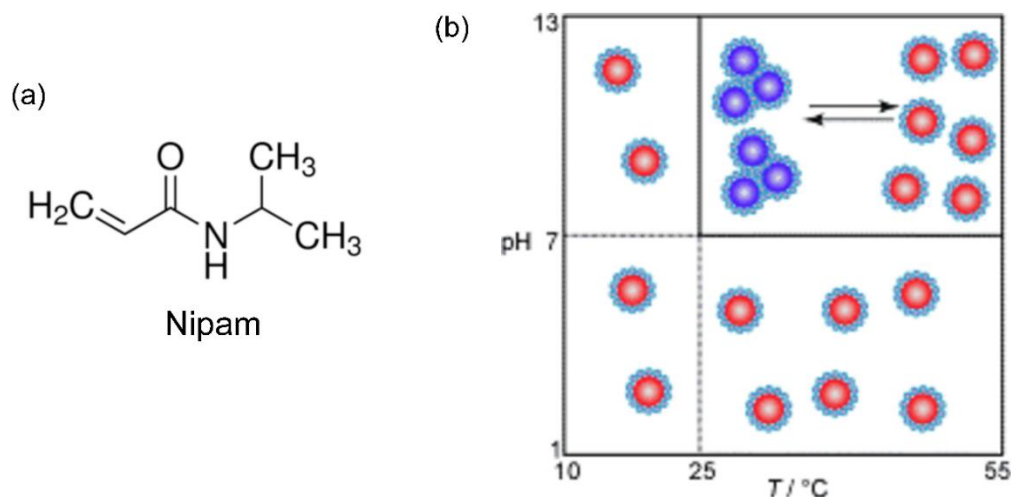


Figure 126: (a) Nipam (*N*-isopropylacrylamide) formula. (b) Illustration of effects of pH and temperature on dual-responsive Au NPs coated with polyglycerol-Nipam¹⁸⁹.

Tokareva *et al.*¹⁵⁶ have designed a similar type of nanosensor based on Au NPs plasmon response. Their system is schematized in Figure 127 (a). Polymer brushes (carboxyl group-terminated poly(2-vinylpyridine)) are anchored on the Au NPs on one end and on a substrate bearing gold nanoislands on the other end. An increase or a decrease in pH causes the brushes to shrink or swell respectively. The brushes swell due to the increase of the charges inside the polymer brushes which stretch out by electrostatic repulsion and solvation. The swelling of the polymer leads to an increase of the distance between the Au NPs and to a shift of the plasmon response of the nanosensor towards the lower wavelength in Figure 127 (b). The maximum of the plasmon peak as a function of pH presented in Figure 127 (c) shows that 50% of the polymer is protonated at pH ~ 3.8 which correspond to 50% swelling of the polymer brushes. The swelling process is reversible.

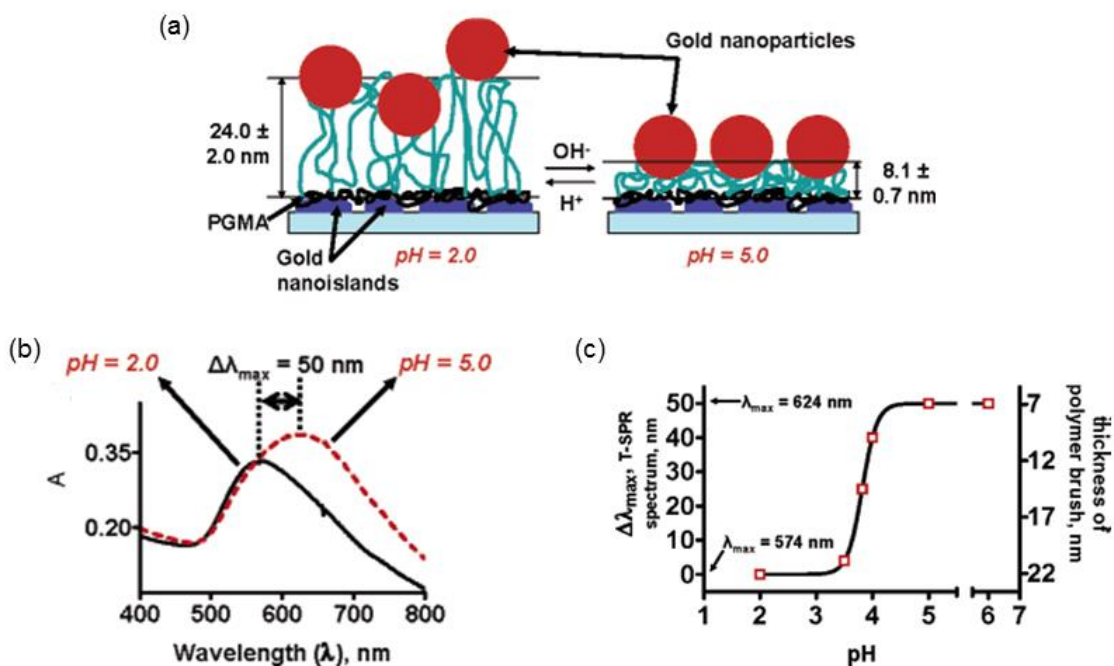


Figure 127: (a) Illustration of the reversible pH change-induced swelling of Au NPs-coated P2VP. (b) Absorption spectra of the nanosensor at pH 2 and 5. (c) Absorption maximum and thickness of the polymer brush as a function of the pH¹⁵⁶.

Based on these concepts of polymer swelling and plasmon coupling we show in section 3.2.1 of this chapter how the gold-acrylate microcapsules can be used as optical pH sensor.

3.2.pH responsive gold-acrylate microcapsules

In this part, the pH sensitivity of gold-acrylate microcapsules synthesized as presented in section 2.3.1 is tested.

3.2.1. pH sensitivity of Poly(acrylic acid)

Polymers holding carboxylic acid/carboxylate ions such as poly(acrylic acid) are known for their swelling properties^{190,191,192,193}. The swelling of such polymer matrix is due to three main phenomena illustrated in Figure 128.

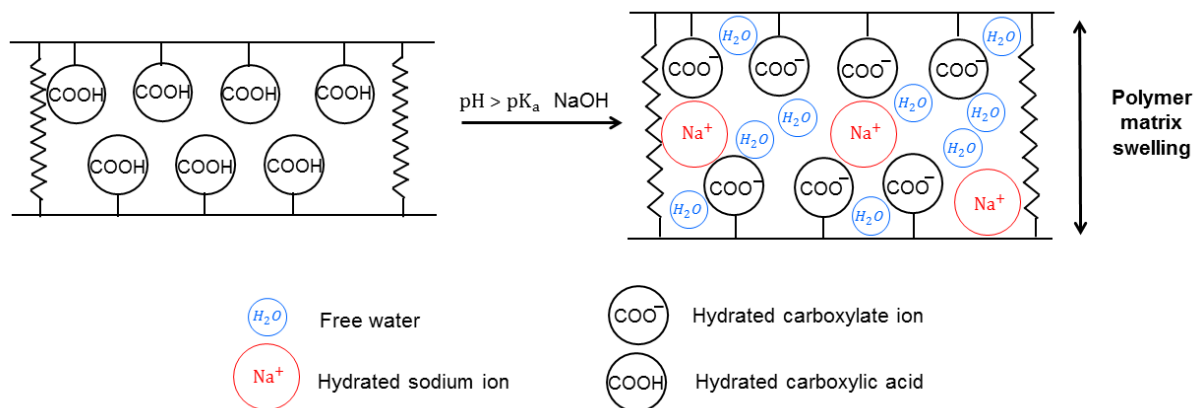


Figure 128: Polymer matrix swelling.

- i) When $\text{pH} > \text{pK}_a$ of the carboxylic acid, these carboxylic acid groups lose their protons and turn into their conjugate bases, the carboxylate ions as illustrated in Figure 129. These carboxylate ions repel each other electrostatically.

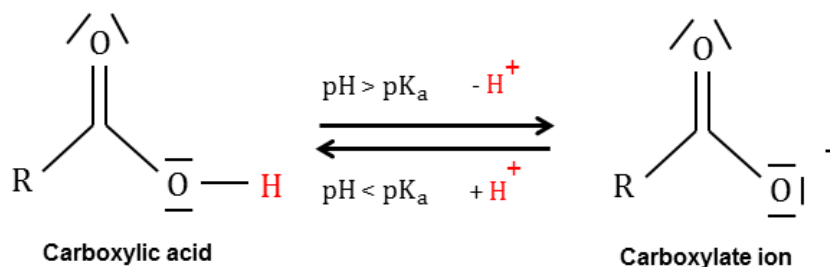


Figure 129: Carboxylic acid/carboxylate ion equilibrium. R represents an alkane group.

- i) The hydrated cationic counter ions (in the case of our example, Na^+) enter the polymer matrix to equilibrate the osmotic pressure between the outside media and the polymer matrix. Ions are said hydrated due to the clustering of water molecules in their vicinity.
- ii) Free water molecules penetrate inside the matrix.

Then, the polymer matrix relaxes to an equilibrium state (tensile stress release) by ejecting water molecules from its matrix.

The swelling of a polymer matrix bearing carboxylic acid groups non-exhaustively depends on the number of carboxylic groups, the pH, the type of counter ions¹⁹¹ (in particularly their size when hydrated), the polymer backbone chemical and mechanical characteristics¹⁹² (number of reticulation points, type of monomer units, polymer conformation, etc).

3.2.2. Gold-acrylates microcapsules response to pH

As I explained in Chapter 3, the gold-acrylate microcapsules (MMA/BA, 50/50 wt%) shells bare methacrylic acid and acrylic acid groups due to the hydrolysis of their respective acetate groups under very acidic conditions. These carboxylic acid groups can turn into their conjugate bases by increasing the pH of the media in which they are dispersed above their respective pK_a . The pK_a of methacrylic acid is 4.7 and the one of acrylic acid is 4.1¹⁹⁴. The pK_a of polymer made of methacrylic acid monomers and the pK_a of polymer made of methacrylic acid monomers are different than the pK_a of their respective monomers. Indeed, the dissociation of carboxylic acid on polymer chains is strongly influenced by the dissociation of the neighboring carboxylic acid¹⁹³. Once a carboxylic acid has been deprotonated on the polymer chain, the neighboring carboxylic acid is harder to deprotonate. While the pK_a value is unique and well-defined for a monomeric acid; weak polyelectrolytes such as poly(acrylic acid), usually display an apparent broad pK_a distribution with a mean apparent pK_a value larger than that of its monomeric constituent.¹⁹⁵ The mean apparent pK_a of poly(acrylic acid) is 5.4¹⁹⁵ and the one of poly(methacrylic acid) is 5.7¹⁹². Based on these pK_a values, we expect half of the acrylic acid and methacrylic acid groups within the gold-acrylate microcapsules to be deprotonated at pH above 6.

The gold-acrylate microcapsules (MMA/BA, 50/50 wt%) swelling behavior was recorded by optical microscopy imaging. These microcapsules initially dispersed in water at pH = 1 were inserted in a capillary and the pH of the dispersion was gradually changed by adding a sodium hydroxide (NaOH, 10^{-1} M) solution at pH = 14 on one end of the capillary. The goal of this experiment is to slowly establish a change in pH in the capillary. After the NaOH solution is deposited, hydroxyl ions diffuse in the capillary (see Figure 130). We observe the behavior of the capsules as pH increases in the capillary. Figure 131 shows that at the beginning of the experiment, the microcapsules dispersed in a very acidic water are blue (Figure 131 (a)) and as the NaOH diffuses within the capillary, the color of the microcapsule is changed from blue to pink/red (Figure 131 (b-d)). By adding a concentrated solution of NaOH, the pH increases above the pK_a of both acrylic acid and methacrylic acids, thus the carboxylic acids are transformed into carboxylate ions. Concomitantly, the sodium ions and free water molecules penetrate the polymer matrix causing it to swell. The swelling of the microcapsules entails an increase of the inter-particles distance and therefore a change of color of the microcapsules.

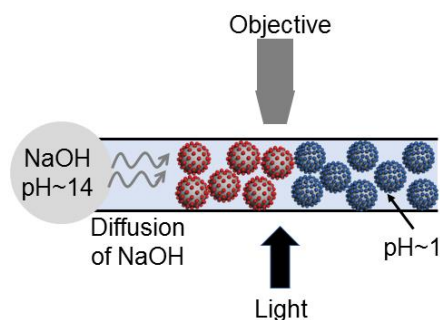


Figure 130: Schematic illustration of the local pH change.

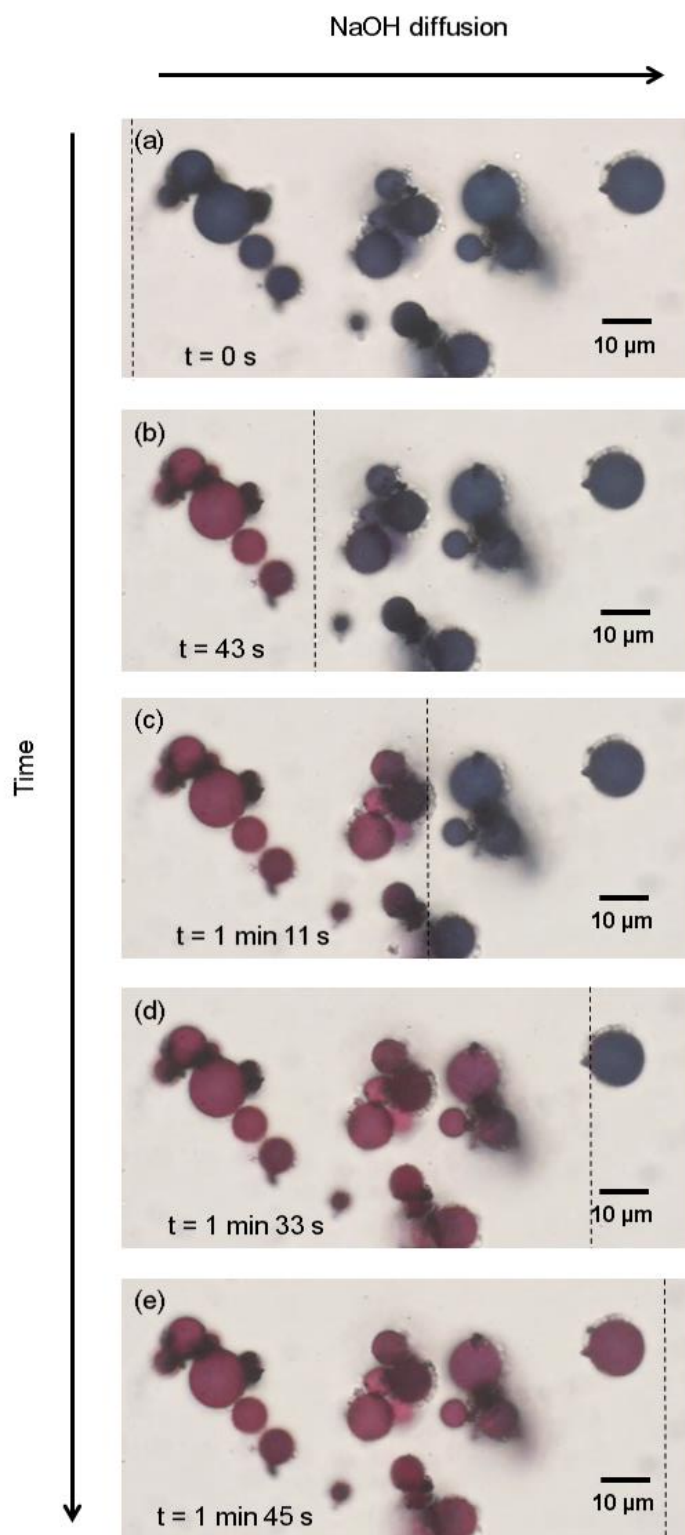


Figure 131: Gold-acrylate microcapsules swelling. Initially in acid solution ($\text{pH}=1$). The pH is slowly changed by flowing a solution of sodium hydroxide ($\text{pH}=14$) from left to right (a-e).

A magnified view onto a larger gold-acrylate microcapsule better illustrates the change of color during diffusion of sodium hydroxide ($\text{pH} = 14$, 10^{-1} M) in the dispersion of microcapsules (see Figure 132). Before addition of the base, the microcapsule is blue and spherical (Figure 132 (a)). As the base is added and diffuses from left to right inside the capillary, the blue microcapsule changes color and gradually turn pink/red (Figure 132 (b-j)). A close look at the red area on the microcapsule shows that the microcapsule slightly deforms (Figure 132 (b-e)) during the increase of pH. This deformation is attributed to the swelling of the microcapsule.

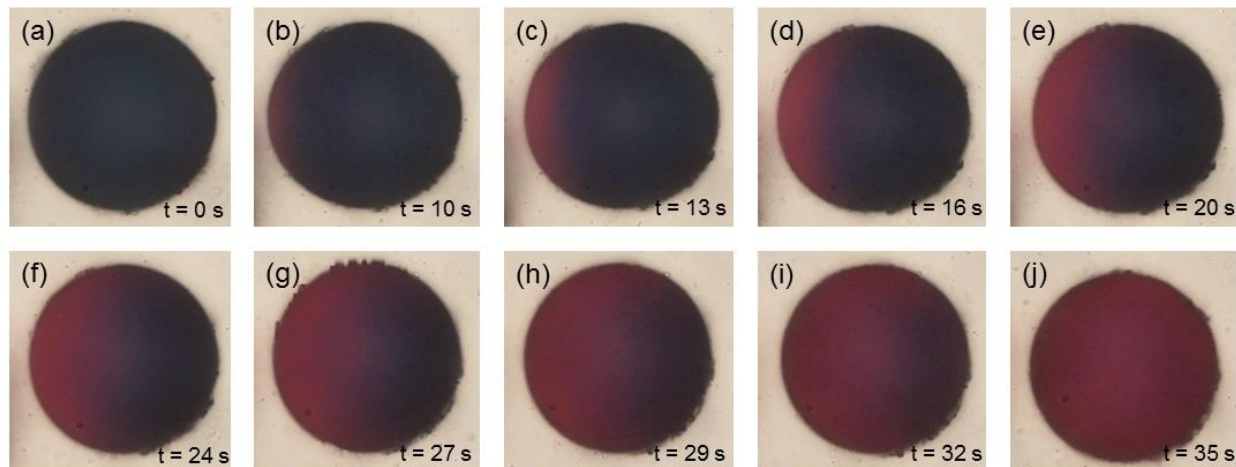


Figure 132: Gold-acrylate microcapsules swelling. Initially in acid solution ($\text{pH} = 1$). The pH is slowly changed by diffusion of a solution of sodium hydroxide ($\text{pH} = 14$, 10^{-1} M) from right to left (a-j). The diameter of the microcapsule is $82 \mu\text{m}$.

The way color and diameter change as a function of time as pH increases is analyzed by videomicroscopy. The analysis is done on a $13 \mu\text{m}$ microcapsule and the results are shown in Figure 133. The diameter was measured by adjusting a circle on a capsule. Color was quantified using the intensity of the red (R), green (G) and blue (B) channels on the CCD of the color camera. The microcapsule diameter increases by about 10% as pH increases. This small increase in the diameter of the microcapsule is enough to induce a drastic change of color. The R, G, B color analyses show that as the microcapsule is swelling, it becomes redder and less blue and green. Once the microcapsule stops to swell, the red, blue and green colors remain constant. These observations show that gold nanoparticles are brought further apart when the microcapsules swell.

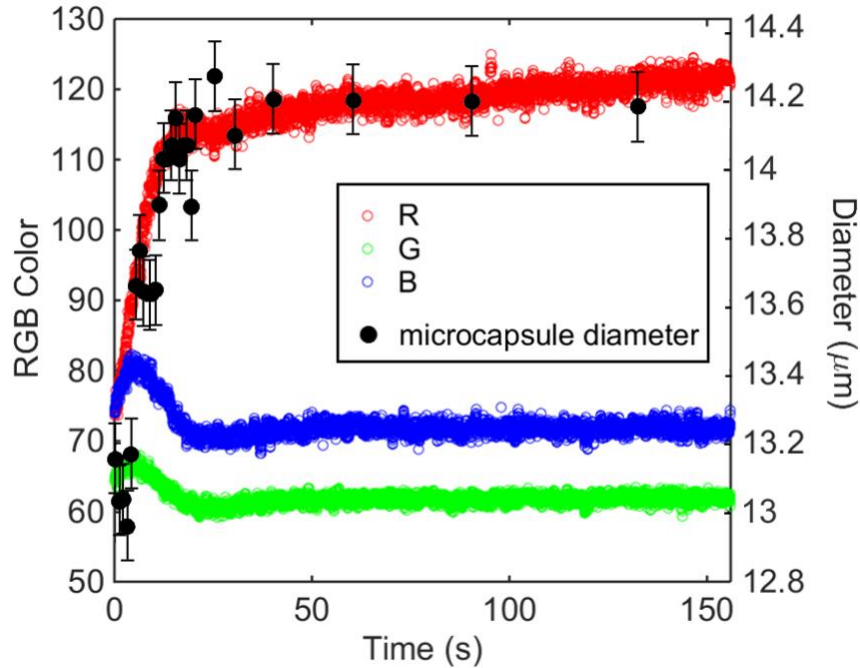


Figure 133: RGB temporal analysis on a 13 μm gold-acrylate microcapsule changing color while flowing a solution of NaOH (10^{-1} M) inside the capillary containing the microcapsule.

We can estimate the average increase of the distance inbetween the nanoparticles present on the microcapsules during swelling (see Figure 134).

Let's work with the 13 μm size microcapsule. The know parameters are listed below:

r = radius of the Au NPs ~ 20 nm.

s = interparticle distance. Estimated to be about 2 nm on blue microcapsules from SEM images.

R = radius of the blue microcapsule = 6.6 μm .

R' = radius of the red microcapsule after swelling = 7.1 μm .

ϕ = packing fraction of the Au NPs on the microcapsules

The parameter s' is the interparticle distance after swelling. It is the distance we want to estimate.

Assuming that the nanoparticles are equally wet by the ater and by the oil phase ($\theta = 90^\circ$), the number, N , of Au NPs on the sphere of diameter D is estimated by:

$$N = \frac{\text{Surface sphere}}{\text{cross section AuNPs} * \phi}$$

$$N = \frac{4\pi R^2}{\phi\pi(r + \frac{s}{2})^2}$$

$$N = \frac{4}{\phi} \frac{R^2}{r^2} \frac{1}{\left(1 + \frac{s}{2r}\right)^2}$$

And for $\frac{s}{2r} \ll 1$,

$$N \approx \frac{4}{\phi} \frac{R^2}{r^2} \left(1 - \frac{s}{r}\right)$$

After swelling the number of Au NPs on the microcapsules is the same but the diameter of the microcapsules, R' , and the distance in-between the Au NPs, s' , are larger.

$$N \approx \frac{4}{\phi} \frac{R'^2}{r^2} \left(1 - \frac{s'}{r}\right)$$

$$\frac{4}{\phi} \frac{R^2}{r^2} \left(1 - \frac{s}{r}\right) = \frac{4}{\phi} \frac{R'^2}{r^2} \left(1 - \frac{s'}{r}\right)$$

$$\frac{R'^2}{R^2} \approx \frac{\left(1 - \frac{s}{r}\right)}{\left(1 - \frac{s'}{r}\right)}$$

And for $\frac{s}{r} \ll 1$,

$$\frac{R'^2}{R^2} \approx 1 + \frac{s' - s}{r}$$

Therefore, for $\frac{s}{r} \ll 1$,

$$s' \approx \left(\frac{R'^2 - R^2}{R^2}\right)r + s$$

For an initial distance $s \sim 2 \text{ nm}$ between gold nanoparticles, we find $s' \sim 5 \text{ nm}$. The increase of the interparticle distance for the $13 \mu\text{m}$ size microcapsule is about **150%** during swelling.

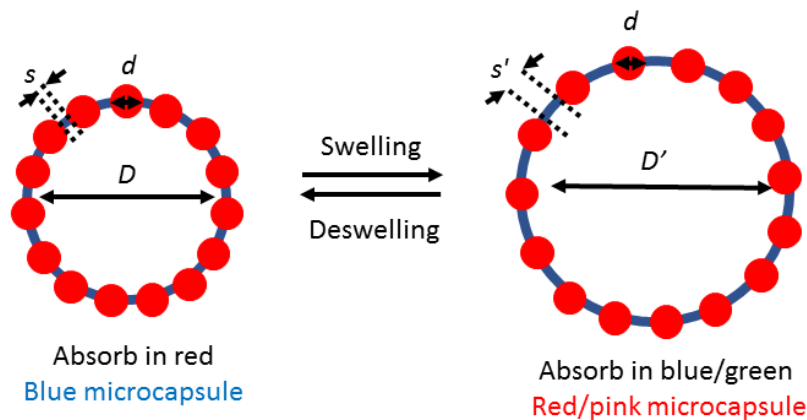


Figure 134: Increase/decrease of the interparticle distance during swelling/deswelling of a gold-acrylate microcapsule.

Based on the work of Myroshnychenko *et al.*¹⁴⁶, we calculated the extinction of two gold nanoparticles for different interparticle distance s . We repeated the calculation for Au NPs of diameter 30, 40 and 50 nm (see Figure 135). We chose these diameters because most of the Au NPs assembled on the microcapsules have a diameter between 30 and 50 nm. The results suggest that the maximum of the extinction is located at 850 nm when the Au NPs are separated by a distance of about 0.2 nm. The maximum of the extinction is shifted to 550 nm when the distance between the Au NPs reaches 6 nm. Here the increase of the interparticle distance is about 2900% which is far from the 155% obtained before. The observed discrepancy can come from the fact that the curves shown in Figure 135 are obtained considering only two nanoparticles. This does not mimic the real system in which the Au NPs on surface of the microcapsules have multiple neighbors.

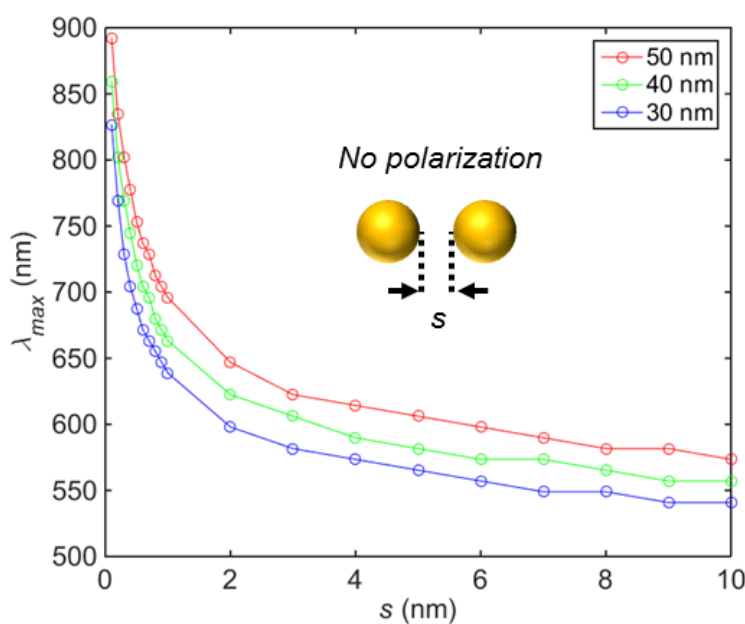


Figure 135: Maximum of the extinction peak for two Au NPs with a diameter of either 50, 40 or 30 nm separated by a distance s . The environment containing the Au NPs is silica.

3.2.3. Reversibility of the color change

The color change is reversible (see Figure 136). We demonstrated the reversibility by performing the following experiment: pH was changed alternately by injecting in the capillary containing the microcapsules a droplet of solutions of NaOH (pH = 14, 10^{-1} M) and HCl (pH = 1, 10^{-1} M) in a sequential way. The addition of NaOH brings the pH above the pK_a of the carboxylic acids and triggers the microcapsule swelling and change color from blue to pink. The addition of HCl brings the pH below the pK_a of the carboxylic acids, the carboxylic acid form dominates and the microcapsule shrinks and changes color from pink to blue. Three color cycles blue-pink-blue

and pink-blue-pink were performed on the same microcapsule. For each cycle, the microcapsules change color and then return to their initial color. We did not perform more cycles but it seems that our microcapsules are resistant to multiple swelling/shrinking transitions.

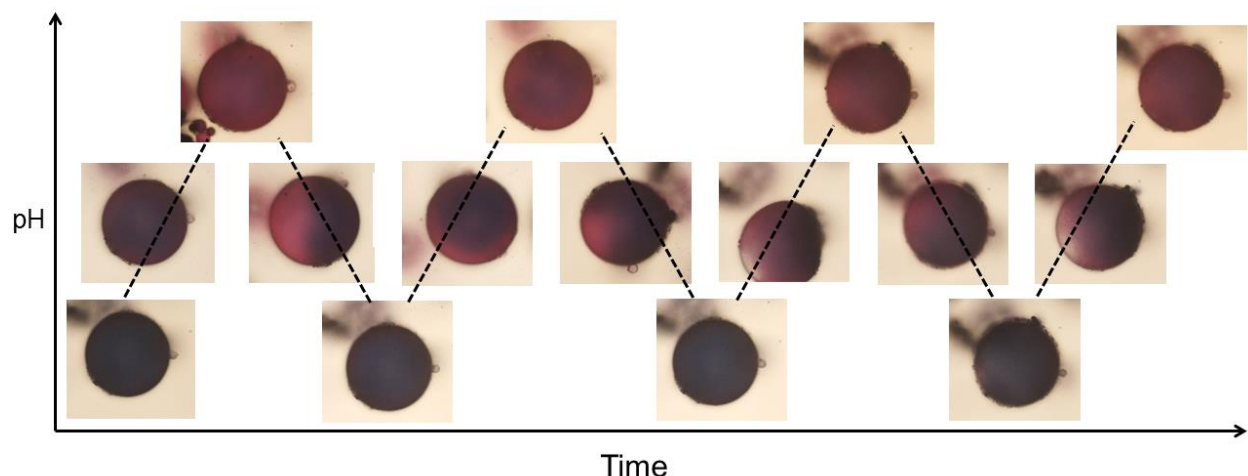


Figure 136: Reversibility of the color change by changing the pH back and forth. Three full cycles blue-pink-blue and three full cycles pink-blue-pink were performed. The blue microcapsule in solution at pH=1 turns pink by adding sodium hydroxide at pH = 14. It turns back from pink to blue by adding HCl at pH = 1. The diameter of the microcapsule is 64 μm .

3.2.4. Color as a function of pH

Buffer solutions at different pH (1, 3.2, 4.9, 7.1, 7.6, 9.1, 10.1, 10.8, 13.6) were prepared (see Table 3) and the gold-acrylate microcapsules were re-dispersed in these solutions. Multiple optical microscope images of the microcapsules were taken at the different pH and the mean intensities of the three colors red, blue and green of the microcapsules were plotted as a function of pH. Figure 137 shows the mean intensity by color channels. A transition at pH ~ 8.2 is observed. At pH below 8.2, the intensity of the blue color is the highest. At pH above 8.2, the intensity of the red color dominates the blue and green color intensities. This transition is more obvious in Figure 138 showing the red mean intensity normalized by the blue intensity as a function of pH. Figure 139 show the typical color of the microcapsules at different pH. In this figure, each microcapsule is different and comes from a different buffer solution. This explains the variation in the size of the capsule. At pH < 8.2 , the microcapsule is blue, whereas at pH > 8.2 , the microcapsule is pink/red.

pH	Citric acid (0.75 M)	Na ₂ HPO ₄ (1.5 M)
3	19.86 mL	5.13 mL
5	12.12 mL	12.87 mL
7	4.42 mL	20.58 mL
7.6	1.58 mL	23.42 mL
pH	Na ₂ CO ₃ (0.75 M)	NaHCO ₃ (0.75 M)
9.2	2.5 mL	22.5 mL
10.8	22.5 mL	2.5 mL
9.9	12.5 mL	12.5 mL

Table 3: Buffer solutions.

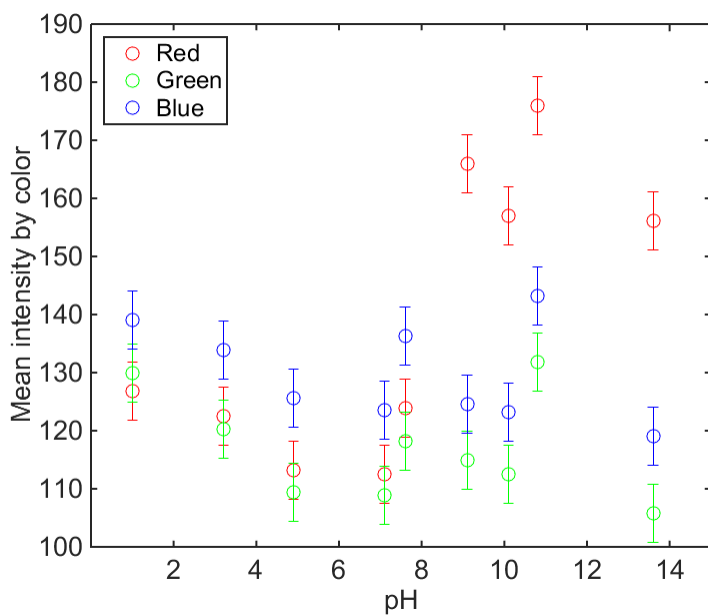


Figure 137: Mean intensities of the red blue and green colors of the gold-acrylate microcapsules as a function of pH.

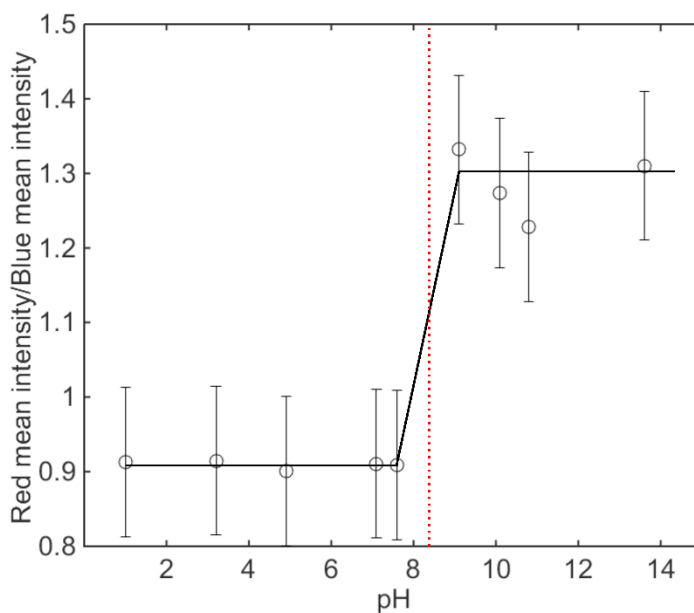


Figure 138: Red mean intensity normalized by the blue mean intensity as a function of pH.

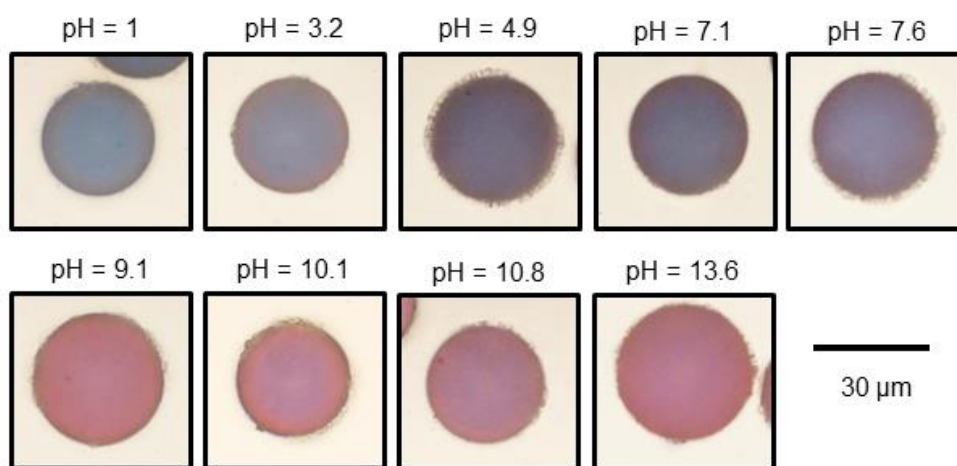


Figure 139: Typical gold-acrylate microcapsules' color as a function of pH.

In this section, we have demonstrated that gold-acrylate microcapsules can serve as pH sensors because they have the property to swell when the pH of the solution in which they are dispersed is above the apparent pK_a of the polymer capsules. Experimental results show a very sharp transition at large pH ~ 8.2 . To better understand the optical response of the gold acrylate microcapsules as a function of the pH, many characterizations still have to be carried out. Amongst them, chromatography and NMR analyses to estimate the number and weight average molecular

weight of the polymer forming the shell and how much monomers are left inside the oil phase in case the polymerization is not total. Moreover, the quantification of the carboxylic acid groups formed on the acrylate polymer shell have to be done. This is an important parameter to know about because it is responsible for the swelling behavior of the microcapsules. Indeed, depending on the number of acrylate and acrylic acid groups on the polymer chain, the pK_a of the polymer will vary¹⁹⁶. Bendejack *et al.*¹⁹⁵ showed that upon grafting of hydrophobic groups non ionizable in water (such as styrene) onto poly(acrylic acid), the apparent pK_a of the polymer chains increases (see Figure 140). Because of these added hydrophobic units, the overall polymer solubility in water decreases and it is even harder to ionize the polymer acid groups.

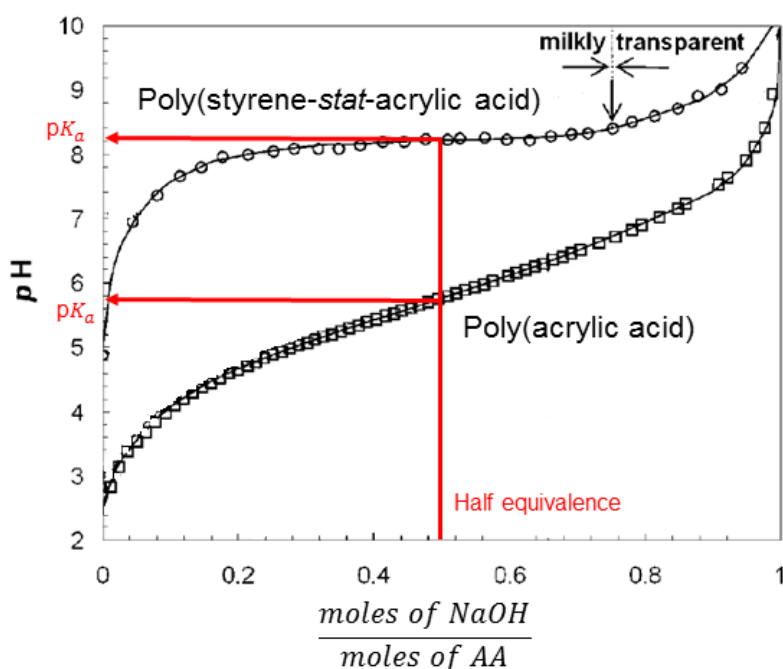


Figure 140: (a) Titration of poly(acrylic acid) and poly(styrene-stat-acrylic acid)¹⁹⁵.

3.3.pH responsive microcapsules vs other pH sensors

In this part, we compare the pH responsive gold-acrylate microcapsules with other optical pH sensors. Giving a full overview of all the other existing technologies is out of the scope of this manuscript. However, the examples chosen here already enable us to establish the performances of the gold-acrylate microcapsules.

Techniques	Advantages	Drawbacks
Polyaniline polymer films ¹⁸⁷	<ul style="list-style-type: none"> - Easy synthetic process - Straightforward relation between pH and optical response 	<ul style="list-style-type: none"> - Aging - Hysteresis of the optical response during pH cycles - Sensor not mobile
Fluorescent dye encapsulated ¹⁸⁸	<ul style="list-style-type: none"> - Straightforward relation between pH and optical response - Can be used in numerous applications - High local concentration of sensor molecules - Mobile sensors 	<ul style="list-style-type: none"> - Dye encapsulated has a lower sensitivity than “free” dye - Photo-bleaching - Aging
Au NPs coated with Polyglycerol-Nipam ¹⁸⁹	<ul style="list-style-type: none"> - Polymer synthesis not straightforward - Small variation of the optical response as a function of the pH 	<ul style="list-style-type: none"> - Gold is expensive - Aging
Plasmon responsive polymer brushes ¹⁵⁶	<ul style="list-style-type: none"> - Easy synthesis - Small variation of the optical response as a function of the pH 	<ul style="list-style-type: none"> - Gold is expensive - Hysteresis - Aging - Sensor not mobile
Plasmon-based microcapsules	<ul style="list-style-type: none"> - Very sharp color transition at a specific pH - Facile synthesis - Mobile sensors - One microcapsule = one pH sensor 	<ul style="list-style-type: none"> - Complex optomechanic coupling - Microcapsules’ aging - Gold is expensive

Table 4: pH responsive microcapsules vs other technologies

The pH responsive plasmon-based microcapsules differentiate themselves from all the other pH sensor technologies by providing a very sharp change of color at a specific pH. However, additional experiments must be carried out to improve the understanding of the complex optical response of these microcapsules when pH is changed.

4. Conclusion

In this chapter, we have used the protocols established in Chapter 3 to synthesize two types of plasmonic microcapsules sensors. Our approach is based on the control of dense packings of Au NPs at the surface of emulsion droplets by tuning the charge of the nanoparticles. By forming a silica crust at the interface of the emulsion, we obtained capsules made of Au NPs embedded in a solid shell. By polymerizing acrylate monomers at the interface, we obtained elastic hydrogel microcapsules made of Au NPs embedded in a polymer shell.

We have shown two potential applications of the gold-silica and gold-acrylate microcapsules. Both types of microcapsules can be used as optical sensors to detect mechanical deformations. The hard silica mechanochromic shells mixed in paints, fabrics or polymers can be used to gather local and/or global information about the material in which they are incorporated. It allows the early detection of cracks or bullet/rock impact locations. The gold-acrylate microcapsules could be used

to study polymeric material resistance through mechanical stress-release cycles. For instance, they could be incorporated within the miniature models of bridges or buildings to study the response of these constructions to wind blow, weight, etc. The elasticity of the gold-acrylate microcapsule will allow to study the mechanical behavior of these constructions once the stress is released. The gold-acrylate microcapsules can also be used as optical pH sensors. Indeed, due to the carboxylic acid groups present on their polymeric shells, these microcapsules have the property to swell upon pH increase above the pK_a of the carboxylic acids. These micron size capsules could find applications in living systems such as biofilms where change in pH occurs.

Our lab scale synthesis allows the fabrication of billions of microcapsules in a few milliliters of solution, each one of them being one optical sensor by itself. This number could be easily increased by scaling up our fabrication process.

Conclusion and perspectives

In the last few decades, nanoparticles have attracted lot of attention from the scientific community. Indeed, arising from their small sizes, nanoparticles have unique physical and chemical properties. When ordered into two- or three-dimensional architectures, these small particles offer new collective optical, magnetic, and electronic properties. The objective of this Ph.D. work was to assemble particles in bulky tridimensional materials and dispersed spherical materials.

In the first chapter, we presented two types of metallic nanoparticles: the gold and silver nanospheres. We introduced the concept of plasmon resonance. We saw that the absorption of light by these nanoparticles depends on their size, shape, environment and interparticle distance. Then, we described the most commonly used methods for the synthesis of spherical silver and gold nanoparticles. Finally, we presented several methods to assemble nanoparticles. At first, we focused on the assembly of particles in bulky tridimensional materials by microfluidic pervaporation. Then, we explained how dispersed spherical materials can be obtained from the self-assembly of particles on emulsion droplets.

In the second chapter, we concentrated dispersions of micro- and nano-particles in microchannels by pervaporation of water through a thin PDMS membrane. Different types of particles were assembled by this technique: small metallic particles (40 nm gold nanoparticles) and larger polymer particles (0.5 μm and 1 μm polystyrene particles). Through our studies, we observed that the concentration of salts in the dispersion of particles can destabilize the particles during their concentration inside microchannels. In that case, the particles assemblies did not show any specific order. On the contrary, when particles do not aggregate during their concentration, they organize in superb hexagonal crystals. With the technique of microfluidic pervaporation we obtained crystalline packings of gold nanospheres and of spherical latex micron-size particles. This powerful technique did not only allow us to organize nanoparticles in dense arrays but it did allow us to tune the size, shape and geometry of the final assemblies. Our results widen the horizons as to the fabrication of new optomaterials such as electromagnetic metamaterials, photonic bandgap structures and high refractive index materials.

In the third chapter, we demonstrated the successful synthesis of dispersed plasmonic microcapsules. Our approach was based on controlled packings of plasmonic nanoparticles at the surface of emulsion droplets by tuning the charge and wettability of the metallic nanoparticles. By solidifying the interface with PEOS or acrylate monomers, we obtained capsules made of NPs embedded in a hard silica crust or in a soft polyacrylate shell. The nanoparticles were highly packed in the shell. In the case of gold nanoparticles, the nanoparticles were so close to each other that they absorbed light at a higher wavelength. In the case of silver nanoparticles, the polymer layer capping the particles prevented them from getting very close and plasmon coupling between the particles was not observed. The color of the silica microcapsules was tuned from yellow to

blue by mixing Au and Ag NPs in different ratios. Moreover, we established the conditions for which the microcapsules are resistant to drying. It depends on the oil polarity and on the concentration of PEOS. In future work, other types of nanoparticles such as nanophosphors and quantum dots could be combined with gold nanoparticles, to synthesize microcapsules, which would exhibit not only a color change but a fluorescence change when stretched. Dyes could also be polymerized within the shell.

In the fourth chapter, we showed that the hybrid plasmonic microcapsules present direct real-life applications. First, we demonstrated that the gold-silica microcapsules can be used as optical sensors to detect mechanical deformations. Indeed, when these microcapsules are embedded inside a polymer matrix, upon stretching of the polymer, the microcapsules color changes from blue to red. A change of color was also observed when the polymer film doped with the microcapsule was impacted and pinched. This phenomenon is due to the increase of the spacing between the nanoparticles during elongation. The gold-silica microcapsules could be used for the early detection of cracks or bullet/rock impact locations. Second, we showed that the elastic gold-acrylate microcapsules exhibit a reversible color change upon stress and release of the stress. Gold-acrylate microcapsules can also be used as optical pH sensors. Indeed, due to the carboxylic acid groups present on their polymeric shells, these microcapsules have the property to swell when pH increases above the pK_a of the carboxylic acids. These micron size capsules could find applications in living systems such as biofilms where changes in pH occur. In the future, other types of plasmon-based microcapsule sensors could be engineered. These sensors could measure change in temperature, humidity or pressure through a color change.

The fabrication process of all the plasmonic microcapsules is very easy. Via this method we make billions of microcapsules, each one of them being one optical sensor by itself. This process could easily be scaled up for commercial applications. However, before reaching this stage, many details remain to be understood. For instance, a better comprehension of the complex optomechanical properties of the microcapsules is needed. Why do we have such large plasmon peaks? Also, an overall greater characterization of the microcapsules physico-chemical properties is required (number of acrylic acid groups in the acrylate polymer shell, polymer chains lengths, degree of polymerization, elasticity of the shell, etc). Furthermore, the size-dispersity of the microcapsules can be greatly improved. Microfluidics is technique that we will use to synthesize highly monodisperse microcapsules. Finally, a great need exists as for measurements of local stresses in materials. We believe that our microcapsules could help filling this need: we plan on investigating the optical response of elastic microcapsules to stresses.

Bibliography

- (1) Edwards, P. P.; Thomas, J. M. Gold in a Metallic Divided State - From Faraday to Present-Day Nanoscience. *Angew. Chemie - Int. Ed.* 2007, 46, 5480–5486.
- (2) Hough, R. M.; Noble, R. R. P.; Reich, M. Natural Gold Nanoparticles. *Ore Geol. Rev.* 2011, 42, 55–61.
- (3) Sciau, P. Nanoparticles in Ancient Materials: The Metallic Lustre Decorations of Medieval Ceramics. *The Delivery of Nanoparticles* 2012; pp 525–540.
- (4) Eustis, S.; El-sayed, M. A.; Kasha, M. Why Gold Nanoparticles Are More Precious than Pretty Gold: Noble Metal Surface Plasmon Resonance and its Enhancement of the Radiative and Nonradiative Properties of Nanocrystals of Different Shapes. 2006, 209–217.
- (5) Willets, K. A.; Van Duyne, R. P. Localized Surface Plasmon Resonance Spectroscopy and Sensing. *Annu. Rev. Phys. Chem.* 2007, 58, 267–297.
- (6) Moores, A.; Goettmann, F. The Plasmon Band in Noble Metal Nanoparticles: An Introduction to Theory and Applications. *New J. Chem.* 2006, 30, 1121–1132.
- (7) Link, S.; El-sayed, M. A. Shape and Size Dependence of Radiative, Non-Radiative and Photothermal Properties of Gold Nanocrystals. *Int. Rev. Phys. Chem.* 2000, 19, 409–453.
- (8) Link, S.; El-Sayed, M. A. Size and Temperature Dependence of the Plasmon Absorption of Colloidal Gold Nanoparticles. *J. Phys. Chem. B* 1999, 103, 4212.
- (9) Paramelle, D.; Sadovoy, A.; Gorelik, S.; Free, P.; Hobley, J.; Fernig, D. G. A Rapid Method to Estimate the Concentration of Citrate Capped Silver Nanoparticles from UV-Visible Light Spectra. *Analyst* 2014, 139, 4855–4861.
- (10) Barchiesi, D.; Grosjes, T. Fitting the Optical Constants of Gold, Silver, Chromium, Titanium, and Aluminum in the Visible Bandwidth. *J. Nanophotonics* 2014, 8, 83097.
- (11) Malassis, L. Elaboration et Caractérisation de Films Composites Métal / Diélectrique Nanostructurés pour une Application aux Métamatériaux, Université de Bordeaux, 2012.
- (12) Liz-Marzán, L. M. Tailoring Surface Plasmons through the Morphology and Assembly of Metal Nanoparticles. *Langmuir* 2006, 22, 32–41.
- (13) Rodríguez-Fernández, J.; Pérez-Juste, J.; García De Abajo, F. J.; Liz-Marzán, L. M. Seeded Growth of Submicron Au Colloids with Quadrupole Plasmon Resonance Modes. *Langmuir* 2006, 22, 7007–7010.
- (14) Jiang, R.; Qin, F.; Liu, Y.; Ling, X. Y.; Guo, J.; Tang, M.; Cheng, S.; Wang, J. Colloidal Gold Nanocups with Orientation-Dependent Plasmonic Properties. *Adv. Mater.* 2016, 28, 6322–6331.

- (15) Chen, H.; Kou, X.; Yang, Z.; Ni, W.; Wang, J. Shape- and Size-Dependent Refractive Index Sensitivity of Gold Nanoparticles. *Langmuir* 2008, *24*, 5233–5237.
- (16) NanoComposix.Inc. Gold Nanoparticles: Optical Properties <http://nanocomposix.com/pages/gold-nanoparticles-optical-properties#local-refractive-index> (accessed Jan 1, 2017).
- (17) Malassis, L.; Jishkariani, D.; Murray, C. B.; Donnio, B. Dendronization-Induced Phase-Transfer, Stabilization and Self-Assembly of Large Colloidal Au Nanoparticles. *Nanoscale* 2016, *8*, 13192–13198.
- (18) Jishkariani, D.; Diroll, B. T.; Cargnello, M.; Klein, D. R.; Hough, L. A.; Murray, C. B.; Donnio, B. Dendron-Mediated Engineering of Interparticle Separation and Self-Assembly in Dendronized Gold Nanoparticles Superlattices. *J. Am. Chem. Soc.* 2015, *137*, 10728–10734.
- (19) Dolinnyi, A. I. Nanometric Rulers Based on Plasmon Coupling in Pairs of Gold Nanoparticles. *J. Phys. Chem. C* 2015, *119*, 4990–5001.
- (20) Jain, P. K.; Huang, W.; El-sayed, M. A. On the Universal Scaling Behavior of the Distance Decay of Plasmon Coupling in Metal Nanoparticle Pairs : A Plasmon Ruler Equation. *Nano Lett.* 2007, *7*, 2080–2088.
- (21) Sheikholeslami, S.; Jun, Y. W.; Jain, P. K.; Alivisatos, A. P. Coupling of Optical Resonances in a Compositionally Asymmetric Plasmonic Nanoparticle Dimer. *Nano Lett.* 2010, *10*, 2655–2660.
- (22) Zhao, L.; Zhao, L. L.; Kelly, K. L.; Kelly, K. L.; Schatz, G. C.; Schatz, G. C. The Extinction Spectra of Silver Nanoparticle Arrays: Influence of Array Structure on Plasmon Resonance Wavelength and Width. *J. Phys. Chem. B* 2003, *107*, 7343–7350.
- (23) Goia, D. V.; Matijević, E. Preparation of Monodispersed Metal Particles. *New J. Chem.* 1998, *22*, 1203–1215.
- (24) Jana, N. R.; Gearheart, L.; Murphy, C. J. Wet Chemical Synthesis of High Aspect Ratio Cylindrical Gold Nanorods. *J. Phys. Chem. B* 2001, *105*, 4065–4067.
- (25) Chandran, S. P.; Chaudhary, M.; Pasricha, R.; Ahmad, A.; Sastry, M. Synthesis of Gold Nanotriangles and Silver Nanoparticles Using Aloe Vera Plant Extract. *Biotechnol. Prog.* 2006, *22*, 577–583.
- (26) Zhang, J.; Liu, H.; Wang, Z.; Ming, N. Shape-Selective Synthesis of Gold Nanoparticles with Controlled Sizes, Shapes, and Plasmon Resonances. *Adv. Funct. Mater.* 2007, *17*, 3295–3303.
- (27) Jana, N. R.; Gearheart, L.; Murphy, C. J. Evidence for Seed-Mediated Nucleation in the Chemical Reduction of Gold Salts to Gold Nanoparticles. *Chem. Mater.* 2001, *13*, 2313–2322.
- (28) Turkevich, J.; Stevenson, P.C.; Hillier, J. A Study of the Nucleation and Growth Processes in the Synthesis of Colloidal Gold. *Discuss. Faraday Soc.* 1951, *11*, 55.

- (29) Frens, G. Controlled Nucleation for the Regulation of the Particle Size in Monodisperse Gold Suspensions. *Nat. Phys. Sci.* 1973, *241*, 20–22.
- (30) Brown, K. R.; Walter, D. G.; Natan, M. J. Seeding of Colloidal Au Nanoparticle Solutions. 2. Improved Control of Particle Size and Shape. *Chem. Mater.* 2000, *12*, 306–313.
- (31) Bastús, N. G.; Comenge, J.; Puentes, V. Kinetically Controlled Seeded Growth Synthesis of Citrate-Stabilized Gold Nanoparticles of up to 200 nm: Size Focusing versus Ostwald Ripening. *Langmuir* 2011, *27*, 11098–11105.
- (32) Jana, N. R.; Gearheart, L.; Murphy, C. J. Seeding Growth for Size Control of 5 - 40 Nm Diameter Gold Nanoparticles. *Langmuir* 2001, *17*, 6782–6786.
- (33) Malassis, L.; Dreyfus, R.; Murphy, R. J.; Hough, L. A.; Donnio, B.; Murray, C. B. One-Step Green Synthesis of Gold and Silver Nanoparticles with Ascorbic Acid and their Versatile Surface Post-Functionalization. *RSC Adv.* 2016, *6*, 33092–33100.
- (34) Lee, P. C.; Meisel, D. Adsorption and Surface-Enhanced Raman of Dyes on Silver and Gold Sols. *J. Phys. Chem.* 1982, *86*, 3391–3395.
- (35) Rycenga, M.; Cobley, C. M.; Zeng, J.; Li, W.; Moran, C. H. Controlling the Synthesis and Assembly of Silver Nanostructures for Plasmonic Applications. *Chem. Rev.* 2012, *111*, 3669–3712.
- (36) Wiley, B.; Sun, Y.; Xia, Y. Synthesis of Silver Nanostructures with Controlled Shapes and Properties. *Acc. Chem. Res.* 2007, *40*, 1067–1076.
- (37) Kilin, D. S.; Prezhdo, O. V.; Xia, Y. Shape-Controlled Synthesis of Silver Nanoparticles: Ab Initio Study of Preferential Surface Coordination with Citric Acid. *Chem. Phys. Lett.* 2008, *458*, 113–116.
- (38) Qin, Y.; Ji, X.; Jing, J.; Liu, H.; Wu, H.; Yang, W. Size Control over Spherical Silver Nanoparticles by Ascorbic Acid Reduction. *Colloids Surfaces A Physicochem. Eng. Asp.* 2010, *372*, 172–176.
- (39) LaMer, V. K.; Dinegar, R. H. Theory, Production and Mechanism of Formation of Monodispersed Hydrosols. *J. Am. Chem. Soc.* 1950, *72*, 4847–4854.
- (40) Seydou Hebié, Yaovi Holade, Karine Servat, B. K. K. and; Napporn., T. W. Electrochemical Reactivity at Free and Supported Gold Nanocatalysts Surface. *Catalytic Application of Nano-Gold Catalysts*; 2016; pp 101–130.
- (41) Atiyah, A. A. *Homogeneous Nucleation*; 2016, https://www.researchgate.net/profile/Alaa_Atiyah
- (42) Polte, J. Fundamental Growth Principles of Colloidal Metal Nanoparticles – A New Perspective. *Cryst. Eng. Comm.* 2015, *17*, 6809–6830.
- (43) Polte, J.; Ahner, T. T.; Delissen, F.; Sokolov, S.; Emmerling, F.; Thünemann, A. F.; Kraehnert, R. Mechanism of Gold Nanoparticle Formation in the Classical Citrate Synthesis

- Method Derived from Coupled in Situ XANES and SAXS Evaluation. *J. Am. Chem. Soc.* 2010, *132*, 1296–1301.
- (44) Abécassis, B.; Testard, F.; Spalla, O.; Barboux, P. Probing in Situ the Nucleation and Growth of Gold Nanoparticles by Small-Angle X-Ray Scattering. *Nano Lett.* 2007, *7*, 1723–1727.
- (45) Shevchenko, E. V.; Talapin, D. V.; Kotov, N. A.; Brien, S. O.; Murray, C. B. Structural Diversity in Binary Nanoparticle Superlattices. *Nature* 2006, *439*, 55–59.
- (46) Rupich, S. M.; Shevchenko, E. V.; Bodnarchuk, M. I.; Lee, B.; Talapin, D. V. Size-Dependent Multiple Twinning in Nanocrystal Superlattices. *J. Am. Chem. Soc.* 2009, *132*, 289–296.
- (47) Nie, Z.; Fava, D.; Kumacheva, E.; Zou, S.; Walker, G. C.; Rubinstein, M. Self-Assembly of Metal – Polymer Analogues of Amphiphilic Triblock Copolymers. *Nature* 2007, *6*, 609–614.
- (48) Hickey, R. J.; Koski, J.; Meng, X.; Riggleman, R. A.; Zhang, P.; Park, S. Size-Controlled Self-Assembly of Superparamagnetic Polymersomes. *ACS Nano* 2014, *8*, 495–502.
- (49) Mifsud, A.; Moya, J. S.; Va, L. Evidence of FCC Crystallization of SiO₂ Nanospheres. *Langmuir* 1997, *7*, 6009–6011.
- (50) García-Santamaría, F.; Salgueiriño-Maceira, V.; López, C.; Liz-Marzán, L. M. Synthetic Opals Based on Silica-Coated Gold Nanoparticles. *Langmuir* 2002, *18*, 4519–4522.
- (51) Denkov, N. D.; Velev, O. D.; Kralchevsky, P. a.; Ivanov, I. B.; Yoshimura, H.; Nagayama, K. Two-Dimensional Crystallization. *Nature*. 1993, 26–26.
- (52) Yan, Q.; Zhou, Z.; Zhao, X. S. Inward-Growing Self-Assembly of Colloidal Crystal Films on Horizontal Substrates. *Langmuir* 2005, *21*, 3158–3164.
- (53) Ming, T.; Kou, X.; Chen, H.; Wang, T.; Tam, H. L.; Cheah, K. W.; Chen, J. Y.; Wang, J. Ordered Gold Nanostructure Assemblies Formed by Droplet Evaporation. *Angew. Chemie - Int. Ed.* 2008, *47*, 9685–9690.
- (54) Jiang, P.; Bertone, J. F.; Hwang, K. S.; Colvin, V. L. Single-Crystal Colloidal Multilayers of Controlled Thickness. *Chem. Mater.* 1999, *11*, 2132–2140.
- (55) Park, S. H.; Gates, B.; Xia, Y. A Three-Dimensional Photonic Crystal Operating in the Visible Region. *Adv. Mater.* 1999, *11*, 462–466.
- (56) Merlin, A.; Salmon, J.-B.; Leng, J. Microfluidic-Assisted Growth of Colloidal Crystals. *Soft Matter* 2012, *8*, 3526.
- (57) Kumacheva, E.; Garstecki, P.; Wu, H.; Whitesides, G. M. Two-Dimensional Colloid Crystals Obtained by Coupling of Flow and Confinement. *Phys. Rev. Lett.* 2003, *91*, 128301.
- (58) Dziomkina, N. V.; Vancso, G. J. Colloidal Crystal Assembly on Topologically Patterned

- Templates. *Soft Matter* 2005, 1, 265.
- (59) Kitaev, V.; Ozin, G. A. Self-Assembled Surface Patterns of Binary Colloidal Crystals. *Adv. Mater.* 2003, 15, 75–78.
- (60) Tao, A. R.; Huang, J.; Yang, P. Langmuir-Blodgett of Nanocrystals and Nanowires. *Acc. Chem. Res.* 2008, 41, 1662–1673.
- (61) Pieranski, P. Two Dimensional Interfacial Colloidal Crystals. *Phys. Rev. Lett.* 1980, 45, 569.
- (62) Huang, S.; Tsutsui, G.; Sakaue, H.; Shingubara, S.; Takahagi, T. Experimental Conditions for a Highly Ordered Monolayer of Gold Nanoparticles Fabricated by the Langmuir–Blodgett Method. *J. Vac. Sci. Technol. B* 2001, 19, 2045.
- (63) Paul, S.; Pearson, C.; Molly, A.; Cousins, M. A.; Green, M.; Koliopoulou, S.; Dimitrakis, P.; Normand, P.; Tsoukalas, D. Langmuir-Blodgett Assembly of One-Dimensional Nanostructures and their application to electronic memory structures. *Nano Lett.* 2003, 3, 503–506.
- (64) Vogel, N.; Fernández-Lopez, C.; Pérez-Juste, J.; Liz-Marzán, L. M.; Landfester, K.; Weiss, C. K. Ordered Arrays of Gold Nanostructures from Interfacially Assembled Au@PNIPAM Hybrid Nanoparticles. *Langmuir* 2012, 28, 8985–8993.
- (65) Favre, E.; Schaetzel, P.; Nguyen, Q. T.; Clément, R.; Néel, J. Sorption, Diffusion and Vapor Permeation of Various Penetrants through Dense Poly(dimethylsiloxane) Membranes: A Transport Analysis. *J. Memb. Sci.* 1994, 92, 169–184.
- (66) Watson, J. M.; Baron, M. G. The Behaviour of Water in Poly(dimethylsiloxane). *J. Memb. Sci.* 1996, 110, 47–57.
- (67) Verneuil, E.; Buguin, A.; Silberzan, P. Permeation-Induced Flows: Consequences for Silicone-Based Microfluidics. *Europhys. Lett.* 2004, 68 (3), 412–418.
- (68) Randall, G. C.; Doyle, P. S. Permeation-Driven Flow in Poly(Dimethylsiloxane) Microfluidic Devices. *Proc. Natl. Acad. Sci. U. S. A.* 2005, 102, 10813–10818.
- (69) Leng, J.; Lonetti, B.; Tabeling, P.; Ajdari, A. Microevaporators for Kinetic Exploration of Phase Diagrams. *Phys. Rev. Lett.* 2006, 96, 1–4.
- (70) Moreau, P.; Dehmoune, J.; Salmon, J. B.; Leng, J. Microevaporators with Accumulators for the Screening of Phase Diagrams of Aqueous Solutions. *Appl. Phys. Lett.* 2009, 95, 1–4.
- (71) Daubersies, L.; Leng, J.; Salmon, J.-B. Steady and out-of-Equilibrium Phase Diagram of a Complex Fluid at the Nanolitre Scale: Combining Microevaporation, Confocal Raman Imaging and Small Angle X-Ray Scattering. *Lab. Chip* 2013, 13, 910–919.
- (72) Leng, J.; Joanicot, M.; Ajdari, A. Microfluidic Exploration of the Phase Diagram of a Surfactant/water Binary System. *Langmuir* 2007, 23, 2315–2317.
- (73) Merlin, a; Angly, J.; Daubersies, L.; Madeira, C.; Schöder, S.; Leng, J.; Salmon, J.-B. Time-

- Resolved Microfocused Small-Angle X-Ray Scattering Investigation of the Microfluidic Concentration of Charged Nanoparticles. *Eur. Phys. J. E.* 2011, *34*, 1–7.
- (74) Salmon, J. B.; Leng, J. Application of Microevaporators to Dynamic Exploration of the Phase Diagram. *J. Appl. Phys.* 2010, *107*, 1–10.
- (75) Ziane, N. Outils Microfluidiques pour l'Exploration de Diagrammes de Phase: De La Pervaporation à la Microdialyse, Université de Bordeaux, 2015.
- (76) Angly, J.; Iazzolino, A.; Salmon, J. B.; Leng, J.; Chandran, S. P.; Ponsinet, V.; Désert, A.; Le Beulze, A.; Mornet, S.; Tréguer-Delapierre, M.; Correa-Duarte, Miguel A. Microfluidic-Induced Growth and Shape-up of Three-Dimensional Extended Arrays of Densely Packed Nanoparticles. *ACS Nano* 2013, *7*, 6465–6477.
- (77) Ramsden, W. Separation of Solids in the Surface-Layers of Solutions and 'Suspensions' (Observations on Surface-Membranes, Bubbles, Emulsions, and Mechanical Coagulation). -- Preliminary Account. *Proc. R. Soc. Lond.* 1903, *72*, 156-164.
- (78) Pickering, S. U. Emulsions. *J. Chem. Soc., Trans.* 1907, *91*, 2001–2021.
- (79) Levine, S.; Bowen, B. D.; Partridge, S. J. Stabilization of Emulsions by Fine Particles I. Partitioning of Particles between Continuous Phase and Oil/water Interface. *Colloids and Surfaces* 1989, *38*, 325–343.
- (80) Velev, O. D.; Furusawa, K.; Nagayama, K. Assembly of Latex Particles by Using Emulsion Droplets as Templates .1. Microstructured Hollow Spheres. *Langmuir* 1996, *12*, 2374–2384.
- (81) Tang, J.; Quinlan, P. J.; Tam, K. C. Stimuli-Responsive Pickering Emulsions: Recent Advances and Potential Applications. *Soft Matter* 2015, *11*, 3512–3529.
- (82) Norton, J. E.; Norton, I. T. Designer Colloids-towards Healthy Everyday Foods? *Soft Matter* 2010, *6*, 3735–3742.
- (83) Bragg, J. R. Oil Recovery Method Using an Emulsion. U.S. 5927404, 1999.
- (84) Sullivan, A. P.; Kilpatrick, P. K. The Effects of Inorganic Solid Particles on Water and Crude Oil Emulsion Stability. *Ind. Eng. Chem. Res.* 2002, *41*, 3389–3404.
- (85) Simovic, S.; Prestidge, C. A. Nanoparticle Layers Controlling Drug Release from Emulsions. *Eur. J. Pharm. Biopharm.* 2007, *67*, 39–47.
- (86) Frelichowska, J.; Bolzinger, M.-A.; Chevalier, Y. Pickering Emulsions with Bare Silica. *Colloids Surfaces A Physicochem. Eng. Asp.* 2009, *343*, 70–74.
- (87) Binks, B. P.; Lumsdon, S. O. Pickering Emulsions Stabilized by Monodisperse Latex Particles: Effects of Particle Size. *Langmuir* 2001, *17*, 4540–4547.
- (88) Cui, Z. G.; Shi, K. Z.; Cui, Y. Z.; Binks, B. P. Double Phase Inversion of Emulsions Stabilized by a Mixture of CaCO₃ Nanoparticles and Sodium Dodecyl Sulphate. *Colloids Surfaces A Physicochem. Eng. Asp.* 2008, *329*, 67–74.

- (89) Wang, X.; Zhou, W.; Cao, J.; Liu, W.; Zhu, S. Preparation of Core-Shell CaCO₃ Capsules via Pickering Emulsion Templates. *J. Colloid Interface Sci.* 2012, *372*, 24–31.
- (90) Gelot, A.; Friesen, W.; Hamza, H. A. Emulsification of Oil and Water in the Presence of Finely Divided Solids and Surface-Active Agents. *Colloids and Surfaces* 1984, *12*, 271–303.
- (91) Ngai, T.; Auweter, H.; Behrens, S. H. Environmental Responsiveness of Microgel Particles and Particle-Stabilized Emulsions. *Macromolecules* 2006, *39*, 8171–8177.
- (92) Duan, H.; Wang, D.; Kurth, D. G.; Möhwald, H. Directing Self-Assembly of Nanoparticles at Water/oil Interfaces. *Angew. Chemie - Int. Ed.* 2004, *43*, 5639–5642.
- (93) Lin, Y.; Böker, A.; Skaff, H.; Cookson, D.; Dinsmore, A. D.; Emrick, T.; Russell, T. P. Nanoparticle Assembly at Fluid Interfaces : Structure and Dynamics. *Langmuir* 2005, *21*, 191–194.
- (94) Destribats, M. Emulsions Stabilisées Par Des Particules Colloïdales Stimulables : Propriétés Fondamentales et Matériaux, Université de Bordeaux, 2010.
- (95) Finkle, P.; Draper, H. D.; Hildebrand, J. H. The Theory of Emulsification. *J. Am. Chem. Soc.* 1923, *45*, 2780–2788.
- (96) Schulman, J. H.; Leja, J. Control of Contact Angles at the Oil-Water-Solid Interfaces. *Trans. Far. Soc.* 1954, *50*, 598–605.
- (97) Binks, B. P.; Lumsdon, S. O. Catastrophic Phase Inversion of Water-in-Oil Emulsions Stabilized by Hydrophobic Silica. *Langmuir* 2000, *16*, 2539–2547.
- (98) Aveyard, R.; Binks, B. P.; Clint, J. H. Emulsions Stabilized Solely by Colloidal Particles. *Adv. Colloid Interface Sci.* 2003, *100–102*, 503–546.
- (99) Nie, Z.; Petukhova, A.; Kumacheva, E. Properties and Emerging Applications of Self-Assembled Structures Made from Inorganic Nanoparticles. *Nat. Nanotechnol.* 2010, *5*, 15–25.
- (100) Binks, B. P.; Fletcher, P. D. I. Particles Adsorbed at the Oil - Water Interface : A Wettability and “ Janus ” Particles. *Langmuir* 2001, *17*, 4708–4710.
- (101) Madivala, B.; Vandebril, S.; Fransaeer, J.; Vermant, J. Exploiting Particle Shape in Solid Stabilized Emulsions. *Soft Matter* 2009, *5*, 1717.
- (102) Binks, B. P.; Lumsdon, S. O. Effects of Oil Type and Aqueous Phase Composition on Oil Water Mixtures Containing Particles of Intermediate Hydrophobicity. *Phys. Chem. Chem. Phys.* 2000, *2*, 2959–2967.
- (103) Marinova, K. G.; Alargova, R. G.; Denkov, N. D.; Velev, O. D.; Petsev, D. N.; Ivanov, I. B.; Borwankar, R. P. Charging of Oil - Water Interfaces Due to Spontaneous Adsorption of Hydroxyl Ions. *Langmuir* 1996, *4*, 2045–2051.
- (104) Leunissen, M. E.; van Blaaderen, A.; Hollingsworth, A. D.; Sullivan, M. T.; Chaikin, P. M.

- Electrostatics at the Oil-Water Interface, Stability, and Order in Emulsions and Colloids. *Proc. Natl. Acad. Sci. U. S. A.* 2007, *104*, 2585–2590.
- (105) Giermanska-Kahn, J.; Laine, V.; Arditty, S.; Schmitt, V.; Leal-Calderon, F. Particle-Stabilized Emulsions Comprised of Solid Droplets. *Langmuir* 2005, *21*, 4316–4323.
- (106) Westcott, S. L.; Oldenburg, S. J.; Lee, T. R.; Halas, N. J. Formation and Adsorption of Clusters of Gold Nanoparticles onto Functionalized Silica Nanoparticle Surfaces. *Langmuir* 1998, *14*, 5396–5401.
- (107) Fokkink, L. G. J.; Ralston, J. Contact Angles on Charged Substrates. *Colloids and Surfaces* 1989, *36*, 69–76.
- (108) Binks, B. P.; Rodrigues, J. A. Inversion of Emulsions Stabilized Solely by Ionizable Nanoparticles. *Angew. Chemie - Int. Ed.* 2005, *44*, 441–444.
- (109) Golemanov, K.; Tcholakova, S.; Kralchevsky, P. A.; Ananthapadmanabhan, K. P.; Lips, A. Latex-Particle-Stabilized Emulsions of Anti-Bancroft Type. *Langmuir* 2006, *22*, 4968–4977.
- (110) Gautier, F.; Destribats, M.; Perrier-Cornet, R. Dechézelles, J.-F.; Giermanska, J.; Héroguez, V.; Ravaine, S.; Leal-Calderon, F.; and Schmitt, V. Pickering Emulsions with Stimulable Particles: From Highly- to Weakly-Covered Interfaces. *Phys. Chem. Chem. Phys.* 2007, *9*, 6455–6462.
- (111) Arditty, S.; Whitby, C. P.; Binks, B. P.; Schmitt, V.; Leal-Calderon, F. Some General Features of Limited Coalescence in Solid-Stabilized Emulsions. *Eur. Phys. J. E* 2003, *11*, 273–281.
- (112) McGorty, R.; Fung, J.; Kaz, D.; Manoharan, V. N. Colloidal Self-Assembly at an Interface. *Mater. Today* 2010, *13*, 34–42.
- (113) Nikolaidis, M. *Colloids at Liquid-Liquid Interfaces*, Université de Munich, 2001.
- (114) Chan, D. Y. C.; Henry, J. D.; White, L. R. The Interaction of Colloidal Particles Collected at Fluid Interfaces. *J. Colloid Interface Sci.* 1981, *79*, 410–418.
- (115) Binks, B.; Horozov, T. *Colloidal Particles at Liquid Interfaces*; Cambridge University Press, 2006.
- (116) Dinsmore, A. D.; Hsu, M. F.; Nikolaidis, M. G.; Marquez, M.; Bausch, A. R.; Weitz, D. A. Colloidosomes: Selectively Permeable Capsules Composed of Colloidal Particles. *Science* 2002, *298*, 1006–1009.
- (117) Hsu, M. F.; Nikolaidis, M. G.; Dinsmore, A. D.; Bausch, A. R.; Gordon, V. D.; Chen, X.; Hutchinson, J. W.; Weitz, D. A.; Marquez, M. Self-Assembled Shells Composed of Colloidal Particles: Fabrication and Characterization. *Langmuir* 2005, *21*, 2963–2970.

- (118) Thompson, K. L.; Armes, S. P.; Howse, J. R.; Ebbens, S.; Ahmad, I.; Zaidi, J. H. York, D. W. Burdis, J. A. Covalently Cross-Linked Colloidosomes. *Macromolecules* 2010, 43, 10466–10474.
- (119) Fielding, L. A.; Armes, S. P. Preparation of Pickering Emulsions and Colloidosomes Using either a Glycerol- Functionalised Silica Sol or Core – Shell Polymer / Silica Nanocomposite Particles. *J. Mater. Chem.* 2012, 22, 11235–11244.
- (120) Bon, S. A. F.; Cauvin, S.; Colver, P. J. Colloidosomes as Micron-Sized Polymerisation Vessels to Create Supracolloidal Interpenetrating Polymer Network Reinforced Capsules. *Soft Matter* 2007, 3, 194–199.
- (121) Patra, D. Colloidal Microcapsules : Surface Engineering of Nanoparticles for Interfacial Assembly, University of Massachusetts, 2011.
- (122) Zhao, Y.; Li, Y.; Demco, D. E.; Zhu, X.; Möller, M. Microencapsulation of Hydrophobic Liquids in Closed All-Silica Colloidosomes. *Langmuir* 2014, 30, 4253–4261.
- (123) Wang, H.; Zhu, X.; Tsarkova, L.; Pich, A.; Möller, M. All-Silica Colloidosomes with a Particle-Bilayer Shell. *ACS Nano* 2011, 5, 3937–3942.
- (124) You, J. O.; Rafat, M.; Auguste, D. T. Cross-Linked, Heterogeneous Colloidosomes Exhibit pH-Induced Morphogenesis. *Langmuir* 2011, 27, 11282–11286.
- (125) Lawrence, D. B.; Cai, T.; Hu, Z.; Marquez, M.; Dinsmore, A. D. Temperature-Responsive Semipermeable Capsules Composed of Colloidal Microgel Spheres. *Langmuir* 2007, 23, 395–398.
- (126) Shah, R. K.; Kim, J. W.; Weitz, D. A. Monodisperse Stimuli-Responsive Colloidosomes by Self-Assembly of Microgels in Droplets. *Langmuir* 2010, 26, 1561–1565.
- (127) Zhang, C.; Hu, C.; Zhao, Y.; Yan, K.; Zhu, X. Encapsulation of Laccase in Silica Colloidosomes for Catalysis in Organic Media. 2013.
- (128) Noble, P. F.; Cayre, O. J.; Alargova, R. G.; Velev, O. D.; Paunov, V. N. Fabrication Of “hairy” colloidosomes with Shells of Polymeric Microrods. *J. Am. Chem. Soc.* 2004, 126 (26), 8092–8093.
- (129) Cauvin, S.; Colver, P. J.; Bon, S. A. F. Polymerization: Preparation of Clay. *Macromolecules* 2005, 38, 7887–7889.
- (130) Lee, B. D.; Weitz, D. A. Double Emulsion-Templated Nanoparticle Colloidosomes with Selective Permeability. 2008, 3498–3503.
- (131) Lee, D.; Weitz, D. A. Nonspherical Colloidosomes with Multiple Compartments from Double Emulsions. *Small* 2009, 5, 1932–1935.
- (132) Subramaniam, A. B.; Abkarian, M.; Stone, H. a. Controlled Assembly of Jammed Colloidal Shells on Fluid Droplets. *Nat. Mater.* 2005, 4, 553–556.
- (133) San-Miguel A, L. H. *Microfluidics as a Tool for C. Elegans Research.*; 2013.

- (134) McDonald, J. C.; Whitesides, G. M. Poly(dimethylsiloxane) as a Material for Fabricating Microfluidic Devices. *Acc. Chem. Res.* 2002, 35, 491–499.
- (135) Angly, J. Assemblage par Évaporation Microfluidique: De la Dispersion Diluée aux États Denses de Nanoparticules d'Or, Bordeaux, 2013.
- (136) Raimundo, D. S.; Fernandez, F. J. R.; Salcedo, W. J. Self-Assembled Polystyrene Micro-Spheres Applied for Photonic Crystals and Templates Fabrication. *J. Integr. Circuits Syst.* 2006, 1, 39–43.
- (137) Armstrong, E.; O'Dwyer, C. Artificial Opal Photonic Crystals and Inverse Opal Structures – Fundamentals and Applications from Optics to Energy Storage. *J. Mater. Chem. C* 2015, 3, 6109–6143.
- (138) Jana, N. R. Nanorod Shape Separation Using Surfactant Assisted Self-Assembly. *Chem. Commun.* 2003, March, 1950–1951.
- (139) Baron, A.; Iazzolino, A.; Ehrhardt, K.; Salmon, J.-B.; Aradian, A.; Kravets, V.; Grigorenko, A. N.; Leng, J.; Le Beulze, A.; Tréguer-Delapierre, M.; Correa-Duarte, Miguel A.; Barois, Philippe Bulk Optical Metamaterials Assembled by Microfluidic Evaporation. *Opt. Mater. Express* 2013, 3, 1792–1797.
- (140) Venditti, I. Gold Nanoparticles in Photonic Crystals Applications: A Review. *Materials* 2017, 10, 1–18.
- (141) Samanta, B.; Patra, D.; Subramani, C.; Ofir, Y.; Yesilbag, G.; Sanyal, A.; Rotello, V. M. Stable Magnetic Colloidosomes via Click-Mediated Crosslinking of Nanoparticles at Water-Oil Interfaces. *Small* 2009, 5, 685–688.
- (142) Saien, J.; Akbari, S. Interfacial Tension of Toluene + Water + Sodium Dodecyl Sulfate from 20 to 50°C and pH between 4 and 9. *J. Chem. Eng. Data* 2006, 51, 1832–1835.
- (143) Graf, C.; Dembski, S.; Hofmann, A.; Rühl, E. A General Method for the Controlled Embedding of Nanoparticles in Silica Colloids. *Langmuir* 2006, 22, 5604–5610.
- (144) Graf, C.; Vossen, D. L. J.; Imhof, A.; Blaaderen, A. Van. A General Method To Coat Colloidal Particles with Silica. *Langmuir* 2003, 19, 6693–6700.
- (145) Xia, H.; Bai, S.; Hartmann, J.; Wang, D. Synthesis of Monodisperse Quasi-Spherical Gold Nanoparticles in Water via Silver (I)-Assisted Citrate Reduction. *Langmuir* 2010, 26, 3585–3589.
- (146) Myroshnychenko, V.; Rodríguez-Fernández, J.; Pastoriza-Santos, I.; Funston, A. M.; Novo, C.; Mulvaney, P.; Liz-Marzán, L. M.; García de Abajo, F. J. Modelling the Optical Response of Gold Nanoparticles. *Chem. Soc. Rev.* 2008, 37, 1792–1805.
- (147) Agnihotri, S.; Mukherji, S.; Mukherji, S. Size-Controlled Silver Nanoparticles Synthesized over the Range 5–100 nm using the same protocol and their Antibacterial Efficacy. *RSC Adv.* 2014, 4, 3974–3983.

- (148) Carreira, A. S.; Teixeira, R. F. A.; Beirão, A.; Vieira, R. V.; Figueiredo, M. M.; Gil, M. H. Preparation of Acrylic Based Microcapsules Using Different Reaction Conditions for Thermo-Regulating Textiles Production. *Eur. Polym. J.* 2017, *NA*, NA.
- (149) Sánchez, Luz; Sánchez, Paula; de Lucas, Antonio; Carmona, Manuel; Rodríguez, Juan F. Microencapsulation of PCMs with a Polystyrene. *Colloid Polym. Sci.* 2007, *285*, 1377–1385.
- (150) Sánchez-silva, L.; Rodríguez, J. F.; Romero, A.; Borreguero, A. M.; Carmona, M.; Sánchez, P. Microencapsulation of PCMs with a Styrene-Methyl Methacrylate Copolymer Shell by Suspension-like Polymerisation. *Chem. Eng. J.* 2010, *157*, 216–222.
- (151) Bingyi, L. I.; Hi, Y. S.; Hu, W. Z.; Zhifeng, F. U.; Ang, W. Y. Synthesis of Amphiphilic Polystyrene-B-Poly(acrylic Acid) Diblock Copolymers by Iodide-Mediated Radical Polymerization. *Polym. J.* 2006, *38*, 387–394.
- (152) Shen, Z.; Chen, Y.; Barriau, E.; Frey, H. Multi-Arm Star Polyglycerol- Block-Poly(tert - Butyl Acrylate) and the Respective Multi-Arm Poly(acrylic Acid) Stars. *Macromolecular Chem. Phys.* 2006, *207*, 57–64.
- (153) Crow. Polymer Properties Database, <http://polymerdatabase.com/>, (accessed Jul 1, 2017).
- (154) Rojanathanes, R.; Sereemasapun, A.; Pimpha, N.; Buasorn, V.; Ekawong, P.; Wiwanitkit, V. Gold Nanoparticle as an Alternative Tool for a Urine Pregnancy Test. *Taiwan. J. Obstet. Gynecol.* 2008, *47*, 296–299.
- (155) Ali, M. E.; Hashim, U.; Mustafa, S.; Che Man, Y. B.; Adam, T.; Humayun, Q. Nanobiosensor for the Detection and Quantification of Pork Adulteration in Meatball Formulation. *J. Exp. Nanosci.* 2014, *9*, 152–160.
- (156) Tokareva, I.; Minko, S.; Fendler, J. H.; Hutter, E. Nanosensors Based on Responsive Polymer Brushes and Gold Nanoparticle Enhanced Transmission Surface Plasmon Resonance Spectroscopy. *J. Am. Chem. Soc.* 2004, *126*, 15950–15951.
- (157) Lange, H.; Juárez, B. H.; Carl, A.; Richter, M.; Bastús, N. G.; Weller, H.; Thomsen, C.; Von Klitzing, R.; Knorr, A. Tunable Plasmon Coupling in Distance-Controlled Gold Nanoparticles. *Langmuir* 2012, *28*, 8862–8866.
- (158) Liu, Y.; Han, X.; He, L.; Yin, Y. Thermoresponsive Assembly of Charged Gold Nanoparticles and their Reversible Tuning of Plasmon Coupling. *Angew. Chemie - Int. Ed.* 2012, *51*, 6373–6377.
- (159) D'souza, S. L.; Pati, R. K.; Kailasa, S. K. Ascorbic Acid Functionalized Gold Nanoparticles as a Probe for Colorimetric and Visual Read-out Determination of Dichlorvos in Environmental Samples. *Anal. Methods* 2014, *6*, 9007–9014.
- (160) Naebe, M.; Abolhasani, M. M.; Khayyam, H.; Amini, A.; Fox, B. Crack Damage in Polymers and Composites: A Review. *Polym. Rev.* 2016, *56*, 31–69.
- (161) Jiang, H.; Browning, R.; Sue, H. J. Understanding of Scratch-Induced Damage Mechanisms

- in Polymers. *Polymer* 2009, 50, 4056–4065.
- (162) Kambour, R. P. A Review of Craze and Fracture in Thermoplastics. *J. Polym. Sci. Macromol. Rev.* 1973, 7, 1–154.
- (163) Pawlak, A.; Galeski, A. Determination of Stresses around Beads in Stressed Epoxy Resin by Photoelasticity. *J. Appl. Polym. Sci.* 2002, 86, 1436–1444.
- (164) Shiga, T.; Narita, T.; Tachi, K.; Okada, A.; Takahashi, H.; Kurauchi, T. Measurement of Internal Stresses in Coatings Using Time Resolved Fluorescence. *Polym. Eng. Sci.* 1997, 37 (1), 24–30.
- (165) Davis, D. A.; Hamilton, A.; Yang, J.; Cremar, L. D.; Gough, D. Van; Potisek, S. L.; Ong, M. T.; Braun, P. V; Martínez, T. J.; White, S. R.; Moore, Jeffrey S.; Sottos, N. R. Force-Induced Activation of Covalent Bonds in Mechanoresponsive Polymeric Materials. *Nature* 2009, 459 (7243), 68–72.
- (166) Klajn, R. Spiropyran-Based Dynamic Materials. *Chem. Soc. Rev.* 2014, 43, 148–184.
- (167) Crenshaw, B. R.; Weder, C. Self-Assessing Photoluminescent Polyurethanes. *Macromolecules* 2006, 39, 9581–9589.
- (168) Crenshaw, B. R.; Weder, C. Phase Separation of Excimer-Forming Fluorescent Dyes and Amorphous Polymers : A Versatile Mechanism for Sensor Applications . *Adv. Mater.* 2005, 17, 1471–1476.
- (169) Crenshaw, B. R.; Burnworth, M.; Khariwala, D.; Hiltner, A.; Mather, P. T.; Simha, R.; Weder, C. Deformation-Induced Color Changes in Mechanochromic Polyethylene Blends. *Macromolecules* 2007, 40, 2400–2408.
- (170) Cellini, F.; Block, L.; Li, J.; Khapli, S.; Peterson, S. D.; Porfiri, M. Mechanochromic Response of Pyrene Functionalized Nanocomposite Hydrogels. *Sensors Actuators B Chem.* 2016, 234, 510–520.
- (171) Kling, S.; Czigány, T. Damage Detection and Self-Repair in Hollow Glass Fiber Fabric-Reinforced Epoxy Composites via Fiber Filling. *Compos. Sci. Technol.* 2014, 99, 82–88.
- (172) Li, W.; Matthews, C. C.; Yang, K.; Odarczenko, M. T.; White, S. R.; Sottos, N. R. Autonomous Indication of Mechanical Damage in Polymeric Coatings. *Adv. Mater.* 2016, 28, 2189–2194.
- (173) Odom, S. A.; Jackson, A. C.; Prokup, A. M.; Chayanupatkul, S.; Sottos, N. R.; White, S. R.; Moore, J. S. Visual Indication of Mechanical Damage using Core–Shell Microcapsules. *Appl. Mater. Interfaces* 2011, 3, 4547–4551.
- (174) Credico, B. Di; Gri, G.; Levi, M.; Turri, S. Microencapsulation of a UV-Responsive Photochromic Dye by Means of Novel UV-Screening Polyurea-Based Shells for Smart Coating Applications. *Appl. Mater. Interfaces* 2013, 5, 6628–6634.
- (175) Vidinejevs, S.; Aniskevich, A. N.; Gregor, A.; Sjöberg, M.; Alvarez, G. Smart Polymeric Coatings for Damage Visualization in Substrate Materials. *J. Intell. Mater. Syst. Struct.*

- 2012, 23, 1371–1377.
- (176) Vidinejevs, S.; Strelakova, O.; Aniskevich, A.; Gaidukov, S. Development of a Composite with an Inherent Function of Visualization of a Mechanical Action. *Mech. Compos. Mater.* 2013, 49, 77–84.
- (177) Löwe, C.; Weder, C. Oligo(p-Phenylene Vinylene) Excimers as Molecular Probes: Deformation-Induced Color Changes in Photoluminescent Polymer Blends. *Adv. Mater.* 2002, 14, 1625–1629.
- (178) Crenshaw, B. R.; Weder, C. Deformation-Induced Color Changes in Melt-Processed Photoluminescent Polymer Blends. *Chem. Mater.* 2003, 15, 4717–4724.
- (179) Roberts, D. R. T.; Holder, S. J. Mechanochromic Systems for the Detection of Stress, Strain and Deformation in Polymeric Materials. *J. Mater. Chem.* 2011, 21, 8256–8268.
- (180) Kinami, M.; Crenshaw, B. R.; Weder, C. Polyesters with Built-in Threshold Temperature and Deformation Sensors. *Chem. Mater.* 2006, 18, 946–955.
- (181) Klajn, R. Immobilized Azobenzenes for the Construction of Photoresponsive Materials. *Pure Appl. Chem.* 2010, 82, 2247–2279.
- (182) Han, X.; Liu, Y.; Yin, Y. Colorimetric Stress Memory Sensor Based on Disassembly of Gold Nanoparticle Chains. *Nano Lett.* 2014, 14, 2466–2470.
- (183) Fernández-López, C.; Mateo-Mateo, C.; Álvarez-Puebla, R. A.; Pérez-Juste, J.; Pastoriza-Santos, I.; Liz-Marzán, L. M. Highly Controlled Silica Coating of PEG-Capped Metal Nanoparticles and Preparation of SERS-Encoded Particles. *Langmuir* 2009, 25, 13894–13899.
- (184) Hodge, I. M.; Hodge, I. M. Physical Aging in Polymer Glasses. *Science.* 1995, 267, 1945–1947.
- (185) Cangialosi, D.; Boucher, V. M.; Alegria, A.; Colmenero, J. Physical Aging in Polymers and Polymer Nanocomposites : Recent Results and Open Questions. *Soft Matter* 2013, 9, 8619–8630.
- (186) Guirguis, O. W.; Moselhey, M. T. H. Thermal and Structural Studies of Poly (Vinyl Alcohol) and Hydroxypropyl Cellulose Blends. *Nat. Sci.* 2012, 4, 57–67.
- (187) Jin, Z.; Su, Y.; Duan, Y. Improved Optical pH Sensor Based on Polyaniline. *Sensors Actuators B Chem.* 2000, 71, 118–122.
- (188) Kreft, O.; Mun, A.; Sukhorukov, B.; Parak, W. J. Polymer Microcapsules as Mobile Local pH-Sensors. *J. Mater. Chem.* 2007, 17, 4471–4476.
- (189) Shen, Y.; Kuang, M.; Shen, Z.; Nieberle, J.; Duan, H.; Frey, H. Gold Nanoparticles Coated with a Thermosensitive Hyperbranched Polyelectrolyte : Towards Smart Temperature and pH Nanosensors. *Angew. Chemie - Int. Ed.* 2008, 47, 2227–2230.
- (190) Kim, B.; Shin, Y. pH-Sensitive Swelling and Release Behaviors of Anionic Hydrogels for

- Intelligent Drug Delivery System. *J. Appl. Polym. Sci.* 2007, *105*, 3656–3661.
- (191) Rieka, J.; Tanaka, T. Swelling of Ionic Gels: Quantitative Performance of the Donnan Theory. *Macromolecules* 1984, *17*, 2916–2921.
- (192) Ruiz-Pérez, L.; Pryke, A.; Sommer, M.; Battaglia, G.; Soutar, I.; Swanson, L.; Geoghegan, M. Conformation of Poly(methacrylic Acid) Chains in Dilute Aqueous Solution. *Macromolecules* 2008, *41*, 2203–2211.
- (193) Ikawa, T.; Abe, K.; Honda, K.; Tsuchida, E. Interpolymer Complex between Poly (Ethylene Oxide) and Poly(Carboxylic Acid). *J. Polym. Sci. Polym. Chem. Ed.* 1975, *13*, 1505–1514.
- (194) Ibarra-Montaña, E. L.; Rodríguez-Laguna, N.; Sánchez-Hernández, A.; Rojas-Hernández, A. Determination of pK_a Values for Acrylic, Methacrylic and Itaconic Acids by ¹H and ¹³C NMR in Deuterated Water. *J. Appl. Solut. Chem. Model.* 2015, *4*, 7–18.
- (195) Bendejacq, D. D.; Ponsinet, V. Double-Polyelectrolyte, Like-Charged Amphiphilic Diblock Copolymers: Swollen Structures and pH- and Salt-Dependent Lyotropic Behavior. *J. Phys. Chem. B* 2008, *112*, 7996–8009.
- (196) Borukhov, I.; Andelman, D.; Borrega, R.; Cloitre, M.; Leibler, L.; Orland, H. Polyelectrolyte Titration: Theory and Experiment. *J. Phys. Chem. B* 2000, *104*, 11027–11034.

Annex 1: Characterizations

Chromatography analysis: Size exclusion chromatography was conducted on two Oligopore columns in series with an Agilent refractive index detector in negative polarity. The mobile phase used was toluene at a flow rate of 1 mL/min. The sample was dissolved in toluene at a concentration of 1%. Calibration with polystyrene standards was used to estimate the molecular weight. The analysis gave $M_n = 766$ g/mol, $M_w = 1235$ g/mol and $PD = 1.61$.

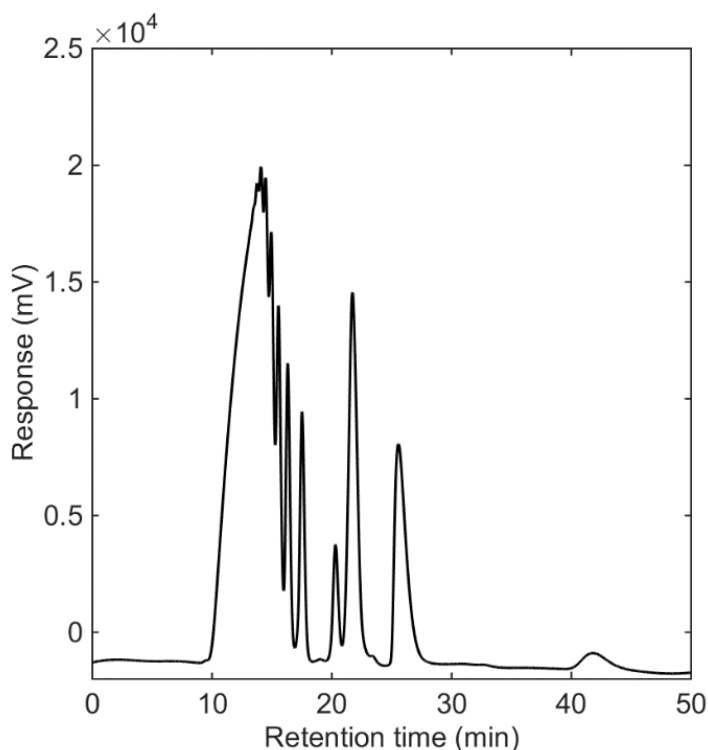


Figure 141: Chromatogram of PEOS.

NMR analysis: The sample was analyzed in ^1H and ^{13}C on a Bruker Avance 500 MHz, after dilution in CDCl_3 . Standard conditions have been used to record NMR experiments. NMR spectra of PEOS sample are shown in Figure 142 and Figure 143. They are compatible with the expected molecule. An addition of EtOH (ethanol) has been done in the PEOS sample in order to validate the different signal assignments. The so obtained spectra are compared with the one from the PEOS alone. Two environments are clearly observed in both ^1H and ^{13}C spectra, a main one resulting from the PEOS (1.2 and 3.8 ppm in ^1H / 17.8 and 59.1 ppm in ^{13}C), a minor one resulting from the presence of EtOH (certainly from a partial hydrolysis of the PEOS, detected at 1.1 and 3.7 ppm in ^1H / 18.3 and 58.1 ppm in ^{13}C).

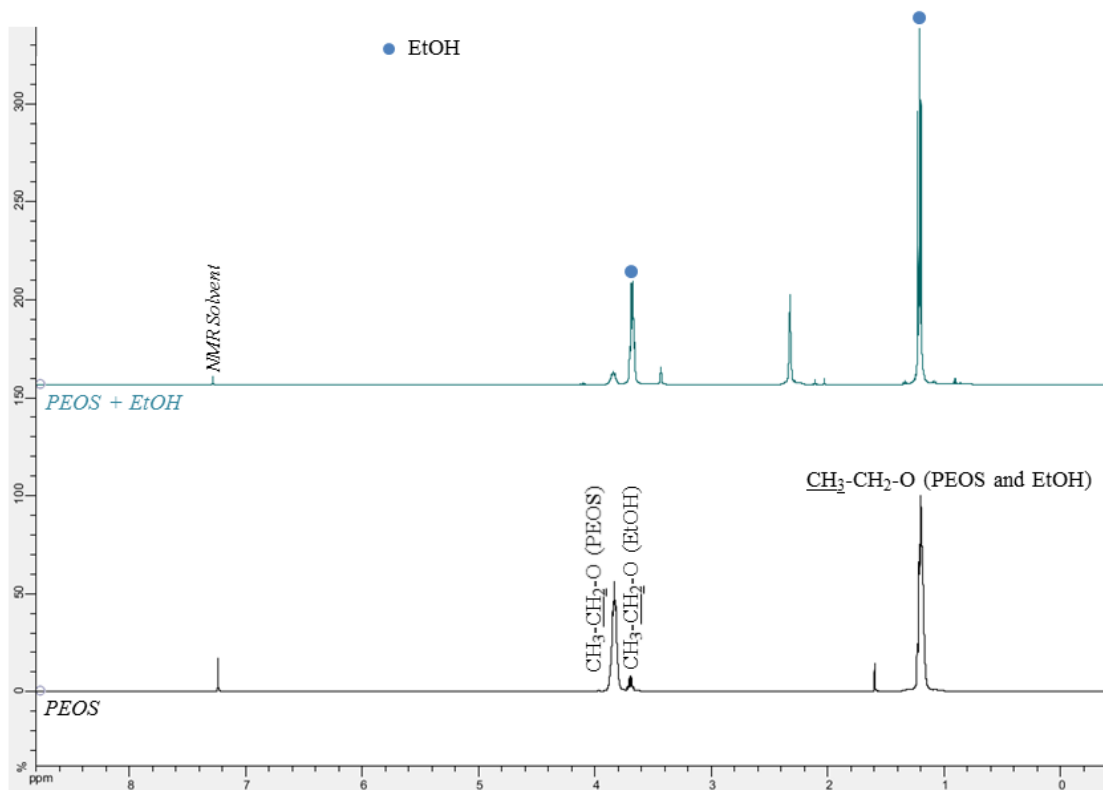


Figure 142: $^1\text{H-NMR}$ spectra of PEOS and PEOS with ethanol.

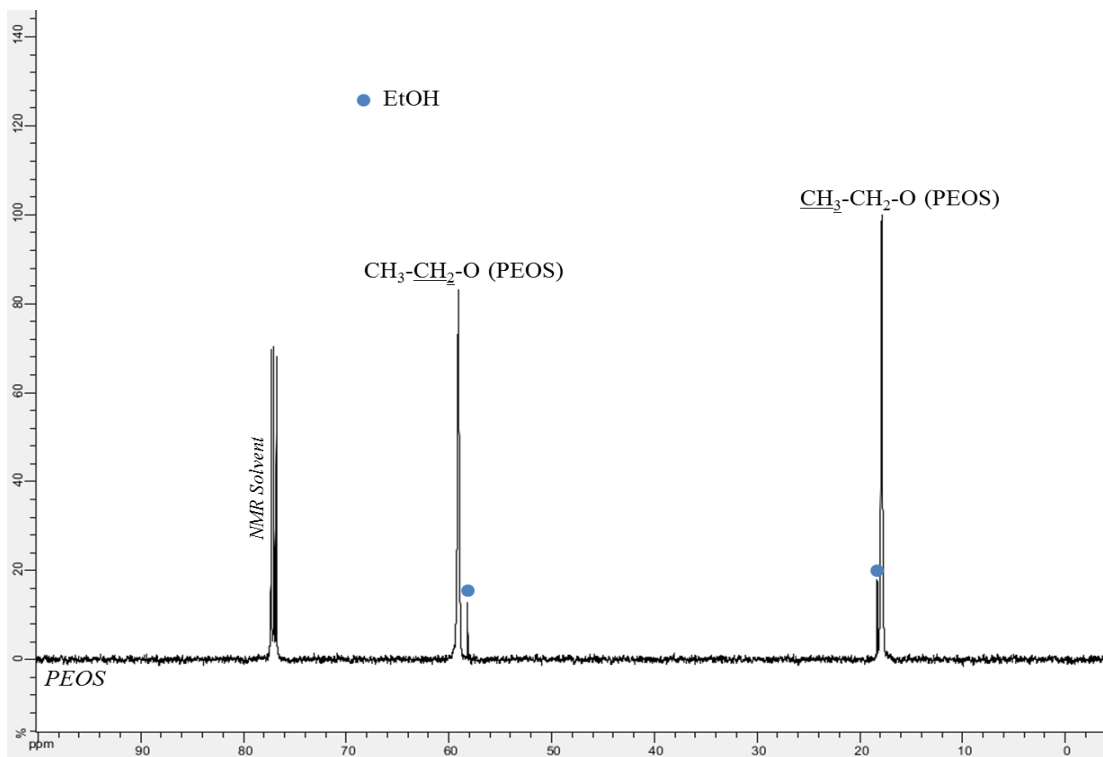


Figure 143: $^{13}\text{C-NMR}$ spectra of PEOS.

Plasmonic-Based Mechanochromic Microcapsules as Strain Sensors

Céline. A. S. Burel, Ahmed Alsayed, Ludivine Malassis, Christopher B. Murray, Bertrand Donnio, and Rémi Dreyfus*

Efficiently detecting mechanical deformations within materials is critical in a wide range of devices, from micro-electromechanical systems to larger structures in the aerospace industry. This communication reports the fabrication of new mechanochromic micrometer-size capsules enabling the detection of strains. These microcapsules are synthesized using an emulsification approach. They are made of densely packed gold nanoparticles embedded in a spherical silica crust. Billions of these composite spherical microcapsules are fabricated in a single batch. Each microcapsule is an opto-mechanosensor by itself, and can easily be recovered and incorporated into polymer films. When the films are stretched, the microcapsules are deformed into elongated ellipsoidal shapes and the distance between the Au NPs embedded in their shells concomitantly increases. As the extinction of Au NPs depends on the separation between the Au NPs, microcapsules exhibit different colors when they are elongated. These novel sensitive microcapsules can be used to detect and measure strain in polymer films by outputting color information.

Polymeric materials such as plastics, composites, and coatings are commonly used in many daily applications. These materials may be subject to high stresses, which can lead to deformations, defects, or cracks and entail the diminution of their performances.^[1–5] Therefore, an efficient and reliable way to detect early strain is of high interest.

Dr. C. A. S. Burel, Dr. A. Alsayed,
Dr. L. Malassis, Dr. R. Dreyfus
Complex Assemblies of Soft Matter Laboratory
(COMPASS), UMI 3254
CNRS-Solvay-University of Pennsylvania
RIC, Bristol, PA 19007, USA
E-mail: rdreyfus@sas.upenn.edu

Prof. C. B. Murray
Department of Chemistry and Department
of Materials Science and Engineering
University of Pennsylvania
Philadelphia, PA 19104, USA

Dr. B. Donnio
Institut de Physique et Chimie des Matériaux de Strasbourg (IPCMS)
CNRS-Université de Strasbourg
UMR 7504, 67 034 Strasbourg, France

DOI: 10.1002/sml.201701925



Traditionally, most of the methods used to detect internal strain within polymeric films have mainly been invasive, destructive, and have not allowed for real-time in situ analysis.^[1,6,7] Recently, more direct and efficient techniques for the visual detection of deformations have been developed. These methods are based on the use of dye molecules, which are either encapsulated,^[8–11] crosslinked with the polymer matrix,^[12,13] or incorporated as simple additives within the polymer matrix.^[14–16] However, in many of these cases, the mechanochromic efficiency of the dispersed dyes depends on many factors including the type of polymer matrix, external parameters such as the temperature, an optimal phase separation between the dyes and the polymer host, and on the concentration of the dyes themselves.^[17–19]

Very recently, a new generation of optical sensors, which respond to mechanical strains have been developed. They are based on gold nanoparticles of which localized plasmon resonance maximum depends on surrounding environment and interparticle distance.^[20–23] Very few examples of those sensors exist and they rely on either assembling nanogold by lithography using classical top-down approaches,^[24] or on careful tuning of the particle dispersion ionic strength.^[25] Though very precise and efficient, these sensors lack versatility because their efficiency depends on the particle

compatibility with the polymeric substrates. Plasmonic-based micro or nanosensors that could be easily dispersed in a very diverse set of media such as polymer materials could have enormous impact in detecting and measuring in situ strains. Such sensors could lead to myriad applications where the early detection of deformations is critical: in small objects such as NEMS (nanoelectromechanical systems) or MEMS (microelectromechanical systems), also in small parts used in the airline and space industry, and in large objects such as dams or bridges. In those applications, the detection of the damages from the very early stage would leave the possibility to repair or replace the material before irreversible deterioration and possible catastrophes occur.

In this communication, we present a novel kind of strain sensors made of gold nanoparticles (Au NPs) embedded in silica microcapsules. We demonstrate how their optical properties respond to various mechanical stresses and how they can be used to detect and measure local deformations in materials. Briefly, these microcapsules are obtained from Pickering emulsions made of Au NPs adsorbed at an oil/water emulsion interface.^[26,27] Then a silanization reaction forms a silica crust around the Au NPs, locking the nanoparticles at the interface and giving the final shape to the Au NPs-silica (Au-Si) microcapsules, also named (Au-Si) colloidosomes.^[28–34] After insertion of the capsules in a stretchable polymer film, we detect a change in color of the microcapsules upon mechanical stress due to the shift in the plasmonic extinction maximum of the Au-Si microcapsules. The results presented in this work thus widen the horizons with regard to designing the next generations of optomechanical sensors based on the optical coupling between plasmonic nanoparticles.

The preparation of Au-Si microcapsules is illustrated in **Figure 1**. The first step consists in mixing an aqueous phase containing the Au NPs with an oily toluene phase in which polyethoxyorthosilicate (PEOS) is dissolved as schematically shown in **Figure 1a**. The two phases are then strongly agitated by sonication, forming an oil-in-water emulsion. We found that with the right conditions, that we will describe and explain, the Au NPs adsorb onto the oil droplets, as seen in **Figure 1b,c**, to form so-called Pickering emulsions. These emulsions are stable with no coarsening. To obtain this stable Pickering emulsion, three conditions have to be fulfilled: (i) Au NPs in the vicinity of droplets must adsorb at the interface by reaching a minimum of energy, (ii) the solution should contain enough Au NPs to cover the emulsion droplets, and (iii) the energy barrier hindering adsorption of Au NPs must be lowered. These three conditions guided our synthesis protocol.

(i) *Adsorption at the interface.* The adsorption of the Au NPs at the water/oil interface results from a decrease in the system free energy.^[33,35,36] Equation (1) shows the free energy of adsorption of a nanoparticle from the interface, where γ_{ow} is the oil/water interfacial tension (in our case, $\gamma_{ow} = 37.1 \text{ mN m}^{-1}$),^[37] θ_{ow} is the three-phase contact angle between the solid and the oil/water interface; R is the radius of the nanoparticles:

$$\Delta G = -\pi R^2 \gamma_{ow} (1 - |\cos(\theta_{ow})|)^2 \quad (1)$$

It is clear from Equation (1) that particles are best adsorbed at the interface for $\theta_{ow} = 90^\circ$, when particles have equal affinity for oil and water. To tune this property, the Au NPs were partially functionalized with poly(diallyldimethylammoniumnitrate-co-1-vinylpyrrolidone) (PVP-DADMAN, full structural formula available in **Figure S1** of the Supporting Information). PVP is a neutral amphiphilic polymer known to adsorb onto gold nanoparticles.^[38–40] The long backbone of the PVP results in increased hydrophobicity of the functionalized Au NPs, therefore facilitating the adsorption of the particles at the toluene/water interface by bringing the contact angle closer to 90° .

(ii) *Number of nanoparticles.* The number of nanoparticles necessary to form a stable Pickering emulsion can be approximately estimated from Equation (2) where N_p is the number of Au NPs needed to cover droplets of radius R with particles of radius r , f is the packing density of the particles and V is the total volume of the oil dispersed phase:

$$N_p = \frac{3fV}{\pi Rr^2} \quad (2)$$

The above equation is obtained by assuming that the nanoparticles are equally wet by the water and oil phases. An estimation shows that for 1 mL of dispersed phase, a surface packing fraction $f = 0.74$, nanoparticles of 40 nm in diameter, and colloidosomes of 10 μm in diameter; $\approx 10^{14}$ Au NPs are needed. However, the most common methods used to synthesize monodisperse 40 nm Au NPs use metal-ion assisted reduction, work at low concentration in gold salt, or require multiple syntheses steps.^[41–43] Therefore we chose to follow an easier synthesis approach at larger scale, adapted from the method explored by Malassis et al.^[44] and described in the Experimental Section. This straightforward one-step synthetic method using PVP-DADMAN as an Au NP capping agent led to polydisperse gold nanoparticles measured by transmission electron microscopy (TEM) image analyses. The mean diameter d was $d = 40 \text{ nm} \pm 25 \text{ nm}$. Interestingly, in this size range, the polydispersity does not alter much the optical response of the particles. This is consistent with the theoretical results of Myroshnychenko et al.,^[20] which show that in this range of Au NP diameters and surrounding refraction index, the position of the extinction peak shifts in a range of 20 nm. For these reasons, the polydispersity does not affect the position of the plasmonic peak but results in a small broadening of the peak. Indeed, the plasmonic peak maximum of this dispersion is at the same position as that of a monodisperse 40 nm dispersion of gold nanoparticles synthesized using traditional seed growth method (synthetic process available in the Supporting Information).^[41] TEM images, histograms, and extinction spectrum of the gold nanoparticles size distributions for monodisperse 40 nm particles and for our new synthetic method can be found in **Figures S2–S4** of the Supporting Information.

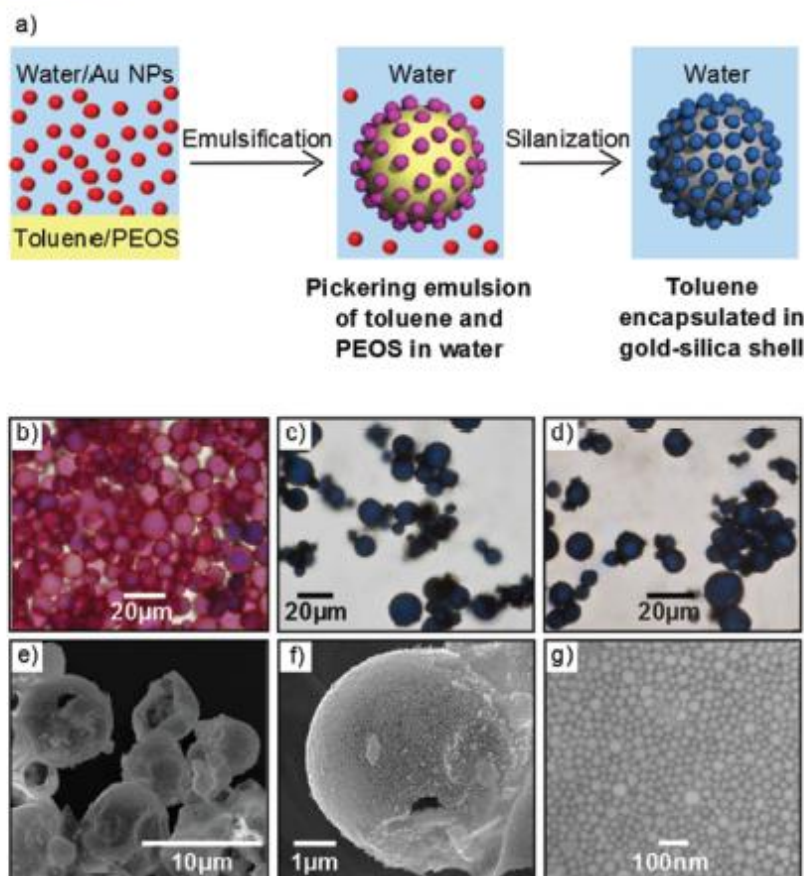


Figure 1. a) Schematic representation of the formation of gold–silica microcapsules. b–c) Optical microscope images of typical emulsions at 0.02 M of gold at pH \approx 1 right after sonication and after one day, respectively. d) Optical microscope images of typical microcapsules after polymerization at 0.02 M of gold and pH \approx 1. e,f) SEM images of microcapsules obtained at 0.02 M of gold and pH \approx 1. g) SEM image of a typical microcapsule surface covered by Au NPs at 0.02 M of gold and pH \approx 1.

(iii) *Decrease of an energy barrier.* Malassis et al. have shown that bare Au NPs were stable due to the presence of residual negative charges from ascorbic acid at their surface.^[44] Above pH = 4, Au NPs appear to be weakly negatively charged (ζ potential \approx -5 mV) and well dispersed in water showing a sharp plasmon peak ($\lambda \approx 527$ nm) and a red color as shown in the left picture of **Figure 2**. Below pH = 4, Au NPs seem to have no charge (ζ potential \approx 0 mV) and therefore flocculate forming a blue solution as seen in the right picture of **Figure 2** which has a large red-shifted plasmon peak ($\lambda \approx 720$ nm). By decreasing the pH below 4, the charges at the droplets surface are decreased thus cancelling any electrostatic repulsion and enabling the adsorption of Au NPs at the oil/water interface.

With all these three requirements fulfilled, we are able to synthesize an Au NPs-stabilized emulsion. Shortly after the sonication, the emulsion exhibits a strong pink color due to the adsorption of the AuNPs as seen in **Figure 1b**. The

emulsion becomes blue after one day as shown in **Figure 1c**. This change of color proves that nanoparticles adsorb and get more and more densely packed at the interface. The emulsion is then gently shaken mechanically for a few days to allow the formation of the silica shell by polymerization of the PEOS at the interface of the emulsion. PEOS is a very hydrophobic hyperbranched silica polymer (SEC (size exclusion chromatography) chromatogram, molecular weights, and polydispersity available in **Figure S5** of the Supporting Information) soluble in oil only. PEOS hydrolyzes at the emulsion interface and condensates to form a silica shell embedding the nanoparticles.^[29] After a day, the silica shell is visible by optical microscopy. It takes 3 d to fully convert the PEOS to a thin silica film because of the slow interfacial sol–gel reaction under acidic condition.^[29] Images of the dried microcapsules formed after 3 d are shown on **Figure 1d–g**. The color, shape, and size of the microcapsules were analyzed by optical microscopy and scanning electron microscopy (SEM). The resulting microcapsules are spherical with dimensions

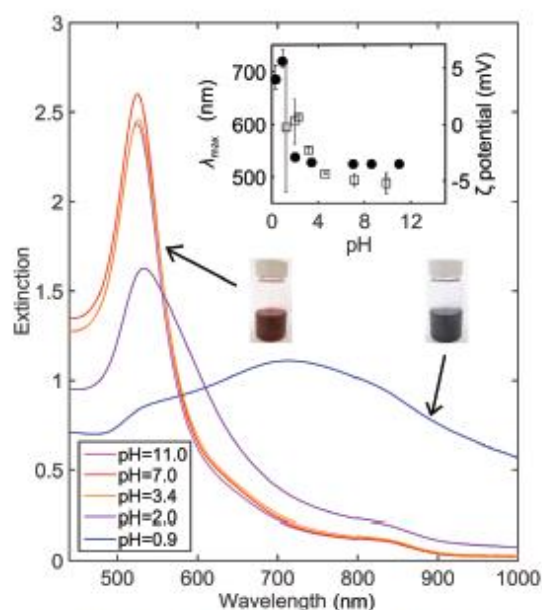


Figure 2. Plasmonic response of Au NPs solutions $[Au] = 0.57 \times 10^{-3} \text{ M}$ as a function of pH. The two pictures respectively show a well dispersed solution of Au NPs (red) and a solution of flocculated Au NPs (blue) of the same concentration. Inset: plasmonic peak maximum as a function of the pH (filled circular points) and Zeta potential of the Au NPs at $[Au] = 0.57 \times 10^{-3} \text{ M}$ as a function of the pH (square unfilled points).

ranging from several hundredths of nanometers to several tenths of micrometers (4–30 μm). As seen in Figure 1d, the microcapsules present a deep blue color which comes from a monolayer of densely packed gold nanoparticles on their surface as shown in Figure 1g. Under the high vacuum of the SEM, the gold silica capsules tend to buckle due to the thin silica shell. The silica shell thickness as measured from SEM images ranged between 30 and 60 nm.

To test the chromatic properties of the microcapsules, they were dried in a polymer matrix (PVA: polyvinyl alcohol), which can be further mechanically deformed. During the drying step, the silica crust provides the blue microcapsules with enough rigidity to retain their spherical shape as seen in Figure 3a. Their intrinsic color conferred to the film a slight blue color. After drying, a uniaxial stretching of the polymer film was then performed (See the Experimental Section for more information). A magnified view of the elongated polymer film displays pink stretched microcapsules as seen in Figure 3c. This color change is noticeable by the naked eye and is attributed to the deformation of the spherical microcapsules into an ellipsoid-like shape along with the increase of the interparticle distance, as schematically depicted in Figure 3d. Indeed, during this anisotropic deformation, the distance between the Au NPs increases, thus entailing a color change. To support this hypothesis, the film extinction curve was recorded by spectrophotometry for each stretching step. A typical extinction curve at low deformations of microcapsules results from two overlapping peaks. There is a first small

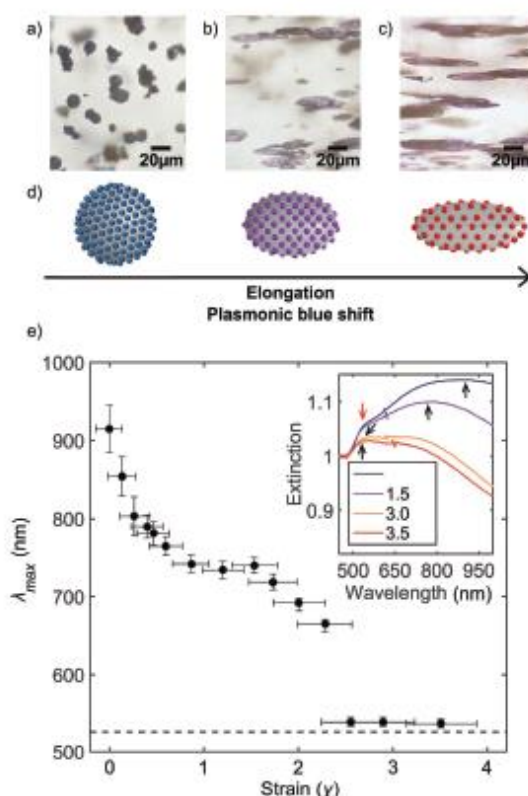


Figure 3. a–c) Microcapsules dispersed in dried PVA film: a) before strain, b) during strain, c) after strain. d) Schematic representation of the microcapsules shape deformation and visible colors under 1D mechanical stretching. e) Position of the plasmonic peak maximum as the polymer is elongated. Dashed line corresponds to the wavelength of maximum extinction of the Au NPs in water. Inset: UV response as a function of film strain, black arrows show where the maxima are detected, the red arrow corresponds to the position of the maximum of extinction of single Au NPs (the extinction is normalized at 450 nm).

plasmonic peak around 540 nm, indicated by a red arrow in the inset of Figure 3e, which corresponds to single Au NPs and a second broad plasmonic peak at a higher wavelength. The second peak at a higher wavelength is broad because of the very large number of dipolar couplings between the randomly placed Au NPs. As the microcapsules are stretched, the second peak's width decreases, its position shifts toward smaller wavelengths, and its amplitude decreases. The maximum of each extinction curve, λ_{max} , was measured by performing a crude first assessment of the position of the peak, followed by a more accurate measurement of the position of the maximum using a second-order polynomial fit around the maximum. Because the width of the second peak decreases as the particles are elongated, this procedure is fairly accurate at large deformations and less accurate at low deformations. λ_{max} was plotted as a function of the strain $\gamma = (L_t - L_0)/L_0$, where L_t is the length of the film after each stretching step and L_0 is the initial length of the film before

mechanical deformation as seen in Figure 3e. The error bars in Figure 3e reflect the difference in accuracy regarding the measurement of the position of λ_{\max} . The λ_{\max} -strain curve shows that for small strains ($\gamma < 0.3$), the film absorbs light in the red/infrared region ($\lambda_{\max} \approx 850\text{--}900$ nm) of the visible spectrum, thus appearing blue. As the amplitude of the strains increases, the optical properties of the microcapsules embedded in the film change and the maximum of the extinction curve is shifted toward the blue/green visible region of the spectrum ($\lambda_{\max} \approx 540$ nm), thus the film appears pink. At very large deformations of the microcapsules, the second peak of the extinction curve becomes weak in amplitude compared to the first peak of single particles, and hard to measure as both peaks overlap. At that point, we consider λ_{\max} to be the λ_{\max} of single particles. This is the reason why there is a jump in the λ_{\max} -strain curve in Figure 3c. This jump does not physically exist. λ_{\max} reaches a plateau when the absorption of the stretched microcapsules ($\lambda_{\max} \approx 540$ nm) is close to the absorption of the free Au NPs in solution ($\lambda_{\max} = 527$ nm, as represented by the dashed line in Figure 3c). The very small difference in the absorption wavelength (≈ 13 nm) is due to two phenomena: first, the silica shell surrounding the particles is known to displace the absorbance maximum of gold toward slightly larger wavelengths,^[45] and second, the absorbance maxima positions of the PVA film slightly shift to longer wavelength with increasing strain.^[46] The observed decrease of peak height extinction during stretching is attributed to the decrease of film thickness.^[46] So far we have demonstrated that the plasmon response of our films doped with AuSi microcapsules can be shifted from high wavelength number to low wavelength number by an increase of the average Au NPs interparticle distance through uniaxial strain of the microcapsules.

Finally, we tested the optical response of PVA films doped with microcapsules for two other mechanical deformations, namely impact and perforation tests. For the impact test, a 0.91 kg weight was dropped from several different heights on top of the film. The extinction was recorded for each impact height and the maximum of the extinction peak was plotted versus the kinetic energy of the weight at impact in Figure 4a. The graphs show that as the kinetic energy of the weight at impact increases, the extinction of the plasmonic peak shifts from the red/infrared region ($\lambda \approx 970$ nm) to the green/blue visible region of the spectrum ($\lambda \approx 540$ nm). Interestingly, at low impact energy, the analysis using the spectrophotometer exhibits a very small shift of the maximum of the plasmonic peak that cannot be detected by the human eye (circled in black on film on top picture, Figure 4a). At higher kinetic energy of impact, the human eye is capable of seeing the area of impact by noticing a red spot at the place of the impact zone as displayed in Figure 4a, bottom picture.

The second test consists in perforating the film. As a hole is poked in the film, the polymer film undergoes very large strains in the vicinity of the hole (white dashed circle in Figure 4b). Observations under an optical microscope show that the microcapsules lying far from the hole remain undisturbed and spherical and thus display a blue color as seen in Figure 4c, whereas those located close to the edge

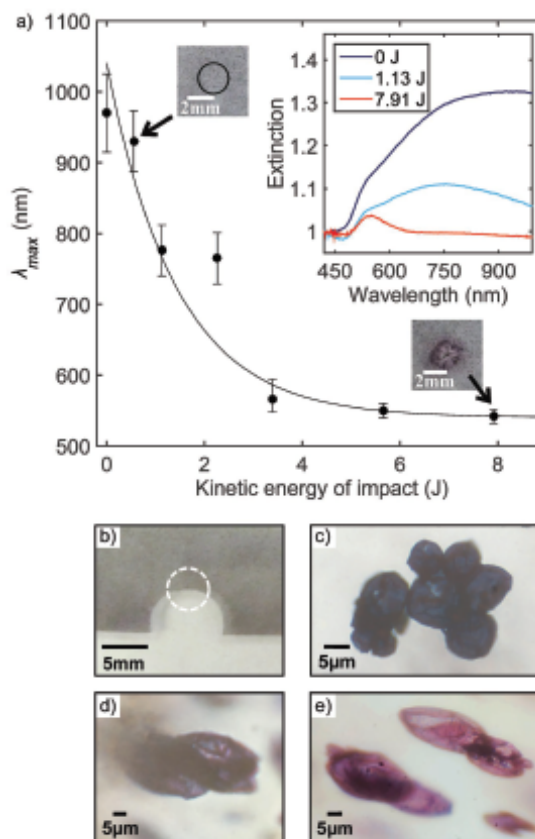


Figure 4. a) Position of the plasmonic peak maximum as a function of kinetic energy of impact, Inset; UV response as the polymer is impacted (the extinction is normalized at 420 nm), b) Picture of the pinched polymer film with embedded microcapsules, c–e) Optical microscope pictures of the microcapsules after pinching: c) far from the hole, d) closer to the hole, e) nearby to the hole.

of the perforation are likely deformed into an ellipsoidal shape as indicated by their purple (Figure 4d) and pink color (Figure 4e).

In conclusion, we have evidenced the synthesis of plasmonic-based microcapsules, which can be used as strain sensors. Our approach is based on controlled dense packing of Au NPs at the surface of emulsion droplets by tuning the charge of the nanoparticles. By solidifying the interface with PEOS, we obtained solid capsules made of Au NPs embedded in a silica crust. As the Au NPs are densely packed at the surface of the capsules, the microcapsule plasmon resonance is shifted toward the red region of the visible spectrum ($\lambda \approx 900\text{--}950$ nm). Moreover, when embedded in a polymer film any applied mechanical strain is found to deform the capsules, bringing the Au NPs further apart, therefore changing their extinction properties and underlying color. This is demonstrated by three experiments: a uniaxial strain, an impact test, and a perforation test. It has to be highlighted here that despite the broad distribution of the particles size and microcapsules dimensions, our prototypical sensory

device is sensitive enough to enable the detection of a color change by spectrophotometry arising from very tiny deformations not detectable by the eye. Moreover, our lab scale synthesis allows the fabrication of billions of microcapsules, each one of them being one opto-mechanosensor by itself. This number could be easily increased by scaling up our fabrication process. The underlying industrial potential applications are numerous. For instance, such mechanochromic shells mixed in paints, fabrics, or polymers could be used to gather local and/or global information about the material they have been embedded in; allowing the early detection of cracks or bullet/rock impact locations. Preliminary results showed that our method is not limited to Au NPs only, but can be applied to other types of nanoparticles. Silver nanoparticles, nanophosphors, or mixtures of nanoparticles can also be embedded in microcapsules shells potentially bringing other new functional properties to the microcapsules bearing them.

Experimental Section

Materials: Gold (III) chloride trihydrate (99.9%, Sigma-Aldrich), L-ascorbic acid (99%, Sigma-Aldrich), PEOS (Scientific Polymer Products Inc), hydrochloric acid (ACS reagent, 37%, Sigma-Aldrich), toluene (Chromasolv Plus, 99.9%, Sigma-Aldrich), 1-butanol (ACS reagent, 99.4%, Alfa Aesar), polyvinyl alcohol (PVA, 98%, Sigma-Aldrich), poly(diallyldimethylammoniumnitrate-co-1-vinylpyrrolidone (PVP-DADMAN, Solvay). Deionized water was used for all experiments unless specified otherwise.

Gold Nanoparticles Synthesis: The Au NPs used in this procedure were synthesized by reduction of HAuCl_4 with ascorbic acid in presence of PVP-DADMAN. A solution of 5.7×10^{-6} M PVP-DADMAN and 2.5×10^{-3} M HAuCl_4 was brought to boil. Then, 12.5 mL of ascorbic acid (0.1 M) was added. The solution protected from light by aluminum foil was stirred for 1 h at 97 °C. After synthesis, the Au NPs were left to rest for one day to remove the biggest nanoparticles. The rest of the dispersion was centrifuged and concentrated into a few milliliters solution.

Microcapsules Synthesis: 0.2 g of PEOS was diluted in 1 mL of toluene. The water phase of the emulsion contains a solution of diapered Au NPs with 0.2 mL of HCl and 0.1 mL of butanol. The oil and water phases were emulsified together with a Brandson 3210 ultrasonic bath at 30 °C for 15 min. After 3 d, the silica shell was fully formed. The microcapsules were recovered, cleaned, and concentrated by simple sedimentation.

PVA Films Preparation, Stretching, and Perforation: 20 g of a 10 wt% solution of PVA in water was prepared and degassed. Then the as-previously synthesized microcapsules were concentrated in 1 g of water and dispersed in the PVA solution under gentle stirring to avoid the formation of air bubbles, which could make the final film inhomogeneous and more fragile. The final polymer-microcapsules solution was left to dry at room temperature for several days. Stretching experiments were performed using a vise while heating the film above the glass transition. Perforation experiments were performed using a paper puncher.

Electron Microscopy: SEM was performed on JEOL 7500 HRSEM. The samples were prepared by air drying under ambient conditions by laying a drop of microcapsules dispersion in water

on an electron microscopy science carbon-coated copper grid. TEM was carried out on a JEOL JEM-1400 electro-microscope. The accelerating voltage was set at 120 kV.

Optical Characterizations: Optical microscopy images were acquired on an Olympus microscope in bright field and transmission mode. Optical extinction spectra were recorded in transmission mode using a Cary 5000 spectrophotometer.

pH Measurements: The pH of the Au NPs solutions was measured with a WWR Scientific digital pH temperature meter (model 8015).

Zeta Potential Measurements: The Zeta potential of the gold nanoparticle solutions ($[\text{Au}^0] = 0.574 \times 10^{-3}$ M and $[\text{NaCl}] = 10^{-2}$ M) in function of the pH was measured on a Zetasizer Nano Serie 200.

Chromatography Analysis: Size exclusion chromatography was conducted on two OligoPore columns in series with an Agilent refractive index detector in negative polarity. The mobile phase used was toluene at 1 mL min⁻¹ flow rate. The sample was dissolved in toluene at a 1% concentration. Calibration with polystyrene standards was used to estimate the molecular weight.

Supporting Information

Supporting Information is available from the Wiley Online Library or from the author.

Acknowledgements

The authors thank the ANRT, GIE AIFOR, CNRS, and Solvay for financial support. The authors acknowledge the support of the French National Agency of Research (ANR) to the project REACT through the grant ANR15-PIRE-0001-06. The authors also thank A. Yodh, J.-B. Salmon, J. Hutchinson, J. Jose, and A. Van Blaaderen for fruitful discussions.

Conflict of Interest

The authors declare no conflict of interest.

- [1] M. Naebe, M. M. Abolhasani, H. Khayyam, A. Amini, B. Fox, *Polym. Rev.* **2016**, *56*, 31.
- [2] H. Jiang, R. Browning, H. J. Sue, *Polymer* **2009**, *50*, 4056.
- [3] R. P. Kambour, *J. Polym. Sci. Macromol. Rev.* **1973**, *7*, 1.
- [4] W. Zhang, I. Srivastava, Y.-F. Zhu, C. R. Picu, N. A. Koratkar, *Small* **2009**, *5*, 1403.
- [5] M. A. Rafiee, J. Rafiee, I. Srivastava, Z. Wang, H. Song, Z.-Z. Yu, N. Koratkar, *Small* **2010**, *6*, 179.
- [6] A. Pawlak, A. Galeski, *J. Appl. Polym. Sci.* **2002**, *86*, 1436.
- [7] T. Shiga, T. Narita, K. Tachi, A. Okada, H. Takahashi, T. Kurauchi, *Polym. Eng. Sci.* **1997**, *37*, 24.
- [8] W. Li, C. C. Matthews, K. Yang, M. T. Odarzenko, S. R. White, N. R. Sottos, *Adv. Mater.* **2016**, *28*, 2189.
- [9] S. A. Odom, A. C. Jackson, A. M. Prokup, S. Chayanupatkul, N. R. Sottos, S. R. White, J. S. Moore, *Appl. Mater. Interfaces* **2011**, *3*, 4547.

- [10] S. Vidinejevs, A. N. Aniskevich, A. Gregor, M. Sjöberg, G. Alvarez, *J. Intell. Mater. Syst. Struct.* **2012**, *23*, 1371.
- [11] S. Vidinejevs, O. Strelakova, A. Aniskevich, S. Gaidukov, *Mech. Compos. Mater.* **2013**, *49*, 77.
- [12] D. A. Davis, A. Hamilton, J. Yang, L. D. Cremer, D. Van Gough, S. L. Potisek, M. T. Ong, P. V. Braun, T. J. Martínez, S. R. White, J. S. Moore, N. R. Sottos, *Nature* **2009**, *459*, 68.
- [13] R. Klajn, *Chem. Soc. Rev.* **2014**, *43*, 148.
- [14] B. R. Crenshaw, C. Weder, *Adv. Mater.* **2005**, *17*, 1471.
- [15] B. R. Crenshaw, M. Burnworth, D. Khariwala, A. Hiltner, P. T. Mather, R. Simha, C. Weder, *Macromolecules* **2007**, *40*, 2400.
- [16] F. Cellini, L. Block, J. Li, S. Khapli, S. D. Peterson, M. Porfiri, *Sens. Actuators, B* **2016**, *234*, 510.
- [17] A. Pucci, G. Ruggeri, *J. Mater. Chem.* **2011**, *21*, 8282.
- [18] D. R. T. Roberts, S. J. Holder, *J. Mater. Chem.* **2011**, *21*, 8256.
- [19] M. Kinami, B. R. Crenshaw, C. Weder, *Chem. Mater.* **2006**, *18*, 946.
- [20] V. Myroshnychenko, J. Rodríguez-Fernández, I. Pastoriza-Santos, A. M. Funston, C. Novo, P. Mulvaney, L. M. Liz-Marzán, F. J. García de Abajo, *Chem. Soc. Rev.* **2008**, *37*, 1792.
- [21] K.-H. Su, Q.-H. Wei, X. Zhang, *Nano Lett.* **2003**, *3*, 1087.
- [22] K. A. Willets, R. P. Van Duyne, *Annu. Rev. Phys. Chem.* **2007**, *58*, 267.
- [23] J. M. Slocik, J. S. Zabinski, D. M. Phillips, R. R. Naik, *Small* **2008**, *4*, 548.
- [24] L. Minati, A. Chiappini, C. Armellini, A. Carpentiero, D. Maniglio, A. Vaccari, L. Zur, A. Lukowiak, M. Ferrari, G. Speranza, *Mater. Chem. Phys.* **2017**, *192*, 94.
- [25] X. Han, Y. Liu, Y. Yin, *Nano Lett.* **2014**, *14*, 2466.
- [26] S. U. Pickering, *J. Chem. Soc., Trans.* **1907**, *91*, 2001.
- [27] J. Wu, G.-H. Ma, *Small* **2016**, *12*, 4633.
- [28] A. D. Dinsmore, M. F. Hsu, M. G. Nikolaidis, M. Marquez, A. R. Bausch, D. A. Weitz, *Science* **2002**, *298*, 1006.
- [29] H. Wang, X. Zhu, L. Tsarkova, A. Pich, M. Möller, *ACS Nano* **2011**, *5*, 3937.
- [30] T. Chen, P. J. Colver, S. A. F. Bon, *Adv. Mater.* **2007**, *19*, 2286.
- [31] D. Lee, D. A. Weitz, *Small* **2009**, *5*, 1932.
- [32] S. A. F. Bon, S. Cauwin, P. J. Colver, *Soft Matter* **2007**, *3*, 194.
- [33] Y. Zhao, Y. Li, D. E. Demco, X. Zhu, M. Möller, *Langmuir* **2014**, *30*, 4253.
- [34] B. Samanta, D. Patra, C. Subramani, Y. Ofir, G. Yesilbag, A. Sanyal, V. M. Rotello, *Small* **2009**, *5*, 685.
- [35] Y. Lin, A. Böker, H. Skaff, D. Cookson, A. D. Dinsmore, T. Emrick, T. P. Russell, *Langmuir* **2005**, *21*, 191.
- [36] Y. Lin, H. Skaff, T. Emrick, A. D. Dinsmore, T. P. Russell, *Science* **2003**, *299*, 226.
- [37] J. Saien, S. Akbari, *J. Chem. Eng. Data* **2006**, *51*, 1832.
- [38] J. Zhang, H. Liu, Z. Wang, N. Ming, *Adv. Funct. Mater.* **2007**, *17*, 3295.
- [39] C. Graf, D. L. J. Vossen, A. Imhof, A. Van Blaaderen, *Langmuir* **2003**, *19*, 6693.
- [40] C. Graf, S. Dembski, A. Hofmann, E. Rühl, *Langmuir* **2006**, *22*, 5604.
- [41] J. Rodríguez-Fernández, J. Pérez-Juste, F. J. García De Abajo, L. M. Liz-Marzán, *Langmuir* **2006**, *22*, 7007.
- [42] N. R. Jana, L. Gearheart, C. J. Murphy, *Langmuir* **2001**, *17*, 6782.
- [43] H. Xia, S. Bai, J. Hartmann, D. Wang, *Langmuir* **2010**, *26*, 3585.
- [44] L. Malassis, R. Dreyfus, R. J. Murphy, L. A. Hough, B. Donnio, C. B. Murray, *RSC Adv.* **2016**, *6*, 33092.
- [45] C. Fernández-López, C. Mateo-Mateo, R. A. Álvarez-Puebla, J. Pérez-Juste, I. Pastoriza-Santos, L. M. Liz-Marzán, *Langmuir* **2009**, *25*, 13894.
- [46] B. M. I. Van Der Zande, L. Pagès, R. A. M. Hikmet, A. Van Blaaderen, *J. Phys. Chem. B* **1999**, *103*, 5761.

Received: June 7, 2017
Revised: July 10, 2017
Published online:

Abstract

Nanoparticles (NPs) assembled into two- or three-dimensional architectures offer new collective optical, magnetic and electronic properties. For instance, closely packed gold (Au) and silver (Ag) nanoparticles absorb light at higher wavelength than when they are far apart.

In the first part of this thesis, the technique of microfluidic pervaporation is used to assemble micron size latex particles and gold NPs in bulky materials of controlled dimensions. By reducing the concentration of salts in the particles dispersions, the particles organize in hexagonal crystals. Millimeter-long materials of small well-organized densely packed particles are collected, offering solid groundwork as for the design of new functional microscale optomaterials.

In the second part of this thesis, the assembly of NPs on droplets is used to fabricate dispersed materials. By tuning the charges and wettability of gold and silver NPs, they adsorb and pack at the surface of emulsion droplets. A subsequent polymerization at the interface of the emulsion allows to lock the NPs inside an organic shell. NP-silica and NP-polyacrylate microcapsules are obtained by that process. The mechanical and optical properties of the microcapsules are tuned by the type and thickness of the organic shell and by the type of NPs and distance between the NPs. In well-defined conditions, novel microcapsules responsive to mechanical deformations and pH variations are engineered. Upon elongation, the Au NP-silica microcapsules change color. Upon increase of pH, the Au NPs-polyacrylate microcapsules swell and change color. The change of color of the different microcapsules is due to the increase of the distance between the Au NPs during the deformation of the capsules. Each one of the microcapsules being one sensor by itself, these results pave the way as for the design of new microscale sensors.

Résumé

Les nanoparticules (NPs) assemblées en architectures bi- ou tri-dimensionnelles présentent de nouvelles propriétés optiques, magnétiques et électroniques collectives. Par exemple, des particules d'argent (Ag) ou d'or (Au) absorbent la lumière à des longueurs d'onde plus grandes lorsqu'elles sont compactées que lorsqu'elles sont éloignées.

Dans la première partie de cette thèse, des microparticules de latex et des nanoparticules d'or sont assemblées par la technique de pervaporation microfluidique afin de former des matériaux denses aux dimensions contrôlées. En réduisant la concentration en sels contenus dans les dispersions de particules, ces dernières s'organisent en cristaux hexagonaux. Des matériaux millimétriques constitués de petites particules densément ordonnées sont collectés, offrant ainsi une base solide quant à la conception de nouveaux optomatériaux fonctionnels à l'échelle micrométrique.

Dans la seconde partie de cette thèse, des NPs d'or et d'argent sont assemblées sur des gouttes d'émulsion afin de fabriquer des matériaux dispersés. En contrôlant les charges et la mouillabilité des particules, celles-ci s'adsorbent et se compactent en surface de gouttes. Les NPs sont ensuite fixées dans une croûte organique par une polymérisation à l'interface de l'émulsion. Des microcapsules NP-silice et NP-polyacrylate sont obtenues par ce procédé. Les propriétés mécaniques et optiques des microcapsules sont ajustées en modifiant le type et l'épaisseur de l'écorce organique ainsi que le type et la distance entre les NPs. Dans des conditions bien définies, des microcapsules innovantes sensibles aux déformations mécaniques et aux variations de pH sont obtenues. Les microcapsules Au NP-silice changent de couleur lorsqu'elles sont étirées. Les microcapsules Au NP-polyacrylate gonflent et changent de couleur lorsque le pH augmente. Le changement de couleur des différentes microcapsules est dû à l'augmentation de la distance entre les Au NPs lors de la déformation des capsules. Chacune de ces microcapsules étant un capteur à elle toute seule, ces résultats ouvrent la voie vers la conception de nouveaux capteurs à l'échelle micrométrique.